Sensorless Vector Control of Surface Mounted Permanent Magnet Machines Without Restriction of Zero Frequency

by César Armando Silva

Submitted to the University of Nottingham for the degree of Doctor of Philosophy,

May 2003

Acknowledgments

I would like to express my most sincere gratitude to my supervisor Professor Greg M. Asher for his guidance and support over the course of this project. I would also like to thank Dr. Mark Sumner and Dr. Keith Bradley for their valuable assistance.

I would like to acknowledge the CVCP ORS AWARDS SCHEME for the financial support received to carry out this research work at The University of Nottingham.

Finally I would also like to thank all the academic staff, technical staff and friends and colleagues of the PEMC group at The University of Nottingham for providing such an enjoyable working environment and all their support during the course of this work. I would like to thank especially Dr. Nikolas Teske, Dr. Lee Empringham, Miss Liliana de Lillo and Dr. James Campbell for their help and friendship.

Contents

List of Figures

List of Symbols

Characterisation by Style of Writing:

i_q^*, ω_r^*	Reference value.
$\hat{\theta}_r$, $\hat{r}_s$	Estimated variable or parameter.
$\underline{\tilde{i}}_{\alpha\beta}$, $\tilde{i}_q$, $\tilde{v}_\alpha$	Injection component.

Symbols:

ψ_{sa}, ψ_{sb}, ψ_{sc}	Stator windings linkage fluxes.
ψ_m	Maximum flux linkage due to the rotor magnets.
$\underline{\psi}_r$	Flux linkage vector due to the rotor magnets.
$\underline{\psi}_s$	Stator linkage flux vector.
θ_δ	Saliency angle.
$\Delta\theta_\delta$	Error in the estimated saliency orientation.
θ_r	Rotor angle.
θ_s	Stator flux angle.
ω_δ	Saliency speed.
ω_i	Injection frequency.
ω_r	Rotor speed.
ζ	Saliency orientation error signal.
$\underline{e}$	Back-EMF induced by the rotor magnets.
$\underline{i}$	Stator current vector.
i_a, i_b, i_c	Stator phase currents.
$\underline{i}_{pos}$	Demodulated position signal vector.

i_{pos}^{α} , i_{pos}^{β}	Demodulated position signals.
$\underline{v}$	Stator voltage vector.
v_a , v_b , v_c	Stator phase-to-neutral voltages.
L_a , L_b , L_c	Stator windings self-inductances.
L_d , L_q	d and q-axis stator inductances.
L_δ , L_γ	δ and γ-axis stator inductances.
L_l , L_m	Leakage and magnetizing inductance.
$\overline{L}_m$	Average magnetizing inductance.
ΔL_m	Magnetizing inductance difference (salient machines).
L_s	Stator inductance matrix.
L_s	Average stator inductance.
ΔL_s	Stator inductance difference (salient machines).
M_{ab} , M_{bc} , M_{ca}	Stator windings mutual inductances.
r_s	Stator resistance.
t	Time.
T_e	Electric torque.
Y_s	Inverse stator inductance matrix.

Subscripts:

$\underline{i}_{\alpha\beta}$, $\underline{v}_{\alpha\beta}$	$\alpha\beta$ denotes variables in stator reference frame.
$\underline{i}_{dq}$, $\underline{v}_{dq}$	dq denotes variables in rotor oriented reference frame.
$\underline{\tilde{i}}_{\delta\gamma}$	$\delta\gamma$ denotes variables in saliency oriented reference frame.
$\underline{i}_{ps}$, $\underline{i}_{ns}$	ps and ns denotes positive and negative sequence respectively

Superscripts:

$\tilde{i}_{\delta}^{e}$, $\tilde{i}_{\gamma}^{e}$.	e denotes variables in a estimated $\delta\gamma$ frame.
$\tilde{i}_{\delta}^{m}$, $\tilde{i}_{\gamma}^{m}$	m denotes variables in a measurement $\delta\gamma$ frame.
$\underline{\hat{\psi}}_{s\,\alpha\beta}^{v}$, $\underline{\hat{\psi}}_{r}^{v}$	v denotes flux estimated using voltage model.

$\underline{\hat{\psi}}^{c}_{s\,\alpha\beta}$, $\underline{\hat{\psi}}^{c}_{r}$	*c* denotes flux estimated using current model.
$\underline{\hat{\psi}}^{inj}_{r}$, $\hat{\theta}^{inj}_{r}$	*inj* denotes variables estimated using the injection method.

Abstract

Permanent magnet motors have a series of characteristics that make them attractive for the use in industrial drives: low maintenance, high dynamics, small size and mass to power ratio. In particular its higher efficiency means that permanent magnet synchronous motors may be used instead of electro-magnetically exited motors (such induction machines or commutator DC motors) in applications where the energy savings compensate the higher initial cost. Nevertheless, the need for a shaft mounted position measurement to perform the orientation of the control of the synchronous machine is of concern, because it increases the total drive cost and reduces reliability.

In this work the sensorless vector control of a surface mounted permanent magnet machine is presented. The emphasis is in the control at low and zero speed, including position control, by means of saturation saliency tracking. Two different strategies for rotor position detection used in salient synchronous machines and in induction machines are analysed. These are *hf* voltage injection in the stationary, stator, reference frame of the machine (α-β injection) and *hf* voltage injection on the estimated rotor axis (so called *d-axis* or pulsating injection). These two methods are optimised for its application to the surface mounted PM machine. The small magnitude of the saliency present difficulties and disturbances are significant. A commissioning based method (SMP) is used for enhanced rotor position estimation by the α-β rotating injection. The two methods are implemented on a 4 kW experimental rig and the sensorless controlled results are compared and discussed. A hybrid structure combining the saliency tracking method with a flux-observer is also presented and provides sensorless control capability over the whole speed range.

Chapter 1

1 Introduction

1.1 PM machines

As it's name indicates permanent magnet (PM) machines are characterised by the use of magnetic material to establish the flux. Several designs of PM machines are possible and they are broadly catalogue into brushless DC and AC synchronous motors. This thesis deals with the sensorless control at low/zero speed of AC synchronous machines.

In a modern industrialized country about 65% of the electrical energy is consumed by electrical drives [1]. The cage induction motor (IM) is by far the most used motor with the majority of them running directly from the mains supply. The development of semiconductor power converters, microprocessors and high performance control techniques has resulted in considerable expansion of the use of cage induction machines for a wide range of applications. The popularity of the cage IMs arises from their low initial cost, minimal maintenance due to the lack of commutator or slip-rings and high reliability. While IMs still dominate the industrial drives market, considerable attention has been given to permanent magnet motors since the use of permanent magnets to replace electromagnetic field excitation in electric machines has several advantages.

The most obvious advantage for using permanent magnets to replace electromagnetic excitation is the absence of excitation losses which increases the efficiency of the

motor. Additionally, the placement of the magnets in the rotor concentrate the conduction losses in the stator where they are easily dissipated. This allows for smaller rotor diameters and smaller total motor sizes, resulting in high power density and low rotor inertia. The use of high energy magnets produces a high torque per ampere constant giving PM motors superior dynamic performance than that of conventional DC or IM dives. The use of magnets in the rotor to generate the machines flux overcomes the need for brushes and hence such motors are often called "brushless motors". This simple construction results in low maintenance and reliable machines normally built with totally enclosed rotors.

The above advantages have meant that the PM machine has found use in a wide variety of applications. The most common application of PM motors in industry is in machine tools and position servomotors where their high dynamic performances and low maintenance have meant that they have replaced the conventional DC machines. The PM machine's high power density means an overall weight and volume significantly less than those of other type of machines for the same power output. This has meant that it is increasingly attractive for drives in aerospace applications such on aircraft actuators where size and weight are major constraints [2, 3].

The PM machines also have the potential of replacing IMs in general industrial and domestic applications due to their high efficiency and hence energy-saving capability. It is possible that PM machines will be introduced in applications where the savings in energy offset the higher initial cost [4, 5].

1.1.1 Permanent Magnet Materials

A basic knowledge of permanent magnet materials is needed to understand the operation and limitations of PM machines. A permanent magnet produces a magnetic field in an air gap in the absence of current. The most common magnetic materials are Alnicos (Al, Ni, Co, Fe), Ceramics (or Ferrites) and Rare-earth materials such as samarium-cobalt (SmCo) and neodymium-iron-boron (NdFeB). A Typical demagnetisation curves for these PM materials are shown in Fig.1.1. The slope of the demagnetisation curve or recoil permeability of rare earth materials is nearly that of

the air with relative permeability values μ_r ranging typically between 1 and 1.1. Hence the magnet behaves like a constant MMF source. Rare earth magnets can operated in any point upon the third quadrant of the hysteresis curve as shown in Fig. 1.1. However, if an external current reduced the flux density below the knee upon the curve (B_D) the magnet will recoil through a parallel but lower trajectory suffering some permanent demagnetisation.

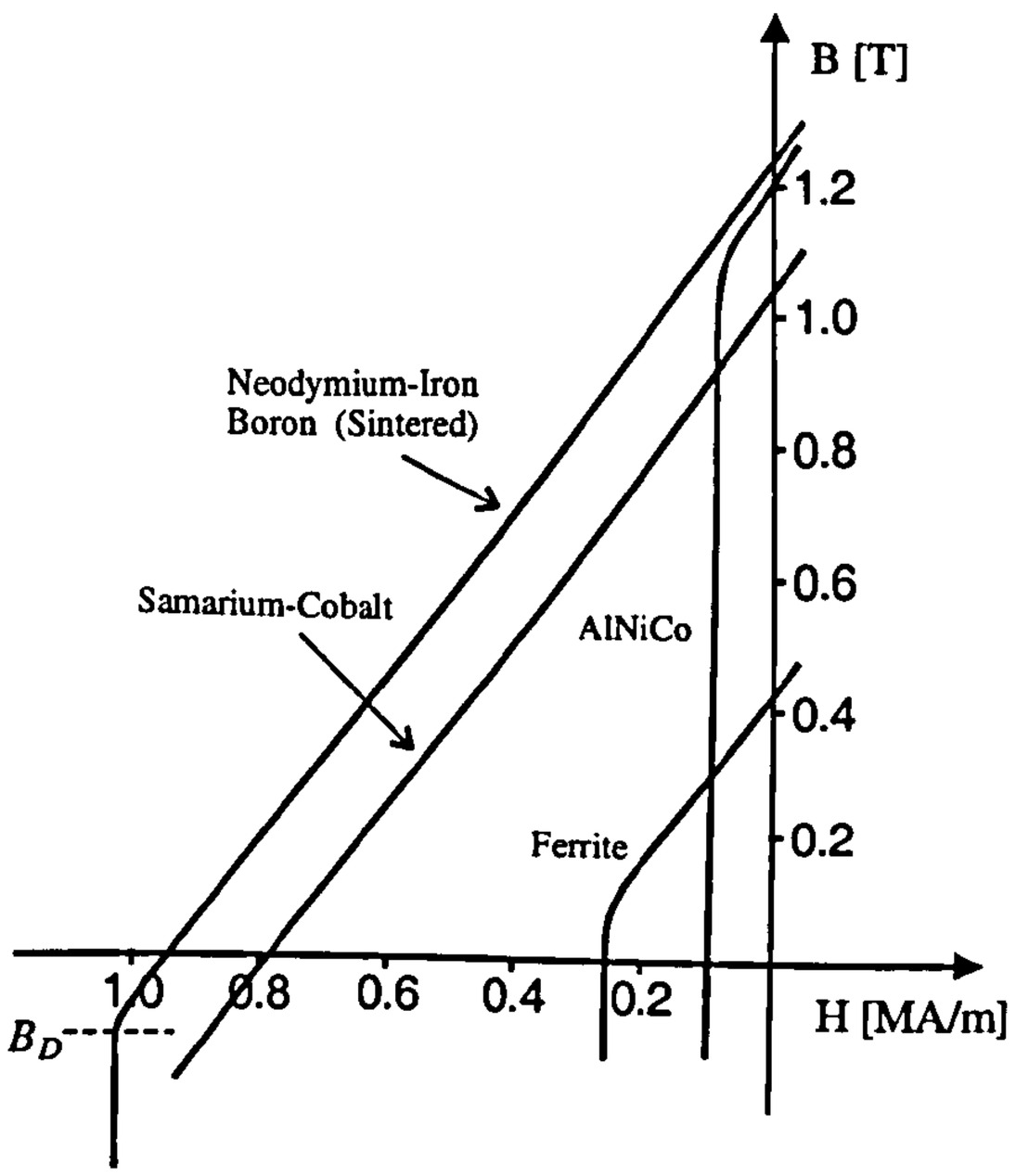

Figure 1.1: Typical demagnetisation curves of different PM materials.

Due to the superior characteristics of high remnant flux density B_r, high coercive force H_c, high energy product $BH_{\max}$ and linear de-magnetization curve in the third quadrant, rare earth magnets are the material used in servomotors (synchronous and brushless DC motors). The value of B_r of rare earth materials is sufficiently high to produce flux densities across an air gap at values 0.8-0.9 T (with reasonable thickness of the magnet material) so achieving good use of the machine's iron and higher power densities.

Since its introduction in 1983, sintered NdFeB magnets have become widely used in PM motors displacing SmCo and boosting the PM motor technology. This is because NdFeB has superior magnetic characteristics at room temperature and a relative lower cost due to the use of a more abundant rare earth (Nd) and cheaper metals [5]. The

major drawback of NdFeB is the strong dependence of its characteristics on temperature. In particular a steep rise in the demagnetisation curve's knee results in a high coercivity temperature coefficient H_c in the range of 0.40 %/°C to 0.80 %/°C. This limits the maximum working temperature to 100-140 °C. SmCo also is sensitive to temperature although it exhibits more stable characteristics allowing working temperatures of up to 250 °C [6].

1.1.2 PM Motors Types

Permanent magnets are constructed in a wide variety of motor designs. The two major classes of PM motors are the brushless DC motor and the synchronous PM motor, sometime referred as the brushless AC motor. It is noted that permanent magnet materials are also used in small conventional commutator DC motors and small stepper motors.

The brushless DC and the PM synchronous are structurally very similar. The magnets are placed on or in the rotor and a poly-phase wound stator is used avoiding the need for commutator or slip-ring; hence their name brushless. Despite the popular name 'brushless DC' both constructions are poly-phase AC machines and predominantly three-phase. For these machines to produce torque the excitation waveform needs to be synchronized with the rotor position. This requires a power converter to generate the excitation, normally a voltage source inverter, and a shaft-mounted position sensor to perform the synchronisation. The main difference between the two machine types is the shape of the back-EMF induced in the stator windings. This results in different excitation waveforms required for their control and hence in the way the driving power converter is commutated.

1.1.2.1 The brushless DC motor

Structurally the brushless DC machine is characterised by wide arc magnet poles of constant thickness mounted on the surface of the rotor and inducing trapezoidal back-EMF in the concentrated stator windings. The resulting amplitude of the back-EMF

and torque equations are very similar to that of the DC commutator motor. The driving inverter acts like an electrical commutator switching stator current to different stator phases depending on the rotor position. The converter also carries out the current amplitude regulation. Both functions are relatively independent, resulting in a simple torque control algorithm, which requires the rotor position to be known only at six points per electrical cycle. This is usually achieved with optical sensors. The ideal operation of this motor would result in ripple-free torque but in practice fringing and imperfect phase commutation result in considerable periodic torque ripple at a frequency of $6f_e$ [4, 6].

1.1.2.2 PM synchronous motors

The ideal back-EMF induced in a synchronous PM machine is sinusoidal. In practice good quasi-sinusoidal waveforms are obtained. This is achieved by distributed AC stator windings like those of a wound rotor synchronous motor and by shorter magnet pole arc on the rotor, typically 120°. Therefore constant torque with very low ripple is produced when synchronous sinusoidal currents flow through the stator windings. This construction is a classical AC synchronous machine and therefore runs from a balanced three-phase sinusoidal supply generated by the driving inverter. The rotor of the synchronous PM machine can be constructed in different configurations giving rise to two main types of synchronous PM machines: the surface mounted PM (SMPM) and the interior PM machine (IPM). Both are shown in Fig 1.2.

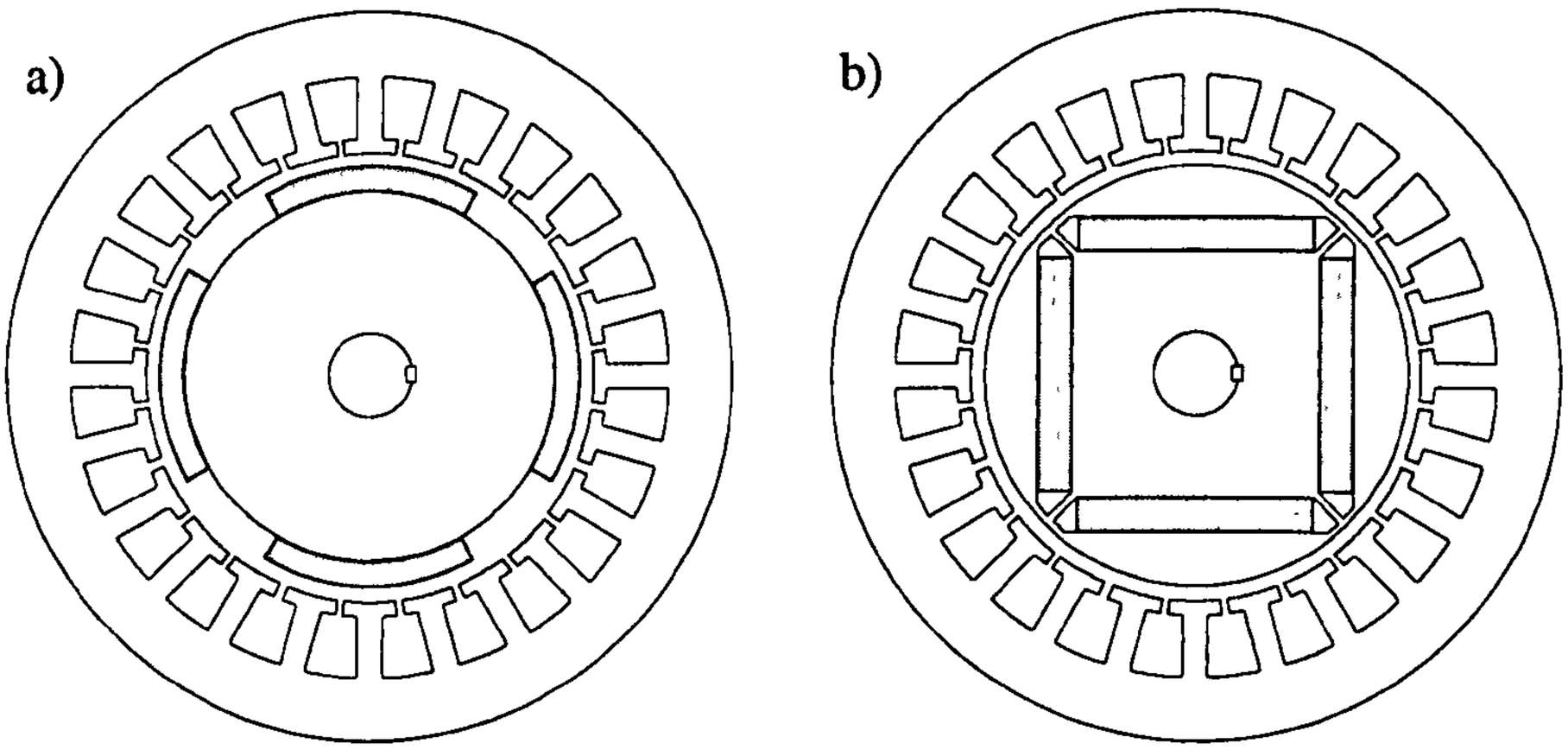

Figure 1.2: Different rotor designs. a) SMPM, b) IPM.

The surface mounted PM machine of (SMPM) is used widely and has a basic rotor design consisting on a cylindrical iron core with the magnets fixed to its surface with epoxy adhesive, generating a radial flux on the air gap. A non-ferromagnetic cylinder may be used to secure the magnets in place under strong centrifugal force. In this type of rotors the thickness of the magnets may be tapered in *bread-loaf* or *decentred* shapes [1] to better approximate a sinusoidal distribution of the magnet flux across the air gap. Because the rare earth magnet's relative permeability is close to unity, the surface mounted PM machine presents a constant effective air gap length resulting in a geometrically non-salient machine. A variation on this design is obtained by placing the magnets in shallow slots in the rotor surface crating an inset-magnet rotor [1]. This is done mainly to increase the mechanical robustness of the rotor. Because of the raised edges of the slots some level of geometric saliency occurs.

The interior-magnet machine (IPM) [7] shown in Fig. 1.2 (b) has rectangular magnets placed in slots inside the rotor. This construction retains the magnets against the centrifugal force and provides some protection against demagnetisation. The magnets are diametrically magnetized and are of alternate poles generating a radial flux in the air gap. The flux in the direction of the magnets (called *d-axis flux*) crosses the magnets in a high reluctance path. The quadrature flux (*q-axis flux*) however, is closed through the steel poles without crossing the magnets resulting in low reluctance path. Therefore the interior PM motor is highly salient with $L_q > L_d$. This causes a significant amount of reluctance torque, this characteristic providing extra torque under flux weakening and making this machine better suited for operation in this region [8, 9].

As a consequence of the sinusoidal back-EMF and the sinusoidal distribution of the windings the PM synchronous motor produce smoother torque than brushless DC machines. The shape of the back-EMF also allows the operation of the PMSM from standard AC drives. Hence the PMSM is considered adequate for a wider range of applications than the brushless DC machine and consequently is built in a wider power range. For these reasons, in this work the focus is on the sensorless control for PM synchronous machines and brushless DC machines are not considered.

1.2 Sensorless Control of PM Synchronous Machines

Both types of synchronous PM machines, the SMPM and IPM are true synchronous machines in the sense that they don't have any rotor damping circuit and can only develop average torque if the stator excitation is properly synchronised with the rotor position. Although, early developments in PM AC machines included rotor cages to produce asynchronous line start capabilities [1, 4], this is not the case with modern high performance PM motors which are designed to operate from a power converter. Therefore the PM AC drive requires rotor position information to perform the flux orientation or *vector control* [10] of the inverter output currents. The most direct way to guarantee the synchronisation is to measure rotor position. For this reason commercial PM AC drives are fitted with a shaft mounted position sensor, normally an optical encoder or a *sin-cos* resolver. The ability to detect the rotor position, and perform the orientation of the vector control without such a position sensor is normally referred to as *sensorless vector control.* Sensorless control is desirable in many applications due to the transducer's cost that can be a significant portion of the total drive's cost, specially in small drives. In addition, the fragility of the position sensors, the mechanical mounting and the electrical connections all undermine the overall drives' robustness and reliability.

The majority of the methods proposed for sensorless estimation of the rotor position consists of the processing of the fundamental stator quantities i.e. voltage and currents, to determine the amplitude and orientation of the machine's flux. These methods rely on a mathematical model of the machine with estimated parameter values, and are generically referred as *model-based methods*. One of the simplest of such methods consist of an open loop estimation of the stator linkage flux by the integration of the stator voltage corrected by the windings resistive drop [11]. The resulting stator flux orientation is not the optimal frame of reference for vector control [4] and therefore strategies to estimate the flux induced by the rotor magnets or rotor position are normally used. To this end, model based reference adaptive system (MRAS) [12], full order observers [13], reduced order observers [14, 15] or Kalman filters [16, 17] have been proposed. All the model-based methods rely directly or indirectly on the back-EMF induced by the rotor magnets in the stator windings of the machine, or the effect of the induced back-EMF on the stator currents. This has the

drawback that, as the speed decreases, the back-EMF goes to zero causing operation at zero speed to break down. Furthermore at low speeds the increasing influence of parameter estimation error, specially stator resistance, due to the decreasing magnitude of the EMF, impose a lower limit to the speed at which model-based methods work.

Many industrial applications such as fans, pumps and compressors operate normally only at medium and high speeds. Adjustable speed drives are suitable for these kinds of applications mainly for the energy saving potential over its speed range so that zero\low speed control capability is not required. Model based methods are the most viable sensorless strategy for these kinds of applications. For these drives, an open-loop starting up procedure to accelerate the machine form standstill to a minimum speed at which the model-based sensorless method estimate the flux reliably is sufficient. For example in [11] a method is proposed by injecting into the stator winding a balanced three-phase current set of constant amplitude and slowly increasing frequency to force the rotor to lock to the rotating MMF generated.

For all applications where constant operation at low or zero speed is required, including position control applications, the model-based sensorless method are not appropriate. A non-model based approach has to be found.

As discussed previously, the rotor geometry of the interior permanent magnet machine (IPM) gives a highly salient machine. In fact the ratio of the stator inductance variation as the rotor rotates is about 3:1 [6, 18]. Detection of this variation with rotor position was proposed in the early 90's a way of tracking rotor position in this type of machines IPM machines [19-21]. To track saliency the effect of the stator inductance change in the amplitude of a high frequency (*hf*) signal is measured. Although some authors have proposed to measure the current switching harmonies [19], in general this is not viable with a standard PWM actuation. Therefore a test *hf* signal is injected. A voltage injection can be applied either by modifying the PWM [22, 23], by injecting discrete test pulses [20] or by superimposing a *hf* carrier to the voltage reference [18, 21]. In all these techniques the resulting switching or *hf* currents are measured. The non-model based sensorless methods have the advantage of not being speed dependent and therefore are well suited for low/zero speed position

detection. The surface mounted PM machine rotor on the other hand is geometrically non-salient and therefore it is not a natural candidate for the application of saliency tracking techniques.

Saliency tracking through high frequency injection has become established as a very active research field in the last years and has included other salient machines such as the Synchronous Reluctance motors [24], and induction machines, the latter being made salient by means of engineering asymmetries in the rotor surface [25, 26] or by tracking higher frequency rotor slot saliencies [27-31]. One of the conclusions of the research on IMs is that magnetic saturation causes saliencies that interfere with the tracking of the rotor [30, 32]. In surface mounted PM machines the flux is mainly produced by the rotor magnets and therefore the saturation saliency is expected to be largely aligned with the rotor position. Only recently has some research attention been conducted to exploit saturation saliency for the control of SMPM [33, 34]. The magnitude of the saturation-induced saliency will depend on the magnetic design of each particular machine, but in general it can be affirmed that its magnitude is significantly smaller than that of the geometrical saliency of the IPM machine.

1.3 Overview of the Research

This thesis principally investigate different types of *hf* voltage signal injection to track saliency position and hence derive rotor position for the closed loop sensorless control of an off-the-shelf surface mounted PM motor at zero and low speeds. The techniques works within a vector control environment so the dynamic equations of the machine and vector control are briefly described in Chapter 2. This Chapter also reviews model-based sensorless methods and illustrates their shortcomings through the experimental investigation of a MRAS sensorless scheme. Deterioration of its performance at low speed is shown.

As mentioned, surface mounted PM machines are normally thought to be non-salient. Nevertheless, a measurable saliency is expected due to the saturation of portions of the machine's iron induced by the high flux density of the rotor magnets. This saturation-induced saliency can be exploited for sensorless control of this type of

machine at low/zero speed. Both the physical aspects of saliency in surface mounted PM machines and the mathematical theory of the different *hf* voltage injection strategies are described in Chapter 3. Different methods of *hf* continuous voltage injection have being reported mainly on induction machines. These methods can be divided in to stationary frame rotating voltage injection [21, 27] and synchronous frame pulsating voltage injection [35]. Although, the application of both methods have been reported for salient IPM machines [18, 36] and synchronous reluctance machines [24], no previous work on applications to SMPM machine existed. Since the start of the present work, two publications applying synchronous frame pulsating voltage injection to this type of machine have appeared [33, 34]. The present work addresses both techniques and provides a comparative analysis under sensorless controlled conditions. The theory of the two considered type of injection and their demodulation structures is discussed in Chapter 3.

The injection methods will be experimentally assessed in a 4 kW off-the-shelf surface mounted PM machine. A test rig has been constructed by interfacing a commercial inverter to drive this machine and a Texas Instrument DSP, the TMS-320C44, performs the vector control and the sensorless position estimation. Chapter 4 deals with the test rig description including the hardware boards constructed for interfacing the inverter to the DSP and to measure the electrical variables of the motor. An overview of the control software is also presented.

Experimental results show clearly that the position tracking using signal injection techniques is not perfect in that the demodulation signals are not sinusoidal but contain harmonics. These are due to the effect of inverter non-linearities such as dead-time and also to some spatial harmonics in the saturation saliency. Hence the closed loop performance in terms of positioning accuracy and dynamic bandwidth will be poor. Chapter 5 deals with ways of improving the position estimate to a level where it can be practically used in a sensorless positioning control. The Chapter also reviews the applicability of these signal enhancing methods for different techniques of injection.

Chapter 6 deals with the closed loop performance of the position and low-speed sensorless vector control of both strategies discussed in Chapter 3. The accuracy and

dynamic results yield by both methods are compared to each other and discussed in relation to that of other researchers. The Chapter also discusses the necessity of embedding the injection methodology in a overall sensorless structure in which a model-based observer takes over above a given threshold frequency. A novel technique is proposed and implemented allowing wide speed range sensorless control that includes zero-speed and positioning operation.

Chapter 2

2 Control of AC Permanent Magnet Machines

This chapter covers the mathematical background for the control of the PM synchronous machine. First the dynamic model of the machine is developed and presented in the two-axis static reference frame and then rotated into the synchronous frame (Park-Transformation) standard for flux-oriented control of synchronous motors. Magnetic saturation is neglected at this stage although the structural saliency characteristic of IPM machines is included to introduce the mathematical treatment of the phenomenon of saliency. The standard vector control structure for the non-salient SMPM is presented and the differences on the control for the IPM are discussed.

From the equations deduced in this chapter, it will be shown that, to achieve vector control of the PM machine, rotor position information is needed to perform the orientation and to derive the feedback signals of position and speed. For this reason standard PM machine drives are normally fitted with position measurement devices such as analog resolvers or digital encoders. The advantages of obtaining this information by other means than direct rotor position measurement are not only economical but also reliability and will be further discussed. Finally the fundamental frequency model of the motor, developed in this chapter, can be exploited to develop flux observers in order to estimate rotor position. However there are practical and theoretical limitations that prevent the application of this technique at very low/zero speed. The short-comings of the model-based methods will be discussed and experimental results of one model-based observer implementation will be shown to illustrate these shortcomings.

2.1 Dynamic Equations and Control for PM Synchronous Machines

The stator of a synchronous PM machine has quasi-sinusoidally distributed windings similar to those of an induction motor (IM). In addition, the magnet flux distribution in the air gap is also made more sinusoidal by means of shortened pole arcs and, in the case of surface mounted magnets, the magnets may be tapered. This produces phase linkage flux and back-EMF which are indeed quasi sinusoidal, allowing the analysis of the PMSM machine using the *space-vector* or *space-phasor* theory [10, 37, 38]. In the following analysis the assumption of sinusoidally distributed windings and sinusoidal flux linkage is made.

2.1.1 Space Vector Transformation

The space vector theory combines the individual phase quantities in to a single vector in the complex plane allowing simple handling and transformation to any rotating frame. In the space vector transformation the direction of magnetic axis of each phase is assigned to its electrical quantities. If the real axis α is aligned with the magnetic axis of phase *a*, as shown in Fig. 2.1, the transformation for the phase currents is given by (2.1). Different scaling factors for the vector transformation may be used. The definition introduced in [38], with a scaling factor of 2/3 to preserve the amplitude of the phase quantities, is used in the present work. By imposing the condition of an isolated neutral (2.2), the simplified expressions (2.3) for the real and imaginary components of the current vector are obtained.

$$\underline{i}_{\alpha\beta} = \frac{2}{3}\left(i_a(t) + i_b(t)e^{j\frac{2\pi}{3}} + i_c(t)e^{j\frac{4\pi}{3}} \right) \tag{2.1}$$

$$i_a(t) + i_b(t) + i_c(t) = 0 \tag{2.2}$$

$$i_\alpha = i_a(t)$$

$$i_\beta = \frac{\sqrt{3}}{3}\left(i_b(t) - i_c(t)\right) \tag{2.3}$$

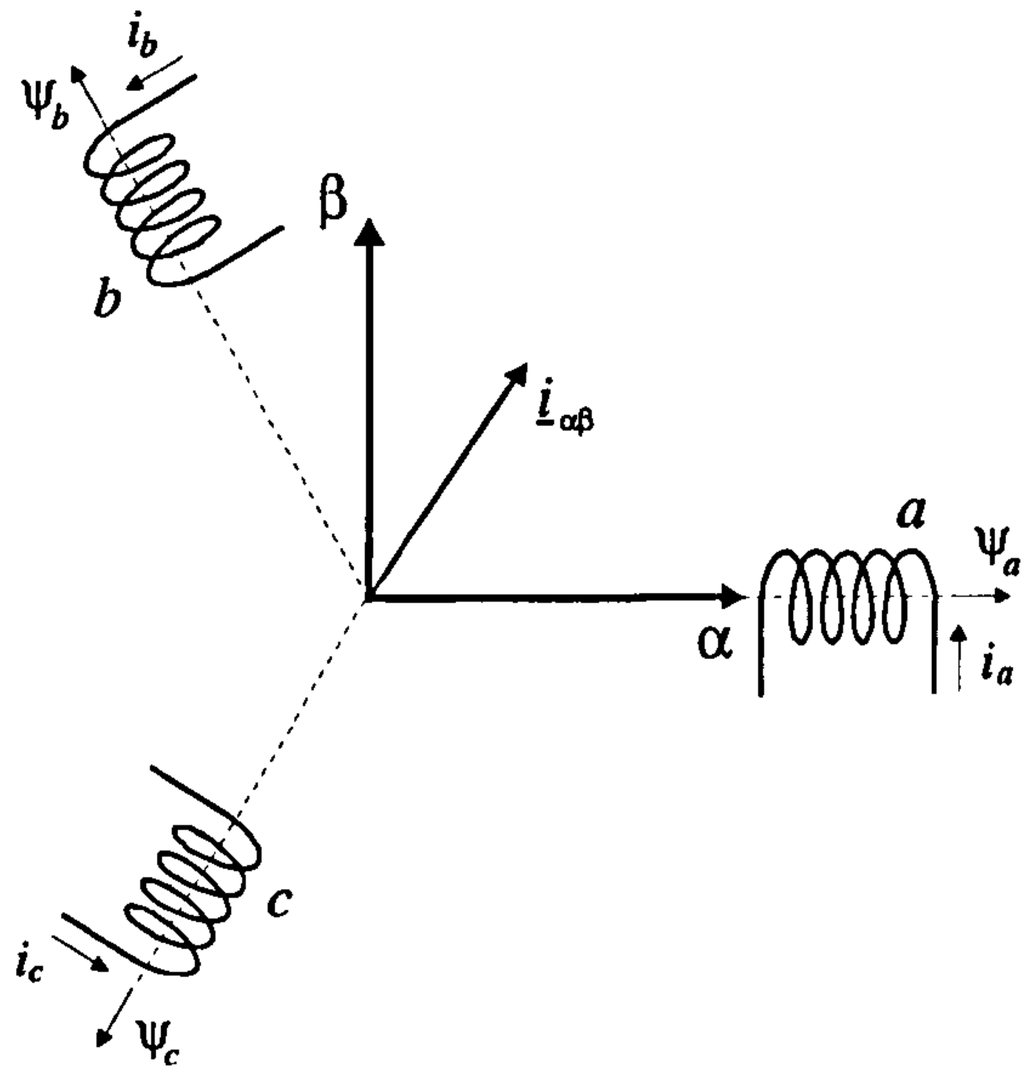

Figure 2.1: Definition of static α-β frame.

Similar transformations are applied to the remaining machine variables to obtain the stator voltages vector $\underline{v}_s$ and stator linkage flux $\underline{\psi}_s$.

A major advantage of this transformation is that the space vectors may be express in any arbitrary rotating *d-q* frame by means of a coordinates rotation (2.4). Of particular interest for the control of synchronous machines is the rotating frame oriented with the rotor field [4], i.e. $\varphi = \theta_r$.

$$\underline{i}_{dq} = \underline{i}_{\alpha\beta} e^{-j\varphi} \tag{2.4}$$

2.1.2 Dynamic Model of the PMSM machine

The basic equations for phase windings voltages of a permanent magnet synchronous machine is:

$$\begin{bmatrix} v_a \\ v_b \\ v_c \end{bmatrix} = r_s \begin{bmatrix} i_a \\ i_b \\ i_c \end{bmatrix} + \frac{d}{dt} \begin{bmatrix} \psi_a \\ \psi_b \\ \psi_c \end{bmatrix} \tag{2.5}$$

In (2.5), the total linkage flux in each phase ψ_a, ψ_b and ψ_c are given by:

$$\begin{bmatrix} \psi_a \\ \psi_b \\ \psi_c \end{bmatrix} = \begin{bmatrix} L_a & M_{ab} & M_{ac} \\ M_{ba} & L_b & M_{bc} \\ M_{ca} & M_{cb} & L_c \end{bmatrix} \cdot \begin{bmatrix} i_a \\ i_b \\ i_c \end{bmatrix} + \psi_m \begin{bmatrix} \cos(\theta_r) \\ \cos(\theta_r - \frac{2\pi}{3}) \\ \cos(\theta_r - \frac{4\pi}{3}) \end{bmatrix} \tag{2.6}$$

where ψ_m is the magnitude of the flux produced by the rotor magnet in each phase when it is aligned with the phase's magnetic axis.

Equations (2.5) and (2.6) are general, i.e. they apply for both types of PM synchronous machines, SMPM and IPM. In the later case, the inherent saliency produces inductances values in (2.6) which are functions of the rotor position. It must be noticed that by reciprocity, the corresponding mutual inductances are equal i.e. $M_{ab} = M_{ba}$, $M_{bc} = M_{cb}$ and $M_{ca} = M_{ac}$. For simplicity the non-salient case of the SMPM machine is first analysed.

For the SMPM machine, by symmetry the values of the self inductances L_a, L_b and L_c have the same value and consist of two components; the leakage inductance L_l and the magnetizing inductance L_m:

$$L_a = L_b = L_c = L_l + L_m \tag{2.7}$$

Due to the angular displacement of the phase windings it can be shown that the mutual inductances are given by:

$$M_{ab} = M_{bc} = M_{ca} = -\frac{L_m}{2} \tag{2.8}$$

Replacing the inductances values (2.7), (2.8) into (2.5) and (2.6) and applying the space vector transformation (2.1), the voltage vector equation in the stationary α-β frame is:

$$\begin{bmatrix} v_\alpha \\ v_\beta \end{bmatrix} = r_s \begin{bmatrix} i_\alpha \\ i_\beta \end{bmatrix} + \left(L_l + \frac{3}{2} L_m \right) \frac{d}{dt} \begin{bmatrix} i_\alpha \\ i_\beta \end{bmatrix} + \psi_m \frac{d}{dt} \begin{bmatrix} \cos(\theta_r) \\ \cos(\theta_r - \frac{\pi}{2}) \end{bmatrix} \tag{2.9}$$

In the IPM machine, due to the low recoil permeability of the magnets $(\mu_r \approx \mu_0)$ the effective air-gap length is larger in the direction of the rotor field (*d-axis*) than it is in the perpendicular direction (*q-axis*); this produces a variation of the stator phase inductances as functions of the rotor position. This is termed saliency. In the following analysis it will be assumed that the variation of the air-gap does not affect the leakage inductances. This is a reasonable assumption due to the large air-gap characteristic of PM machines. By considering only the fundamental variation of the inductances (fundamental saliency) [38], the stator phase inductances may be expressed as:

$$\begin{aligned} L_a &= L_l + \bar{L}_m - \Delta L_m \cos(2\theta_r) \\ L_b &= L_l + \bar{L}_m - \Delta L_m \cos(2\theta_r - \tfrac{4\pi}{3}) \\ L_a &= L_l + \bar{L}_m - \Delta L_m \cos(2\theta_r - \tfrac{2\pi}{3}) \end{aligned} \tag{2.10}$$

This equation indicates that the maximum phase inductance is obtained when the minimum reluctance path of the rotor (*q-axis*) is oriented with the magnetic axis of each phase. Similarly, the mutual inductances are given by:

$$M_{ab} = -\frac{\bar{L}_m}{2} - \Delta L_m \cos(2\theta_r - \tfrac{2\pi}{3})$$
$$M_{bc} = -\frac{\bar{L}_m}{2} - \Delta L_m \cos(2\theta_r) \qquad (2.11)$$
$$M_{ca} = -\frac{\bar{L}_m}{2} - \Delta L_m \cos(2\theta_r - \tfrac{4\pi}{3})$$

Applying (2.1) to the general three phase PM machine (2.5) and (2.6), and using the inductance values given by (2.10) and (2.11), yields the α-β model for the salient IPM given by:

$$\begin{bmatrix} v_\alpha \\ v_\beta \end{bmatrix} = r_s \begin{bmatrix} i_\alpha \\ i_\beta \end{bmatrix} + \frac{d}{dt}\begin{bmatrix} L_s - \Delta L_s \cos(2\theta_r) & \Delta L_s \sin(2\theta_r) \\ \Delta L_s \sin(2\theta_r) & L_s + \Delta L_s \cos(2\theta_r) \end{bmatrix} \cdot \begin{bmatrix} i_\alpha \\ i_\beta \end{bmatrix} + \psi_m \frac{d}{dt}\begin{bmatrix} \cos(\theta_r) \\ \cos(\theta_r - \frac{\pi}{2}) \end{bmatrix} \qquad (2.12)$$

The variable change:

$$L_s = L_l + \frac{3}{2}\bar{L}_m$$
$$\Delta L_s = \frac{3}{2}\Delta L_m \qquad (2.13)$$

has being introduced to simplify notation.

It is noted that (2.9) corresponds to the particular case of (2.12) when $\Delta L_m = 0$ i.e. there is no saliency. The equations (2.9) and (2.12) represent the dynamic model of the PM machines (non-salient and salient respectively) in a stationary reference frame. However, the most convenient frame to implement the field oriented control is the synchronous reference *d-q* frame fixed on the rotor developed by Park [39]. Furthermore, synchronous rotation with the rotor saliency effectively eliminates any variations of the inductance matrix with rotor position. To obtain the synchronous *d-q* frame model (2.12) is rotated using (2.4) and an angle $(\varphi = \theta_r)$. The result of this operation is:

$$\begin{bmatrix} v_d \\ v_q \end{bmatrix} = r_s \begin{bmatrix} i_d \\ i_q \end{bmatrix} + \begin{bmatrix} L_d p & L_q \omega_r \\ -L_d \omega_r & L_q p \end{bmatrix} \cdot \begin{bmatrix} i_d \\ i_q \end{bmatrix} + \psi_m \omega_r \begin{bmatrix} 0 \\ 1 \end{bmatrix} \tag{2.14}$$

Here, p is the differential operator and $L_d = L_s - \Delta L_s$, $L_q = L_s + \Delta L_s$ are the direct and quadrature axis inductances. The symmetry of the surface mounted PM motor yields synchronous inductances $L_d = L_q$.

2.1.3 Control of the PMSM Machine

The choice of vector transformation (2.1) yields the following general expression for the instantaneous torque for the PM synchronous machine [38]:

$$T_e = \frac{3P}{2}\left\{\psi_m i_q + i_d i_q (L_d - L_q)\right\} \tag{2.15}$$

In equation (2.15), two components of the torque can be identified: the first term, usually called *magnet torque*, is directly proportional to i_q and independent of i_d. The second, or *reluctance torque*, is only present in salient machines where $L_d - L_q \neq 0$ and is proportional to the current product $i_d i_q$.

In the SMPM machine, the reluctance torque is zero and therefore the torque is controlled only by changes in i_q. The *d-axis* flux on the other hand is fixed by the rotor magnets, except during flux weakening, and i_d is normally control to zero to achieve maximum torque per ampere operation. This makes the control structure for this type of machines very simple. Figure 2.2 shows a position control implementation for a SMPM machine in which i_q is used as an actuation variable to control the rotor speed, a PI controller being used to achieve zero steady state error. The control of the currents is performed in the rotor coordinates *d-q* also by PI regulators. To perform the coordinate rotation of the current measurements to *d-q* reference frame, and of the reference voltages back to the α-β frame, the rotor position is needed. Rotor position

measurement is also used for speed feedback. Finally position control can be achieved by extending this control structure by an outer position loop usually closed with just a proportional controller [10] and using the measure rotor position for feedback.

The *reluctance torque* is significant on IPM motors and for this reason they are often referred to as *hybrid machine*. In these motors more torque per each ampere of stator current can be achieved by advancing the stator current vector angle and forcing some negative i_d current. The particular mapping of torque reference T_e^* into i_d^* and i_q^* is not unique but if an optimisation criteria such as maximum torque per ampere is used, suitable functions can be found [7]. In flux weakening, negative i_d current is used to counter the fixed air-gap flux produced by the rotor magnets and hence reduce the stator voltage at high speeds. In the IPM motor the negative i_d current contributes to the torque production of the machine and increases the available torque [8], giving an advantage over the SMPM for flux weakening operation.

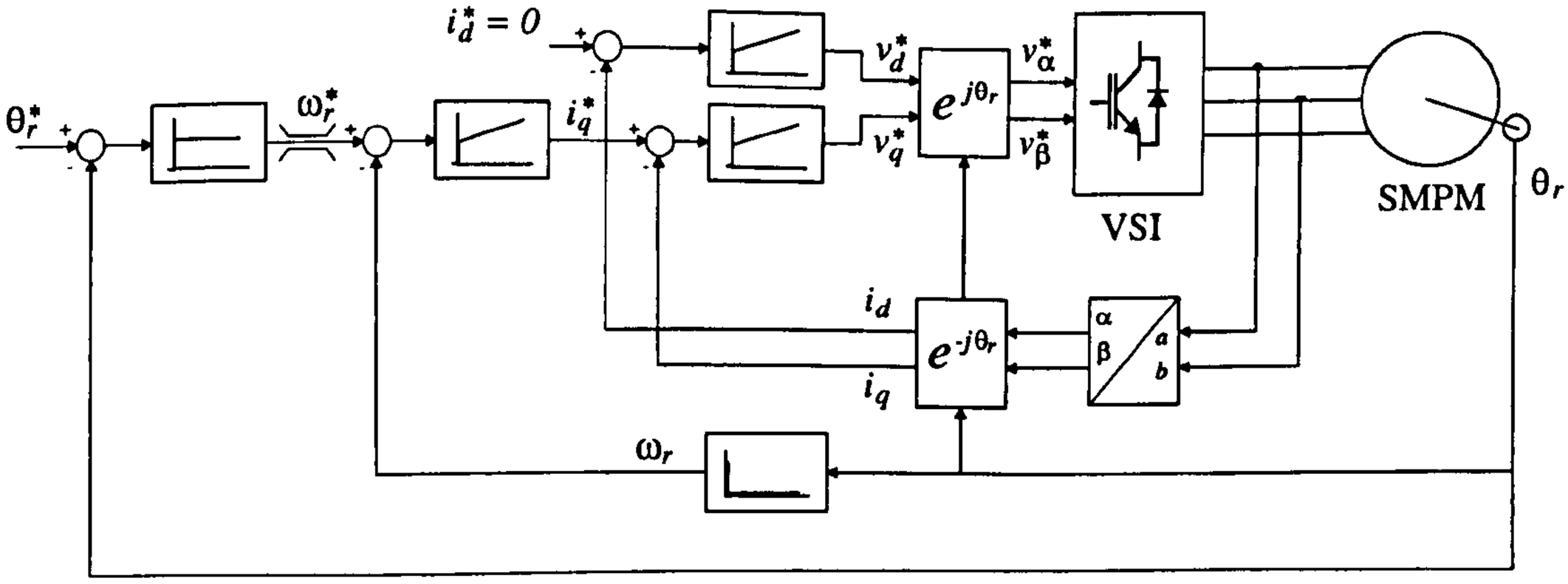

Figure 2.2: Control structure for surface mounted PM machine.

2.1.4 Sensored Control Results

The classic control using a position sensor is a good benchmark for the performance of the *sensorless* system. The results shown in this section are obtained with the same hardware and software discussed in Chapter 4, the obvious exception being the use of an 1024ppr quadrature encoder for orientation and feedback. A faster controller design for the speed and position loops also makes full use of the accuracy and

dynamic performance of the encoder. The control structure corresponds to the cascade control shown in Fig. 2.2.

2.1.4.1 Current control

In the inner layer of the cascade arrangement shown in Fig. 2.2 are the fast current control loops. Due to the symmetry of the SMPM machine both loops are closed by an identical PI controller. The transfer function of $\underline{i}_{dq}(s)/\underline{v}_{dq}(s)$ for the control design is derived from (2.14) with decoupling terms, eliminating the *d-q* channel coupling, being applied in the established manner [10]. With the parameters given in Chapter 4, it yields:

$$\frac{\underline{i}_{dq}(s)}{\underline{v}_{dq}(s)} = \frac{1}{4.15 \cdot 10^{-3} s + 0.47} \tag{2.16}$$

Given the sampling time of 100 μs, it is easily shown that:

$$\frac{\underline{i}_{dq}(z)}{\underline{v}_{dq}(z)} = \frac{0.024}{z \cdot (z - 0.9887)} \tag{2.17}$$

Equation (2.17) contains one sample delay z^{-1} in account of the processing delay between the sampling of the currents and the update of the inverter new PWM reference. The design of all the controllers is carried out using root-locus. The design objective is to obtain a high bandwidth while keeping the dumping factor ζ of the complex response to approximately 0.7. The designed discrete PI controller is:

$$G_c = \frac{17 \cdot (z - 0.854)}{(z - 1)} \tag{2.18}$$

In order to eliminate the overshoot due to the zero $(z - 0.854)$ the current demand $\underline{i}^*_{dq}$ is prefiltered by $H_{pf} = 0.146/(z - 0.854)$. This design gives a nominal closed loop bandwidth of 500 Hz for the transfer function $\underline{i}_{dq}(z)/\underline{i}^*_{dq}(z)$. Figure 2.3 shows the response of i_d and i_q control loops to a step change to the demanded torque while

rotating at constant 200rpm. The response settles in less than 3ms and there is no noticeable coupling between the two axis currents.

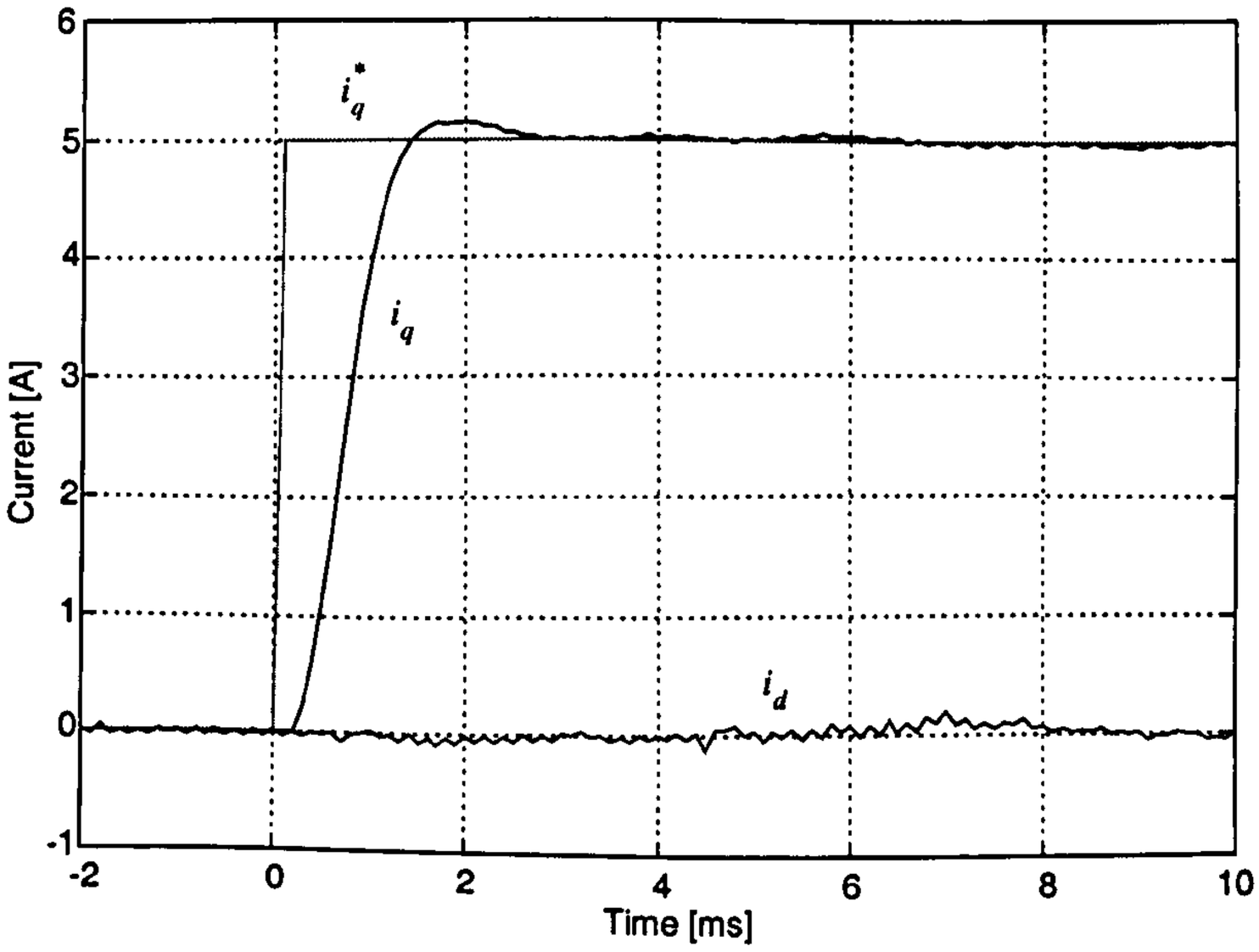

Figure 2.3: Current control response to a step in i_q demand.

2.1.4.2 Speed control

The torque reference current (i_q^*) is derived from the speed loop. This is closed by a PI controller to obtain zero steady state error. Due to the large mechanical time constant (as compared with the bandwidth of the current loops) and the limit imposed on the magnitude of the stator currents of the machine, the speed loop PI controller must have an limited output and an anti windup mechanism [40].

In servo drives a fast speed loop is desirable. However the quantisation error of the speed signal, proportional to the position sampling frequency (200Hz) and inversely proportional to the resolution of the encoder (1024ppr), impose an upper limit to the speed loop proportional gain to avoid torque chattering. The high bandwidth of the current loops allows the closed loop dynamics to be neglected. Hence the nominal plant dynamics for the speed loop is dominated by the mechanical subsystem. Using the nominal values of total inertia and torque constant, given in Chapter 4, and neglecting friction, the mechanical transfer function is given by:

$$G_{p0} = \frac{k_t}{Js + B} = \frac{1.13}{0.0153s} \qquad (2.19)$$

Using this nominal plant, a PI controller is tuned to obtain a nominal close loop bandwidth of 25Hz yielding an *s*-plane controller:

$$G_c(s) \approx \frac{1.6 \cdot (s + 60)}{s} \qquad (2.20)$$

The proportional gain $k_p = 1.6$ limits the torque current chattering to less than 5% of the nominal current. The low bandwidth of the speed loop as compared to the sampling frequency allows the design to be carried out in the s domain and the discretization performed by the *bilinear transformation*. The typical performance of the speed loop is shown in Fig. 2.4 where step changes between 1000 and -1000rpm are applied to the demand.

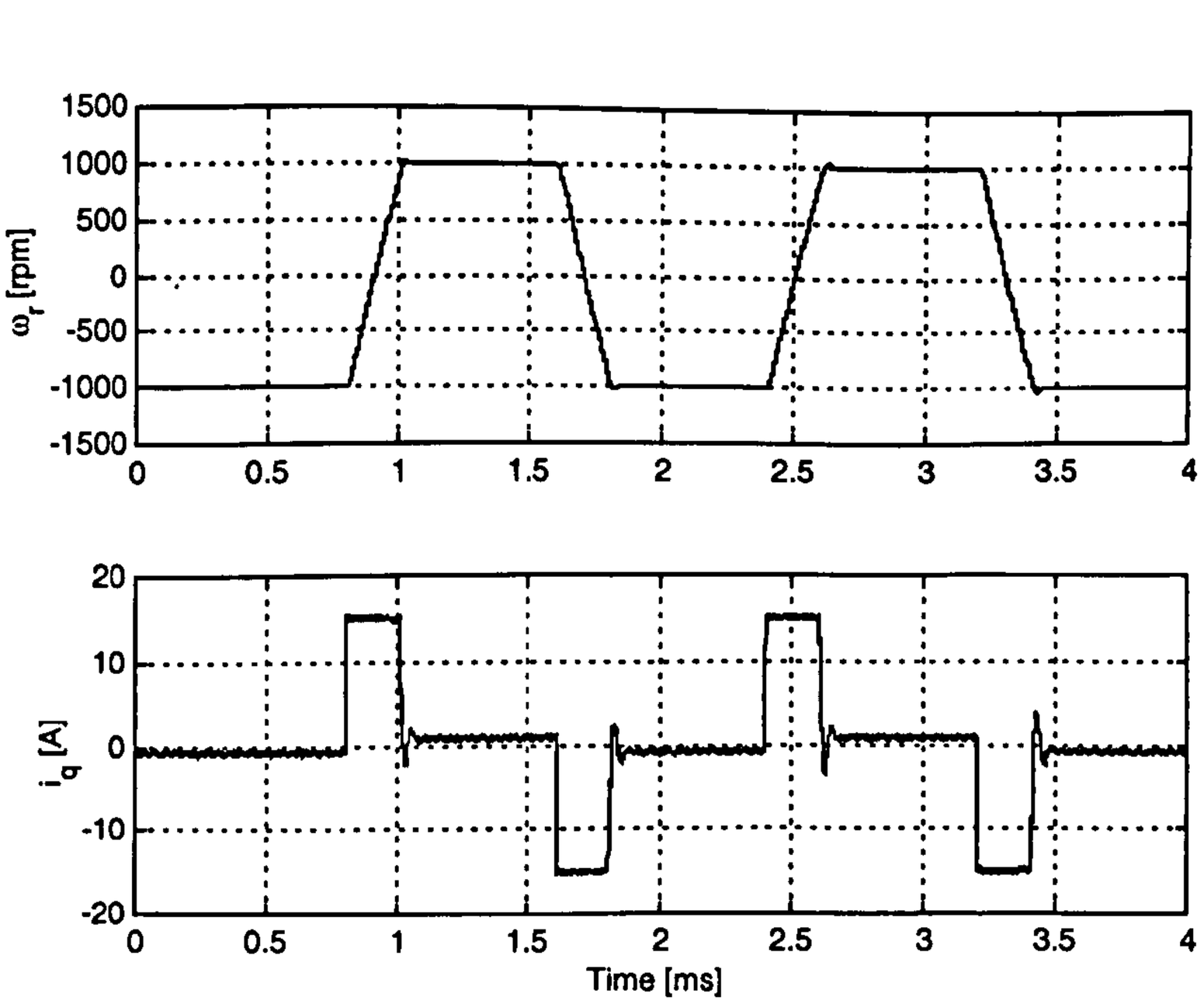

Figure 2.4: Speed loop response to step changes in demand.

2.1.4.3 Position control

The outmost loop of the cascade system correspond to the position loop and is closed by a proportional controller, the inherent integral characteristic of the plant $\theta_r(s)/\omega_r(s)$ providing the necessary open loop integration for zero steady state error to reference demand. The relative low bandwidth of the speed loop means that it's dynamic cannot be neglected for the design of the position loop gain. The selected gain of $k_p = 19$ produces a close loop bandwidth of 5Hz. The response of the complete position control system to step demands of one full mechanical turn is shown in Fig. 2.5.

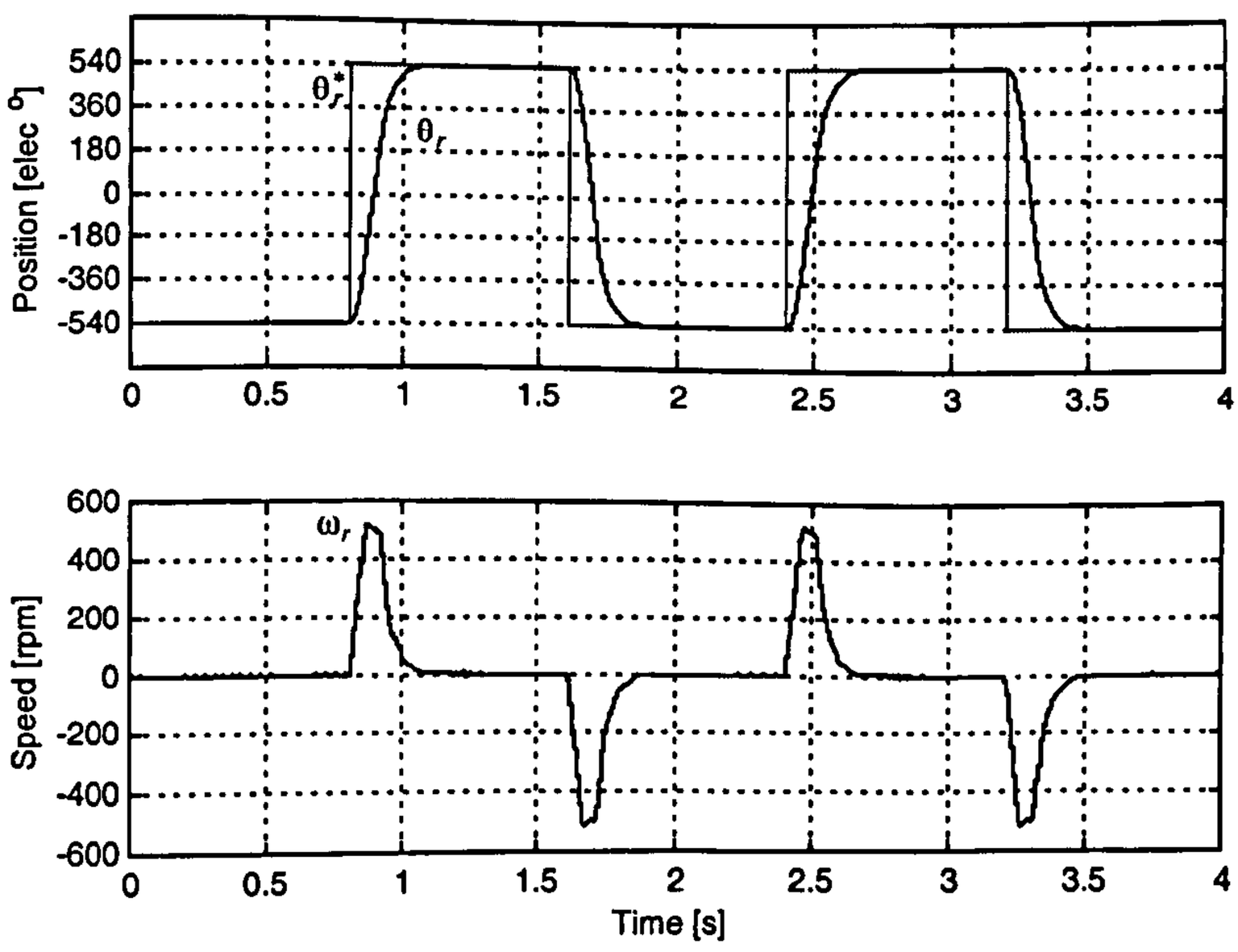

Figure 2.5: Position loop response to step changes in demand.

2.2 Sensorless Control of PM Synchronous Machines

In Section 2.1.3 a position signal is needed to perform the correct coordinate rotation for flux orientation and for the feedback of the position and speed control loop. The ability to perform the control tasks without an position sensor such a encoder or a resolver is normally referred as *sensorless* control and has several advantages that

makes it an attractive alternative [41]. There is a reduction of the total drive cost that may be significant (especially in smaller drives), an easier installation through cabling reduction, and a reduction of the drive's volume by eliminating the housing of a position sensor at the end of the motor shaft. The elimination of the encoder (a delicate instrument that is prone to failure in hazardous environments) and its cabling and connectors, also increases the reliability. All these advantages may come at the cost of sacrificing some of the dynamic response and accuracy provided by a position sensor. However, they are particularly important for the expansion of the PM motors to the wider market of lower-dynamic, general industrial drives where its efficiency makes it a possible competitor to the dominant induction motor [5].

2.2.1 Model-Based Sensorless Control

The aim of sensorless control is to provide an estimate of θ_r to be used for the vector rotation and the position/speed loops in the control of the machine of Fig. 2.2. When the estimate derives from a model, the method is called *model-based sensorless control*.

The simplest methods consist in *stator flux estimators* in the α-β stationary reference frames [11, 12]. These work simply by integration of the stator voltage corrected by the resistive drop to obtain $\underline{\hat{\psi}}_s^v$.

$$\begin{aligned} \underline{\hat{\psi}}_{s\,\alpha\beta}^{v} &= \int (\underline{v}_{\alpha\beta} - \hat{r}_s \underline{i}_{\alpha\beta})dt \\ \hat{\theta}_s &= \tan^{-1}\left(\frac{\hat{\psi}_{s\beta}}{\hat{\psi}_{s\alpha}}\right) \end{aligned} \tag{2.21}$$

In [11] the angle of the stator flux estimation $\hat{\theta}_s$ is used directly for stator flux orientation achieving unity power factor in the operation of the machine. However, rotor position estimation $\hat{\theta}_r$ is not obtained directly, due to the difference between $\underline{\hat{\psi}}_s$ and $\underline{\hat{\psi}}_m$ caused by the flux induced by the stator currents. In [12] a model base reference adaptive system (MRAS) is proposed for the correction of this flux

difference caused by the stator currents. Stator flux $\underline{\hat{\psi}}_s^v$ estimated by the voltage model (2.21) serves as reference. A second estimation of the stator flux is carried out in parallel in the *d-q* frame based on the magnitude of the magnet flux and the stator currents (2.18). This estimate is rotated to the stationary frame using the estimated rotor position $\hat{\theta}_r$. The difference in the orientation of both $\underline{\hat{\psi}}_{s\,\alpha\beta}^v$ and $\underline{\hat{\psi}}_{s\,\alpha\beta}^c$ is used as an error and is driven to zero by changes in the estimated rotor position $\hat{\theta}_r$ by an appropriate adaptation mechanism.

$$\begin{aligned}
\underline{i}_{dq} &= \underline{i}_{\alpha\beta} \cdot e^{-j\hat{\theta}_r} \\
\underline{\hat{\psi}}_{s\,dq}^c &= (\hat{\psi}_m + \hat{L}_d i_d + j\hat{L}_q i_q) \\
\underline{\hat{\psi}}_{s\,\alpha\beta}^c &= \underline{\hat{\psi}}_{s\,dq}^c \cdot e^{j\hat{\theta}_r}
\end{aligned} \tag{2.22}$$

The methods discussed above are affected by the pure integrator drift due to DC offsets in the measured quantities, low frequency content during transients and accumulated numerical error. Different techniques are used to overcome this problem but the integrator drift remains a difficulty at very low speeds. Non-linear integrators have being proposed for flux estimation [42, 43] and have been shown to perform well for sensorless control of induction motors at low speeds [43]. However, the performance of this technique for sensorless PM motor drives has not yet been reported.

Strategies that avoid integration all together have also being explored. An estimation of the stator flux angle obtained by direct angle extraction from $\underline{v}_s - \hat{r}_s \underline{i}_s$ and compensated for the $\pi/2$ fixed offset is proposed in [44]. In [45] a hypothetical coordinates system is defined, that does not necessarily coincide with the actual rotor axis *d-q*. The voltage equation of the stator is solved in this coordinate system and compared with the measured voltage transformed to the same coordinates. The error is used for correction of the hypothetical axis. The inherent high noise content of the voltage signal and the low accuracy of the differentiation of the currents is the main limitations of this method, reducing the dynamic performance and degrading the quality of the control at low speed.

A combined method of flux estimation and position estimation is proposed in [46, 47]. In this method the estimated flux, produced by a single step integration $\underline{v}_s - \hat{r}_s \underline{i}_s$ and a predicted value of rotor position are used to generate a phase current estimation. The error between this estimation and the measured values of the phase currents is used for correction of the predicted position to obtain the estimated rotor position and to generate new flux estimations. These are use as initial conditions in the next step of the integration. This algorithm relies upon good accuracy of the flux estimation and therefore degrades at low speeds.

To overcome the open loop integrator drift and to obtain fast convergence of the rotor position estimate, *close loop state observers* have been proposed. A full order observer in the synchronous reference *d-q* frame is presented in [13]. The states are defined as the currents i_d, i_q and the rotor mechanical variables ω_r and θ_r. The transformation of the electrical variables to the *d-q* frame is done using the latest value of position estimation. Results of this observer are shown for rotor position tracking only and sensorless operation is not presented. This observer is sensitive to errors in the mechanical parameters that are usually unknown. A reduced order observer considering only the electrical sub-dynamics is proposed in [14], the rotor magnet-induced back-EMF is modelled as a disturbance and the observer is extended to estimate it. The rotor position information is extracted from the magnet-induced back-EMF estimate, and good sensorless results are shown above 100 rpm. An *extended Kalman filter* (EKF) in the stationary frame with the state vector defined as $[i_\alpha \quad i_\beta \quad \omega_r \quad \theta_r]^T$ is proposed in [16] for the sensorless control of PM synchronous machine. Such algorithm has been implemented in real time in [17] and presents good sensorless speed performance down to 40 rad/sec. The choice of the covariance matrices is one major difficulty for the implementation of the EKF.

Despite the variety of model-based methods for position estimation of the PM synchronous machine and their differences in performances, all of them fail at low speed due to the inherent unobservability of the PMSM at zero speed resulting from the lack of back-EMF.

2.2.2 Implementation of MRAS System

To illustrate the deterioration of performance of the model based sensorless methods, an model based reference adaptive system (MRAS) based upon that presented in [12] is here implemented. Results are presented at high, medium and low speeds. The implementation will also be used as the basis of a hybrid method considered in Chapter 6.

The MRAS uses two models to generate two estimates for the stator linkage flux, as depicted in Fig. 2.6. The first is the voltage model in the stationary reference frame, estimating the stator linkage flux $\underline{\hat{\psi}}^{v}_{s\,\alpha\beta}$ by integration of the stator voltage corrected by the stator winding resistive drop as defined in (2.21). This is referred to as the *reference model*. The second estimate of the stator flux is produced by a current model in the estimated *d-q* frame and rotated to the stationary α-β frame giving $\underline{\hat{\psi}}^{c}_{s\,\alpha\beta}$ (2.22). Because of its strong dependency on the rotor position estimation $\hat{\theta}_r$, the current model is used as the *adaptive model*. The orientation error between both estimations, calculated as the cross product of both vectors, feeds an appropriate adaptation mechanism to adjust $\hat{\theta}_r$ in order to drive this error to zero. The adaptation mechanism yields position and speed estimations.

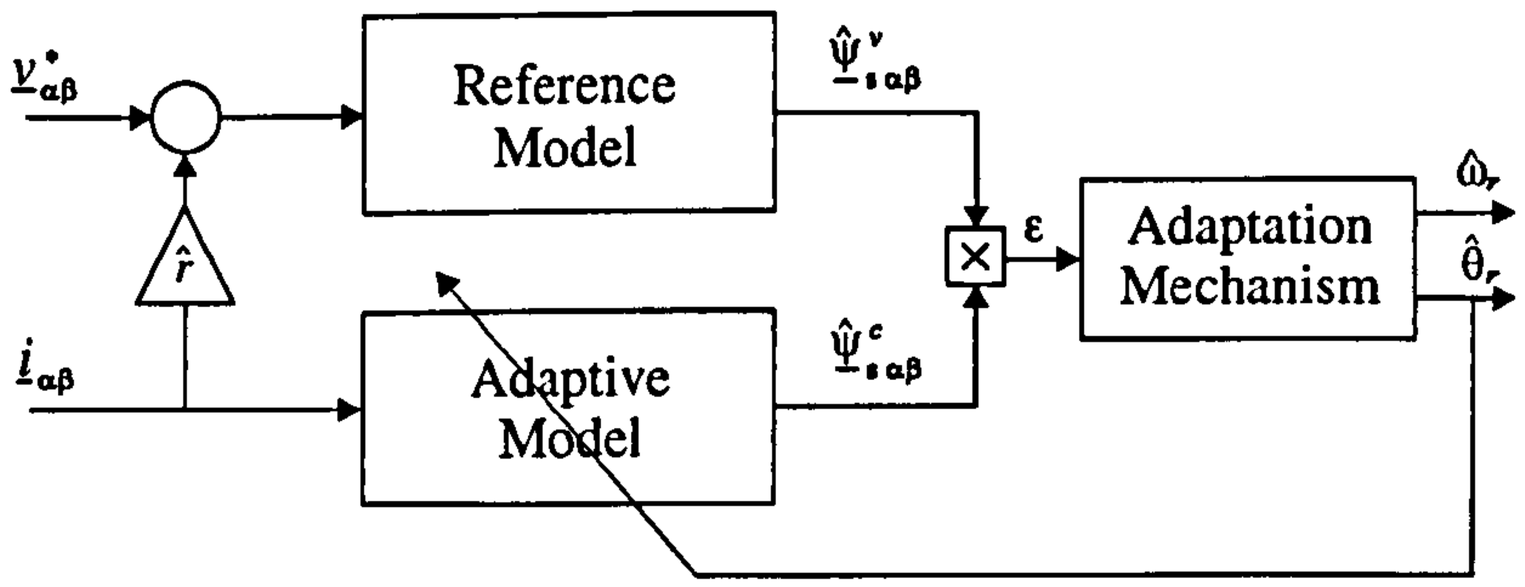

Figure 2.6: MRAS structure.

The adaptation mechanism principle is similar to a phase look loop (PLL) forcing the current estimate $\underline{\hat{\psi}}^{c}_{s\,\alpha\beta}$ to be in phase with the reference voltage estimate $\underline{\hat{\psi}}^{v}_{s\,\alpha\beta}$. To

improve the performance of the rotor position estimation at low speed a mechanical observer and feed-forward of the electric reference torque can be used. The resulting adaptation mechanism is shown in Fig. 2.7, the PI controller plus the feed forward term being equivalent to an ideal PID controller. To avoid drift and overcome the initial condition uncertainty of the open loop integrator of (2.21) a secondary loop is closed with a slow PI controller in order to force the voltage model to follow the current model estimation for frequencies lower than 2Hz. In this way a close loop flux observer [48] is obtained.

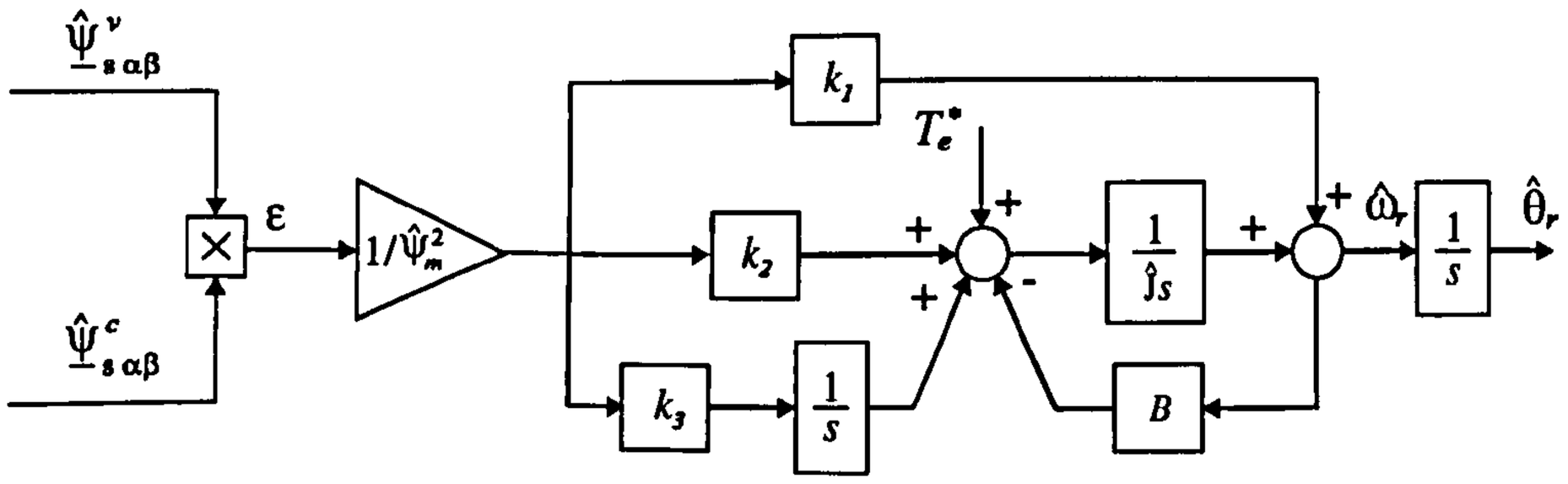

Figure 2.7: Adaptation mechanism implemented with mechanical observer.

At high speeds the large back-EMF yields good stator flux estimation by the reference vector and this results in a clean rotor position estimation and good sensorless operation results. Fig. 2.8 shows the position estimation by the described MRAS at steady state operation at 1000rpm, i.e. 33.3% of nominal speed, under 60% of nominal load. The good quality of the estimation is better appreciated in the estimation error result of Fig.2.9-a. The small amount of deviation in the rotor position estimation produces an estimated speed ($\hat{\omega}_r$) almost within the resolution of the speed measurement given by the encoder (ω_r) and is shown in Fig. 2.9-b.

A deterioration in the steady state performance of the sensorless speed control can be appreciated when the demand speed is reduced, Fig. 2.10 shows the angle estimation error and the estimated and measured speed for a steady state operation at 400rpm (13.3% of nominal speed) and 60% load. The angle error is small ensuring correct orientation, nevertheless oscillations are present in the estimated speed used for feedback (Fig. 2.10-b). The oscillations arise from interactions between the stator current and the voltage model flux estimation and are due to errors in the parameters, mainly the stator resistance which becomes more significant due to the reduction of

the back-EMF with speed. At this frequency the sensorless speed control is acceptable but the degradation in it's speed holding capability is evident, the oscillations in the speed increasing sharply with further reductions on the demanded speed.

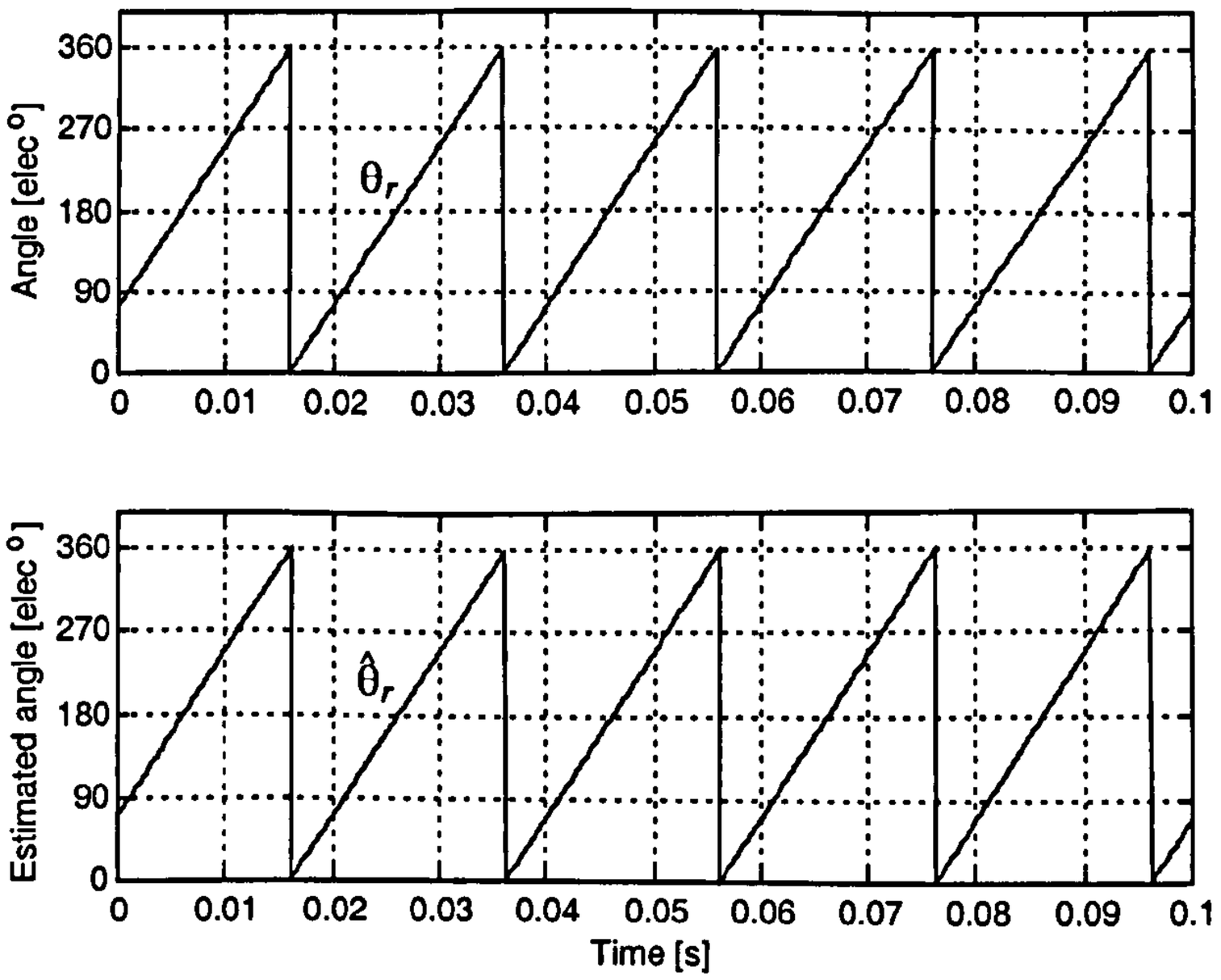

Figure 2.8: Angle estimation under sensorless operation at 1000rpm and 60% load.

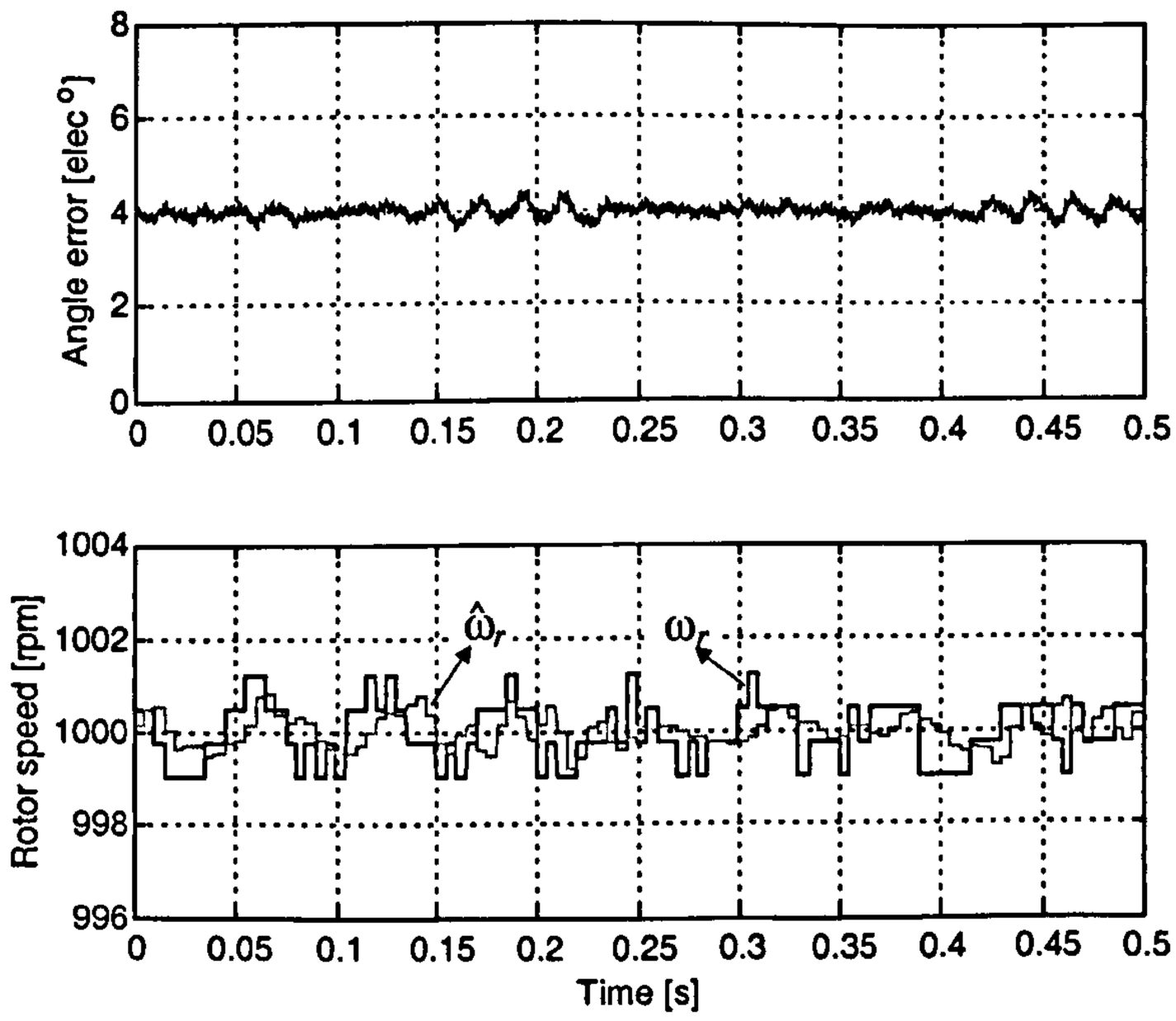

Figure 2.9: MRAS sensorless performance at 1000rpm and 60% load.

The operation at low speeds is depicted in Fig. 2.11. In this figure the rotor position and speed are plotted for operation at a demanded speed of 200rpm (6.7% nominal) at the same load of 60%. Unacceptable large oscillations in the speed make sustained operations below this frequency unfeasible. The error in the position estimation has increased but its magnitude is still small enough to maintain orientation allowing safe transitions through this speed region during transients.

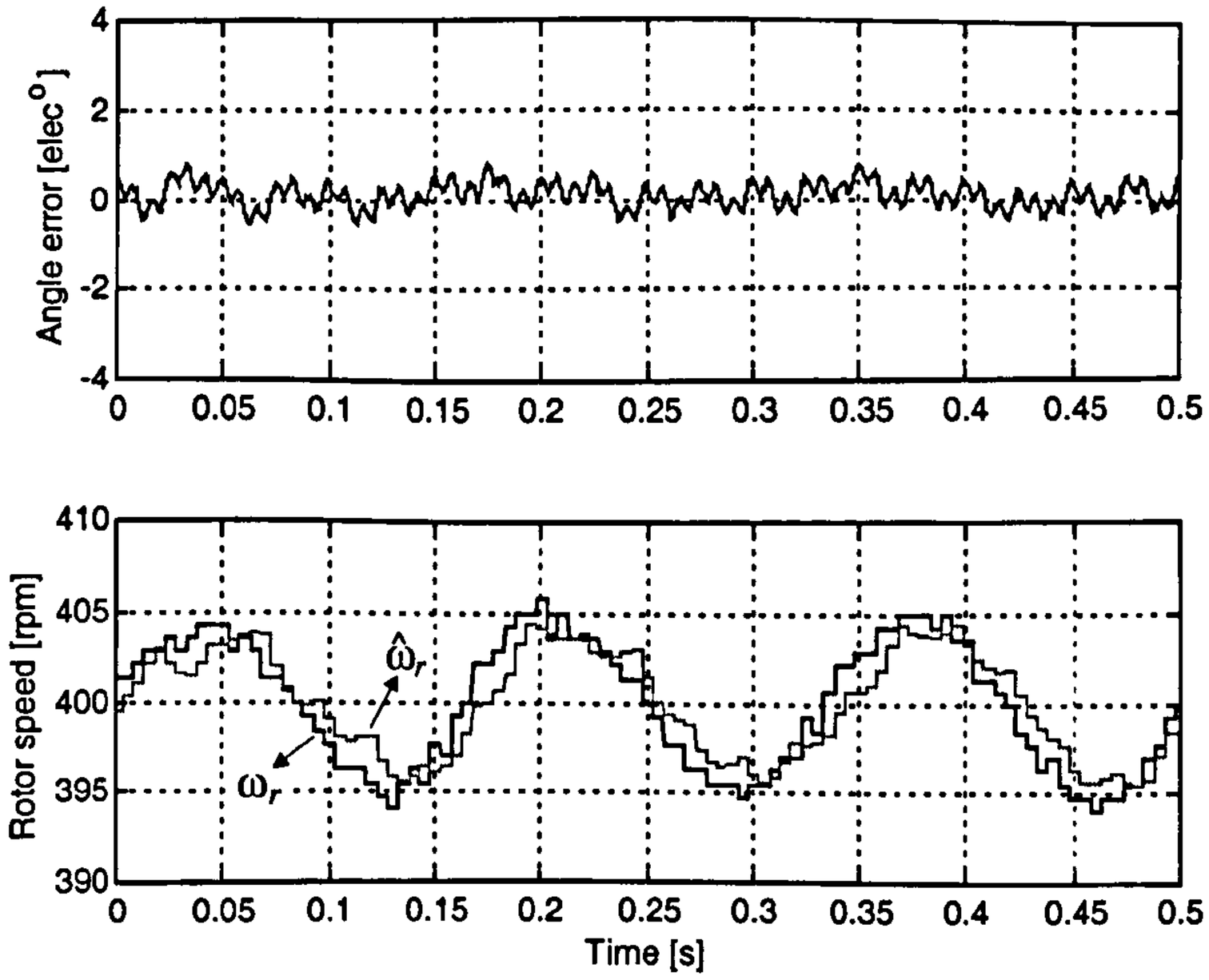

Figure 2.10: MRAS sensorless performance at 400rpm and 60% load.

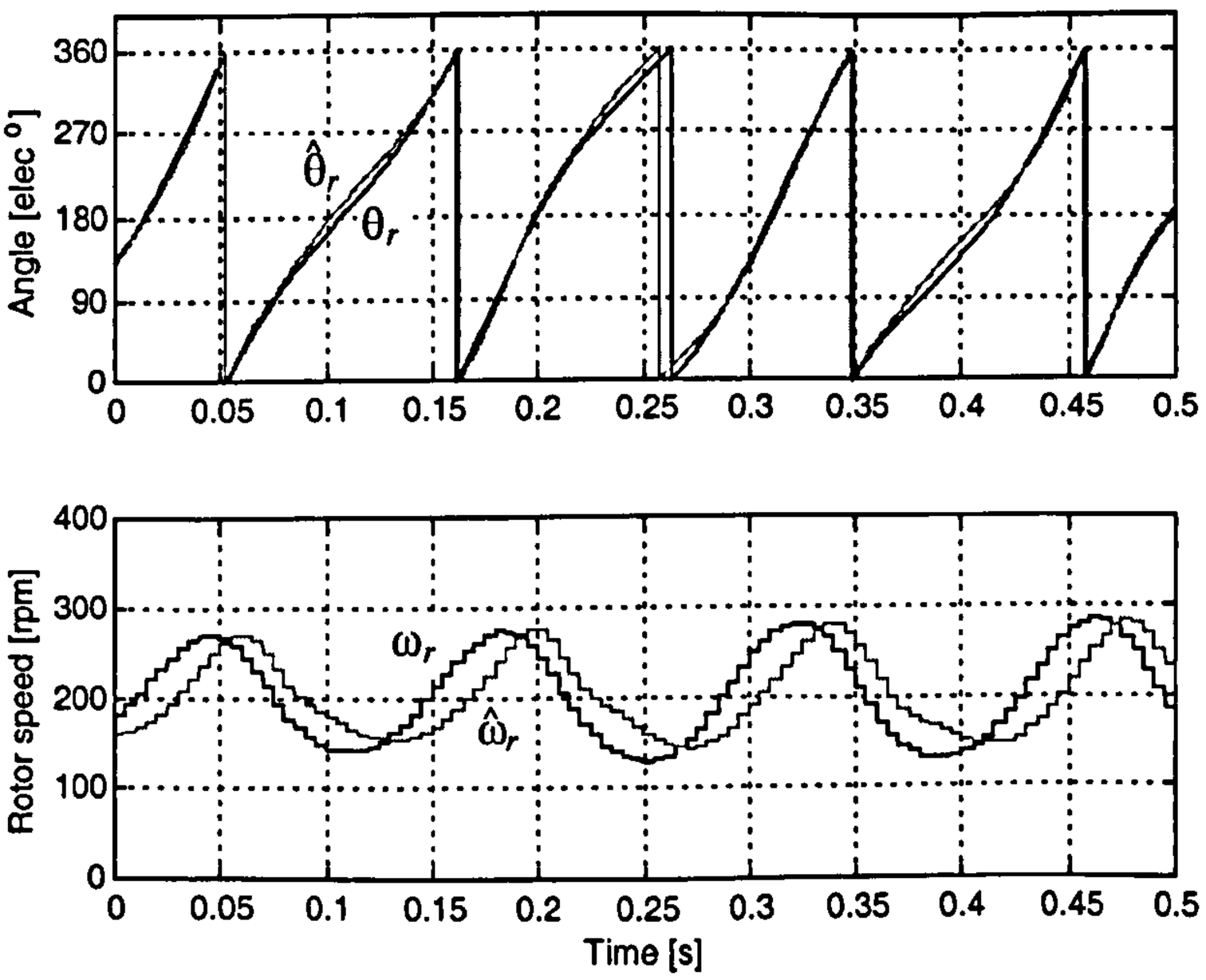

Figure 2.11: MRAS sensorless performance at 200rpm and 60% load.

Chapter 3

3 Sensorless Control through Signal Injection

3.1 Introduction

The previous chapter showed that the small back-EMF induced at low speeds results in poor flux and position estimation at zero speeds when model-based methods are used. For this reason, increasing attention is being paid to alternative methods that do not rely on the fundamental terminal quantities in order to achieve position sensorless control. The tracking of the variations in the impedance with rotor position, or *saliency*, has been proposed by researchers as a mechanism for rotor position detection on salient AC machines such as the interior permanent magnet machine [18, 22, 49, 50] and synchronous reluctance machines [24, 51]. Saliency tracking has also been applied to induction machines with rotor modifications to artificially introduce sufficient impedance variation in the rotor circuit. Modulation of the rotor resistance [25] or the rotor leakage inductance [21] have been used. Alternatively, the higher frequency saliency due to rotor slotting has being exploited to obtain incremental position information [26, 28, 30].

In order to detect saliency position, a test signal is injected on to the machine. According to the type of signal to be injected, the techniques can be broadly classified as: (a) persistent *hf* injection of voltage [18, 21, 28, 35] or current signals [52] or (b) injection of discrete *voltage test pulses* [22, 26, 45, 53].

Surface mounted permanent magnet motors (SMPM) do not exhibit a structural saliency. Nevertheless they will present a variation of the stator inductance due to magnetic saturation, i.e. a saturation induced saliency. The present work presents the exploitation of the saturation-induced saliency for the realization of the sensorless position control of the SMPM by *hf* voltage signal injection. The tracking of saturation induced saliency in SMPM machines presents a particular set of difficulties due to the small saliency magnitude and because it is not fixed to the rotor but rather oriented towards the stator flux position and therefore load dependent.

In this chapter a theoretical background of saliency tracking in SMPM is presented. The sources of saliency in a SMPM are analysed giving a physical understanding of the phenomenon. A mathematical analysis for the different *hf* injection methods and demodulation strategies used for saliency tracking is presented here. Finally a brief review and discussion of *voltage test pulses* injection methods is presented.

3.2 Theory of Saliency in a Surface Mounted PM Motor

The saliency in surface mounted machines is manifested as changes in the stator inductance. This changes are better analysed in the synchronous *d-q* fame. The synchronous *d-axis* and *q-axis* inductance are given by

$$\begin{aligned} L_d &= L_{ld} + L_{md} \\ L_q &= L_{lq} + L_{mq} \end{aligned} \tag{3.1}$$

where L_{ld}, L_{lq} are the stator leakage inductances representing the slot, end-connection and tooth-top leakage flux and L_{md}, L_{mq} are the corresponding magnetising inductances (also called armature reaction inductances) representing the fundamental flux crossing the air-gap. In what follows, an analysis of the effect of the rotor geometry and saturation on these inductances is presented.

3.2.1 Geometrical Saliency

Although the surface mounted PM machine of cylindrical rotor is a non-salient machine, variations of this basic design with surface *inset* or *partially inset* magnets into the rotor core, as shown in figure 3.1, results in some degree of geometrical saliency [1]. If the air-gap is sufficiently large as compared to the stator slot opening this rotor geometry predominantly affects the values of the magnetising inductance but not the stator leakage. The inter-polar iron produces a relative increment in the q axis magnetising inductance and the effect of the rotor geometry can be represented as:

$$\begin{aligned} L_{md} &= k_{fd} L_m \\ L_{mq} &= k_{fq} L_m \end{aligned} \tag{3.2}$$

where L_m is the magnetising inductance of a motor with a equivalent sized cylindrical rotor and air-gap length g, and k_{fd}, k_{fq} are form factors. The values of k_{fd} and k_{fq} can be analytically calculated as function of the rotor geometrical parameters by computing the distribution of the armature winding normal component of magnetic flux density. A good estimation can be obtained by assuming sinusoidally distributed winding and neglecting fringing. The resulting expressions are given by:

$$\begin{aligned} k_{fd} &= \frac{1}{\pi}\left[\frac{1}{c_g}\left(\alpha_i + \sin(\alpha_i)\right) + \left(\pi - \alpha_i - \sin(\alpha_i)\right)\right] \\ k_{fd} &= \frac{1}{\pi}\left[\frac{1}{c_g}\left(\alpha_i - \sin(\alpha_i)\right) + \left(\pi - \alpha_i + \sin(\alpha_i)\right)\right] \end{aligned} \tag{3.3}$$

$$c_g = 1 + h/g \tag{3.4}$$

where α_i is the angle spanned by the permanent magnets and the coefficient c_g is a measure of the magnitude of the insertion of the magnets into the rotor core.

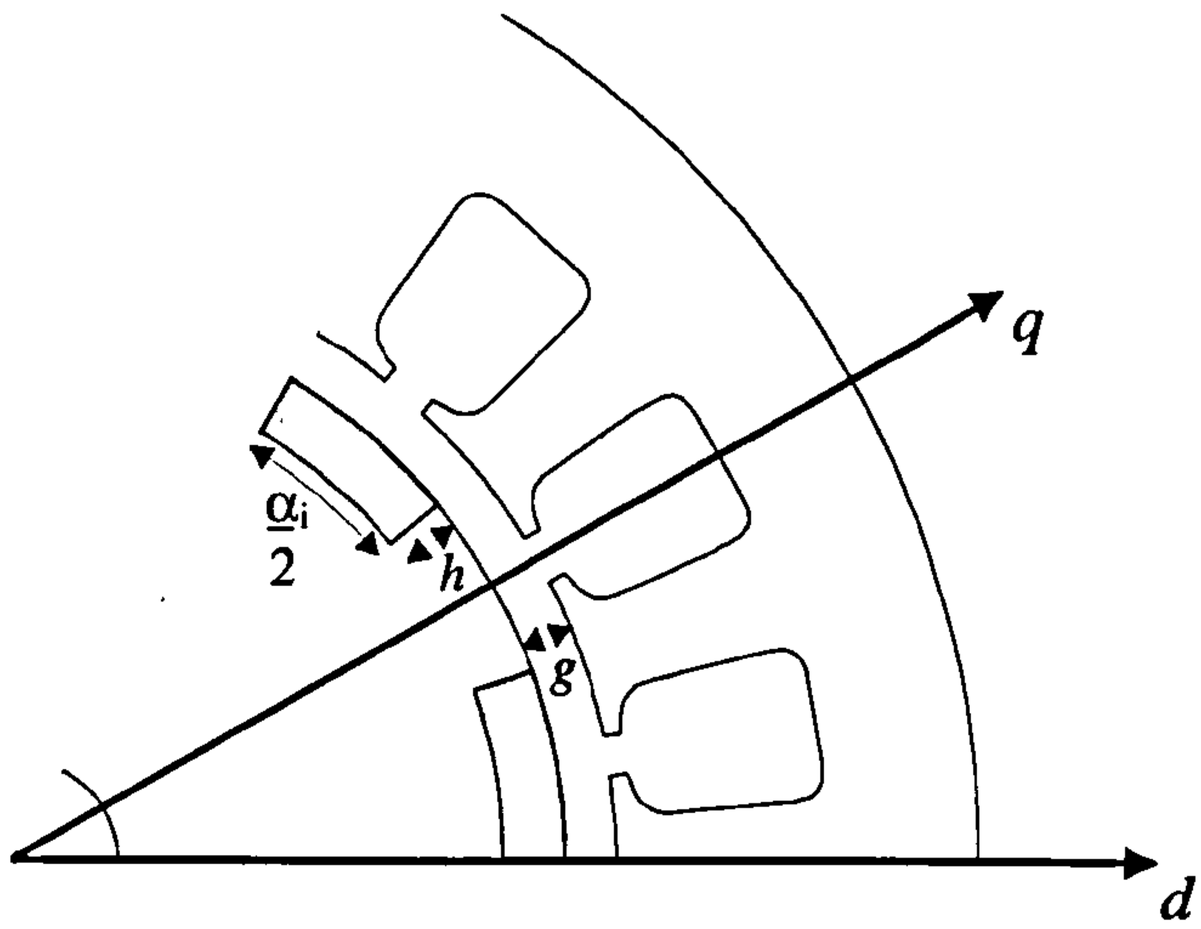

Figure 3.1: Inset magnet motor.

Note that saliency produced by the inset magnets is of the same nature as that of the saliency on interior magnets machine (IPM), i.e. rotor geometry. Hence the saliency is oriented with the rotor $L_{md} < L_{mq}$. Nevertheless the saliency in inset magnets motors is smaller than that in interior magnets motors where ratios of L_q to L_d of 3:1 or higher are common [6].

3.2.2 Saturation Saliency

Surface mounted PM machines without structural saliency will present a spatial difference in the synchronous inductance caused by the magnetic saturation of some sections of the machine iron core due to the high air-gap flux density produced by the rotor magnets. As it is well known, the saturated iron presents a sharp reduction in the differential permeability decreasing the inductance value of any coil whose flux path crosses through the saturated section. The saturation of the machine's iron may affect the main flux path or the leakage flux path producing a spatial modulation in the magnetising and leakage inductances.

For accurate determination of the flux density in the iron core, including the saturation effect, finite element method (FEM) analysis of a particular machine must be carried out. Nevertheless a qualitative explanation based in the findings of FEM analysis [54-56] and experimental data [57] give good insight into the effect that saturation has in

the magnetising and leakage inductance. This is useful in giving a physical interpretation to the experimental results. For this qualitative analysis the simplified surface mounted machine model with concentrated *d* and *q-axis* windings shown in Fig. 3.2 will be considered.

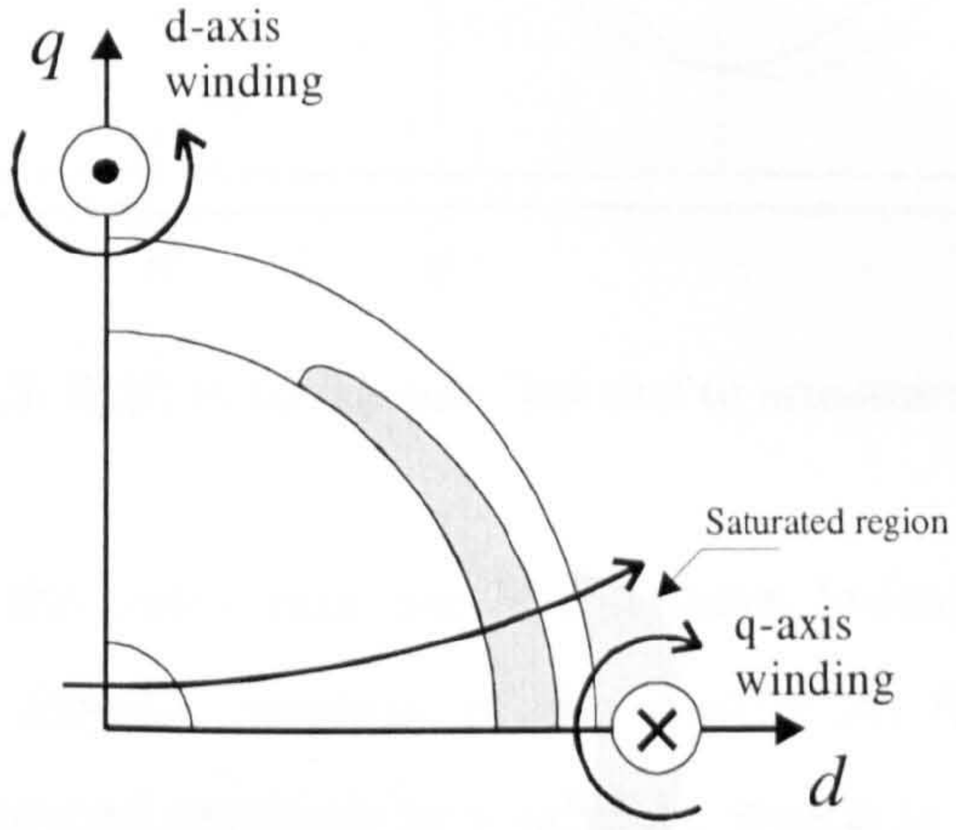

Figure 3.2: Ideal SMPM with concentrated *d-q* windings.

3.2.2.1 Saturation saliency in the magnetising inductance

Under no load the rotor magnets establishes a flux density of approximately sinusoidal distribution on the air-gap with it's maximum in the *d-axis* direction. The stator iron directs and concentrates the flux producing saturation of the stator teeth and tooth tips in the proximity of *d-axis*.

The stator teeth saturation in the *d-axis* produces an increase in the effective air-gap length for the main *d-axis* flux resulting in a reduction of L_{md}. On the other hand, L_{mq} remains relatively unchanged resulting in a saliency where $L_{md} < L_{mq}$.

Under load the torque current in the *q-axis* stator winding creates a term $L_m i_q$ which produces a shift of the air-gap flux distribution toward the *q-axis* direction (*-q-axis* if the current is negative). This is depicted in Fig. 3.3 which assumes a sinusoidal distribution of the magnet and stator current induced air-gap flux.

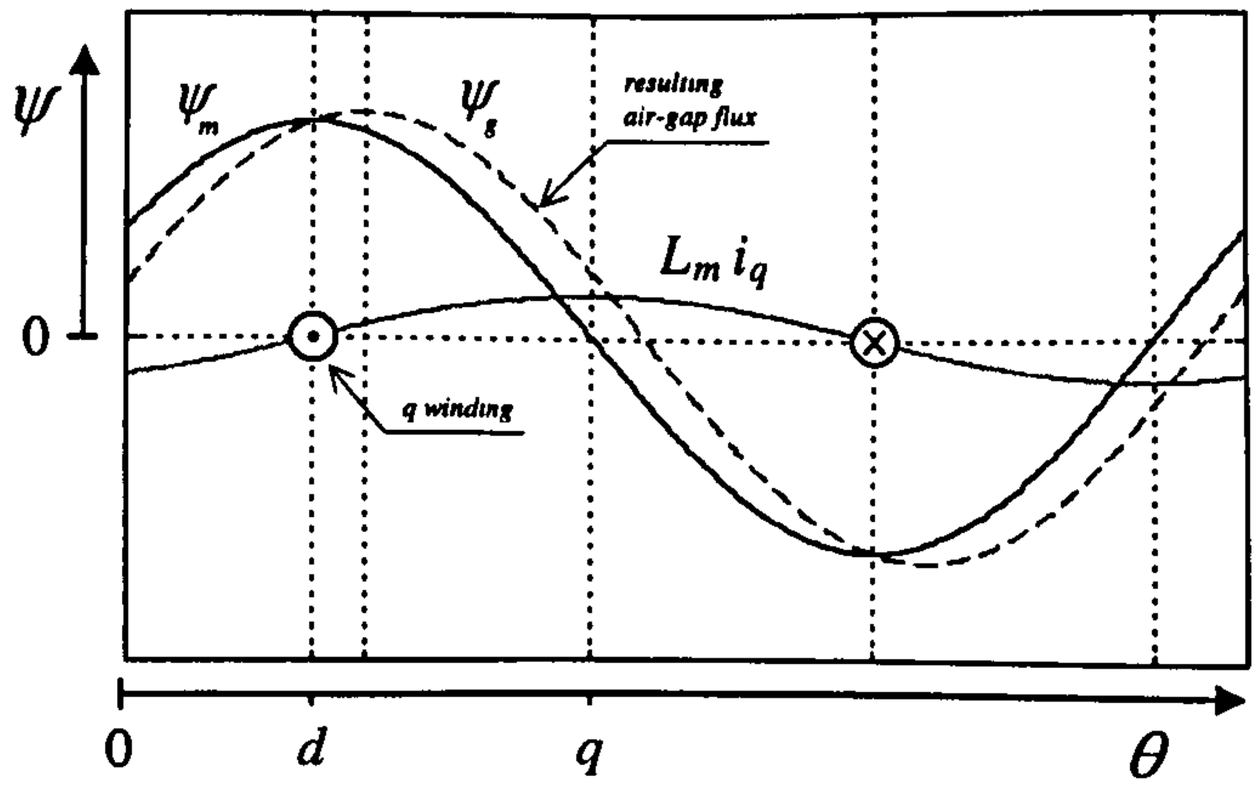

Figure 3.3: Shift in the air-gap flux due to armature reaction.

Further shift occurs in the stator flux due to the stator leakage flux that exacerbates the phenomenon. The angular position of the maximum flux density in the iron determines the area saturated resulting in a saliency which is misaligned with respect to the rotor frame *d-axis*. By defining a new coordinate system δ-γ shifted form *d-q* by the saturation angle $\varphi = \theta_\delta - \theta_r$, the saliency in the magnetising inductance can be described as $L_{m\delta} < L_{m\gamma}$.

3.2.2.2 Saturation saliency in the leakage inductance

The saturation produced by the machine's main flux also affects the stator leakage flux path, mainly via slot and tooth-top leakage, producing a spatial modulation on the leakage inductance. Due to the orthogonal position of the stator windings and their magnetic axis, under no load the main flux saturation produced by the rotor magnets in the *d-axis* affects the stator teeth and tooth tips around the *q-axis* winding as illustrated in Fig. 3.2. The reduction in the permeance of the leakage flux path of the *q-axis* causes a reduction of L_{lq}. Because there is almost no main flux in the *q-axis* direction, the *d-axis* leakage inductance remains largely unaltered resulting in $L_{ld} > L_{lq}$. Under load the angular position of minimum leakage inductance is also shifted by the shift of the stator flux with respect to the *d-axis*. We can represent this as leakage inductance saliency of the type $L_{l\delta} > L_{l\gamma}$.

It is noted that the saturation saliency in the magnetising inductance and in the leakage inductance are opposite and tend to cancel each other. For saliency tracking to be used successfully for rotor or flux position detection, the net effect must be dominated by one of the saliencies over all the operation range. It has being argued by some researchers that due to the high frequency nature of the test signal used to scan the variation on inductance, the flux produced by this signal does not penetrate deep enough into the rotor as to flow through the main flux path so that only the leakage inductance saliency is tracked. This argument originated in the experience with inductance machines where *hf* currents induced in the outer sections of the rotor cage indeed impedes the *hf* flux penetrating the main flux path. In some surface mounted or inset type PM motors, an external nonferromagnetic cylinder is used to help keep the magnets in place against the centrifugal force (this cylinder can be conductive to act as a damper and provide some asynchronous starting torque) and the same argument may be valid for PM machines with such construction. Nevertheless, in the more general case of PM machines with laminated rotors and magnets glued to the surface, the *hf* currents induced in the rotor laminations are not significant and the *hf* flux does penetrate the main flux path. This allows tracking of the magnetising inductance saliency [55].

The experimental results show that the modulation in the magnetising inductance characterised by an *hf* measured impedance with it's minimum in the vicinity of the *d-axis*, is dominant in the machine used in this work. The exact orientation of the saliency with respect to the *d-axis* varies with the load level. In the following mathematical analysis the surface mounted PM machine is represented by the salient model introduced in (2.12) with the minimum value of the total stator inductance shifted from the *d-axis*:

$$\begin{bmatrix} v_\alpha \\ v_\beta \end{bmatrix} = r_s \begin{bmatrix} i_\alpha \\ i_\beta \end{bmatrix} + \begin{bmatrix} L_s - \Delta L_s \cos(2\theta_\delta) & -\Delta L_s \sin(2\theta_\delta) \\ -\Delta L_s \sin(2\theta_\delta) & L_s + \Delta L_s \cos(2\theta_\delta) \end{bmatrix} \cdot \frac{d}{dt} \begin{bmatrix} i_\alpha \\ i_\beta \end{bmatrix} + \omega_r \psi_m \begin{bmatrix} -\sin(\theta_r) \\ \cos(\theta_r) \end{bmatrix} \tag{3.5}$$

where $\theta_\delta = \theta_r + \varphi$ is the angle of the maximum saturation and L_s and ΔL_s are positive quantities given by:

$$L_s = \frac{\hat{L}_s + \breve{L}_s}{2};\ \Delta L_s = \frac{\hat{L}_s - \breve{L}_s}{2}.$$

3.3 HF Injection Techniques

One type of signal injected into the machine to extract the saliency position information is persistent *hf* sinusoidal excitation. This excitation can be current [52] or voltage [21, 35]. The main inconvenience of *hf* current injection is the limitation of the carrier frequency imposed by the bandwidth of the current controllers which have to follow the *hf* reference without considerable phase shift, and the need to measure the voltage response. This is generally noisier than current measurement and requires additional hardware. The most common technique is the injection of *hf* voltages and the measurement of the resulting *hf* currents. The frequency of the injected voltage should be high enough as to fall outside the bandwidth of the current loops providing sufficient spectral separation between the fundamental excitation and the injection signal. The methods of voltage injection found in the literature can be classified in two types, namely: α-β frame rotating injection [21, 25, 36] and *d-q* frame pulsating injection [18, 34, 35, 58]. In this section the mathematical background for these methods is presented and a third injection method is proposed by injection of a rotating voltage in the *d-q* frame.

3.3.1 Rotating α-β Injection

The injection of a balanced three-phase *hf* voltage for saliency tracking has being proposed by several authors [21, 25, 27]. Such voltage injection creates a constant amplitude vector rotating at the injection frequency:

$$\begin{bmatrix} \tilde{v}_\alpha \\ \tilde{v}_\beta \end{bmatrix} = \hat{V}_i \begin{bmatrix} -\sin(\omega_i t) \\ \cos(\omega_i t) \end{bmatrix} \tag{3.6}$$

At voltage injection frequencies typically ranging between 600Hz and 1kHz, the stator impedance of (3.5) are dominated by the stator inductance. Therefore the *hf* response of the machine can be approximated by:

$$\begin{bmatrix}\tilde{v}_\alpha \\ \tilde{v}_\beta\end{bmatrix}=\frac{d}{dt}\begin{bmatrix}L_s-\Delta L_s\cos(2\theta_\delta) & -\Delta L_s\sin(2\theta_\delta) \\ -\Delta L_s\sin(2\theta_\delta) & L_s+\Delta L_s\cos(2\theta_\delta)\end{bmatrix}\cdot\begin{bmatrix}\tilde{i}_\alpha \\ \tilde{i}_\beta\end{bmatrix} \tag{3.7}$$

Applying the voltage injection (3.6) into the *hf* model of (3.7) the current vector is obtained:

$$\begin{bmatrix}\tilde{i}_\alpha \\ \tilde{i}_\beta\end{bmatrix}=\frac{\hat{V}_i}{\omega_i L_\delta L_\gamma}\begin{bmatrix}L_s+\Delta L_s\cos(2\theta_\delta) & \Delta L_s\sin(2\theta_\delta) \\ \Delta L_s\sin(2\theta_\delta) & L_s-\Delta L_s\cos(2\theta_\delta)\end{bmatrix}\cdot\begin{bmatrix}\cos(\omega_i t) \\ \sin(\omega_i t)\end{bmatrix} \tag{3.8}$$

This equation can be simplified to:

$$\begin{bmatrix}\tilde{i}_\alpha \\ \tilde{i}_\beta\end{bmatrix}=\frac{\hat{V}_i}{\omega_i L_\delta L_\gamma}\begin{bmatrix}L_s\cos(\omega_i t)+\Delta L_s\cos(2\theta_\delta-\omega_i t) \\ L_s\sin(\omega_i t)+\Delta L_s\sin(2\theta_\delta-\omega_i t)\end{bmatrix} \tag{3.9}$$

Examining (3.9), it is noted that at constant saliency speed $\theta_\delta=\omega_\delta t$, each of the components of *hf* current vector correspond to a single-sideband amplitude modulated signal. The vector nature of the *hf* current does provide some useful properties: the carrier component of both α and β currents form a positive sequence *hf* currènt vector proportional to the average inductance, and the sidebands form a negative sequence *hf* current vector which is proportional to the amount of saliency of the machine. Only the negative sequence contains saliency position information, therefore the small value of saliency in surface mounted PM machines results in a large carrier component.

3.3.1.1 Demodulation

The *hf* currents of (3.9) are separated form the fundamental currents of the motor by hardware band-pass filters. To extract the saliency angle information $2\theta_\delta$ from $\underline{\tilde{i}}_{\alpha\beta}$, it's vectorial characteristic and the different sequence of rotation of the carrier and the sideband vectors are exploited by using a filter in a rotating frame synchronous with either of the *hf* rotating components. This can be interpreted as a vector equivalent of homodyne or heterodyne demodulation. For homodyne demodulation the carrier is required. Because the carrier current is generated by the known injection voltage applied to the highly inductive impedance of the motor, the carrier's frequency and phase are readily available.

For easier mathematical analysis of the operation of the carrier synchronous filter, (3.9) is written in complex notation and the positive and negative sequence components are defined as:

$$\underline{\tilde{i}}_{\alpha\beta} = \underline{\tilde{i}}_{ps} + \underline{\tilde{i}}_{ns} = \frac{\hat{V}_i}{\omega_i L_\delta L_\gamma}\left\{L_s e^{j\omega_i t} + \Delta L_s e^{j(2\theta_\delta - \omega_i t)}\right\} \tag{3.10}$$

In [21, 25, 36] a heterodyne demodulation strategy is proposed where the filtering is carried out in an estimated frame synchronous with the negative sequence rotating vector:

$$\underline{\tilde{i}}_{\alpha\beta} \cdot e^{-j\left(2\hat{\theta}_\delta - \omega_i t\right)} = \frac{\hat{V}_i}{\omega_i L_\delta L_\gamma}\left\{L_s e^{-j\left(2\hat{\theta}_\delta - 2\omega_i t\right)} + \Delta L_s e^{j\left(2\theta_\delta - 2\hat{\theta}_\delta\right)}\right\} \tag{3.11}$$

This transformation provides the spectral separation between the carrier and the sideband and allows the carrier to be attenuated by a low-pass filter, ideally obtaining:

$$\underline{\tilde{i}}_{ns} \cdot e^{-j\left(2\hat{\theta}_\delta - \omega_i t\right)} \approx \frac{\hat{V}_i \Delta L_s}{\omega_i L_\delta L_\gamma} e^{j\left(2\theta_\delta - 2\hat{\theta}_\delta\right)} \tag{3.12}$$

The imaginary component of (3.12) is therefore proportional to $\sin\left(2\theta_\delta - 2\hat{\theta}_\delta\right)$ and for small angle estimation errors it can be approximated by:

$$\mathrm{Im}\left\{\frac{\hat{V}_i \Delta L_s}{\omega_i L_\delta L_\gamma} e^{j\left(2\theta_\delta - 2\hat{\theta}_\delta\right)}\right\} \approx \frac{2 \cdot \hat{V}_i \Delta L_s}{\omega_i L_\delta L_\gamma}\left(\theta_\delta - \hat{\theta}_\delta\right) \tag{3.13}$$

This signal is used to drive a position and speed observer to estimate $\hat{\theta}_\delta$, as the one shown in Fig. 3.4. [25], a similar structure but including a mechanical observer for improved dynamic is proposed in [21, 31, 36].

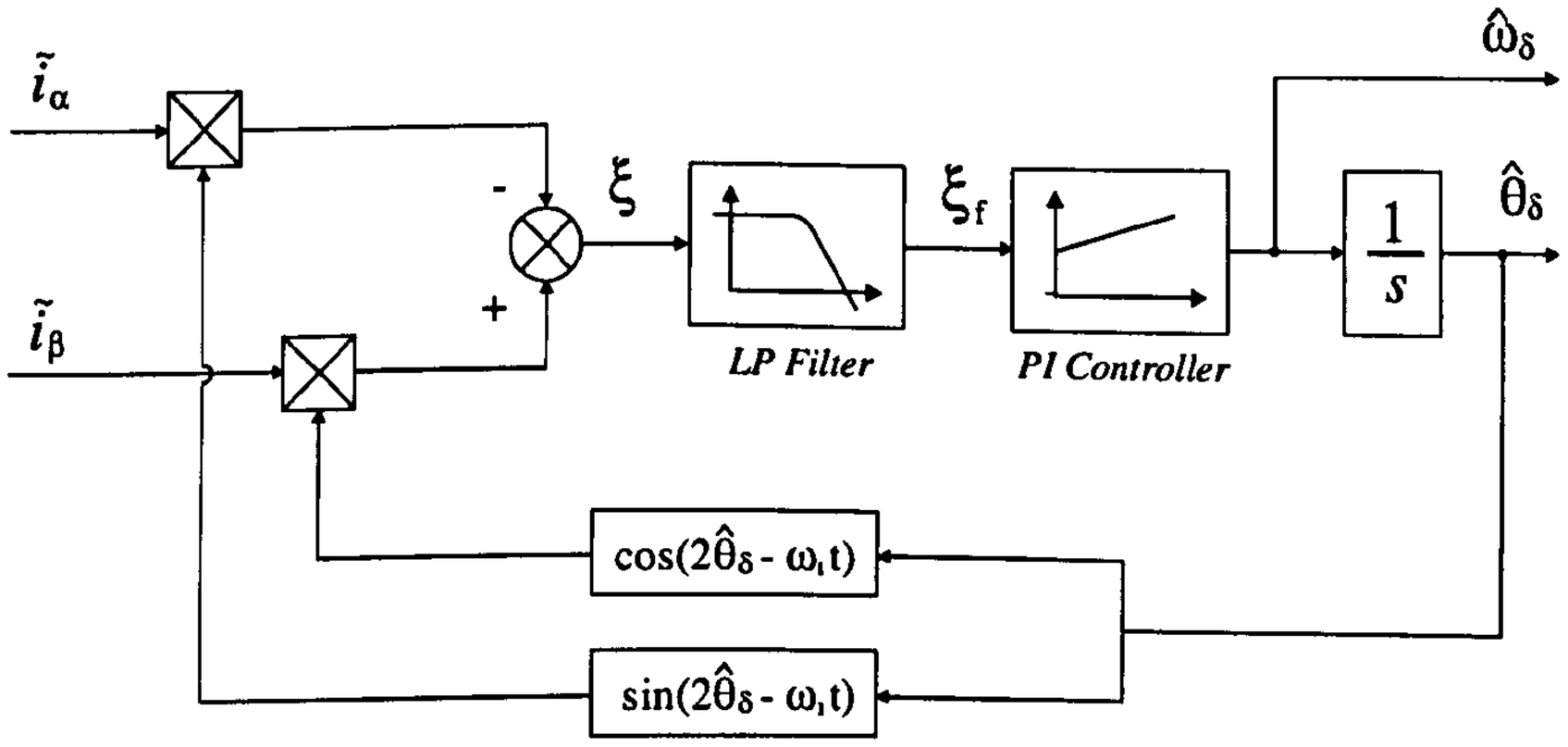

Figure 3.4: Heterodyne demodulation and position observer.

The technique described has a disadvantage when applied to the SMPM machine since the large carrier content makes it difficult to remove it by a low-pass filter due to the finite gain of the filter at the frequencies near $2\omega_i$. A variation of the previous method is presented in this work by direct homodyne demodulation. The implemented filter synchronous with the carrier frequency is shown in Fig. 3.5.

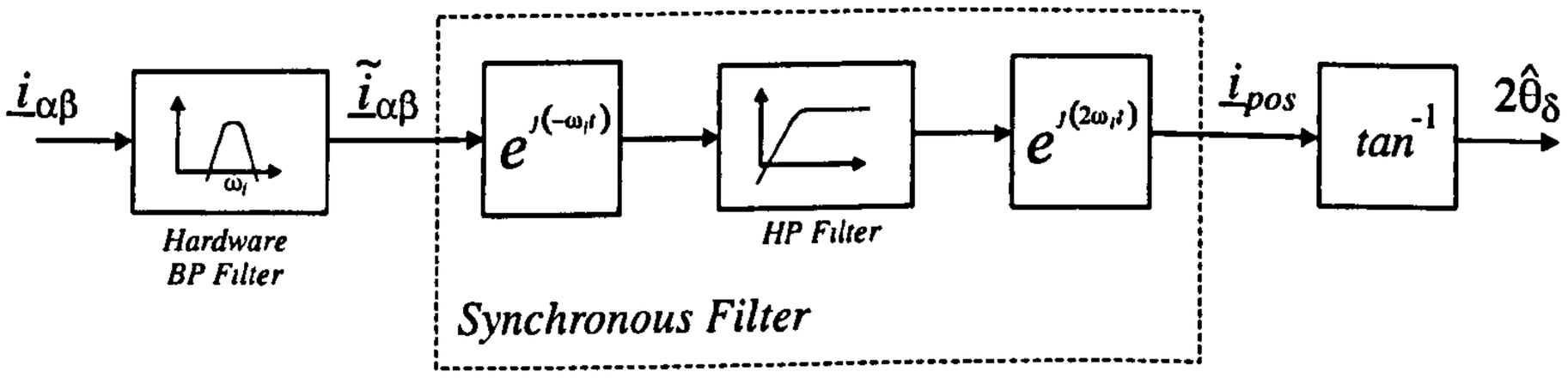

Figure 3.5: Synchronous filter for homodyne demodulation of *hf* current vector.

By transforming the *hf* current to a reference frame synchronous with the injection (positive sequence), the carrier current component becomes DC and the negative sequence $2\omega_i$:

$$\underline{\tilde{i}}_{\alpha\beta} \cdot e^{-j\omega_i t} = \frac{\hat{V}_i}{\omega_i L_\delta L_\gamma}\left\{L_s + \Delta L_s e^{j(2\theta_s - 2\omega_i t)}\right\} \tag{3.14}$$

A high-pass filter implemented in this frame completely eliminates the DC component of the current signal and the low cut-off frequency of this high-pass filter ensures that the component at $2\omega_i$ is largely unaltered yielding:

$$\underline{\tilde{i}}_{ns} \cdot e^{-j\omega_i t} = \frac{\hat{V}_i \cdot \Delta L_s}{\omega_i L_\delta L_\gamma} e^{j(2\theta_s - 2\omega_i t)} \tag{3.15}$$

Finally, the signal is rotated to a frame synchronous with the negative sequence where the saliency position signal becomes base-band:

$$\underline{i}_{pos} = \underline{\tilde{i}}_{ns} \cdot e^{j2\omega_i t} = \frac{\hat{V}_i \cdot \Delta L_s}{\omega_i L_\delta L_\gamma} e^{j(2\theta_\delta)} \tag{3.16}$$

The saliency angle information $2\theta_\delta$ is obtained by direct tan^{-1} extraction from the component of the $\underline{i}_{pos}$ vector [27]. Alternatively a mechanical observer similar to that shown in Fig. 3.4 can perform the last frame rotation and the angle extraction.

3.3.2 Pulsating d-axis Injection

The second method of *hf* signal injection for saliency tracking found in the literature consists of a pulsating signal injected along a synchronous axis (normally *d-axis*, although *q-axis* injection as also been proposed [18]). Blaschke at al. [52] originally presented this method for current injection, nevertheless it has being more extensively applied to voltage injection strategies [18, 34, 35, 58, 59]. As the actual rotor position and the true *d-axis* are unknown *a priori*, a new estimated synchronous frame d^e-q^e is

defined. The pulsating *hf* voltage is superimposed in the d^e voltage reference and signal processing of the resulting *hf* currents is used to obtain the orientation error of d^e-q^e respect to the saliency position. This error signal is used to correct the original estimation driving a PLL or a mechanical observer to track the actual saliency angle. The main advantage of *d-axis* injection is that it minimizes the *hf* current in the torque producing axis, hence minimizing the pulsating torque and acoustic noise.

Because the pulsating injection method tracks saliency rather than rotor position directly, as discussed in section 3.2.2 the saturation saliency is not perfectly oriented with the *d-q* frame. In the following analysis a change of notation is introduced and the saliency oriented frame δ-γ is used instead of the rotor frame *d-q*. Similarly an estimated saliency oriented frame δ^e-γ^e is introduced on which is the *hf* voltage signal is injected. Considering the *hf* salient model for the SMPM machine given by (3.7), and rotating it to the δ^e-γ^e coordinates system, the following relation is obtained:

$$\begin{bmatrix} \tilde{v}_\delta^e \\ \tilde{v}_\gamma^e \end{bmatrix} = \frac{d}{dt}\begin{bmatrix} L_s - \Delta L_s \cos(2\Delta\theta_\delta) & -\Delta L_s \sin(2\Delta\theta_\delta) \\ -\Delta L_s \sin(2\Delta\theta_\delta) & L_s + \Delta L_s \cos(2\Delta\theta_\delta) \end{bmatrix} \cdot \begin{bmatrix} \tilde{i}_\delta^e \\ \tilde{i}_\gamma^e \end{bmatrix} \tag{3.17}$$

where $\Delta\theta_\delta = \hat{\theta}_\delta - \theta_\delta$. By imposing the δ^e-*axis* pulsating voltage given by:

$$\begin{bmatrix} \tilde{v}_\delta^e \\ \tilde{v}_\gamma^e \end{bmatrix} = \hat{V}\begin{bmatrix} \sin(\omega_i t) \\ 0 \end{bmatrix} \tag{3.18}$$

the *hf* current response is

$$\begin{bmatrix} \tilde{i}_\delta^e \\ \tilde{i}_\gamma^e \end{bmatrix} = \frac{-\hat{V}\cos(\omega_i t)}{L_\delta L_\gamma \omega_i}\begin{bmatrix} L_s + \Delta L_s \cos(2\Delta\theta_\delta) \\ -\Delta L_s \sin(2\Delta\theta_\delta) \end{bmatrix} \tag{3.19}$$

It is noted that the currents are pulsating and therefore to obtain an useful error signal they need to be demodulated. Different methods have been proposed for the generation of the error signal: Sul at al. [33, 35, 60, 61] used a extra pair of measurement axis to perform the demodulation. In [18] the direct demodulation of the

hf current induced in the axis opposite to the voltage injection axis ($\tilde{i}_\gamma^e$ in (3.19)) is used. A similar vectorial strategy is applied in [34]. In what follows a detailed mathematical analysis of these strategies is presented and the discussion of the merits of each approach will lead to the selection of the most appropriate algorithm to be implemented in the present work.

3.3.2.1 The measurement axis method

The proposed measurement frame in [33, 35, 60, 61], denoted by δ^m-γ^m, is displaced – 45° from the estimated saliency frame δ^e-γ^e and the *hf* current in this measurement axis are used to obtain the orientation error. The coordinate rotation between the estimated saliency and the measurement frame is given by

$$\begin{bmatrix} \tilde{i}_\delta^m \\ \tilde{i}_\gamma^m \end{bmatrix} = \frac{\sqrt{2}}{2} \begin{bmatrix} 1 & -1 \\ 1 & 1 \end{bmatrix} \cdot \begin{bmatrix} \tilde{i}_\delta^e \\ \tilde{i}_\gamma^e \end{bmatrix} \tag{3.20}$$

applying this rotation to the *hf* currents of (3.19) gives:

$$\begin{bmatrix} \tilde{i}_\delta^m \\ \tilde{i}_\gamma^m \end{bmatrix} = \frac{-\sqrt{2} \cdot \hat{V} \cos(\omega_i t)}{2 L_\delta L_\gamma \omega_i} \begin{bmatrix} L_s + \Delta L_s \cos(2\Delta\theta_\delta) - \Delta L_s \sin(2\Delta\theta_\delta) \\ L_s + \Delta L_s \cos(2\Delta\theta_\delta) + \Delta L_s \sin(2\Delta\theta_\delta) \end{bmatrix} \tag{3.21}$$

In (3.21), the orthogonal pulsating currents $\tilde{i}_\delta^m$ and $\tilde{i}_\gamma^m$ have the same amplitude if the estimated saliency frame δ^e-γ^e is correctly oriented with the actual saliency frame δ-γ. On the other hand, a misalignment of both frames results in one of the amplitude of the measurement axis currents to be larger than the other as illustrated in Fig. 3.6. This principle uses the difference in amplitude of these two currents as the orientation error.

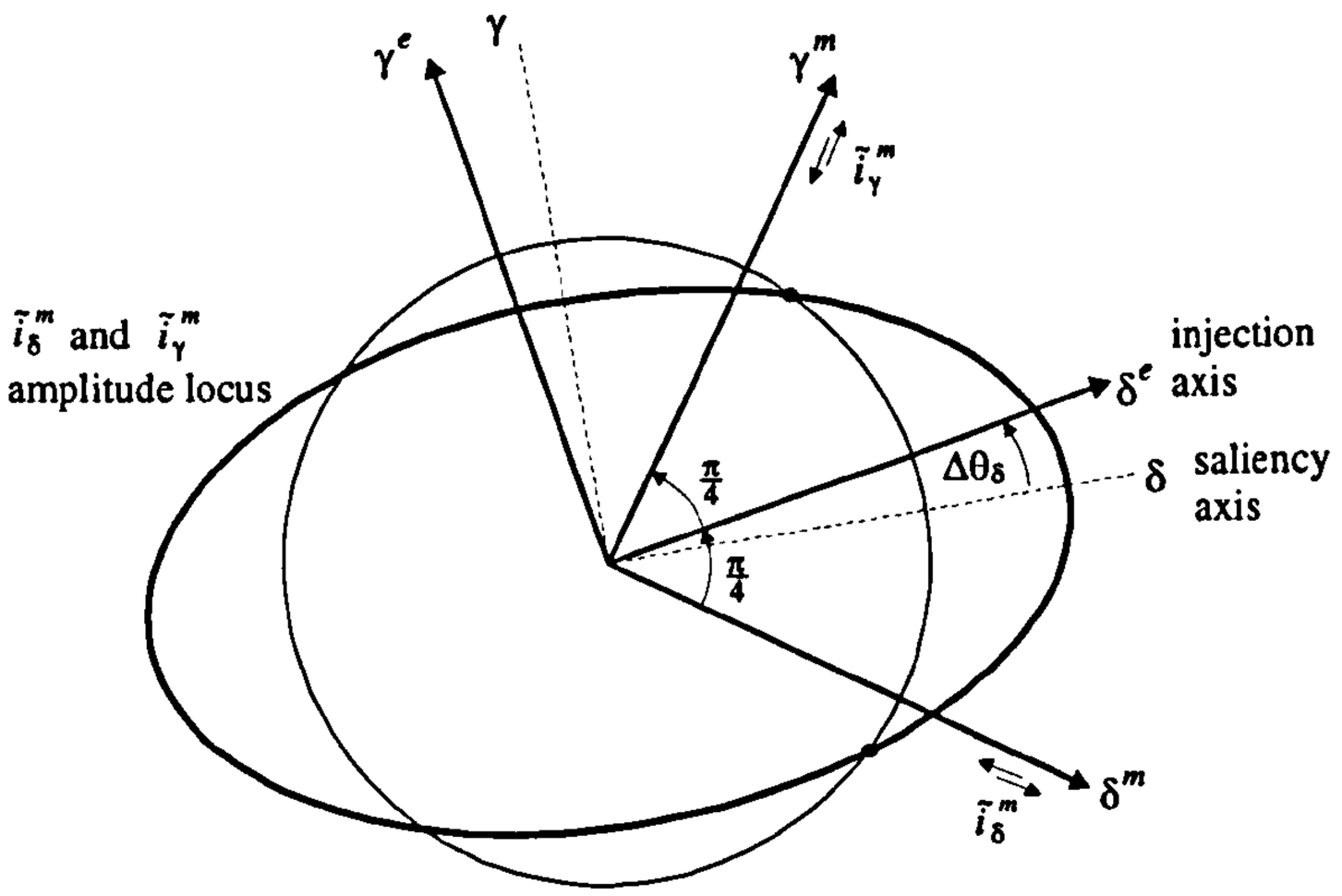

Figure 3.6: Measurement axis method.

The signal processing to generate the error signal is described by the block diagram of figure 3.7. Multiplication by the *hf* carrier and low pass filtering is used to demodulate the measurement axis currents. In order to avoid the influence of any carrier phase shift due to the stator resistance, or processing delay, orthogonal carriers are used and the square of the resulting signals are added yielding the amplitude square of the measurement axis currents:

$$i_1^2 + i_2^2 = \frac{1}{4}\cdot\left[I_0 + I_1\cos(2\Delta\theta_\delta) - I_1\sin(2\Delta\theta_\delta)\right]^2 = \frac{\left|\tilde{i}_\delta^{\,m}\right|^2}{4}$$
$$i_3^2 + i_4^2 = \frac{1}{4}\cdot\left[I_0 + I_1\cos(2\Delta\theta_\delta) + I_1\sin(2\Delta\theta_\delta)\right]^2 = \frac{\left|\tilde{i}_\gamma^{\,m}\right|^2}{4} \qquad (3.22)$$

were $I_0 = \frac{-\sqrt{2}\cdot L_s}{2L_\delta L_\gamma \omega_i}$ and $I_1 = \frac{-\sqrt{2}\cdot \Delta L_s}{2L_\delta L_\gamma \omega_i}$.

Finally the error is calculated as:

$$\zeta = \frac{\left|\tilde{i}_\delta^{\,m}\right|^2}{4} - \frac{\left|\tilde{i}_\gamma^{\,m}\right|^2}{4} = I_0 I_1 \sin(2\Delta\theta_\delta) + \frac{I_1^2}{2}\sin(4\Delta\theta_\delta) \qquad (3.23)$$

Equation (3.23) shows that the error signal ζ is proportional to $\Delta\theta_\delta$ for small values of $\Delta\theta_\delta$. This signal is therefore used to drive a PLL structure to obtain the estimated saliency position.

The main draw back of this demodulation method is that it relies on a sinusoidal saliency. In the presence of higher order saliencies or spatial harmonics the condition $\left|\tilde{i}_\delta^m\right| = \left|\tilde{i}_\gamma^m\right|$ is not unique and it can produce errors in the saliency position estimation that are difficult to compensate since tracking mechanism may lock onto any of the points that satisfy this condition.

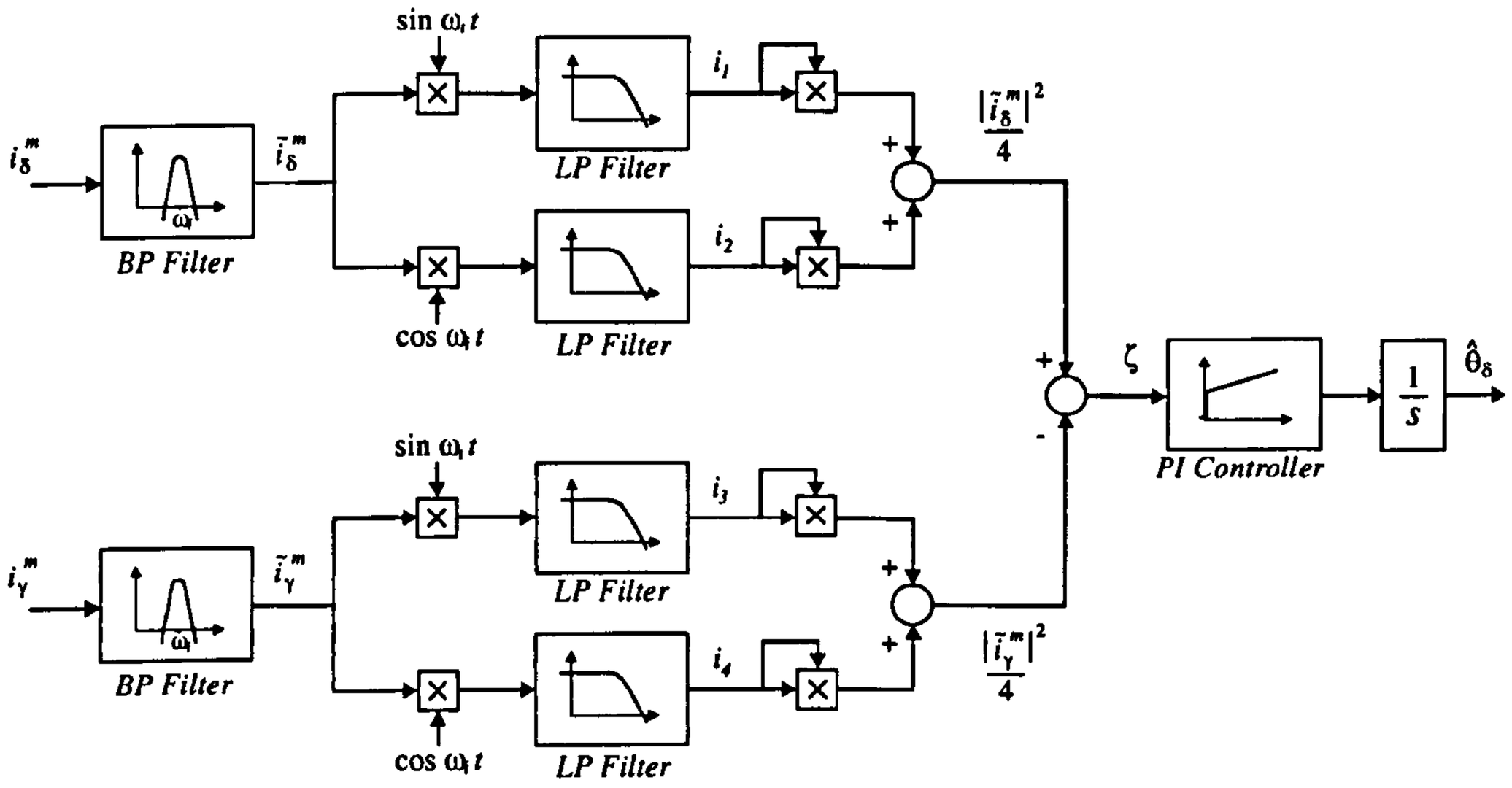

Figure 3.7: Error signal generation for the measurement axis method.

3.3.2.2 Direct demodulation of the estimated synchronous frame currents

An analysis of (3.19) reveals that the amplitude of the pulsating current in the axis orthogonal to that of the injection, i.e. $\tilde{i}_\gamma^e$ is proportional to $\sin(2\Delta\theta_\delta)$ and therefore it can be used as an error signal provided that it is properly demodulated. The easiest way to demodulate $\tilde{i}_\gamma^e$ is by multiplication by it's carrier and then low-pass filtering, as shown in Fig. 3.8. The current carrier is derived from the injection voltage by considering the machine's impedance as perfectly inductive at injection frequency, hence producing a phase shift of 90 degrees. Processing delays will cause a phase

error in the determination of the carrier, but due to the high sampling frequency, this error is small. Furthermore the delay is constant and therefore easy to take in to account.

The algorithm chosen for implementation of pulsating *d-axis* injection is described in Fig. 3.8. The current in the γ^e-*axis* is calculated form the measured α-β currents and then passed through to a band-pass filter with central frequency ω_i to extract the *hf* component. This signal is then multiplied by the current carrier and filtered to extract the low frequency error signal. The error signal drives a PLL to obtain the estimated saliency position angle $\hat{\theta}_\delta$. Finally, the speed of the saliency position can be derived directly from the tracking algorithm. To reduce the noise created by the high gains of the controller of the tracking loop, a first order low pass filter is used.

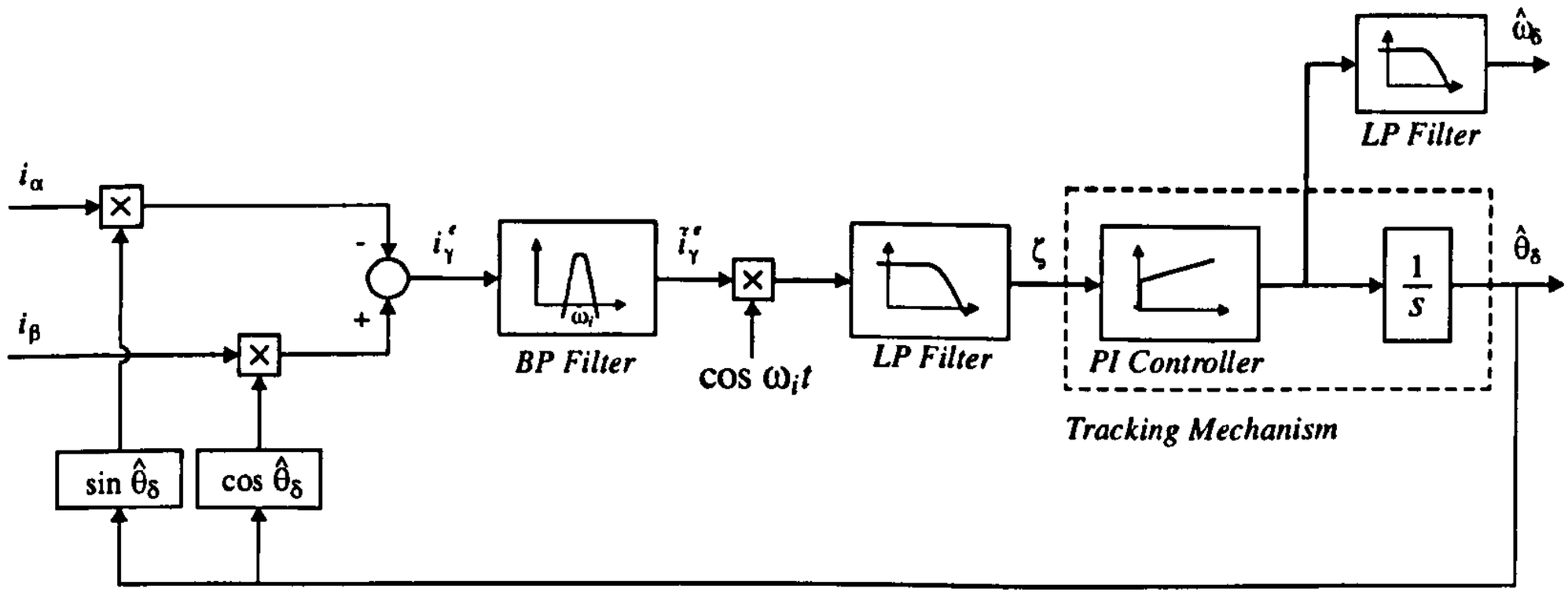

Figure 3.8: Implemented demodulation for *d-axis* injection.

This direct demodulation approach is used in [18, 59] for rotor position detection in salient-pole IPM synchronous machines. Although the authors in [18] propose injection in the *q-axis* equivalent signal processing can be applied to the more advantageous *d-axis* injection considered in the present work. Multiplying the current $\tilde{i}_\gamma^e$ of (3.19) by the carrier $\cos(\omega_i t)$ it yields:

$$\tilde{i}_\gamma^e \cos(\omega_i t) = \frac{\hat{V} \cdot \Delta L_s \sin(2\Delta\theta_\delta)}{2 L_\delta L_\gamma \omega_i} \cdot \{1 + \cos(2\omega_i t)\} \tag{3.24}$$

The low-pass filter shown in Fig. 3.8 attenuates the harmonic at double the carrier frequency producing the error signal:

$$\zeta = \frac{\hat{V} \cdot \Delta L_s}{2 L_\delta L_\gamma \omega_i} \cdot \sin(2\Delta\theta_\delta) \tag{3.25}$$

The error signal given by (3.25) feeds a tracking mechanism to adjust the value of θ_δ and drive this error to zero. A conventional PLL with double integration, as shown in Fig. 3.8, is used for this purpose [59]. Alternatively, the mechanical model of the machine may be included to form a mechanical observer as proposed in [18], this tracking mechanism is shown in Fig. 3.9. In fact the operation of the two tracking algorithms are very similar and the discussion of which structure is better is an ongoing one. The mechanical observer of Fig. 3.9 includes feed forward of the torque demand allowing better dynamic responses to changes in torque demand, e.g. acceleration or deceleration at constant load. This improved performance comes at the cost of knowledge of the mechanical parameters that in general are not always available and may change during the operation of the drive. On the other hand, for changes in the mechanical load, the double integrator PLL of Fig. 3.8 presents similar dynamic performances and it is easier to tune because it requires adjustment of less parameters and does not require knowledge of the mechanical quantities. The simplicity of the standard PLL is favoured in this work.

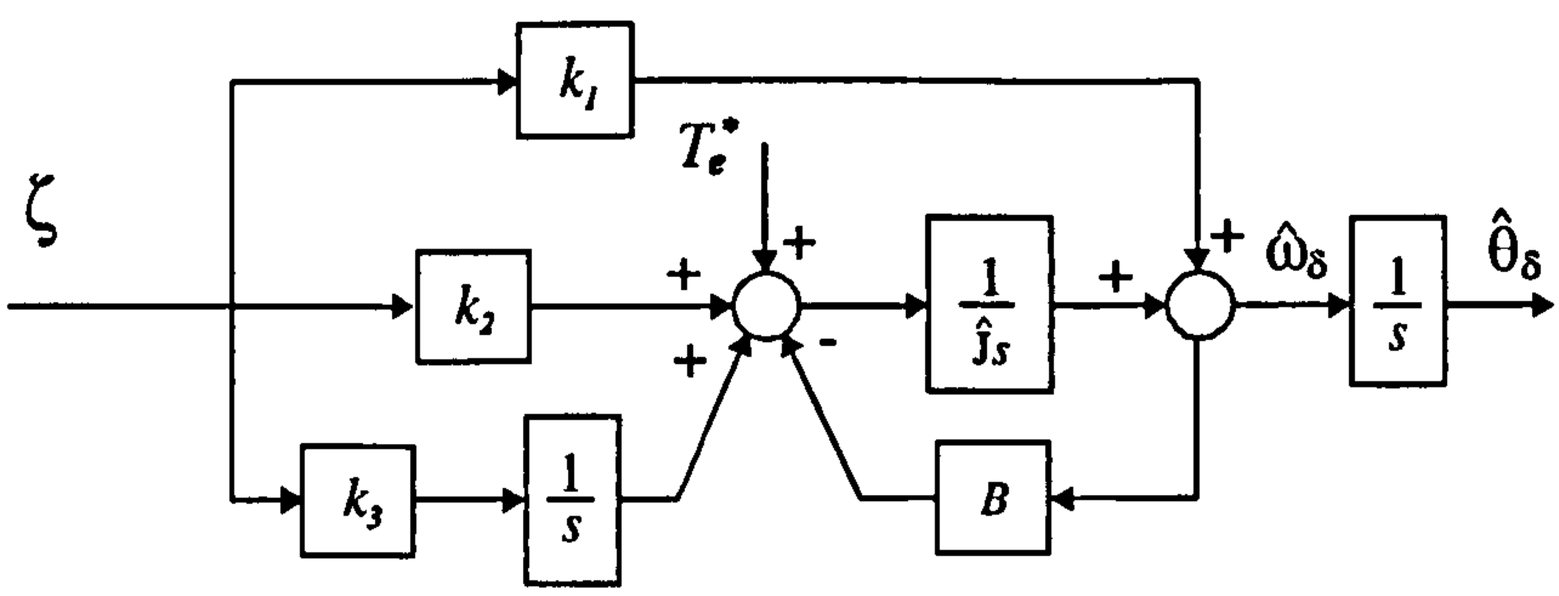

Figure 3.9: Tracking mechanism including mechanical model.

A slightly different way to derive the error signal ζ is proposed in [34]. It extracts the saliency position information contained in both *hf* currents $\tilde{i}_\delta^e$ and $\tilde{i}_\gamma^e$ rather than using only $\tilde{i}_\delta^e$. This vectorial demodulation algorithm is shown in Fig. 3.10. Here, the

complete *hf* currents vector $\tilde{i}^{e}_{\delta\gamma}$ is rotated to a frame synchronous with the positive sequence of the injection carrier. The error signal is derived from the imaginary component of the resulting vector.

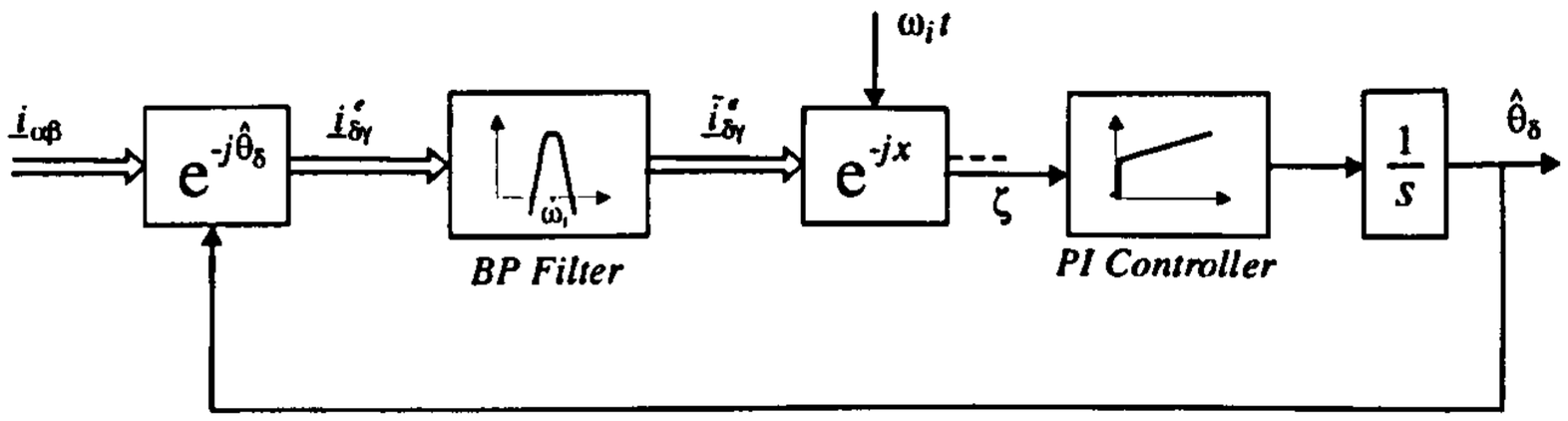

Figure 3.10: Vectorial demodulation for *d-axis* injection.

To understand the signal processing described in Fig. 3.10, it is useful to re-write (3.19) in complex notation:

$$\tilde{\underline{i}}^{e}_{\delta\gamma} = \frac{-\hat{V}}{2L_\delta L_\gamma \omega_i}\left\{L_s e^{j\omega_i t} + L_s e^{-j\omega_i t} + \Delta L_s e^{j(\omega_i t - 2\Delta\theta_\delta)} + \Delta L_s e^{-j(\omega_i t + 2\Delta\theta_\delta)}\right\} \quad (3.26)$$

By rotating this signal to a frame synchronous with the injection, the following vector is obtained:

$$\tilde{\underline{i}}^{e}_{\delta\gamma} \cdot e^{-j\omega_i t} = \frac{-\hat{V}}{2L_\delta L_\gamma \omega_i}\left\{L_s + L_s e^{-2j\omega_i t} + \Delta L_s e^{-j2\Delta\theta_\delta} + \Delta L_s e^{-j(2\omega_i t + 2\Delta\theta_\delta)}\right\} \quad (3.27)$$

Only the imaginary component of 3.27 is extracted and used as an error signal:

$$\zeta = \frac{-\hat{V}}{2L_\delta L_\gamma \omega_i}\left\{-L_s \sin(2\omega_i t) - \Delta L_s \sin(2\Delta\theta_\delta) - \Delta L_s \sin(2\omega_i t + 2\Delta\theta_\delta)\right\} \quad (3.28)$$

Although no filter is explicitly used in [34], the low-pass characteristic of the adaptation mechanism filters the spectral contents at $2\omega_i$ yielding a useful low-frequency error of:

$$\zeta_{LF} = \frac{\hat{V} \cdot \Delta L_s}{2 L_\delta L_\gamma \omega_i} \cdot \sin(2\Delta\theta_\delta) \tag{3.29}$$

A comparison of (3.25) and (3.29) shows that there is no difference in the low-frequency component of the error yield by the demodulation of the orthogonal γ^e-*axes* current and the vectorial demodulation of the δ^e-γ^e axis currents. However, a comparison of the *hf* spectral contents of this error signals prior to filtering (equations (3.24) and (3.28)), reveals that the vectorial demodulation strategy proposed in [34] is disadvantageous because it contains significantly larger *hf* components. In fact, (3.28) contain a spectral component at frequency $2\omega_i$ that is proportional to the average inductance L_s and would be difficult to filter off because its large magnitude. For this reason direct demodulation of $\tilde{i}_\gamma^e$ is used in this work when implementing *d-axis* voltage injection.

It is worth noticing that all the pulsating strategies discussed perform the separation of the *hf* injection current from the fundamental excitation current (i.e. filtering of the measured line currents) in the estimated synchronous frame δ^e-γ^e and therefore by software filters. The reason for using software band-pass filters, instead of the hardware filters (as in the α-β injection), is because the frequency of the injection current, as measured in the lines of the motor, changes with the rotor speed due to the synchronous rotation of the injection axis. Hence, the phase shift introduced by any hardware filter will vary with rotor speed. The magnitude of the phase shift variation is high in high order narrow band-pass filters and may result in loss of orientation at considerable speeds, see Appendix C. The filtering of the currents in the rotated frame solves this problem but this reduces the resolution at which the *hf* currents are digitised because the digital to analogue converters are scaled for maximum fundamental currents.

3.3.3 Rotating d-q Frame Injection

A new injection strategy has being proposed by [62]. It consist of injection synchronous with the δ^e-γ^e frame, as in the method of Section 3.3.2, but includes injection in both axis generating a rotating vector in this frame. The objective is to increase the saliency position information content in the resulting *hf* signal by obtaining relevant position signals in both δ^e-*axes* and γ^e-*axes* currents. The voltage injection is given by:

$$\begin{bmatrix} \tilde{v}_\delta^e \\ \tilde{v}_\gamma^e \end{bmatrix} = \hat{V} \begin{bmatrix} -\sin(\omega_i t) \\ \cos(\omega_i t) \end{bmatrix} \tag{3.30}$$

Applying this voltage to the *hf* model (3.17), the current response is given by:

$$\begin{bmatrix} \tilde{i}_\delta^e \\ \tilde{i}_\gamma^e \end{bmatrix} = \frac{\hat{V}}{L_\delta L_\gamma \omega_i} \begin{bmatrix} L_s \cos(\omega_i t) + \Delta L_s \cos(-\omega_i t - 2\Delta\theta_\delta) \\ L_s \sin(\omega_i t) + \Delta L_s \sin(-\omega_i t - 2\Delta\theta_\delta) \end{bmatrix} \tag{3.31}$$

This current vector is composed by two rotating components and is analogous to the α-β rotating injection, discussed in Section 3.3.1. Again the positive sequence does not contain any position information. The difference to the α-β injection is that the negative sequence component contains information of the saliency orientation error $\Delta\theta_\delta$, rather than absolute saliency position θ_δ. To obtain the saliency position error, the same synchronous filter of Fig. 3.5 is implemented achieving complete elimination of the positive sequence component and yielding the following band current vector:

$$\underline{\tilde{i}}_{ns} \cdot e^{j\omega_i t} = \frac{\hat{V}_i \cdot \Delta L_s}{\omega_i L_\delta L_\gamma} \begin{bmatrix} \cos(2\Delta\theta_\delta) \\ -\sin(2\Delta\theta_\delta) \end{bmatrix} \tag{3.32}$$

The direct tan^{-1} extraction of the quotient of these current components yields the orientation error and it is used in a tracking algorithm. This is implemented in the way of a PLL like the one shown in Fig. 3.8 used for *d-axis* pulsating injection.

The obvious disadvantage of this method over *d-axis* injection is the increase in *q-axis* current and therefore pulsating torque. Accordingly to the original reference [62] this method produced better saliency position error than that of *d-axis* injection only. The performance can only be assessed experimentally and no conclusions can be drawn from the ideal fundamental saliency analysis presented here.

3.4 Other Signal Injection Techniques

Saliency position information can also be extracted by injection of rectangular voltage pulses of short durations rather than persistent sinusoidal excitation. This approach was first suggested in [63] and is known as the INFORM method (INdirect Flux detection by On-line Reactance Measurement) [53, 64]. The test pulses are not injected continuously but intermittently and the current response to the pulses contain the saliency position giving an instantaneous sample of the position estimation. The current response to a voltage pulse is dominated by the stator voltage equation:

$$\underline{v} = L_s \frac{d\underline{i}_s}{dt} + r_s \underline{i} + \underline{e} \tag{3.33}$$

where L_s is the inductance matrix defined by (3.5). In the INFORM method, two short consecutive voltage pulses of opposite polarity are injected. By subtracting the response to both pulses, the influence of the back-EMF and the resistive drop is eliminated. Approximating the derivative of the current by the difference of the sampled currents, the difference of the response to both pulses can be written as:

$$\underline{v}_I - \underline{v}_{II} \approx L_s \left(\frac{\Delta \underline{i}_I}{\Delta t} - \frac{\Delta \underline{i}_{II}}{\Delta t} \right) \tag{3.34}$$

For simplicity this equation is writing in terms of vector differences:

$$\begin{aligned} \underline{v}_\Delta &= \underline{v}_I - \underline{v}_{II} \\ \Delta \underline{i}_\Delta &= \Delta \underline{i}_I - \Delta \underline{i}_{II} \end{aligned} \tag{3.35}$$

Replacing (3.35) into (3.34):

$$\underline{v}_{\Delta} \approx L_s \frac{\Delta \underline{i}_{\Delta}}{\Delta t} \tag{3.36}$$

When solving for the currents derivative it is convenient to express equation (3.36) in terms of the inverse of the inductance matrix $Y_s = L_s^{-1}$:

$$\frac{\Delta \underline{i}_{\Delta}}{\Delta t} \approx Y_s \underline{v}_{\Delta} \tag{3.37}$$

Using the inverse of the inductance matrix calculated previously in (3.8), equation (3.37) can be written in complex notation as:

$$\frac{\Delta \underline{i}_{\Delta}}{\Delta t} \approx y_0 \underline{v}_{\Delta} + \Delta y \cdot e^{j2\theta_s} \cdot (\underline{v}_{\Delta})^T \tag{3.38}$$

where y_0 and Δy are positive quantities and the angle θ_δ indicates the angular position of the minimum inductance. If the voltage pulse is written as $\underline{v}_{\Delta} = V \cdot e^{j(\theta_\delta + \beta_u)}$, where β_u is the angular difference between the saliency position θ_δ (unknown) and the voltage pulse direction (known), then equation (3.38) becomes

$$\frac{\Delta \underline{i}_{\Delta}}{\Delta t} \approx y_0 \cdot V \cdot e^{j(\theta_\delta + \beta_u)} + \Delta y \cdot e^{j2\theta_\delta} \cdot e^{-j(\theta_\delta + \beta_u)} \tag{3.39}$$

from which $\underline{y}_{INFORM}$ may be defined:

$$\frac{\Delta \underline{i}_{\Delta}}{\Delta t} \approx \underline{v}_{\Delta} \cdot \left[y_0 + \Delta y \cdot e^{-j2\beta_u} \right] = \underline{v}_{\Delta} \cdot \underline{y}_{INFORM}(2\beta_u) \tag{3.40}$$

This is the main equation of the INFORM method and although it has been derived for the α-β frame, it is valid in any arbitrary reference frame because the complex

$\underline{y}_{INFORM}$ depends only in the angular difference between the saliency position and the direction of the voltage pulse. From (3.40) can be seen clearly that the saliency position affects the current variation due to the injection of the sequence of pulses $\underline{v}_{s,I}$ and $\underline{v}_{s,II}$. To extract the angle information from (3.40) three sequences of pulses are applied, each in the direction of one of the phases of the machine e.g. inverter switching condition (1,0,0) is followed by (0,1,1) to form the first sequence, (0,1,0) is followed by (1,0,1) and finally (0,0,1) by (1,1,0) to complete the INFORM cycle.

The saliency position estimation can be achieved by measuring the current response in the phase A, B, C for the respective sequence of pulses. This makes use of only the information contained in the real part of $\underline{y}_{INFORM}$.

$$\begin{aligned}
\Delta i_{\Delta A,1} &\approx \Delta t \cdot |v_\Delta| \cdot [y_0 + \Delta y \cdot \cos(2\beta_u)] \\
\Delta i_{\Delta B,2} &\approx \Delta t \cdot |v_\Delta| \cdot [y_0 + \Delta y \cdot \cos(2\beta_u - 4\pi/3)] \\
\Delta i_{\Delta C,3} &\approx \Delta t \cdot |v_\Delta| \cdot [y_0 + \Delta y \cdot \cos(2\beta_u - 2\pi/3)]
\end{aligned} \tag{3.41}$$

It is noted that in (3.41) the angle β_u is being measured with respect to the pulse applied to phase A and therefore by definition it is equal to the saliency position $\beta_u = \theta_\delta$. This angle is calculated by computing the complex linear combination

$$C_{INFORM} = \Delta i_{\Delta A,1} + \Delta i_{\Delta B,2} \cdot e^{j\frac{4\pi}{3}} + \Delta i_{\Delta C,3} \cdot e^{j\frac{2\pi}{3}}. \tag{3.42}$$

From the definition of C_{INFORM} it follows

$$\theta_{\delta\_REAL} = \tan^{-1}\left(\frac{\mathrm{Im}\{C_{INFORM}\}}{\mathrm{Re}\{C_{INFORM}\}}\right) \tag{3.43}$$

A second estimate is obtained by considering only the response to the imaginary part of $\underline{y}_{INFORM}$. The two saliency position estimations are averaged by a stochastically optimal combination to reduce the noise. The optimal combination assumes that the

noise of both measurements have a Gaussian probabilistic density and that they are statistically independent.

The application of the INFORM cycle interrupts the normal PWM pattern of the machine and therefore cannot be applied continuously. This lead to a discrete update of the position and speed of the machine.

Other related pulse strategies have been proposed. Mitzutani et al [50] superimposed a intermittent sequence of two square pulses in opposite directions to the v_d reference voltage. As shown in section 3.3.2, if the estimated frame is oriented with the saliency, no current will be induced in the perpendicular axis; the effect of the *q-axis* current is thus used to correct the estimation of the *d-q* frame orientation.

Ogasawra at al. [22, 23, 65] propose to calculate explicitly the inductance matrix from the information contained in the PWM ripple of the current. The information contained in the normal PWM spectrum is poor, especially at low speed where most of the time zero voltage vector is applied. Therefore a modified PWM pattern that includes all six of the possible active voltage vectors of the inverter is used instead of the zero voltage vector in order to properly excite the stator circuit at low speed. This gives current ripple measurements that are high in magnitude and linearly independent. This method requires current sampling at every switching instant of the inverter in order to calculate the variation of the current as a response to every inverter pulse.

To avoid the calculation of the current derivative which is very noisy due to the short duration of the current measurements, Holtz at al [26, 30] propose to measure the zero sequence component of the phase voltages of a star connected induction machine

$$v_z = (v_a + v_b + v_c) \tag{3.44}$$

The zero sequence voltage for each of the voltage pulses of the inverter contains a strong fundamental component at double the saliency angle $2\theta_s$ and opposite vectors such as $\underline{v_1}$ and $\underline{v_4}$ yield zero sequence components approximately equal in magnitude

but opposite in sign. To extract the position estimation measurements the zero sequence voltage of three linearly independent voltage vectors applied by the inverter are necessary. Under normal PWM only 2 are lineally independent vectors, hence the PWM is modified in a way that does not affect the fundamental voltage but excites the three phases of the machine (e.g. the normal sequence $\underline{v}_0$-$\underline{v}_1$-$\underline{v}_2$ is modified to $\underline{v}_0$-$\underline{v}_1$-$\underline{v}_2$-$\underline{v}_3$-$\underline{v}_6$). Assuming a single fundamental saliency, the saliency position angle $2\theta_\delta$ can be obtained directly form a linear combination of the three measured zero sequence voltages. The method has being proved to track rotor bars saliency in star connected induction machines, but results have not yet been published for PM machines.

All the pulse injection strategies discussed require complex sample and hold circuitry, very fast A/D conversion, and the capability of sampling triggered by the edges of the PWM voltages rather than conventional synchronous sampling. Furthermore, most of them require a modified PWM generation. All of this makes them difficult to implement when compared with methods based on persistent *hf* sinusoidal excitation.

Chapter 4

4 Experimental Rig

An experimental rig consisting of a 4 kW off-the-shelf *Control Techniques* surface mounted PM machine driven by an IGBT inverter has being built in order to implement and test the sensorless strategies discussed in chapters 2 and 3. The control of the drive is programmed in a 32-bit floating-point digital signal processor (DSP). In this chapter an overview of the system's hardware and software is presented.

4.1 Overall Structure

A development system for the Texas Instrument TMS320C44 processor [66] is used as the DSP platform for the control of the PM machine. The motherboard plugs directly in to one ISA-slot of the host PC. This PC runs the user interface software that allows the user to download and run programs in to the DSP, set references and capture data. The C44 is a 32-bit floating point processor with a clock frequency of 60MHz. This DSP platform has been chosen for its computational power and communication capability that allows high frequency implementation of the complex signal processing for sensorless position estimation whilst also allows programming in a high level language such as C. This facilitates development. Nevertheless, this DSP platform does lack specific peripherals for machine control. Therefore additional logic boards have been build for PWM generation, analogue to digital conversion and encoder interfacing. These boards are arranged in a rack that also include an analogue band-pass filter board. The interface boards communicate with the DSP through DSPLINK1, a parallel data bus proprietary to the board's manufacturer, which is

connected to the back-plane of the rack. The communication between the different components of the control hardware is depicted in Fig. 4.1.

An interface board provides the link between the DSP and the power circuit. The PWM board directly controls the switching of a 7.5 kW *Eurotherm 620 vector series* IGBT inverter driving the PM machine. Two phase currents and two line to line voltages of the machine are measured by appropriate transducers and the measured signals are fed back to the DSP in two versions (a) the unaltered signals used for current feedback and model based calculations and (b) the *hf* component, extracted by 4^{th} order Butterworth band-pass filters used for the *hf* sensorless strategy. Two A/D boards with four 16-bit channels each are used to digitise these measurement signals. Finally the encoder board monitors the pulses of a quadrature encoder fitted on the PM machine shaft to obtain the absolute position measurement. This signal is used for comparison with the sensorless estimation and for the commissioning of the compensation strategies.

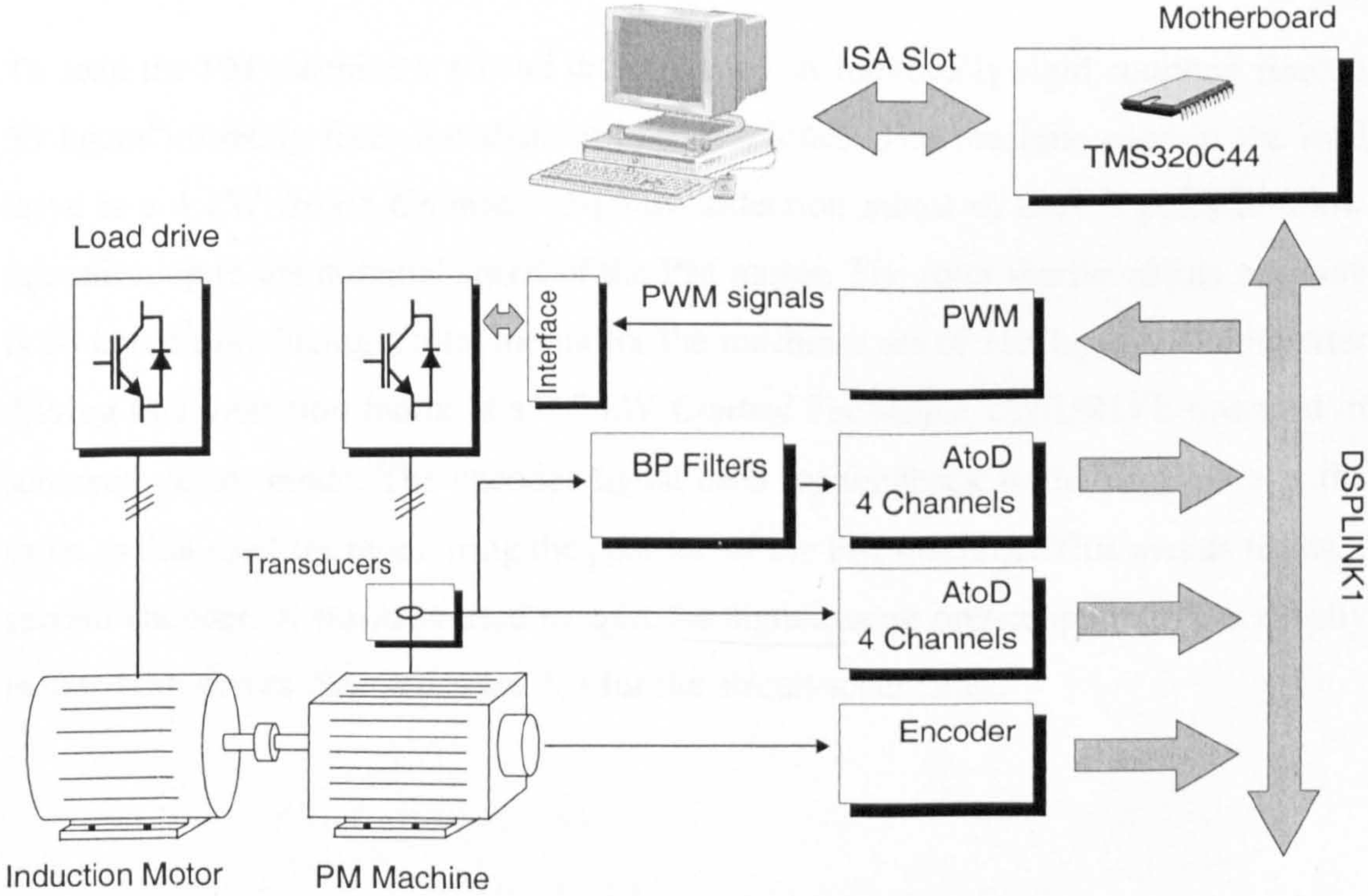

Figure 4.1: General structure of the drive.

The permanent magnet motor used in this work is a 3-phase AC servomotor supplied by *Control Techniques* under the commercial name UNIMOTOR. The machines parameters are listed in Table 4.1.

Model:	142UMC30
Number of poles:	6
Rated speed:	3000 (rpm)
Rated torque:	12.2 (Nm)
Rated power	3.82 (kW)
Kt:	1.6 (Nm/Arms)
Ke:	98.0 (Vrms/krpm):
Inertia:	20.5 (kgcm²)
R (ph-ph):	0.94 (Ohms)
L (ph-ph):	8.3 (mH)
Continuous stall:	15.3 (Nm)
Peak:	45.9 (Nm)

Table 4.1: Manufacturer's data for the PM machine.

To load the PM machine a second drive is used. A torsionally rigid coupling (inertia 53 kgcm^2) directly fixes the shaft of both machines. The machine used in the load drive is a 4 kW *Brook Crompton* 3-phase induction motor of only 2 poles to allow operation up to the nominal speed of the PM motor. The rotor inertia of this machine is 80 kgcm^2, producing a total inertia for the machines set of 153 kgcm^2. The inverter driving this induction motor is a 7.5 kW *Control Technique* UNIDRIVE operated in sensored vector mode. The encoder signal used for feedback in the load drive is the same as that used for monitoring the position of the PM machine. This avoids fitting a second encoder. A board is used to split the signal using optocouplers to electrically isolate both drives. See appendix A.3 for the circuit schematics.

4.2 Processor and Interfaces

4.2.1 DSP Board

The *Blue Wave Systems* QPC/C40S is a motherboard capable of carrying up to four C4X family processor [67]. In the present work the board has being populated by two C44 processors. The board plugs directly into a host PC's ISA bus slot and the processor in Site A can communicate with the PC via two memory mapped interfaces:

- The Link Interface Adapter (LIA) routes the parallel I/O port 5 of the C44 in Site A to the PC memory.
- Dual-Port RAM (DPRAM). This is an 8K x 32-bit words memory that is accessible from the DSP and mapped in to the PC memory.

The libraries supplied with the development package (C4X Network API Support) provide C/C++ routines that make simple the use of the LIA and DPRAM and provide control of the processors. The execution of these libraries use the Test Bus Controller, a JTAG-based interface and its operation is transparent to the user. In this work the LIA interface is used for downloading executable files to the DSP and the DPRAM for data exchange between the DSP and the PC. The lower 192 words of the DPRAM are addressed individually for bi-directional communication; the remaining 8000 words are divided in to 8 channels that are dedicated to data capturing and are all read sequentially.

The communication between the C44 and the logic boards is through the DSPLINK bus. This is a memory mapped parallel bus addressable from the processor in Site A and physically accessible through a 50 way connector in the QPC/C40S carrier board. This bus may be configured in two different modes. For this work the DSPLINK1 mode has been used. It consists of 16 bi-directional data lines, 13 addressed lines and 8 control lines. The signals are buffered and routed to a back plane of 64 ways type C eurocard connectors where the logic boards are plugged, see appendix A.1 for schematic and the connector's pin-out. Each board has a four bit address (A3-A6) allowing a maximum of 16 peripheral boards; the three lower bits of the address bus

(A0-A2) are used to address different devices within a particular board, e.g. individual channels of the A/D board. The remaining address lines may be used for control and configuration of the boards.

4.2.2 PWM Board

The DSP software calculates the lengths of the PWM pulses, but the actual pulses applied to the inverter's gate drivers are generated by dedicated timers in the PWM board (schematic in appendix A.4). The circuit is based on an 82C54 configurable timer. This IC consists of three independent 16-bit timers each one used to control one phase of the inverter. There is considerable experience Nottingham using the timer/counter 82C54 for PWM generation and the design of this board is based upon that used previously in [68]. The 82C54 timers are configured by software to operate in monostable mode (mode-1). This means that the output of the timers is normally high. When triggered, the output of the timer goes low and starts decrementing the value preloaded in the counter register (CR) at the clock frequency (10MHz). When the count reaches zero the output returns to high, achieving a control pulse width. This operation effectively generates asymmetric PWM. To obtain symmetric PWM the timers' outputs must be inverted every other period. This is done by XOR gates and a latched *invert* signal.

The PWM board also includes a watchdog timer to protect the inverter in case the execution of the DSP software overruns the PWM period. This circuit consist of an independent counter and a configurable decoding circuit. The counter is reset with every triggering of the 82C54 timers and starts counting from zero at the clock frequency. In normal operation the next triggering of the PWM arrives before the count reaches the value set on the decoder. If a fault condition occurs and the trigger of the 82C54 fails to arrive, the counter will reaches the set value of 1152 equivalent to 115.2 μs, latching a watchdog trip signal that is sent to the interface board to disable the PWM pulses.

To provide noise immunity the PWM pulses and the watchdog trip signal to be transmitted to the inverter interface board are converted from TTL level signals to

current pulses of approximately 10 mA. This is done using current mirrors circuits as the output stage of this board.

4.2.3 Transducers

Between the inverter output and the PM machine a transducer box is installed to measure the three phase currents and the three line-to-line voltages. Each current is measured using a LEM transducer LTA100/SP1. This is a Hall-effect device that allows for unintrusive measurement and provides electric isolation. The range of the modules is 100 A and four turns are given to the phase conductor achieving a range of 25 A. To measure the line-to-line voltages, PSM voltage Transposers are used. These are electronic differential devices of high input impedance. Their main characteristics are a bandwidth of d.c. to 50 kHz, negligible d.c. drift and isolation of 1kV. The measurement signals are scaled to give a voltage signal of 10 V at full scale (25 A and 1kV respectively). This signals are buffered by op-amps and two current and two voltage measurements are transmitted through coaxial cable to the control rack.

4.2.4 Band-Pass Filter Board

The signal level of the *hf* component of the currents and voltages is relatively small compared with the fundamental and better resolution on the *hf* signals is achieved by filtering in hardware and scaling before the analogue to digital conversion. There are four independent band-pass filters on this board performing this task. Each filter is formed by the cascade of a low-pass and a high-pass fourth order Butterworth filter. The cut-off frequencies of these filters are chosen to be 1.25 kHz and 0.8 kHz respectively to obtain zero phase-shift at the injection frequency (1 kHz).

4.2.5 Analogue to Digital Converter Board.

The measured currents and voltages, and their filtered *hf* component are digitalised using two identical four channels A/D boards. The schematics of this board are shown in appendix A.5. The design of this board is based upon that used previously in [69].

Each channel has a differential amplifier as the input stage followed by the 16-bit analogue to digital converter LTC1605. The four channels of the board are triggered at the same time to achieve synchronous sampling. The result of the conversion is automatically stored in three-state buffers; each channel is then read independently by the DSP.

4.2.6 Encoder Board

A decoder board has been built to convert the incremental quadrature signal of the 1024 pulses per revolution encoder in to an absolute position measurement. The schematics are shown in appendix A.3. The board is built around the quadrature decoder/counter HCTL2016. This IC is specific for this function and it works by counting the positive and negative edges of both the encoder quadrature signals, effectively quadrupling the resolution to 4096 pulses per revolution. The 16-bit counter is incremented or decremented depending the direction of rotation and it is reset by the zero marker signal of the encoder yielding absolute position measurement. Additionally the PM machine encoder include three extra signals U,V and W that gives a absolute position measurement within 30 electrical degrees that can be used during start-up before the first zero pulse synchronizes the counter with the zero rotor position. These signals are directly buffered in the board and are accessible to read from the bus.

4.2.7 The Inverter Interface Board

Under normal operation the *Eurotherm 620 vector series* inverter is control by its onboard microprocessor. The internal control logic also provides protection for the inverter in fault conditions such as load over-currents or DC link over-voltage. The interface board connects between the inverter's control board and its power circuit discarding the inverter's own PWM signals and replacing them by the ones coming from PWM board.

The PWM board current pulses are converted back to TTL levels by optocouplers to provide electrical isolation. Each PWM signals is split in to two complementary

signals to generate the two gate signals per phase and dead-time is introduced by an analogue circuit, see appendix A.6 for details. Finally the six gate pulses are passed through a three-state buffer which is used to disable them in case of fault. The disable signal can be triggered by the watchdog trip signal from the PWM board, from the inverter's own trip signal or manually from a start/stop switch. The disable signal is latched and can only be cleared manually using a reset button once the fault condition has been cleared.

4.3 PWM and Control Parameters

4.3.1 PWM Strategy

This section provides a detailed description of the PWM implemented to control the voltage source inverter used in this work. The chosen PWM technique is Space Vector Modulation (SVM) [70, 71] because its easy implementation and good performance characterised by small current ripple and a possible output voltage amplitude larger than that obtainable with standard sinusoidal PWM.

Space Vector Modulation [72] is based in the voltage vector definition introduced in section 2.1.1. Applying this definition to the phase voltages generated by each of the eight possible inverter commutation states [S_A,S_B,S_C], seven discrete voltage vectors are obtained. Six of these vectors, $\underline{u}_1$ to $\underline{u}_6$, have amplitude $\frac{2}{3}V_{dc}$ and directions in angles multiples of 60°. The remaining vector is the vector zero and is formed by the two redundant states $\underline{u}_0$=[0,0,0] and $\underline{u}_7$=[1,1,1]. The voltage vectors produced by the inverter are shown in Fig. 4.2.

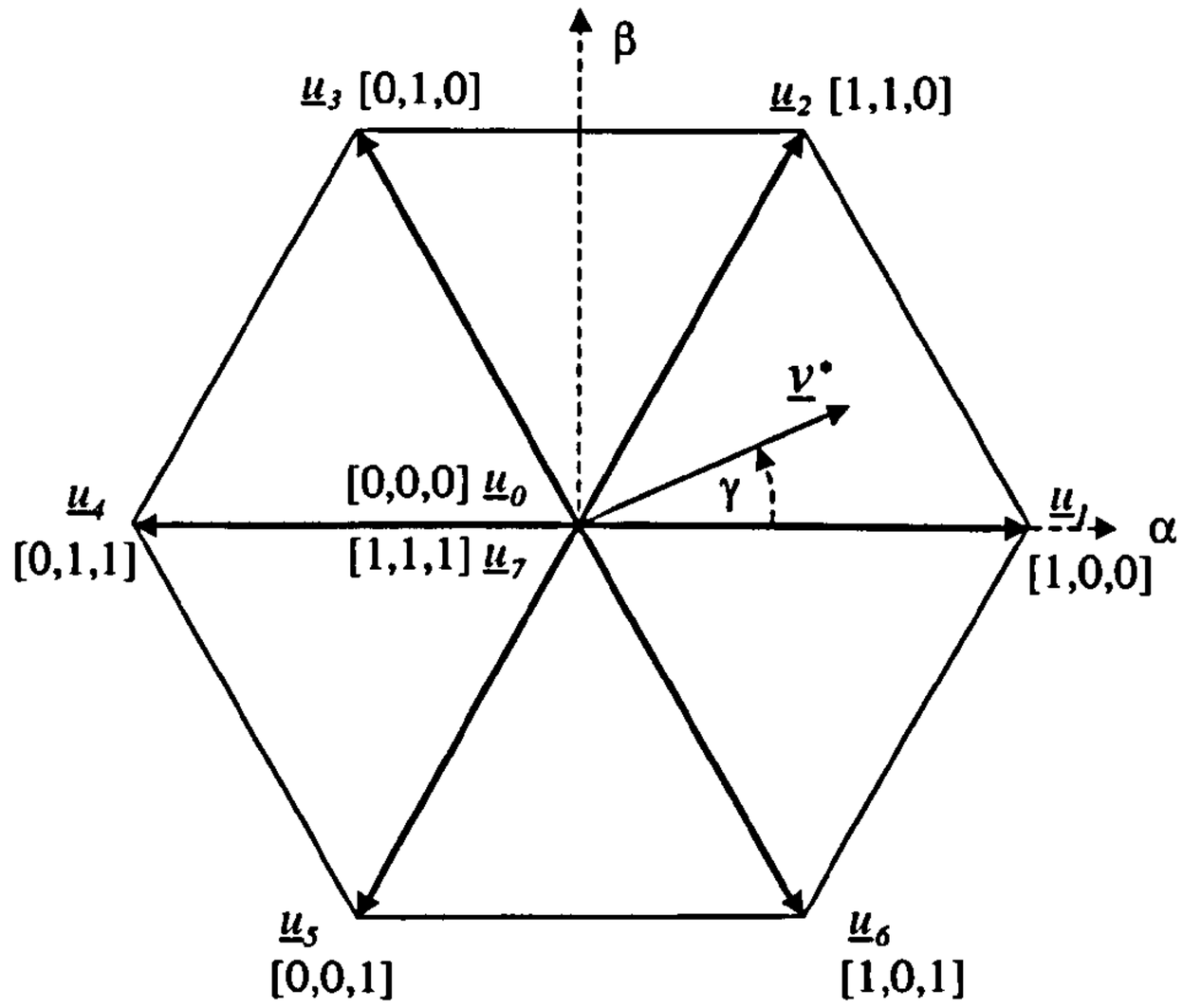

Figure 4.2: Voltage vectors generated by the inverter.

The vector current control gives a voltage reference $\underline{v}_s^*$. To modulate this reference voltage with a minimum of harmonic distortion, the two adjacent voltage vectors and the zero vector voltages are switched consecutively to produce a mean voltage vector during one sample period T_s equal to the reference. The times that each adjacent vector must be applied may be calculated by:

$$T_1 = T_s \frac{|\underline{v}_s^*|}{V_{dc}} \left(\cos\gamma - \frac{\sin\gamma}{\sqrt{3}} \right) \tag{4.1}$$

$$T_2 = T_s \frac{|\underline{v}_s^*|}{V_{dc}} \left(\frac{2 \cdot \sin\gamma}{\sqrt{3}} \right) \tag{4.2}$$

For the remainder of the sample period, the zero vector must be applied. Either of the two redundant states $\underline{u}_0$ or $\underline{u}_7$ will produce the same mean voltage vector, the time shared equally between them:

$$T_0 = T_7 = (T_s - T_1 - T_2)/2 \tag{4.3}$$

The PWM switching times sent to the PWM board, T_{SU}, T_{SV} and T_{SW}, are function of the vectors times T_1, T_2 and T_0 and of the sector that the reference voltage falls into. They are calculated according to the table 4.2.

Sector	T_{SU}	T_{SV}	T_{SW}
1	T_0	T_0+T_1	$T_0+T_1+T_2$
2	T_0+T_1	T_0	$T_0+T_1+T_2$
3	$T_0+T_1+T_2$	T_0	T_0+T_1
4	$T_0+T_1+T_2$	T_0+T_1	T_0
5	T_0+T_1	$T_0+T_1+T_2$	T_0
6	T_0	$T_0+T_1+T_2$	T_0+T_1

Table 4.2: PWM switching times as function of the sector.

Finally, to obtain asymmetric PWM pulses every other pulse is toggled in the PWM board as explained in section 4.2.2. When the pulse is to be inverted the switching times are complemented according to (4.4) to produce the correct mean voltage. A complete switching cycle corresponding to a commanded voltage vector in sector 1 is show in Fig. 4.3; due to the pulse inversion the switching period is double the sampling period. T_s.

$$T_{SU}' = T_s - T_{SU}$$
$$T_{SV}' = T_s - T_{SV} \qquad (4.4)$$
$$T_{SW}' = T_s - T_{SW}$$

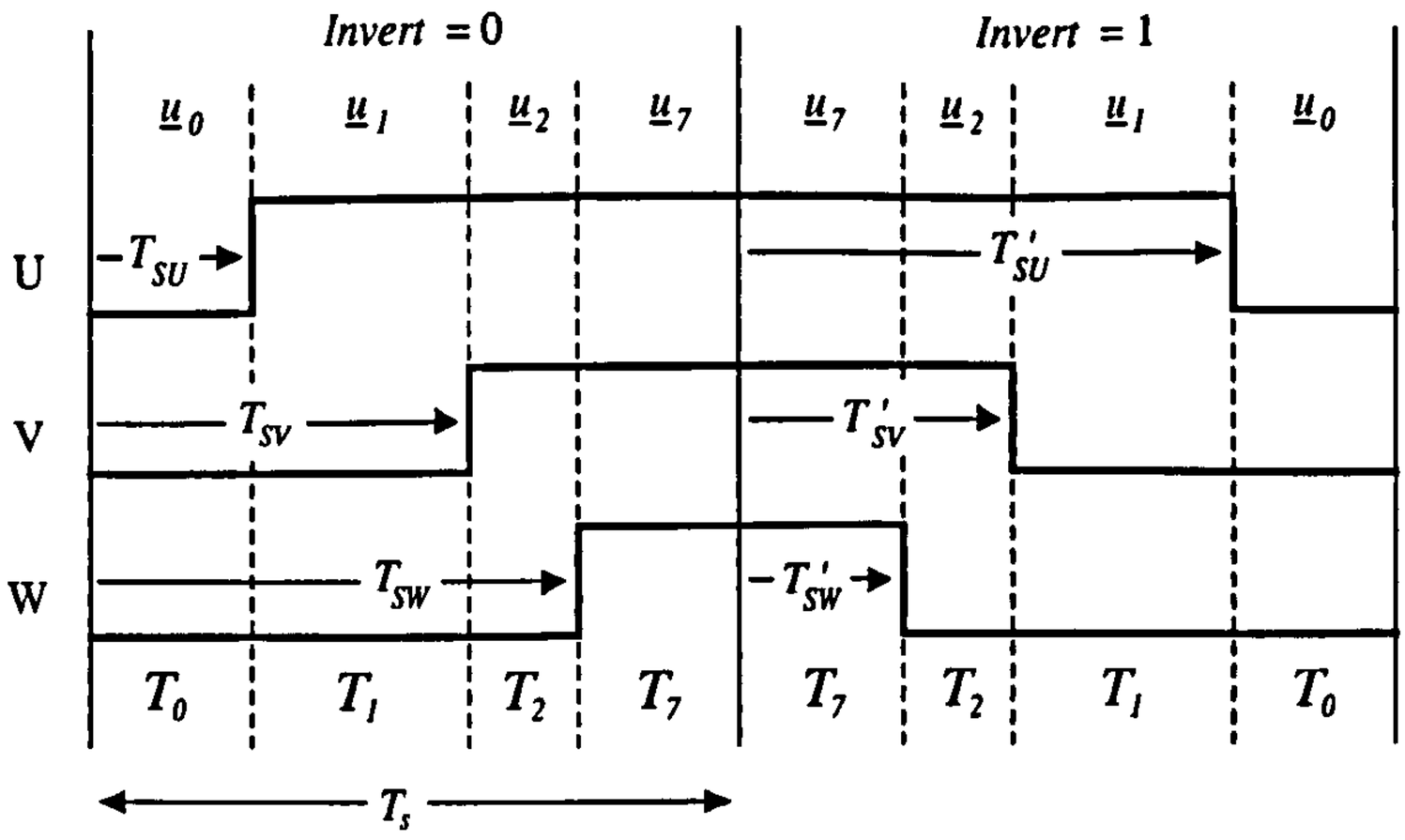

Figure 4.3: Switching cycle for a commanded voltage vector in sector 1.

4.3.2 Current Control

The voltage injection for sensorless position estimation acts as a disturbance to the current control loop as shown in Fig 4.4. Current control loops with too high bandwidth compensate for this injection reducing the useful saliency signal. For this reason, the current control loop bandwidth must be limited to values such that the current response to the injection voltage is dominated by the open loop characteristic at injection frequency. The current controllers introduced in Chapter 2 $C(z)=\frac{17\cdot(z-0.854)}{z-1}$ produced a nominal bandwidth of approximately 500 Hz for reference tracking, sufficient for a vector control drive. The bode-plot of the response to injection voltage of both the discrete close loop and ideal (purely inductive) continuous open loop plant are compared in Fig. 4.5. At injection frequency, the amplitude of the close-loop responses is already influenced by the open loop transfer function of the plant assuring good saliency position signal level and therefore this controller design is kept for sensorless control by *hf* voltage injection. The phase difference between the assumed purely inductive load and the close loop (real system) at injection frequency (1kHz) results in a constant phase error in the current position estimation of $\phi_0 \approx -13.8^\circ$ electrical and is easily compensated for.

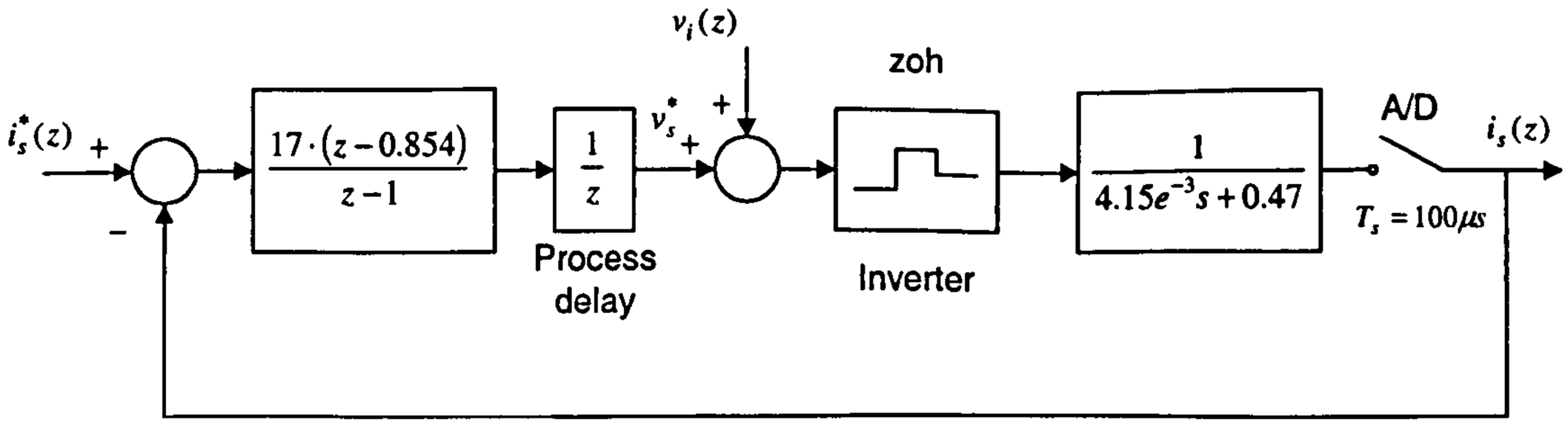

Figure 4.4: Nominal current control loop including *hf* voltage injection.

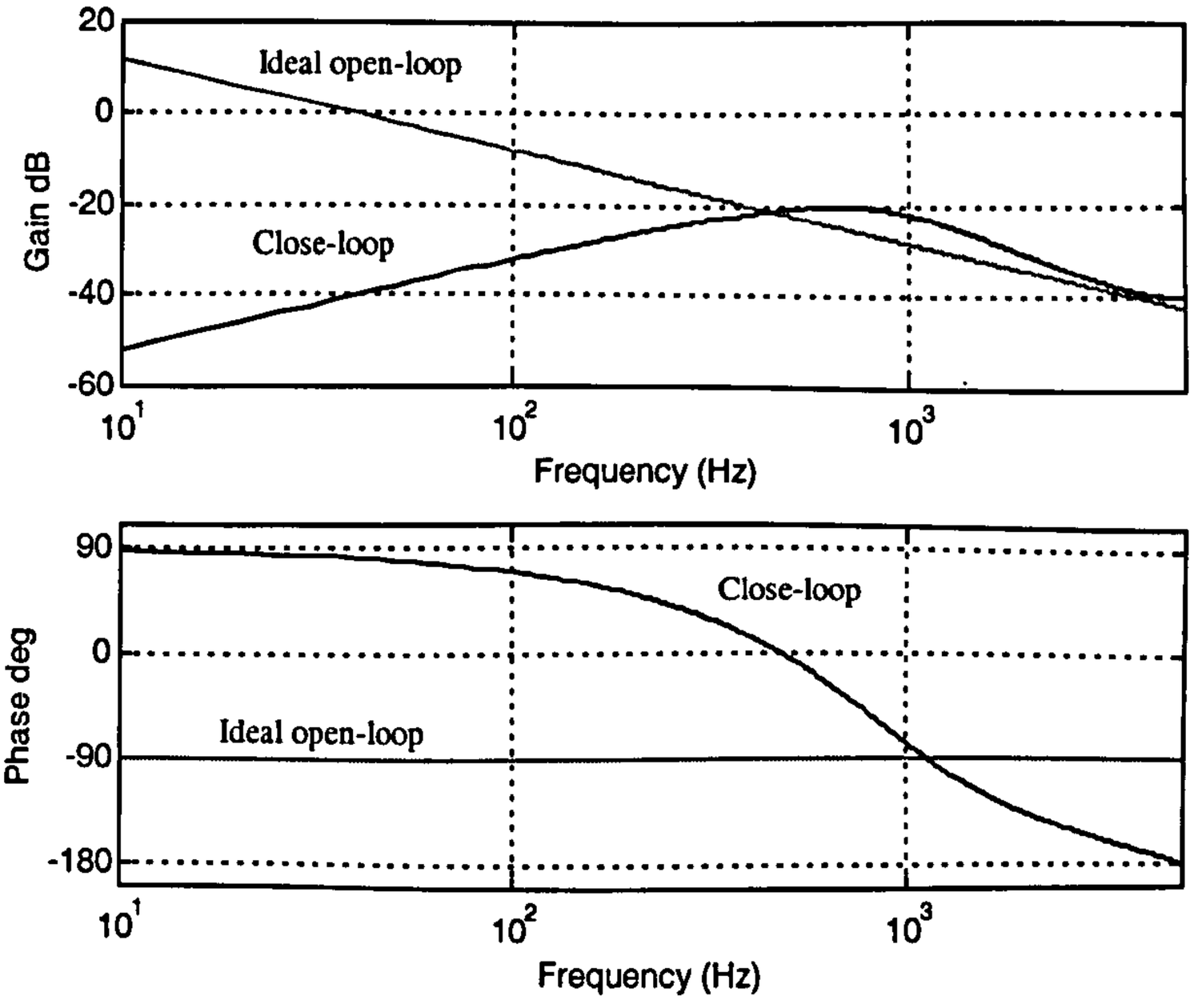

Figure 4.5: Bode response for injection signal of the discrete close loop plant and the continuous open loop ideal plant (purely inductive).

4.3.3 Bandwidth Restrictions in the Torque Demand

The sensorless position detection by signal injection relies on the fact that all the spectral components of the current at the vicinity of the injection frequency are a consequence of the voltage injection and the saliency of the machine only. Fast transients in the stator currents, produced by a fast change in torque demand, contain spectral components in the injection current band. The negative sequence of this transient *hf* current perturb the saliency position estimation. The influence of this phenomenon in the rotating α-β voltage injection strategy has been first reported in [73]. Similar phenomenon also exists in the *d-axis* injection where the spectral component of the transient *q-axis* current directly affects the orientation error estimation.

Ultimately, the effect of the transient in the position estimation depends on the bandwidth of the current loops, and the design of the band-pass filters. To illustrate and quantify the effect of the transient in the strategies implemented in this work a step change of 5 A (50 % nominal) is applied to the torque current demand in absence of *hf* excitation. The effect of this current transient in the signals that normally contain

the position information is measured. In the α-β injection the currents measured at the output of the hardware band-pass filters $\tilde{i}_{s\alpha}$ and $\tilde{i}_{s\beta}$ are shown in Fig. 4.6 (a). Only the negative sequence of this currents have a detrimental impact on the position estimation, the amplitude of the negative sequence currents resulting in the corrupting '*position*' signals i^{α}_{pos} and i^{β}_{pos} plotted in Fig. 4.6 (b). The maximum amplitude of the corrupting signal is approximately double the expected saliency induced position signal as measured in Section 5.4.4. It is noted that this phenomenon is linear and therefore, for any significantly large transients on i_q the distortion will dominate the position estimation.

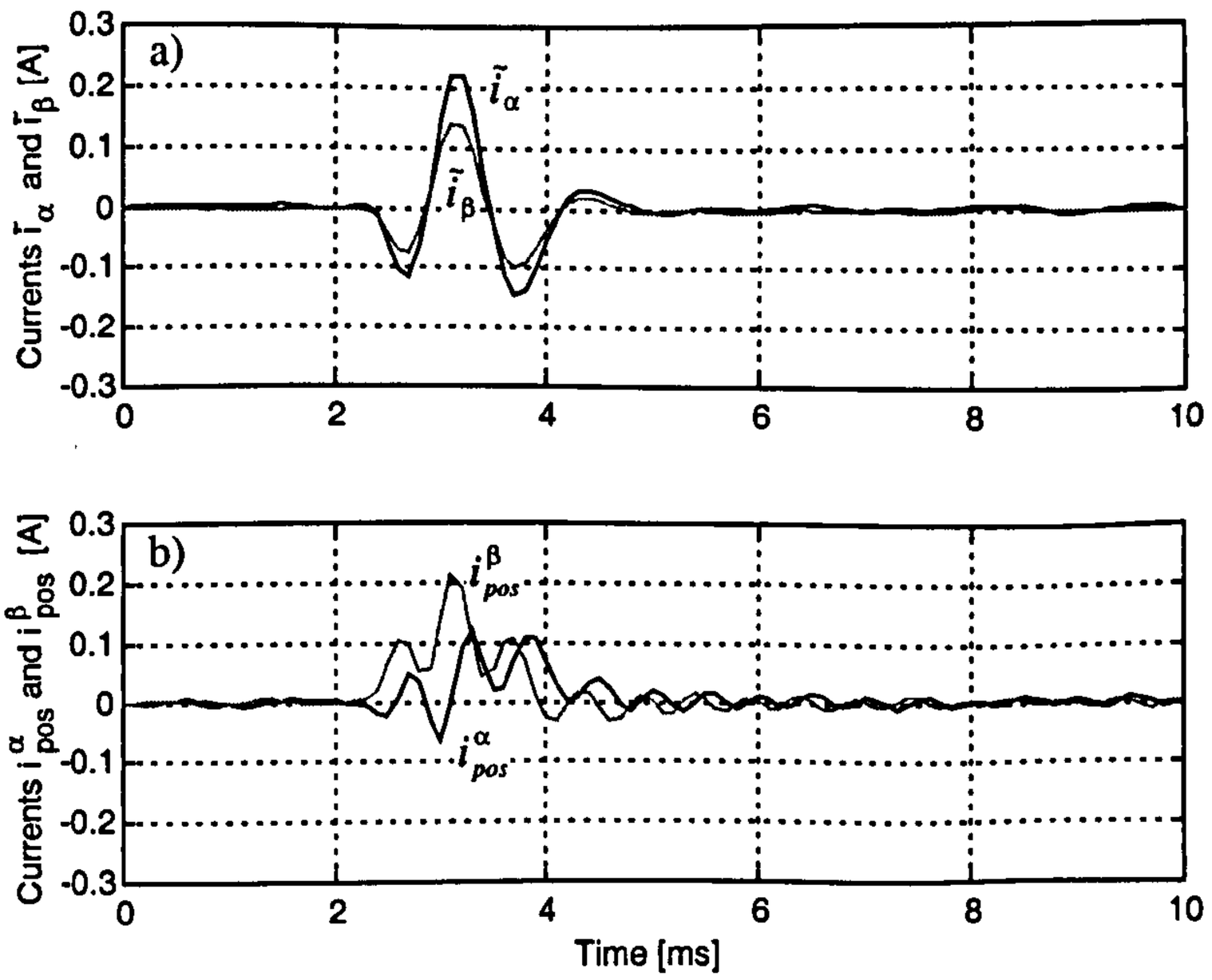

Figure 4.6: Transients disturbance in α-β injection caused by a 50% step in i^{*}_{q}.
a) Measured currents after hardware BP filters, b) Position signals.

In the *d-axis* injection strategy, the injection current component is obtained by software filtering in the *d-q* frame. Only the *q-axis* component of the injection current $\tilde{i}_q$ is used in the calculation of the orientation error and therefore the response of this signal to the step change in i^{*}_{q} is of interest. This signal is shown in Fig. 4.7 (a). The orientation error ζ, which drives the tracking algorithm, is obtained from the demodulation of $\tilde{i}_q$ and therefore the transient in i_q produces a disturbance in ζ,

shown in Fig. 4.7 (b). For the test step the disturbance is of approximately 40° electrical. In sensorless close loop operation this transient disturbance would cause strong corrective actuations by the position and speed controllers, which in turn will cause more transients in the torque current i_q.

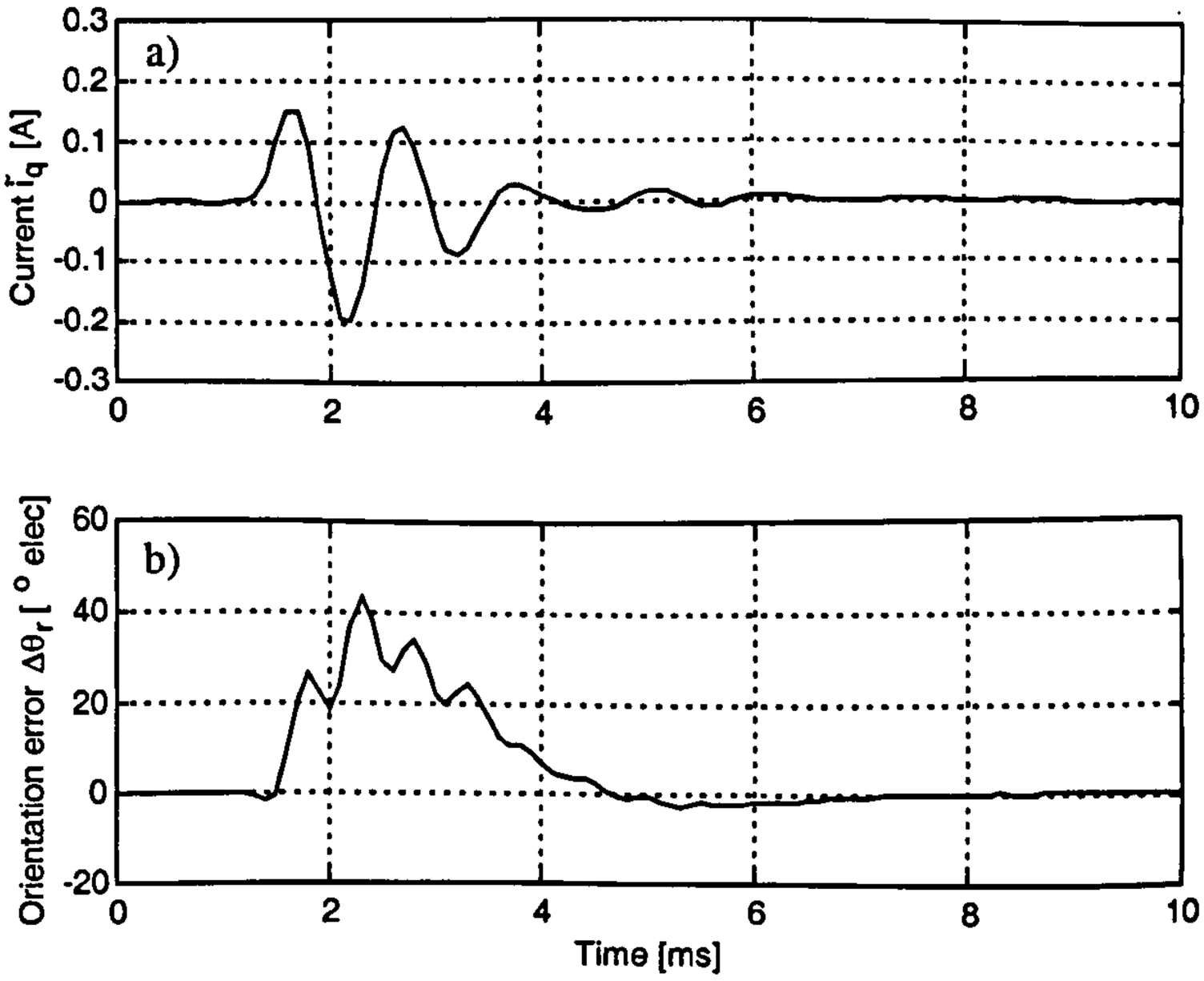

Figure 4.7: Transients disturbance in *d*-axis injection caused by a 50% step in i_q^*. a) $\tilde{i}_q$ after software BP filters, b) Orientation error signal.

The transient disturbance phenomenon happens regularly under position or speed close loop operation, because the discrete implementation of the current loops is sampled at a higher rate than the position and speed loops as discussed in section 2.1.4. This creates step changes in the i_q demand at the sampling frequency of the slower position and speed loops. To suppress the transients in i_q, and reduce the transient disturbance, the spectral contents of i_q^* is limited by a first order low-pass filter with cut-off frequency of 60 Hz which is implemented in discrete form at the fast current sample rate.

4.3.4 Speed and Position Loop

The filter in i_q^* proposed in section 4.3.3 imposes restrictions in the design of the speed and position controllers. To achieve an adequate bandwidth, the structure of these controllers has been changed from the classic PI and P cascaded structure introduced in subsections 2.1.4.2 and 2.1.4.3. The cascade structure is maintained to allow limitation on the speed demand but the speed PI has been replaced by a proportional controller. In the α-β injection method, the speed estimate is obtained by derivative of the sensorless position estimation, to reduce the noise a 60 Hz filter is also applied. The dynamic of this filter is considered in the design of the speed controller and a gain $k_\omega = 0.7$ is obtained. The outer position loop is closed by a lag controller [40] $C_\theta(s) = \frac{24 \cdot (s+63)}{(s+125)}$ instead of a gain only. The resulting nominal bandwidth for the position loop is 2.2 Hz. The complete control structure is shown in Fig. 4.8 (it is noted that in this figure the rotor position and speed are expressed in terms of mechanical quantities). The sample period of the speed and position loop is maintained at 5 ms yielding the discrete implementation of the position controller as $C_\theta(z) = \frac{21.166\,z - 15.406}{z - 0.524}$. This new control structure achieves good over-damped response despite the heavy filter in i_q^*, at the cost of steady state error in the position control when mechanical load is applied.

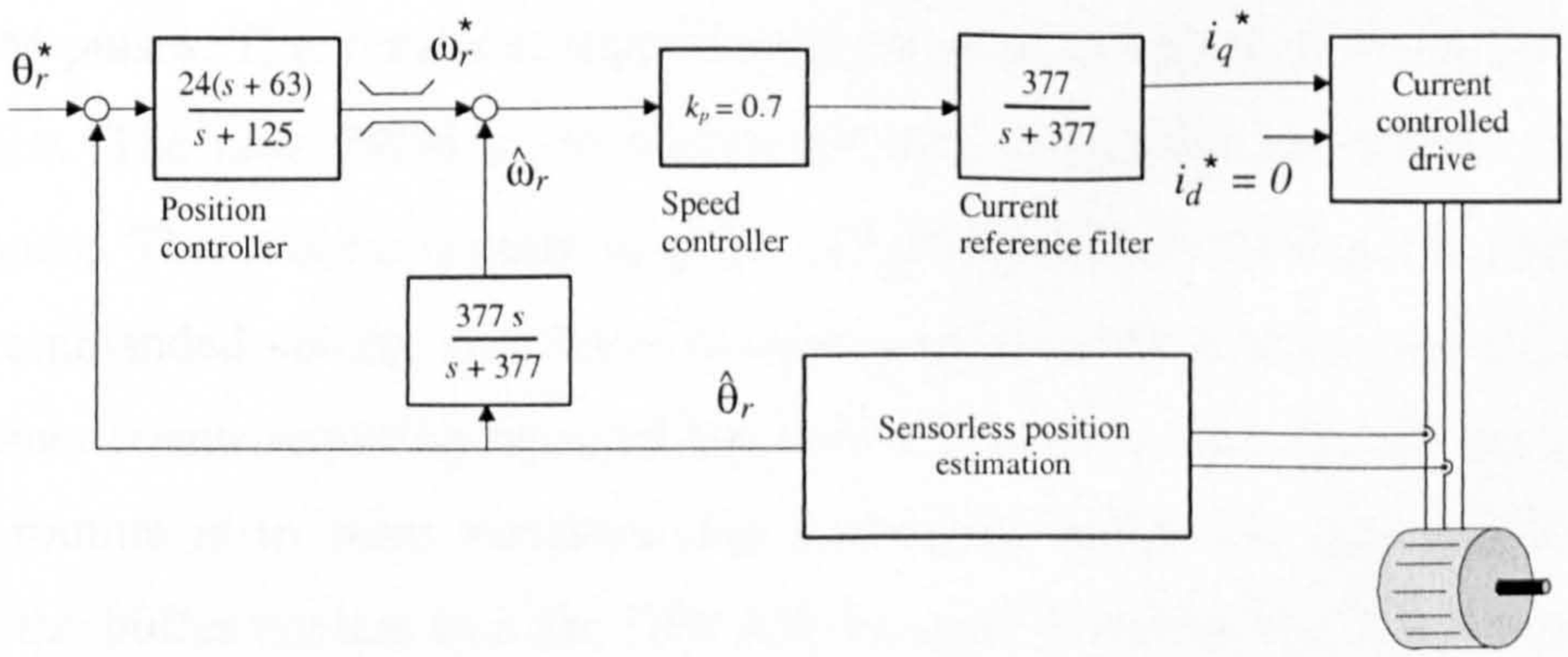

Figure 4.8: Controller structure for sensorless position control.

4.4 DSP Software Structure

The software running in the DSP is timer-interrupt driven and the interrupt time is set to 100 μs fixing the sample frequency to 10 kHz. The first task of the software is to trigger the A/D conversion and the PWM generation. The pulse width loaded in to the PWM board are those calculated in the previous interrupt. The D/A conversion time is 10 μs, the DSP using this time to perform tasks that do not require the sample results such the asynchronous communication with the host PC and the measurement of the encoder position and calculation of measured speed. All of this takes approximately 14 μs. The reading of the eight A/D channels takes approximately 10 μs due to overhead in the call of the functions. Using the values of *hf* currents the program continues with the sensorless position estimation strategy. The execution time depends on the actual sensorless strategy being implemented. For example, the algorithm for α-β rotating injection includes rotations of coordinates, several filters and tan^{-1} extraction as well as SPM compensation and takes approximately 17 μs.

The position and speed control loops are solved next. These are simple numerical algorithms and are executed in a few μs. However the speed controller gives the reference for the current controllers in the *d-q* frame. To solve the current controllers the current measurements have to be rotated into the *d-q* frame and the resulting commanded voltage vector is rotated back to the stationary frame for calculation of the PWM pulses. This results in approximately 8 μs of execution time for the current controllers. The new PWM pulse widths are then calculated and loaded in to the PWM board. This process is quite lengthily (17 μs) because it involves the calculation of the commanded voltage amplitude, involving square-root function and the loading of the timer counts requiring repeated bus write cycles. The final task of the interrupt service routine is to store variables into a memory buffer for data capture or to transfer the buffer content into the DPRAM for data downloading. These actions do not increase significantly the execution time because they consist of few memory access.

The resulting maximum total interrupt service routine execution time is approximately 82 μs. This is adequate for the timer interrupt running at 100 μs giving enough time

for the overhead needed to service the interrupt. Although the code was completely written in C, some measures had been taken to reduce the execution time. Inline coding has been privileged to avoid excessive function calls overhead and the trigonometric functions have been implemented as tables.

Chapter 5

5 Enhanced Position Estimation

The application of the α-β injection strategy to the 4 kW UNIMOTOR surface-mounted PM machine is presented and discussed in this chapter. The issues relating to the small magnitude of the saliency and the effects of non-linearities of the inverter, such as dead time are addressed. The effect of dead time compensation is experimentally assessed and results showing the numerical improvement in position estimation accuracy are presented. Finally, the errors due to residual inverter non-linearities and spatial harmonics of the machines' saliency are characterised and a compensation algorithm based on a commissioning process is developed (SMP).

5.1 Fundamental Saliency Measurement

It is evident that, for any position estimation method based on signal injection to work the machine must present some level of saliency in the impedance measured at the stator terminals. In Section 3.2 it has been stated that all though the surface mounted PM machines are generally regarded as non-salient, a small level of saliency is expected in the stator inductance due to magnetic saturation of the iron in the main flux path. In this section an experimental measurement of this saliency is presented to confirm this presumption and to quantify the saliency of the particular motor used in this work. Although the inductance variation caused by saturation may be not perfectly sinusoidal, only its fundamental component of periodicity $2\theta_r$ gives useful rotor position information. Therefore the test developed in this section is designed to extract only this fundamental component of the saliency. Repeated measurements

under different load levels are carried out to assess the effect of the stator current on the fundamental *hf* inductance saliency of the surface-mounted PM motor.

5.1.1 Measurement Method

The direct measurement of the stator inductance is carried out using a 1 kHz pulsating carrier voltage injected into the *α-axis* stator frame.

$$\begin{bmatrix} \tilde{v}_\alpha \\ \tilde{v}_\beta \end{bmatrix} = \hat{V}_i \begin{bmatrix} -\sin(\omega_i t) \\ 0 \end{bmatrix} \tag{5.1}$$

According to the *hf* model of a machine with a saturation-induced saliency (3.7), the response to the pulsating excitation (5.1) is given by:

$$\begin{bmatrix} \tilde{i}_\alpha \\ \tilde{i}_\beta \end{bmatrix} = \frac{\hat{V}_i}{\omega_i (L_s^2 - \Delta L_s^2)} \begin{bmatrix} L_s + \Delta L_s \cos(2\theta_\delta) & \Delta L_s \sin(2\theta_\delta) \\ \Delta L_s \sin(2\theta_\delta) & L_s - \Delta L_s \cos(2\theta_\delta) \end{bmatrix} \cdot \begin{bmatrix} \cos(\omega_i t) \\ 0 \end{bmatrix} \tag{5.2}$$

Where $L_s + \Delta L_s \cos(2\theta_\delta)$ is the *β-axis*-inductance $L_\beta(\theta_r)$ and θ_δ is the saliency angle. By considering only the current in the *α-axis*, (5.2) can be reduced to:

$$\tilde{i}_\alpha = \frac{\hat{V}_i \cdot L_\beta(\theta_r)}{\omega_i (L_s^2 - \Delta L_s^2)} \cdot \cos(\omega_i t) \tag{5.3}$$

Demodulating $\tilde{i}_\alpha$ the expresion for the *β-axis* self-inductance can be derived:

$$L_\beta(\theta_r) = \frac{\omega_i (L_s^2 - \Delta L_s^2)}{\hat{V}_i} \cdot \tilde{I}_\alpha(\theta_r) \tag{5.4}$$

From (5.4) it follows that the amplitude of the injection current in the *α-axis* $\tilde{I}_\alpha$ has the same distribution over θ_r as the *β-axis* self-inductance $L_\beta(\theta_r)$. Furthermore,

replacing the current minimum and maximum amplitude $\breve{I}_\alpha$, $\hat{I}_\alpha$ in (5.4) the values of L_s and ΔL_s can be determined:

$$L_s + \Delta L_s = \frac{\hat{V}_i}{\omega_i \cdot \breve{I}_\alpha} \tag{5.5}$$

$$L_s - \Delta L_s = \frac{\hat{V}_i}{\omega_i \cdot \hat{I}_\alpha} \tag{5.6}$$

The *β-axis hf* inductance can be quantified using equations (5.4) to (5.6). It is noted that these equations have been derived considering the fundamental saliency only and therefore the spectral content of $\tilde{i}_\alpha$ must be limited to the components at carrier frequency ω_i and the modulation side bands $\omega_i \pm 2\omega_r$. The current measurement also contains higher harmonics discussed in the following sections. For the purpose of fundamental saliency measurement these components are filtered off.

The measurements are carried in the PM machine operating under torque control while the speed is maintain constant at 60 rpm by means of sensored speed control of the loading drive. A pulsating injection of 30 V of amplitude and 1 kHz is added to the *α-axis* commanded voltage. The *hf* voltage and currents are captured for two seconds at a rate of 10 kHz and latter processed off-line. Tests are performed at different torque levels ranging form –150 to 150 % nominal.

The extraction of the envelope of the *hf* current $\tilde{i}_\alpha$ is executed via heterodyne demodulation. For rejection of the higher harmonics of the demodulated current a 5th order low pass Chebyshev filter with cut of frequency $3f_e$ (9 Hz) is used, the magnitude of the fundamental variation of the current being preserved by the low ripple of the pass-band of the filter (0.1 dB). This filter is applied forward and backward to the same data doubling the attenuation of the filter and eliminating any phase shift introduced by the filtering.

The results of the inductance measurement are shown for motoring condition in Fig. 5.1 and for braking in Fig. 5.2. These figures show a fundamental saliency in the

stator inductance L_q/L_d of approximately 17% at no load. Furthermore the magnitude of the saliency is relatively unchanged even at the maximum load level tested (150% nominal). The direction of minimum inductance at no-load is oriented with the *d-axis*, although a phase-shift in the fundamental saliency is observable with variations of i_q. This characteristic is consistent with saturation induced saliency as described in Section 3.2.2.

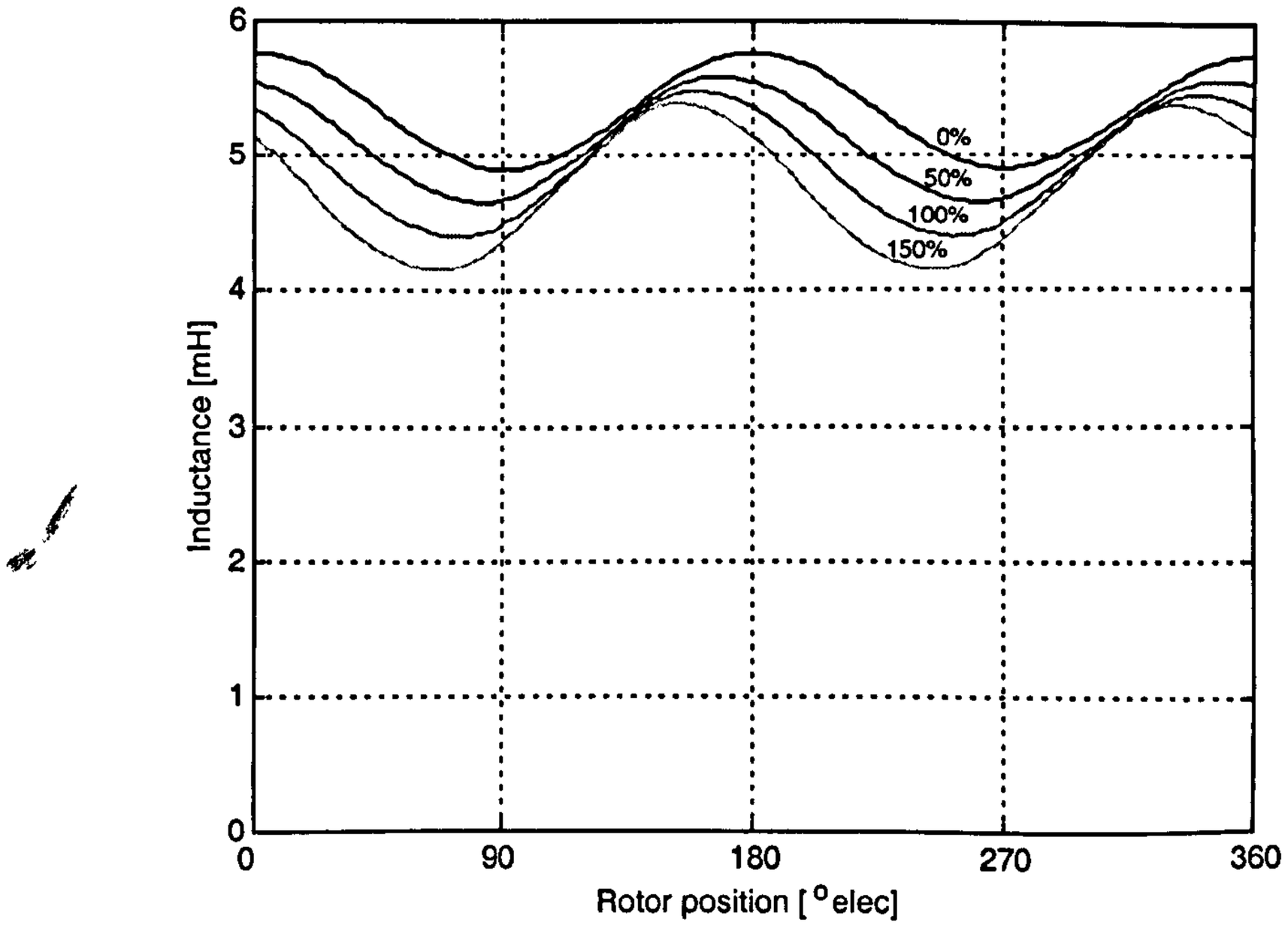

Figure 5.1: Stator inductance L_β measurements under motoring condition.

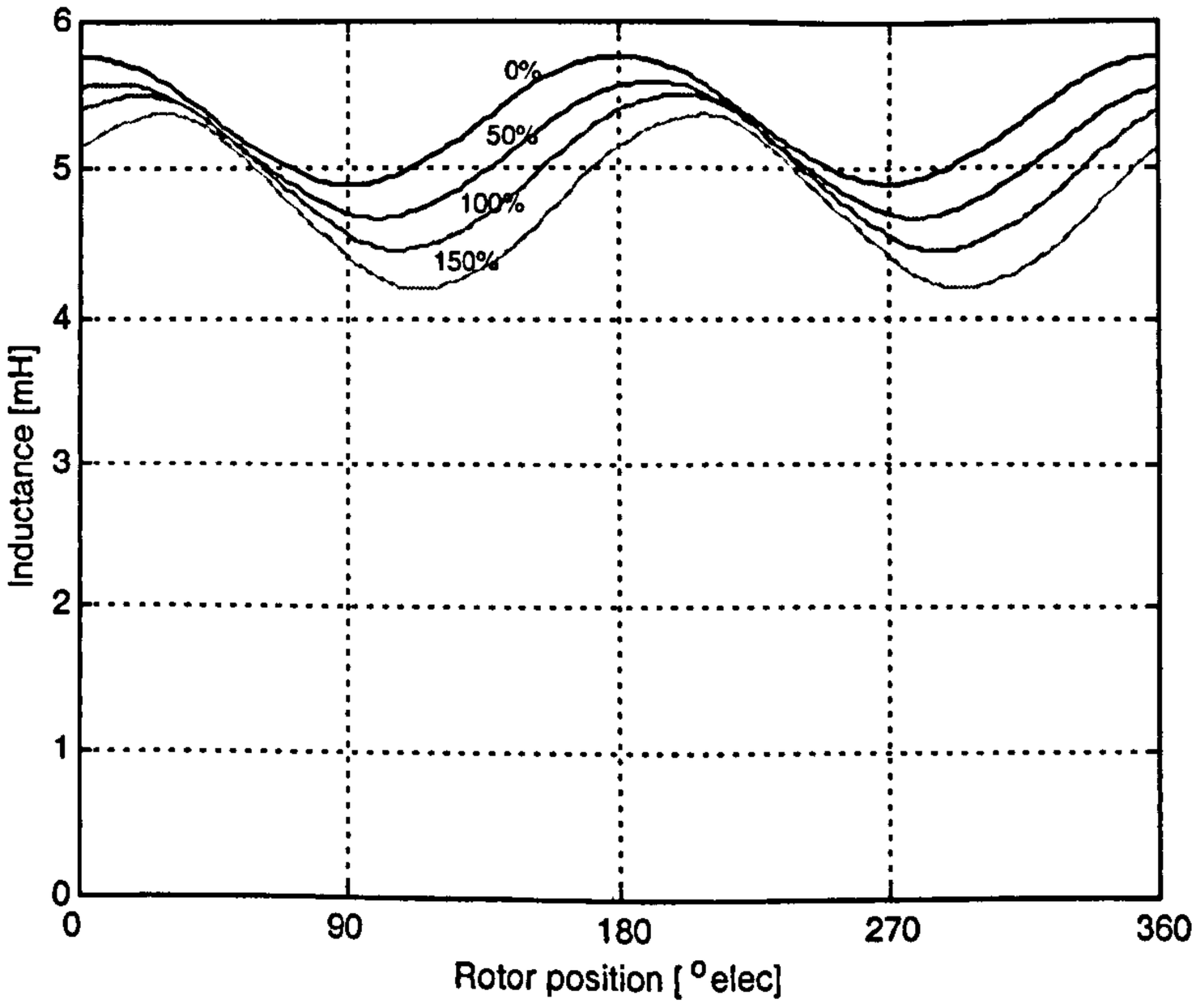

Figure 5.2: Stator inductance L_β measurements under braking conditions.

5.2 Position Estimation of Basic α-β Injection Algorithm

The presence of fundamental saliency, measured in the previous section, implies that the use of signal injection for rotor position tracking is possible. Its small magnitude implies nevertheless that other spurious harmonics in the *hf* current signal will have a strong effect in the final position estimation. In what follows the results of the direct application of the α-β injection described in Section 3.3.1 are presented. A rotating voltage carrier of amplitude 30 V is injected and the current response is used to determine rotor position. Figure 5.3 shows the phase current i_a and the *hf* component $\tilde{i}_\alpha$ and it can be observed that in addition to the fundamental saliency modulation of the *hf* currents, there is also a very localised modulation when the phase current cross zero. The extraction of the position signal from this *hf* current using directly the synchronous filter of Fig. 3.5, results in saliency position signals $\underline{i}_{pos}$ with large harmonics at frequencies $4f_e$, $8f_e$, $10f_e$, $14f_e$, $16f_e$, etc. The sequence of rotation of these harmonics alternates as shown in the spectrogram of Fig. 5.4.

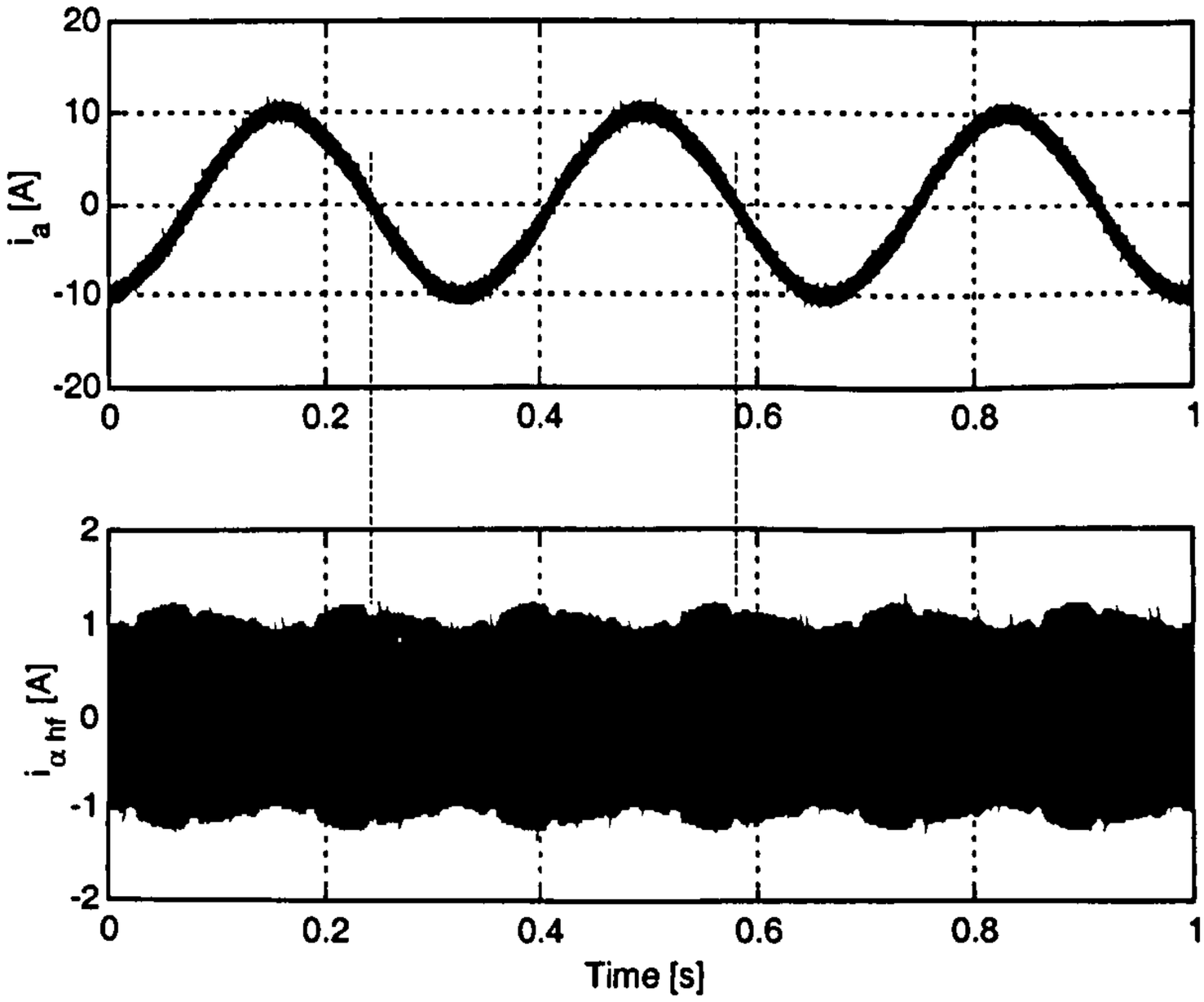

Figure 5.3: Line current i_a and corresponding *hf* component $\tilde{i}_\alpha$.

The harmonics on $\underline{i}_{pos}$ produce large errors in the saliency position estimation at the points of zero crossing by the fundamental phase currents, this is illustrated in Fig. 5.5

by comparing the rotor angle $2\theta_r$ measured by the encoder and the estimated saliency position $2\hat{\theta}_\delta$ obtained by a tan^{-1} operation of the components of the $\underline{i}_{pos}$. The constant offset observable is mainly due to the fundamental saliency shift produced by the load current that has been discussed in section 5.1.

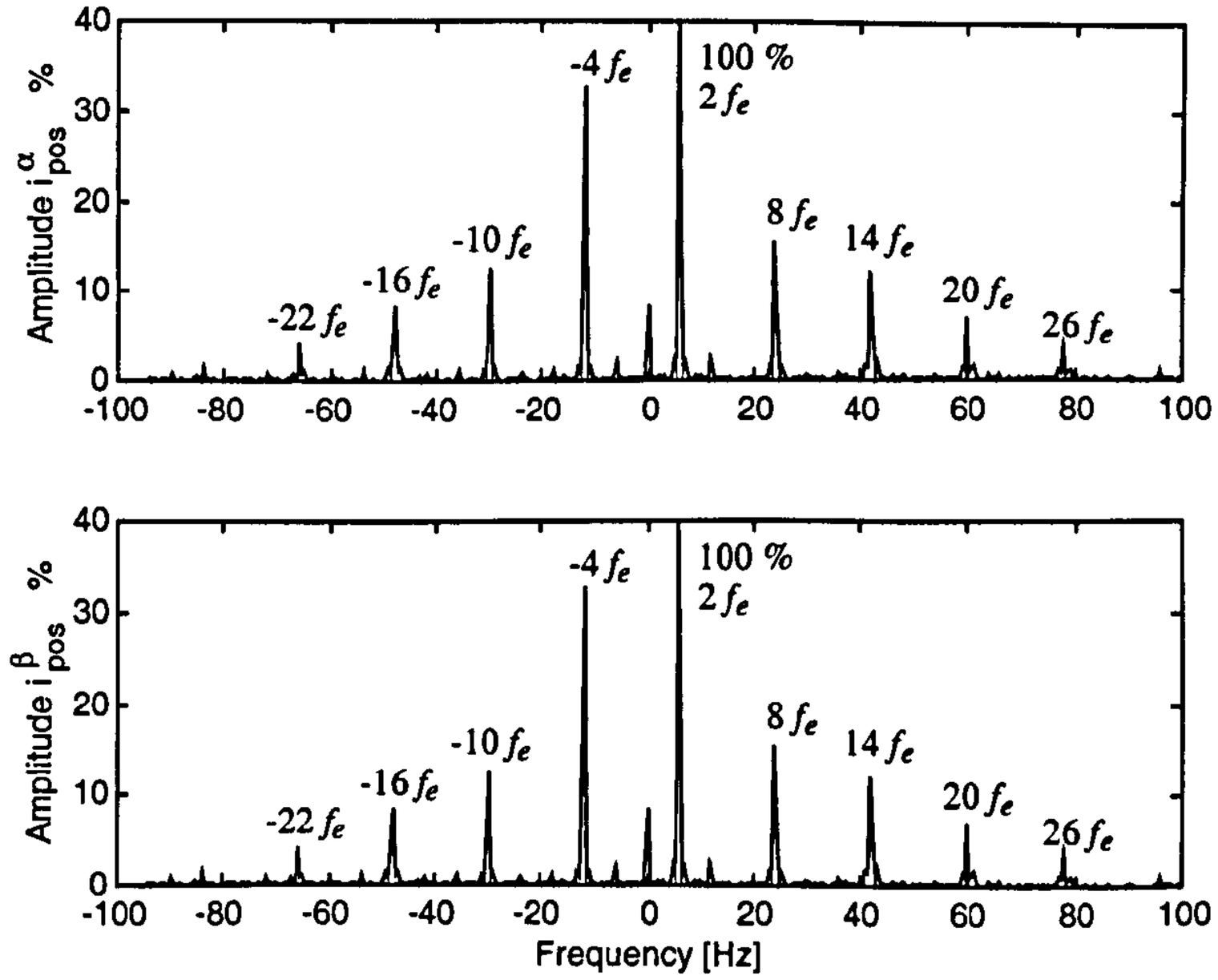

Figure 5.4: Spectrum of the position signal vector $\underline{i}_{pos}$.

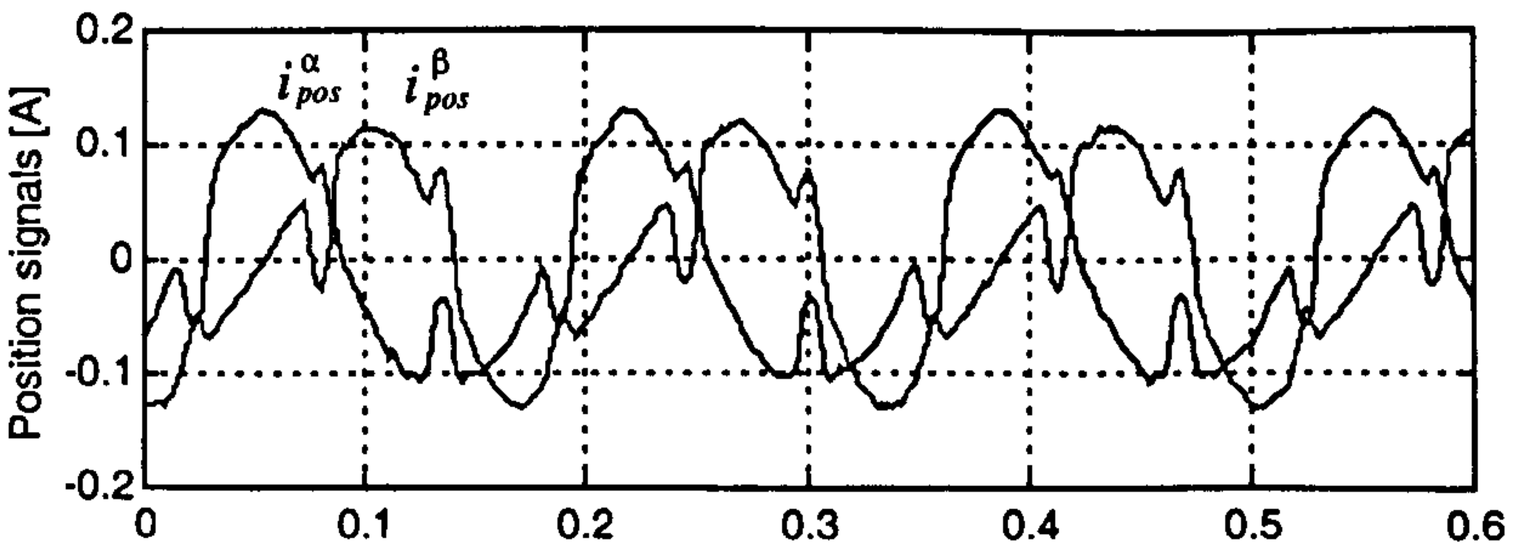

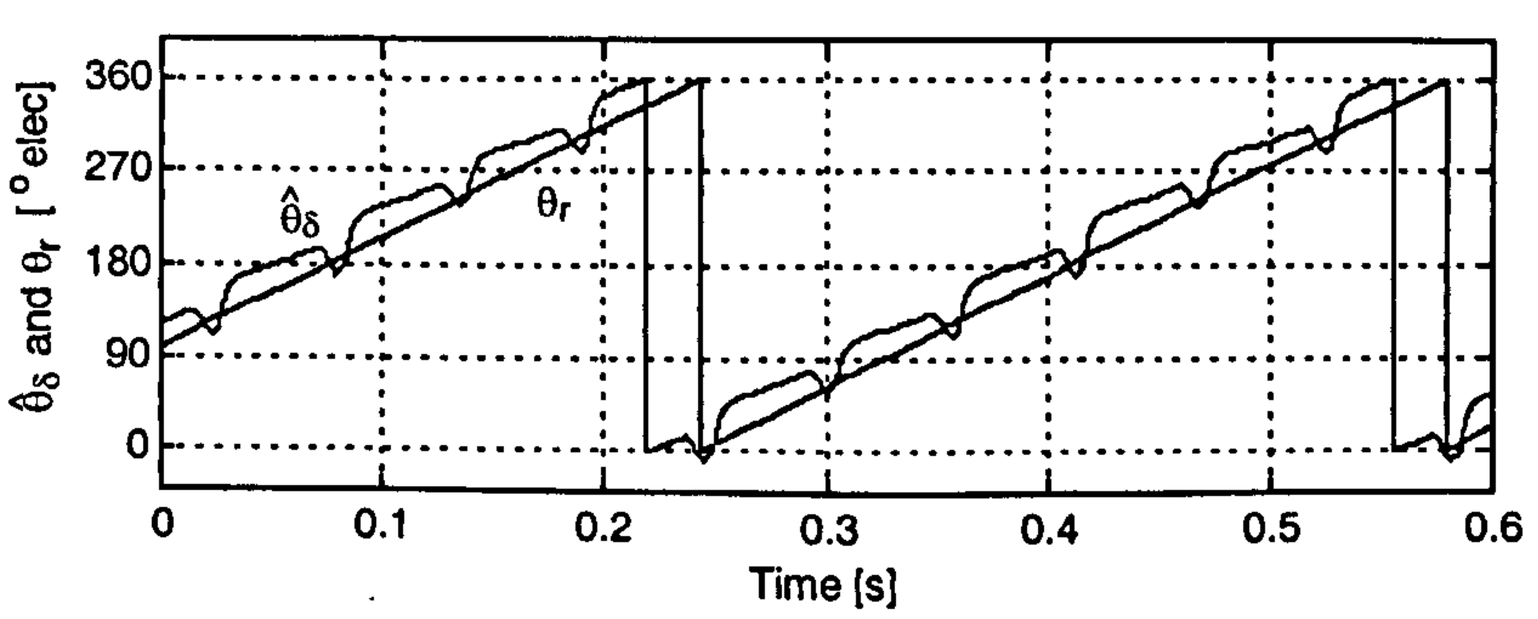

Figure 5.5: Position estimation

The saliency estimation error, measured as the deviation of the estimated saliency position from it's ideal value calculated from the fundamental of the position signals i_{pos}^{α} and i_{pos}^{β}, is shown in Fig. 5.6. The magnitude of this error is significant reaching values of 35 ° electrical.

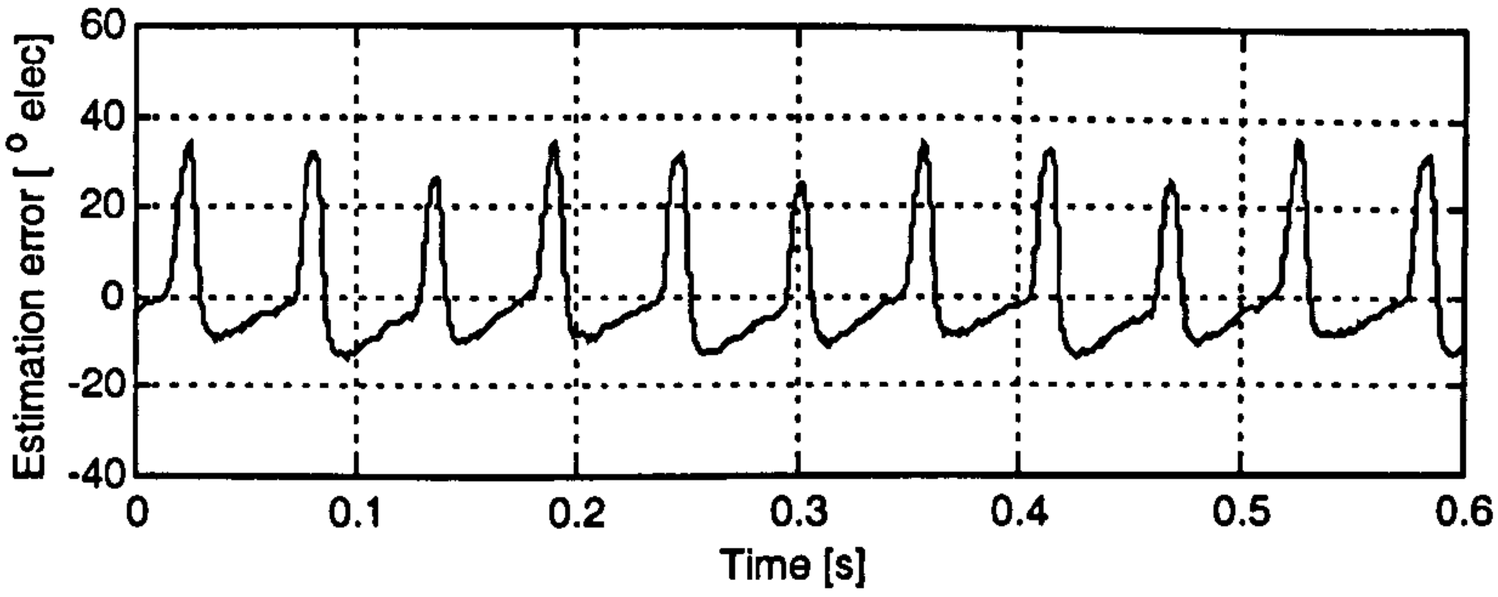

Figure 5.6: Estimation error.

The inverter non-linearities such as dead-time and device-voltage drops are responsible for the errors in the position estimation. These effects produce a voltage distortion in each phase that is dependent on the direction of the phase current effectively opposing the current flow. At the points of fundamental current zero crossing the *hf* injection current produce multiple zero crossings at the carrier frequency causing a disturbance in the *hf* voltage injection and resulting in harmonics in the saliency position signal. The problem is particularly exacerbated in surface mounted PM machines because the small amplitude saliency produces a small amplitude saliency position signal to start with. The locus of amplitude of Fig. 5.4 and simulation results show that this effect produces a spectrum content of $\underline{i}_{pos}$ with components at $2f_e$, $-4f_e$, $8f_e$, $-10f_e$,... The frequencies of the inverter no-linearity distortion can be expressed as:

$$f_{dt} = (2 \pm 6 \cdot i) \cdot f_e ; \quad \text{where } i \in \mathrm{N}_0 \tag{5.7}$$

The relative amplitude of these harmonics depends in the load level. The spectral component of the distortion at $2f_e$ is particularly problematic because it can not be separated from the saliency position signal. At smaller loads this component of the distortion causes significant phase error in the saliency position estimation.

The dead time consists of a delay in the semiconductor switches' turn-on command to protect against the two devices of the same inverter leg short-circuiting the DC link (shoot-through). This delay arises because for IGBT devices, the turn-off time is longer than the turn-on time. Hence the dead or blanking time is unavoidable in the operation of a voltage source inverter [74]. During most of the dead time both devises are off and the load current is conducted through one of the freewheeling diodes. This results in an error between the length of the voltage pulse commanded by the PWM and the real voltage pulse applied to the load. The real pulse is shortened or extended depending on whether the direction of the phase current is positive or negative respectively. The magnitude of the resulting voltage error can be approximated by the volts-second area produced by the DC link voltage and the length of the dead time. The inverter used in this work has a dead time of 2μs, a DC link voltage of 600V and a PWM period of 200μs giving an average dead time voltage error of 6V.

The other significant source of voltage distortion is the forward voltage drop of the conducting IGBT or diode. This also produces error in the voltage applied to the load. The semiconductor voltage drop is always opposed to the current flow and therefore the sign of the resulting voltage again depends on the current direction, adding to the dead-time effect. The datasheet's typical values for the device drops are $V_{CE(sat)}$ = 3.0V for the IGBT and V_F = 2.0V for the diode. These values only give an indication of the error magnitude since they are specified for the maximum current of 50A. In practice the load currents are limited to 15A and therefore the actual vales are smaller.

The magnitude of the error introduced by the inverter non-linearities is significant when compared with the amplitude of the injection voltage (30V). An increase in the injection voltage amplitude would reduce the inverter's distorting effect but this conflicts with the need to minimise the voltage injection to reduce the losses and acoustic noise. The design value is a compromise and further reduction must be achieved by other methods.

5.3 Dead-Time Compensation

From the estimation of the error magnitudes due to the inverter non-linearity it can be noted that the dead-time is the most significant. Therefore dead-time compensation for improving the saliency angle estimation is necesary. Dead-time compensation by adding the estimated volts-second error to the commanded voltage [75] or by advancing the rising or falling edge of the commanded PWM pulses depending on the current direction [38, 76] are both well-established techniques. These are open loop strategies where only a knowledge of current direction is required although calibration may also be applied to take into account the forward drop and even the difference in the turn-on and turn-off times of the devises [75, 76]. Full on-line compensation of the dead-time effect may be achieved by directly measuring the length of the voltage pulse applied to the load and taking corrective action during the next PWM period [77]. All the mentioned methods have being proposed to improve the fundamental current wave form and the stability at low speed of machines operating under *V/f* control. The case of the current injection is analogous since the high frequency is outside of the bandwidth of the current loop and therefore the current distortion caused by the repeated zero crossings at injection frequency (when fundamental current is close to zero) is not compensated by the current controllers.

5.3.1 Basic Dead-Time Compensation

The basic dead time compensation implemented is based in that of [76]. The operation of the technique is depicted in Fig. 5.7 for the case of positive phase current. The commanded PWM pulse is given by V_{ao}^{*}. Under uncompensated operation the delay in the turn-on gate pulse g_1 of the top transistor T_1 would result in the conduction of the diode D_2 during the dead-time, resulting in a shortened pulse V_{ao} applied to the load. By knowing the current direction is positive one can compensate by advancing the ON commutation by T_{comp} generating the new gate pulses g_1' and g_2'. The conduction of the D_2 still happens during the dead time but it generates the desired output voltage V_{ao}'. In similar way if the phase current is negative the OFF commutation is advanced.

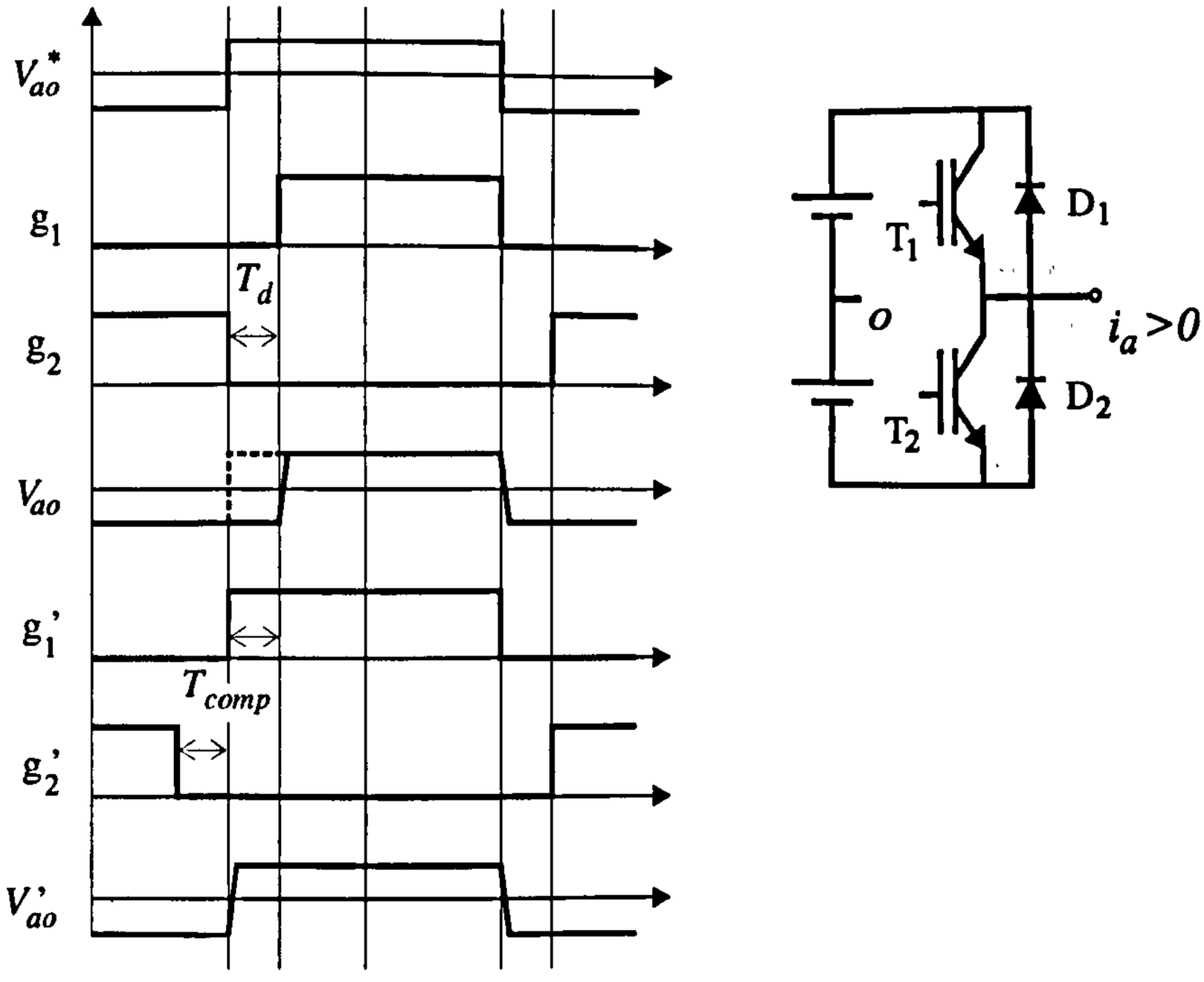

Figure 5.7: Operation of dead time compensation by advancing commutation: V_{ao}^* reference pulse; g_1, g_2 uncompensated gate pulses; V_{ao} uncompensated load voltage; g_1', g_2' compensated gate pulses; V_{ao}' compensated load voltage.

The amount of compensation time T_{comp} is directly related to the dead time T_d, but the finite turn on and turn off times of the IGBT's are significant and therefore are also considered, the final expression for T_{comp} is given by:

$$T_{comp} = T_d - T_{off} + T_{on} \tag{5.8}$$

Although the switching times T_{on}, T_{off} are dependent on the operating condition, the compensation is implemented with a constant value of T_{comp}. Typical datasheet values are used resulting in a value of $T_{comp} = 1.6\mu s$.

The simplest way of implement this dead-time compensation routine would be to derive the current direction information directly form the measurement values also used for current feedback. Nevertheless, the result is poor compensation as shown in Fig. 5.8 and Fig. 5.9. The reason for such large errors is the delay of more than one full sample period introduced by the use of the current measurement. The currents are sampled at the beginning of every interrupt service routine, but due to the finite conversion time of the A/D the PWM is applied with the pulse widths is calculated in

the previous sample period and therefore corrected using the previous current samples. Furthermore, the relevant current direction for the dead time compensation is that at the moment of commutation, which adds to the delay and ultimately to the uncertainty of the correct current direction. The use of the current measurement is suitable for fundamental waveform compensation. But, for *hf* injection the multiple zero crossings and the reduced amount of samples per carrier-current period result in ineffective compensation. The effectiveness of this strategy can be significantly improved by better determination of the current direction as will be discussed in the following section.

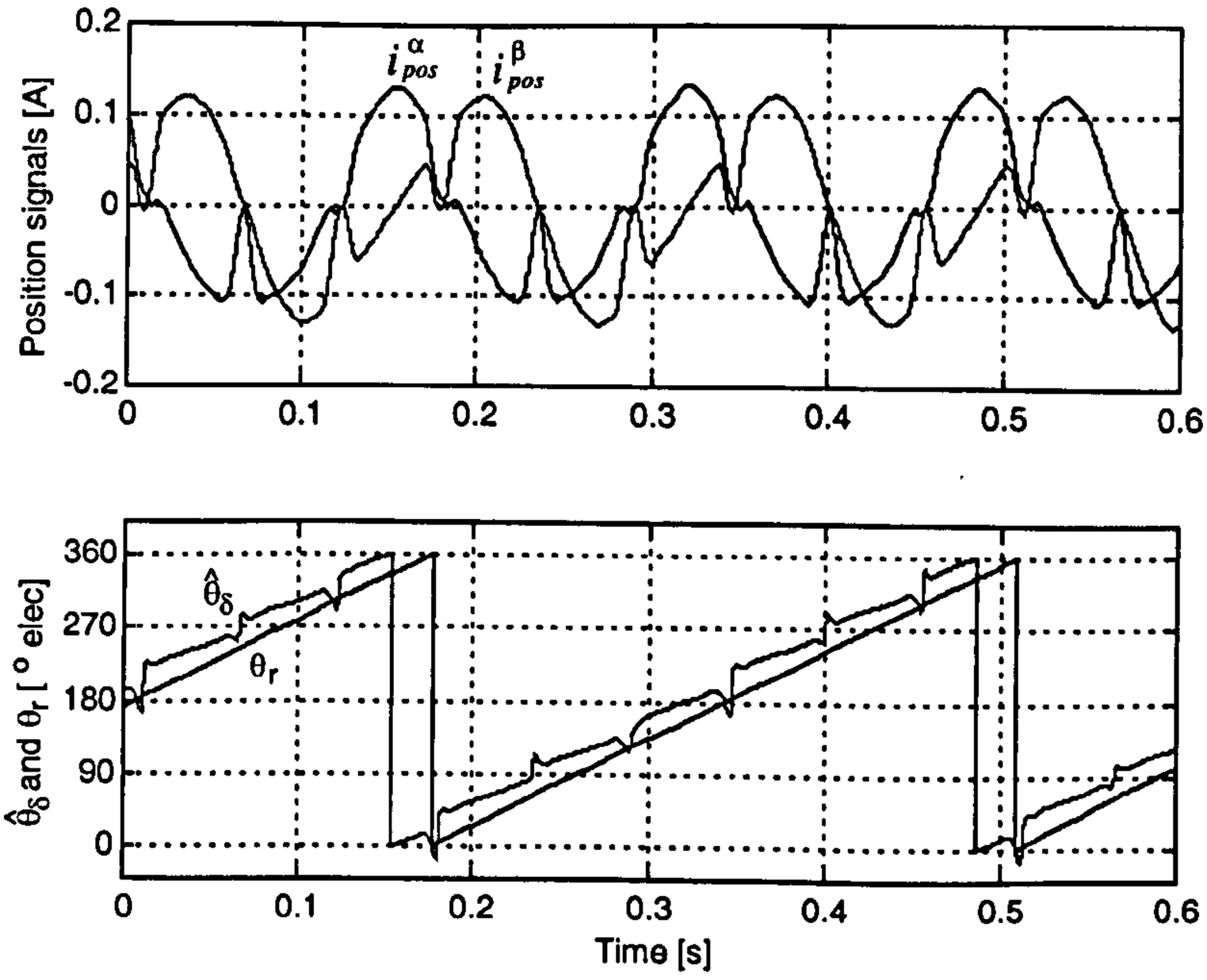

Figure 5.8: Saliency position estimation with standard dead-time compensation.

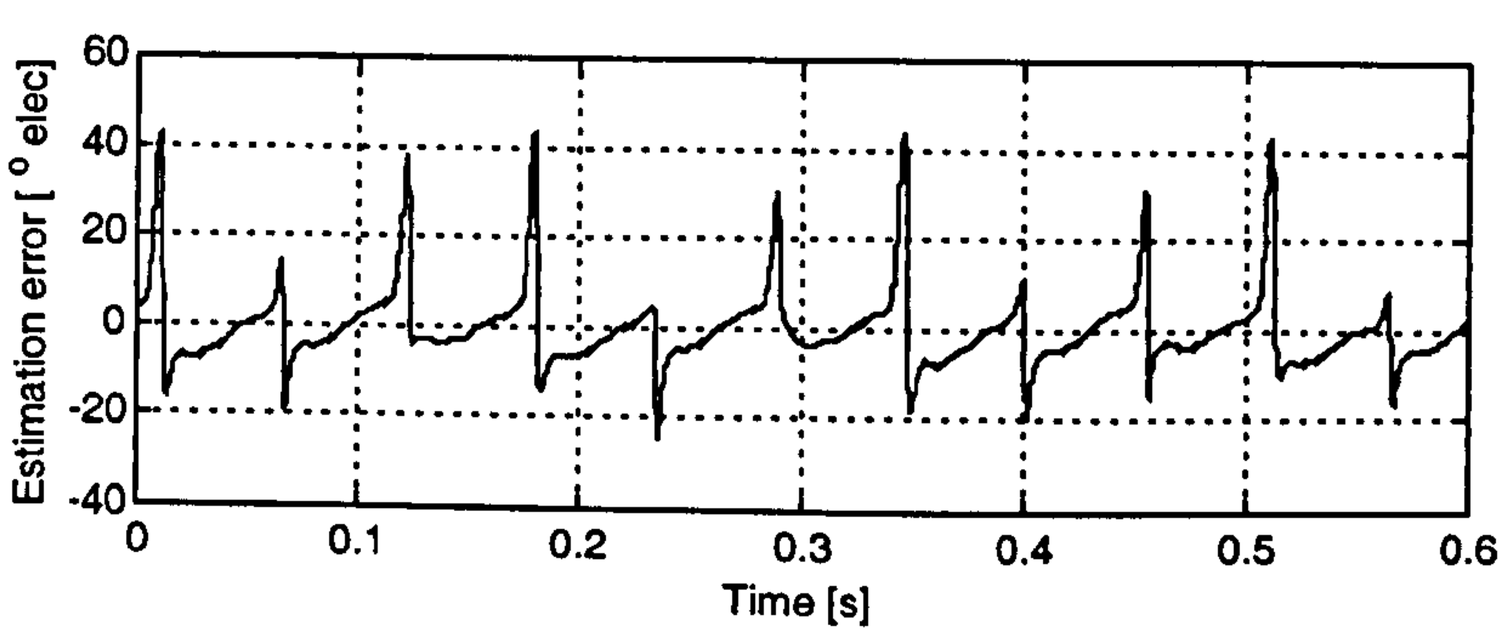

Figure 5.9: Estimation error with standard dead-time compensation.

5.3.2 Improved Dead-Time Compensation

Two different methods have being implemented to enhance the current direction detection and improve the compensation of the dead-time effect in the saliency position estimation. The first method consists of a software prediction of the currents at the moment of commutation; the second is based on hardware current detection capable of providing fast and accurate current direction information.

5.3.2.1 Software current prediction

Starting form the measured values the currents at the actual moment of commutation can be predicted form the reference voltage, the back-EMF and the inductance of the machine. Although the exact value of the back-EMF is not known an approximation can be derived from the estimated position and speed. The full sample period delay in the application of the PWM pulses means that the next current sample must first be predicted. For phase a, the approximate equation for the predicted value of $\hat{i}_a(k+1)$ given $i_a(k)$ is:

$$\hat{i}_a(k+1) \approx i_a(k) + \frac{T_s}{L}\left(v^*_{an}(k) - \hat{E}_{an}(k)\right) \tag{5.9}$$

Where $v^*_{an}(k)$ is the phase to neutral value of the reference voltage to be applied in the sample period k and therefore calculated at k-1 and $\hat{E}_{an}(k)$ is the estimated value of the back-EMF of phase a which is derived using the estimated rotor position and a filtered version of the electrical speed:

$$\hat{E}_{an}(k) = \hat{\psi}_m \hat{\omega}_{r\,filt}(k)\sin\left(\hat{\theta}_r(k)\right) \tag{5.10}$$

The operation of the current predictor is depicted in Fig. 5.10. The approximation for $\hat{i}_a(k+1)$, given by (5.9), is represented by the dotted line in the sampled period k.

Starting from this value of the current a at successive commutations $\hat{i}_{a1}$, $\hat{i}_{a2}$ and $\hat{i}_{a3}$ are approximated from the calculated PWM pulses for $k+1$ as:

$$\hat{i}_{a1} \approx \hat{i}_a(k+1) + \frac{T_1}{L_s}\left(-\hat{E}_{an}(k+1)\right)$$
$$\hat{i}_{a2} \approx \hat{i}_{a1} + \frac{T_2}{L_s}\left(V_{an2} - \hat{E}_{an}(k+1)\right) \qquad (5.11)$$
$$\hat{i}_{a3} \approx \hat{i}_{a2} + \frac{T_3}{L_s}\left(V_{an3} - \hat{E}_{an}(k+1)\right)$$

The values of V_{an2} and V_{an3} are the resulting voltages applied to phase a with respect to neutral during the periods T_2 and T_3 respectively. These voltages only can take the values of $\frac{2}{3}V_{dc}$, $\frac{1}{3}V_{dc}$, $-\frac{1}{3}V_{dc}$ or $-\frac{2}{3}V_{dc}$ depending on the sector of the PWM voltage being commanded.

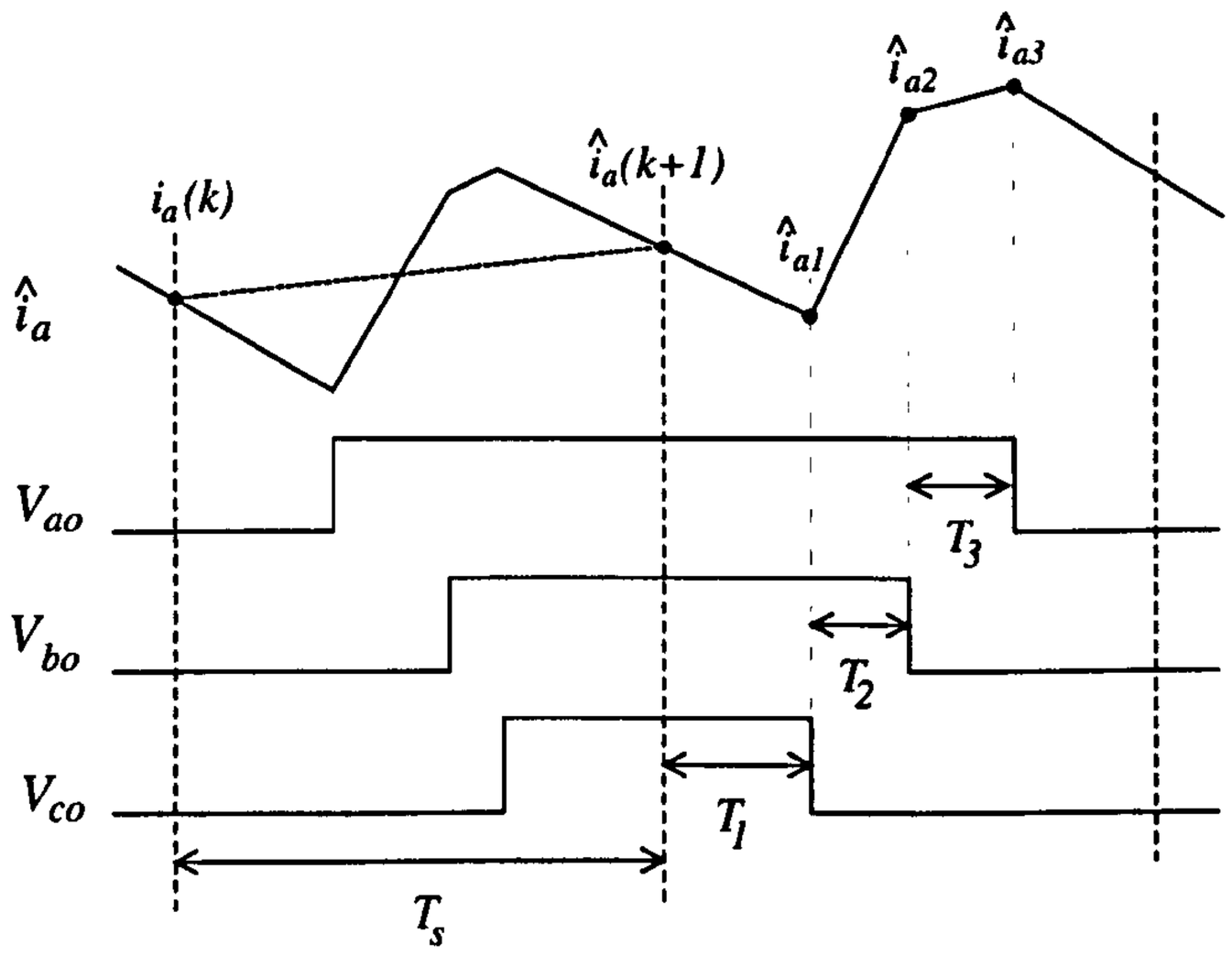

Figure 5.10: Operation of the current prediction algorithm.

Equations analogous to (5.9)-(5.11) are derived for the remaining two phases; this results in nine estimated values for the three phase currents for each of the three commutations. Only the three values that correspond to the phase currents when the corresponding phase itself is commutating are of relevance; these values can be selected by knowing the sector of the command voltage and hence the order of the commutations. In the example shown on Fig. 5.8, these values are $\hat{i}_{c1}$, $\hat{i}_{b2}$ and $\hat{i}_{a3}$. The resulting three currents are used for the dead-time compensation strategy

presented in Section 5.3.1. An illustrative result of saliency position estimation using this enhanced dead-time compensation is shown in Fig. 5.11, the improvement on the estimation being evident when compared with the results on Fig. 5.8. The saliency estimation error is shown in Fig. 5.12. This error is reduced to values within eight electrical degrees.

The prediction of the values of the currents at the commutation allows to compensate for the *current clamping* effect [78]. This phenomenon occurs when commutations happen under low current levels. During the dead-time when both switches are off, the conduction is through one of the free-wheeling diodes. The DC link opposes the flow of the current and therefore the magnitude of the current is decreased. If the current reaches zero before the corresponding switch is turned-on the conducting diode is reverse biased and the load phase will be floating for the remaining dead time. This results in an error of the voltage applied to the motor. The compensation routine proposed in [78] is meant to complement a standard dead-time compensation. This technique has been tried as part of the present work but the results do not show a significant improvement, mainly due to the inaccuracies in the predicted current values.

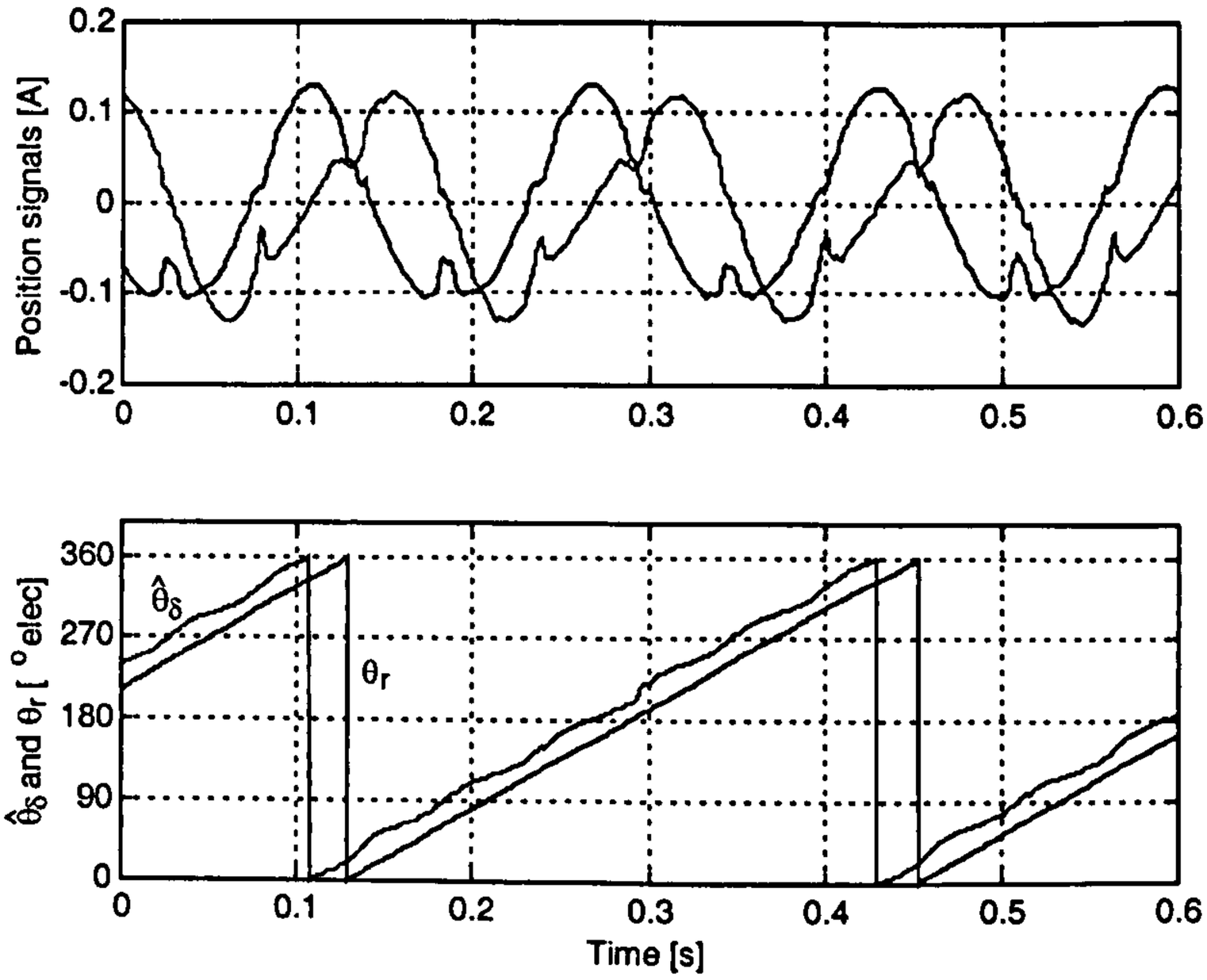

Figure 5.11: Saliency position estimation with dead-time compensation using software current prediction.

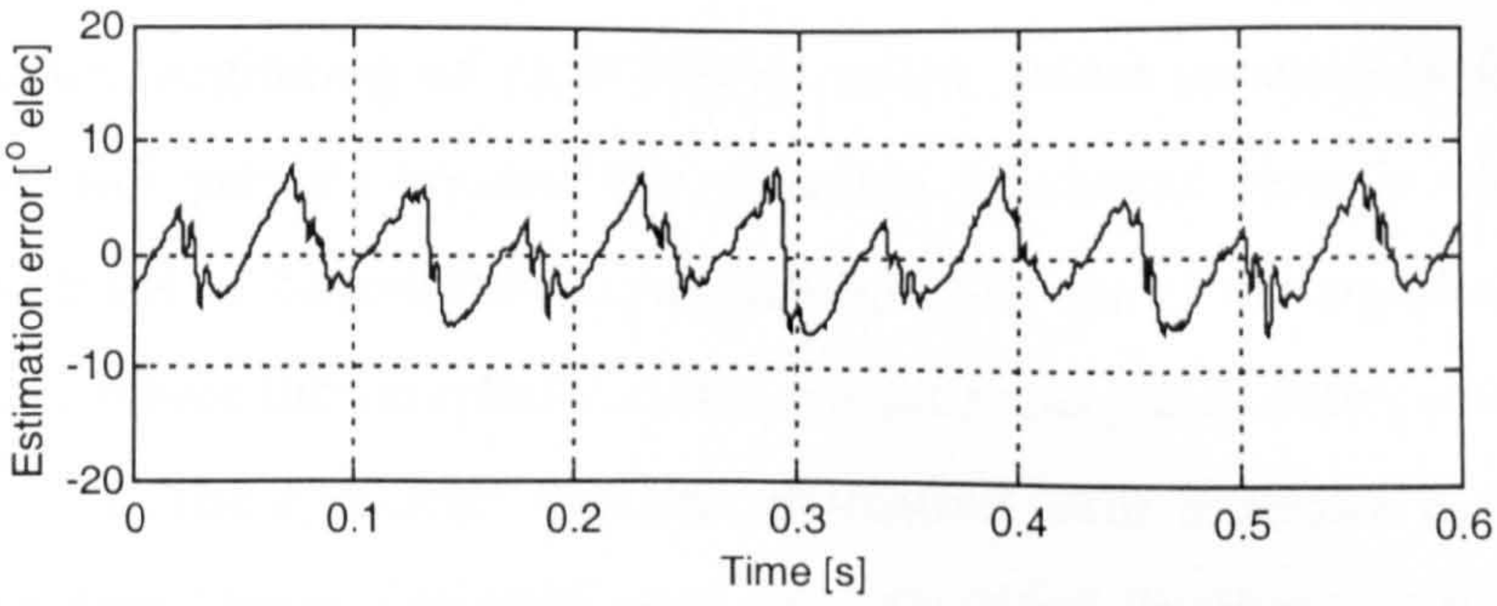

Figure 5.12: Estimation error with dead-time compensation using software current prediction.

5.3.2.2 Hardware current detection

A alternative way of detecting the current direction is using the circuit shown of Fig. 5.13. The power diodes in the line provide paths for positive or negative current. Their forward voltage drop has different polarities depending on the current direction. To minimise interference with the operation of the power circuit, low forward voltage-drop devices such the high frequency switching Schottky barrier rectifier diodes (PBYL3020CT) are used. The voltage drop across the diodes is detected by a comparator to generate a logic current direction signal. This is electrically isolated using an opto-coupler and finally transmitted to the digital I/O board where the three current directions can be read by the DSP in a single bus read operation. For the schematic of the detection circuit see appendix A.7.

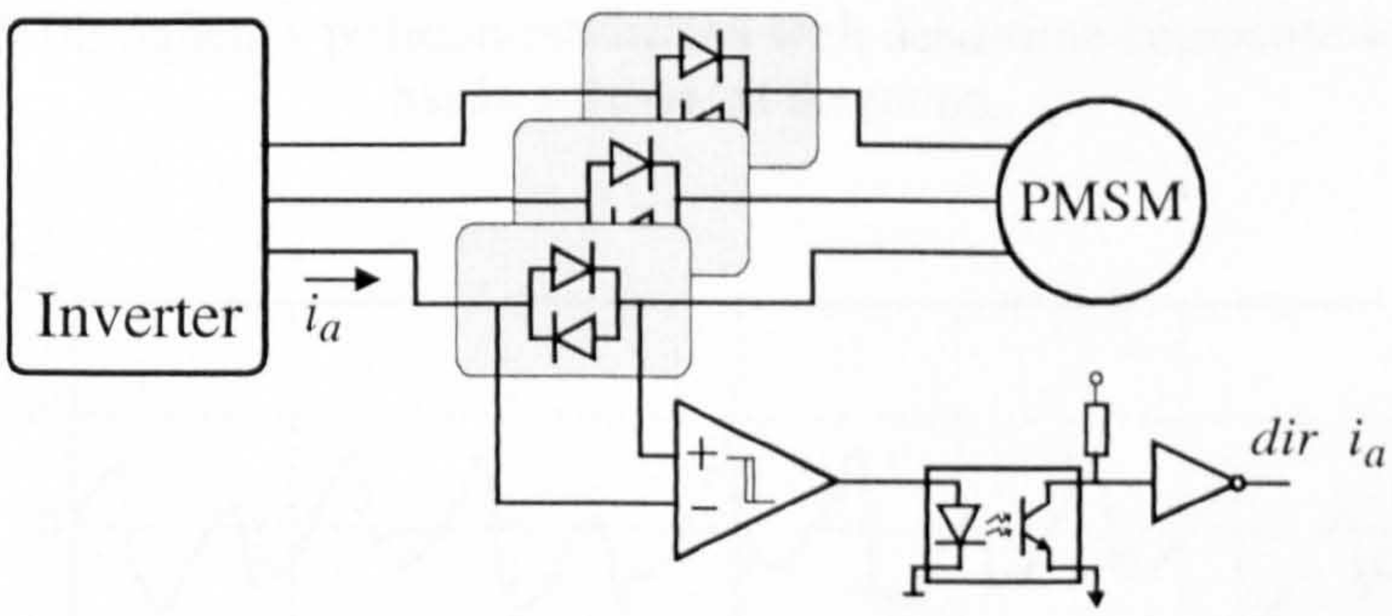

Figure 5.13: Current detection circuit.

The fast detection of the current direction allows the correction of the PWM pulse duration and their down load into the PWM board at the beginning of the sample period before triggering the PWM generation. In this way the delay on the current direction detection is shortened by a full sample period.

Using the current detection circuit the direction of the currents are determined accurately at the beginning of each PWM period. Some uncertainty in the correct compensation still persists because the direction of current flow is not determined exactly at the point of commutation; nevertheless this errors are significantly smaller than in the case where the sampled currents are used and yields better results as can be seen in Fig. 5.14. The e saliency position estimation error is shown in Fig. 5.15, the maximum measured error is slightly over eight electrical degrees i.e. the performance is comparable to that of the software base current prediction.

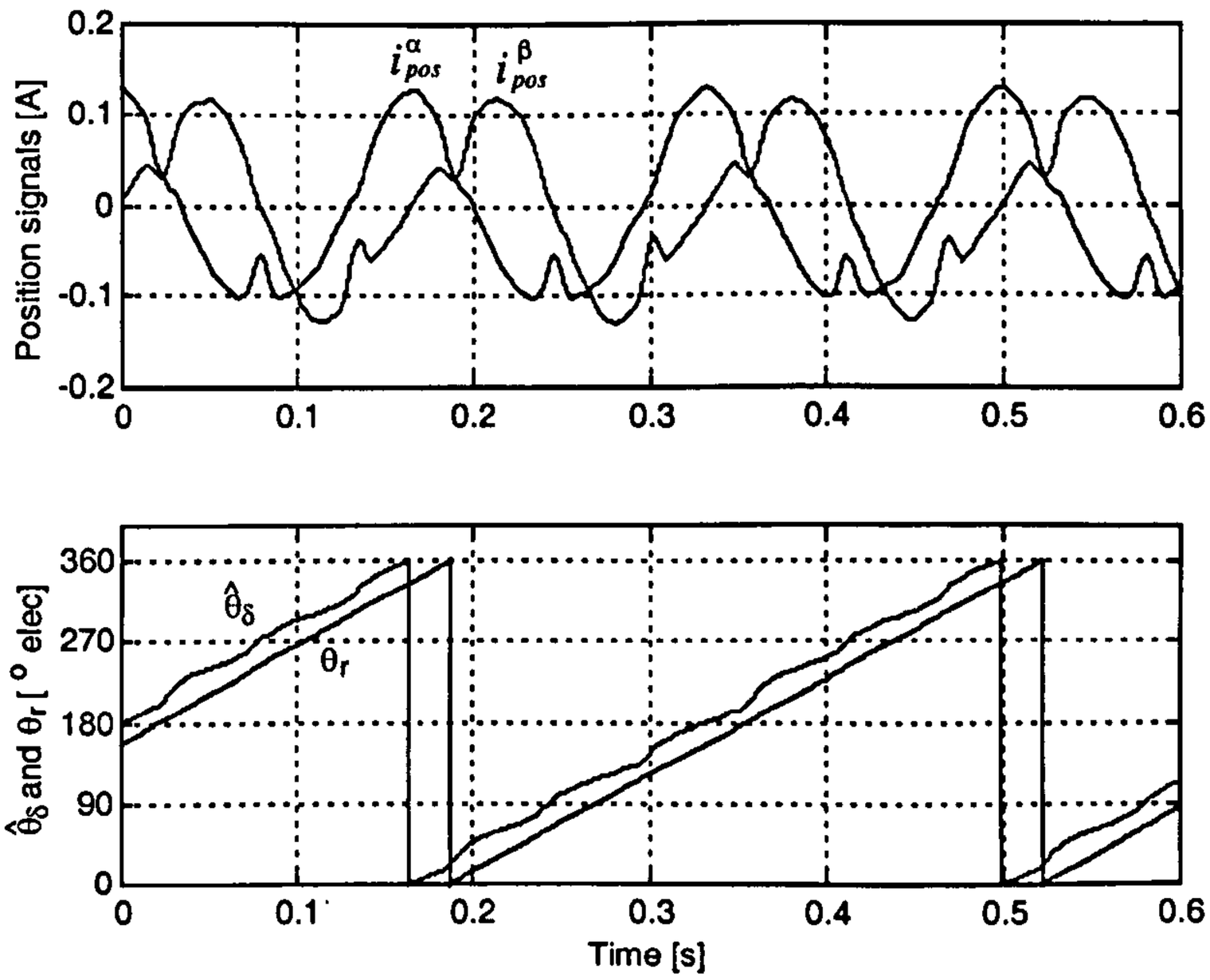

Figure 5.14: Saliency position estimation with dead-time compensation using hardware current detection.

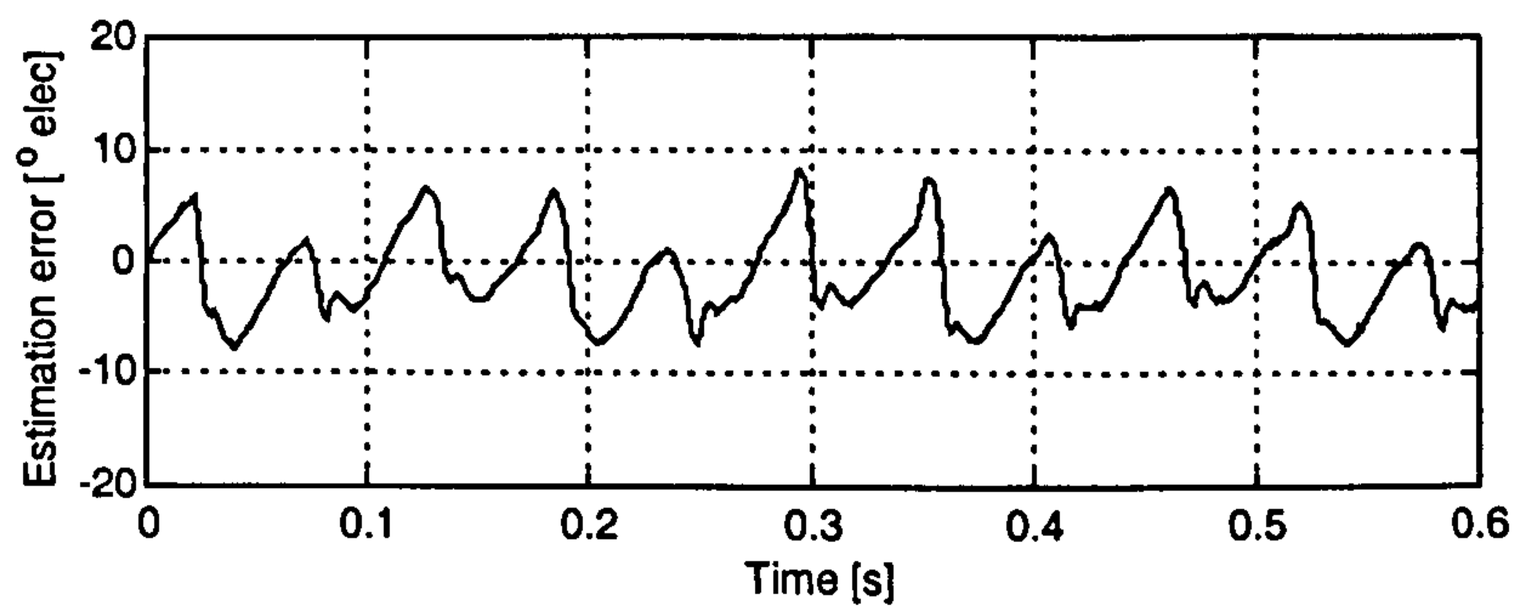

Figure 5.15: Estimation error with dead-time compensation using hardware current detection.

After dead-time compensation, the error in the saliency estimation is produced by the remaining harmonics on the position signals i_{pos}^{α} and i_{pos}^{β} and produces deviations from the ideal position signals given by its fundamental components. These deviations are better illustrated in polar form as a function of the rotor position θ_r angle in a saliency loci plots. The harmonics in the position signals are due to spatial harmonics on the saliency and residual zero current crossing effect; both phenomena are synchronous and therefore fixed in this plot. The traces for the position signal i_{pos}^{α} and i_{pos}^{β} are shown in Fig. 5.16 a) and b) respectively. Note that the amplitude of the signal is represented radially and the zero reference is indicated by a solid circle. The trace is averaged over 10 complete cycles to eliminate random errors and measurement noise. The fundamental components of the signals (ideal position signals) are included in the plots to illustrate the magnitude of the errors in the position signals. From these figures it can be seen that the deviations from the sinusoidal ideal position signals are repetitive and that random errors are small.

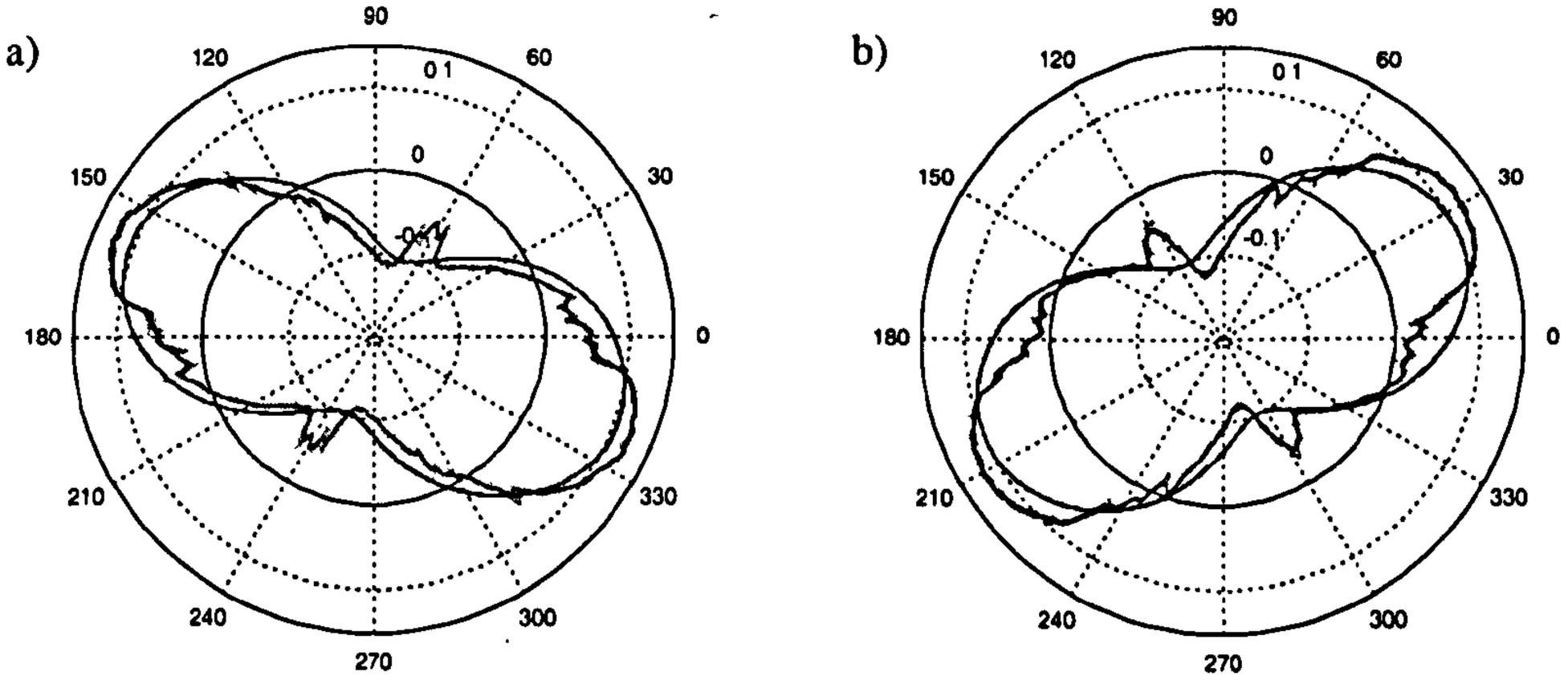

Figure 5.16: Saliency loci plots. a) i_{pos}^{α}, b) i_{pos}^{β}. Gray trace: scatter plot of all data. Bold trace: average.

5.3.3 Summary of Dead-Time Compensation Methods

The implementation of the hardware based current detection has the disadvantage of adding up semiconductors to the power circuit, increasing part count, cost and power dissipation. All this makes implementation unattractive for an industrial applications where a software solution such that presented in subsection 5.3.2.1 is more practical

and has been shown to achieve a similar end result. For research purposes the hardware detection has the advantage of being straightforward and simple to implement. It liberates considerable calculation time from the processor and it is independent of the machine's parameters. More importantly, it decouples the dead time compensation from the performance of the sensorless position estimation as opposed to the software current prediction where position and speed estimations are required for the estimation of the back-EMF and errors in the estimation will affect the quality of the dead time compensation. It is for this reason that the dead-time compensation is implemented using the hardware detection method for the remainder of this work.

As shown in subsection 5.3.2 the dead-time compensation is not achieved perfectly and the resulting position signals present residual errors at the instances of original dead-time induced modulation. The reasons for these errors are incomplete of "missed" compensations due to some uncertainty in the determination of the direction of the currents. Simulations using SABER, including realistic models of the switches, show that similar compensation strategy implemented using the accurate current direction at the moment of commutation greatly reduces the residual error. However, even with this ideal dead-time compensation some second order non-linearities such as the occurrence of current clamping and the device voltage drop will cause some modulation as can be appreciated in the simulation results of Fig. 5.17 and Fig. 5.18. Strategies to compensate for these types of phenomena have been reported in the literature [78] and [79] respectively, but their implementation are costly in terms of processing time, require accurate measurement of the current at the beginning of the commutation process.

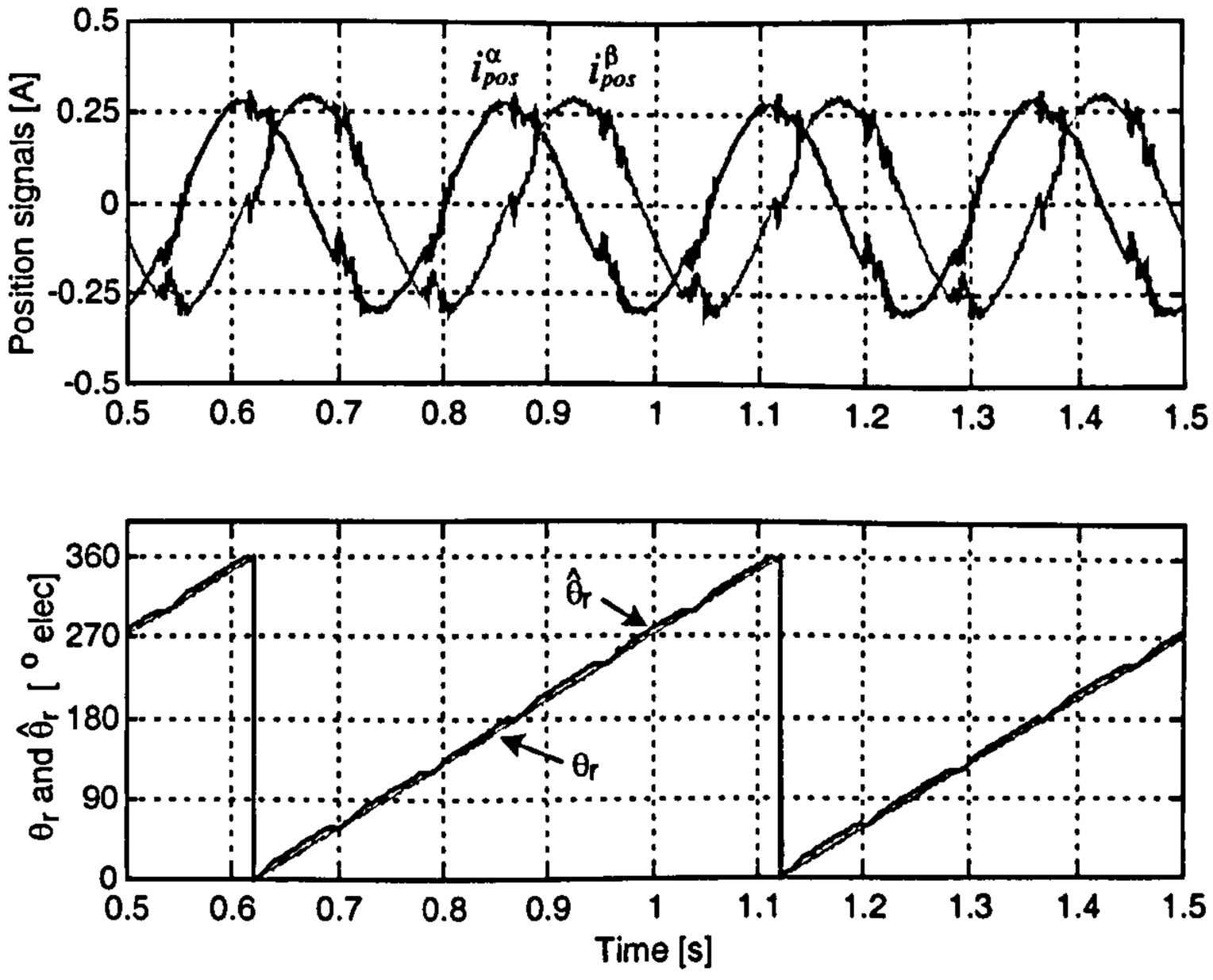

Figure 5.17: SABER simulation saliency tracking result using dead-time compensation with accurate current direction detection.

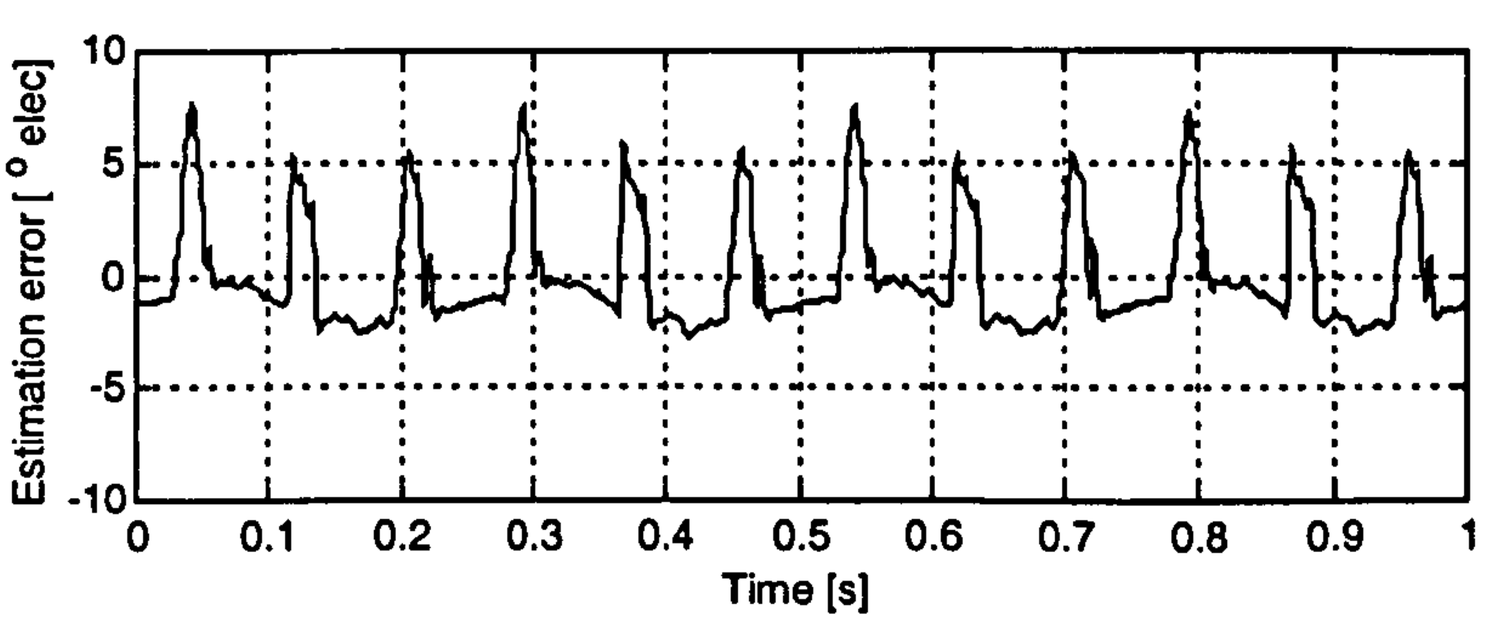

Figure 5.18: SABER simulation estimation error using dead-time compensation with accurate current direction detection.

Finally, even under perfect excitation the position signals i_{pos}^{α} and i_{pos}^{β} are expected to present some harmonics due to non-sinusoidal distributed saliency (spatial harmonics). A method is proposed in [69] to correct the influence of the saliency harmonics in the position estimation. The method is based on a commissioning process or *space modulation profile* (SMP) and its application to the surface mounted PM synchronous machine is explored in detail in the following section. Due to the synchronous nature of the residual dead-time distortion it is difficult to distinguish it from the machine's spatial harmonics and therefore the SMP method is also used for the elimination of the residual dead-time modulations.

5.4 Space Harmonic Profiling

5.4.1 Introduction

The quality of the saliency position estimation achieved with dead-time compensation alone is within eight electrical degrees (just less than 3° mech.) as shown in Fig. 5.15. This is accurate enough for orientation and hence sensorless torque control, but for sensorless position control this error is excessively high and causes position oscillations. The periodicity of the error with rotor position can be exploited to improve the estimation. Direct correction of the estimated position using the uncompensated *hf* injection position estimation to feed a neural-fuzzy error estimation has been proposed in [80], the method being applied in a salient pole PM machine with the variations of the error with load level not considered. In the present work the, correction of the saliency position signals i_{pos}^{α} and i_{pos}^{β} rather than the direct correction of the angle estimation is favoured. In [27, 31, 81] the correction of the position signals has been carried out for individual harmonics, the method having the advantage of only requiring the amplitude and phase (only two values) per each harmonic to be cancelled. This approach is suitable when only a small number of harmonics are to be suppressed. To compensate for position signals with errors of a richer spectrum, such as those produced by remnant inverter non-linearities, the *space-modulation profiling* (SMP) technique proposed in [28, 69] is better suited. A similar technique has also being presented in [30]. These methods have been exploited mainly for elimination of saturation saliency in rotor-bar saliency tracking in inductions machines but its usefulness in compensating for inverter generated modulations has being shown in [82].

In the SMP method the deviations of the measured saliency position signals with respect to its fundamental value are measured in a commissioning procedure and stored in tables, the correction of the saliency position signals i_{pos}^{α} and i_{pos}^{β} being in the time domain. The effect of change of load upon the harmonic content of the saturation-induced harmonic and the remnant inverter modulation is included by making the SMP tables bi-directional and performing the commissioning for the full

rage of load levels. During normal operation the error is obtained by addressing the tables with the rotor position estimation and the torque command. The error estimation is then subtracted from the original position signals to refine the saliency position estimation. The effectiveness of the SMP compensation will depend on the accuracy of the original position estimation. Therefore it is preferable to compensate for the dead-time and not rely entirely in the SMP compensation for the elimination of the inverter induced modulation.

5.4.2 The Space Modulation Profiling Technique

In the commissioning process, the profile of expected differences between saliency position signals i_{pos}^{α}, i_{pos}^{β} and their ideal values (given by their fundamental, as shown in the polar plots of Fig. 5.16) are calculated and stored in the SMP tables. The signal processing for extraction of the profiles is performed off-line. In this research the commissioning process is undertaken with the PM drive operated in sensored torque control. The speed is controlled at an arbitrary value of 60 rpm by the load IM drive, resulting in 3 Hz PM machine excitation frequency and 6 Hz fundamental saliency position signals. The data is captured at a fix rate of 10/3 kHz during 6 seconds (20000 samples). Similar data captures are repeated for different torque current references for the whole load range, from –10 A to 10 A in intervals of 0.5 A.

The profile is created for each individual torque level. The fundamental component of the saliency position signal is extracted by narrow Butterworth band pass filter centred at 6 Hz and the spectral contents of the position signals limited to 600 Hz by a low pass filter. The data is applied backwards and forwards to the filters using the *filtfilt* Matlab command to achieve a non-causal filters that preserve the signals phase. The difference between both signals is calculated and stored as a function of the rotor position. This is done by dividing the complete rotor revolution into a discrete number of intervals (256 was used in this work), all the error measurements corresponding to the same angle interval are averaged to produce the typical error for that position. Approximately 50 samples per position interval, corresponding to 10 different revolutions have been used in the calculation of each average. This signal processing is represented in the flow diagram of Fig. 5.19.

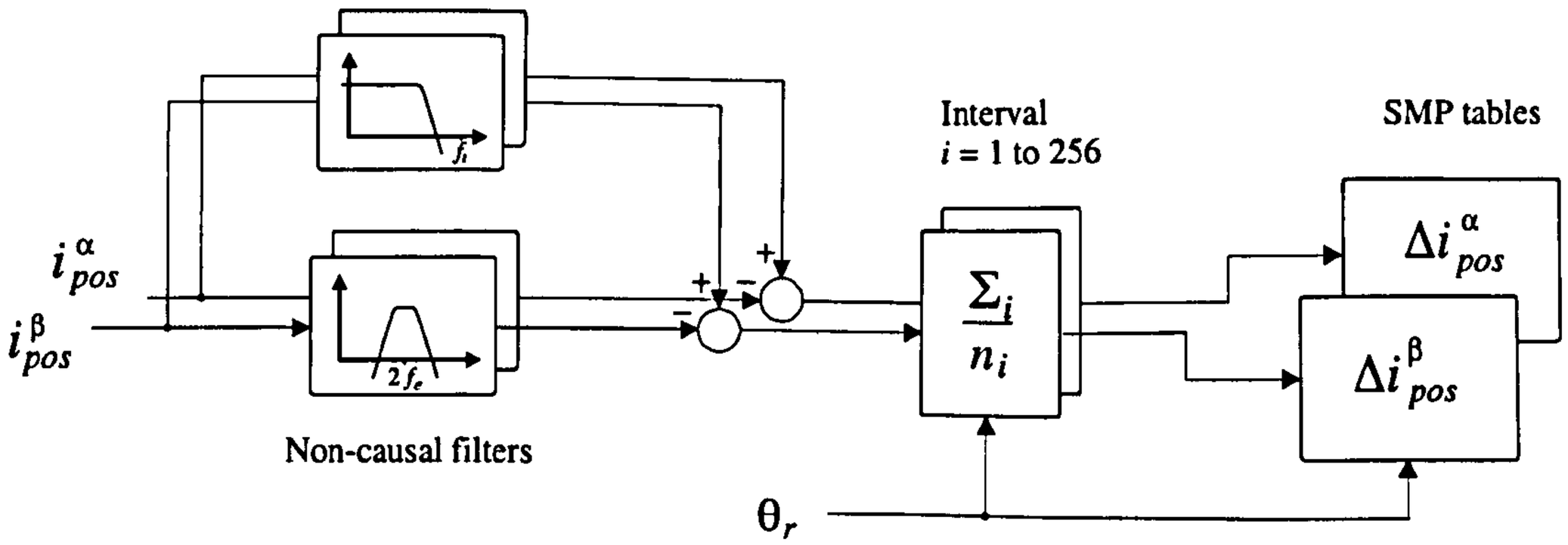

Figure 5.19: Signal processing flow diagram for the profiling of the saliency.

The saliency profile is theoretically independent of the speed, although the influence of the analogue filters used for separating the high frequency current measurement from the fundamental current produce a small phase shift of the saliency position signals which is frequency dependent. The nominal characteristic of these filters is known, allowing their influence to be accounted for during the profiling procedure, see appendix B for details. Figure 5.20 shows the profile obtained at 80% of nominal torque obtained independently for positive and negative speeds. This plot illustrates the consistency of the profile results at different speeds and the effectiveness of the filter phase shift compensation. In Figure 5.20 it can be noted that the larger amplitude of the profile still corresponds to the angles where the fundamental current crosses zero, where the inverter non-linearities manifest, showing that even with the proposed dead-time compensation the inverter accounts for most of the distortion in the position signals. The profiling procedure is repeated for the data obtained with the different torque references generating the two-dimensional SMP tables shown as surfaces in Fig. 5.21.

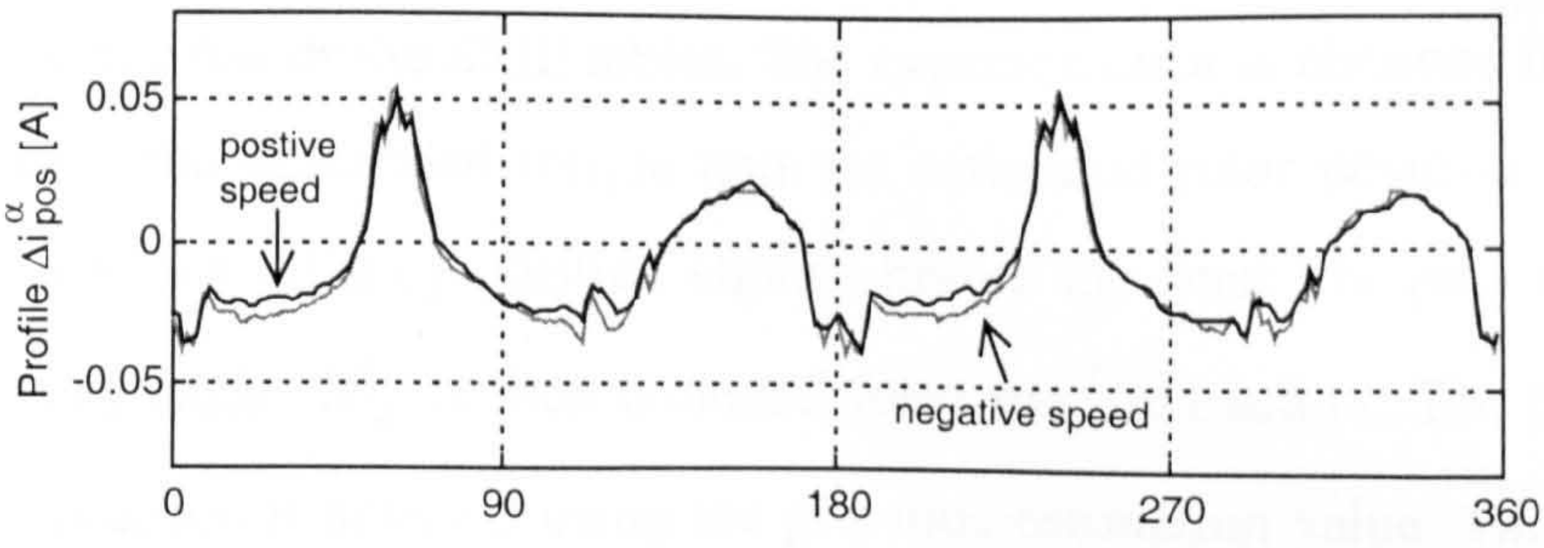

Figure 5.20: Profile of the error on the position signals at 80% nominal current for positive and negative rotational speed.

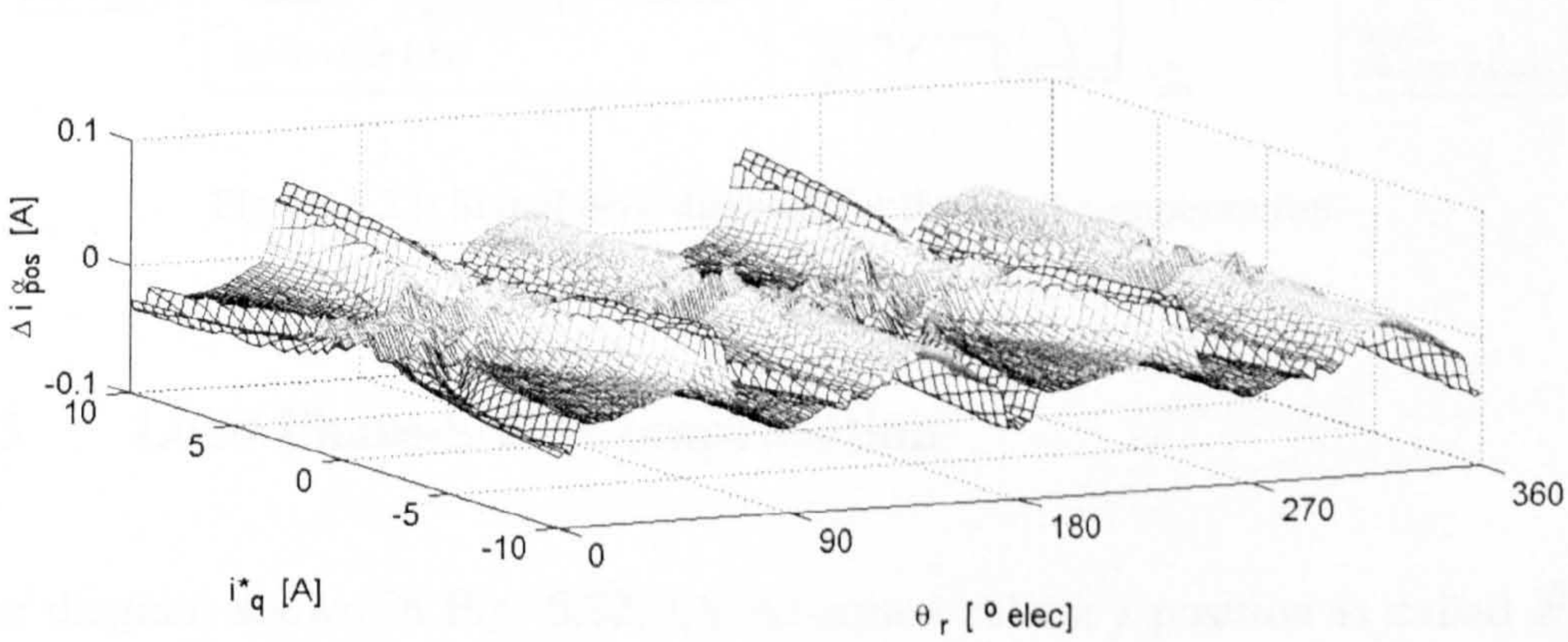

Figure 5.21: Compensation SMP tables.

The commissioning of the SMP tables is a one-off operation. The tables are stored in a non-volatile medium ready for use at normal operation of the drive. Figure 5.22 depicts the online use of the SMP tables. The expected error is obtained by addressing the tables with the demanded torque and the estimated rotor position. The error is subtracted from the saliency position signals before the final low-pass filtering. The double saliency angle $2\hat{\theta}_\delta$ is then obtained form tan^{-1} extraction. The orientation of the saliency position is selected using the previous estimation value. This mechanism ultimately relies on a start-up or initial position detection procedure [83] that imposes some continuous i_d current to change the state of saturation and determines the original polarity of the rotor magnet and hence the orientation of the rotor.

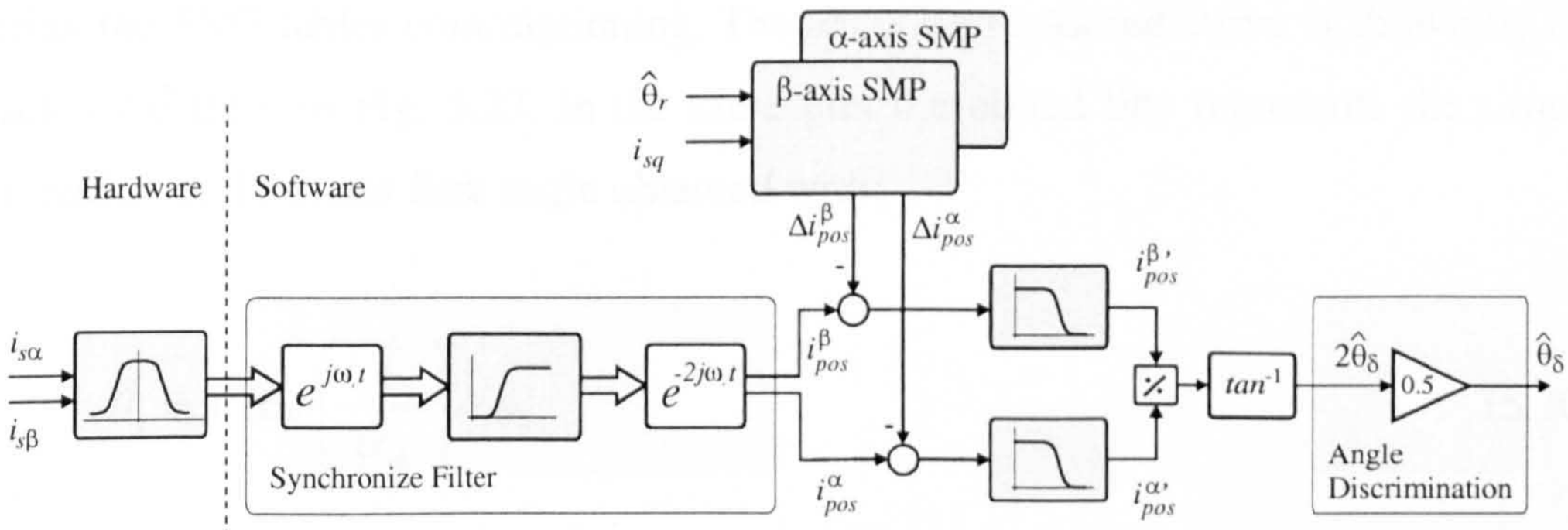

Figure 5.22: Signal flow diagram for the SMP compensation.

5.4.3 Load Phase-Shift Compensation

In the diagram shown in Fig. 5.22, the estimated saliency position is called $\hat{\theta}_\delta$ to distinguish it from the estimated rotor position $\hat{\theta}_r$. This is because the shift in the stator flux and hence tooth saturation produced by i_q has a significant magnitude in the surface mounted PM machine used in this work. This phenomenon is illustrated by the stator inductance L_β measurement of Fig. 5.1 and 5.2. The control of the synchronous machine requires $\hat{\theta}_r$ for orientation and feedback and the objective of the sensorless strategy is actually to obtain $\hat{\theta}_r$ for those purposes. Furthermore $\hat{\theta}_r$ is also required as part of the injection-based sensorless strategy itself for the SMP compensation as Fig. 5.22 shows. Nevertheless, the end result of the demodulation of

the *hf* injection currents yields estimation of the saliency position $\hat{\theta}_s$ and therefore the phase relation $\Delta\theta$ between these two angles has to be characterised to complete the sensorless estimation.

Although the physical principle of the phase shift is understood, as discussed in subsection 3.1.2, the phenomenon of saturation is complex and only over-simplistic approximations can be derived theoretically. On the other hand the data obtained from the SMP table commissioning process contain the information necessary to derive the relation between both angles empirically. The procedure consists in taking the average difference between the measured rotor angle and the estimated saliency angle, obtained from the fundamental components of the position signals, and is executed during the SMP tables commissioning. The resulting measured curve is shown by the black solid trace in Fig. 5.23. In the same plot the dotted line represents the simple estimation of the stator flux angle obtained with:

$$\hat{\theta}_s = \arctan\left(\frac{i_q \hat{L}_q}{\hat{\psi}_m}\right) + \phi_0 \tag{5.10}$$

The angle ϕ_0 in (5.10) represents the phase shift measured when tracking a saliency perfectly oriented with the *d-axis*. This angle is generated by the shift in carrier current due to the controllers. In section 4.3.2 the angle ϕ_0 has been be theoretically estimated to be -13.8° elec. through calculating the difference between the phase of the nominal close-loop transfer functions $i_s(z)/v_i(z)$ of Fig. 4.3 (at the injection frequency) and the 90° phase expected from an ideal inductive load in open loop.

The correlation between the theoretical stator flux angle and the measured saliency is evident and gives strong evidence that the saliency being tracked is influenced by stator flux saturation. The measured curve also shows deviations that are not explicable by shifts in the saturation position, particularly at low levels of i_q. This difference is explained by the presence of the $2f_e$ harmonics produced by the uncompensated inverter non-linearities (5.7). Evidence of this is given by the curve measured without dead-time compensation shown by the grey trace in Fig. 5.23. In

this curve the deviations are larger in magnitude but present similar tendencies. The inverter non-linearity does in fact generate a sub-harmonic at $2f_e$ and this spectral component cannot be compensated using the SMP tables because it is at the same frequency as that of the saliency being tracked. Nevertheless Fig. 5.23 shows that dead-time compensation is an effective means of reducing the magnitude of this phenomenon.

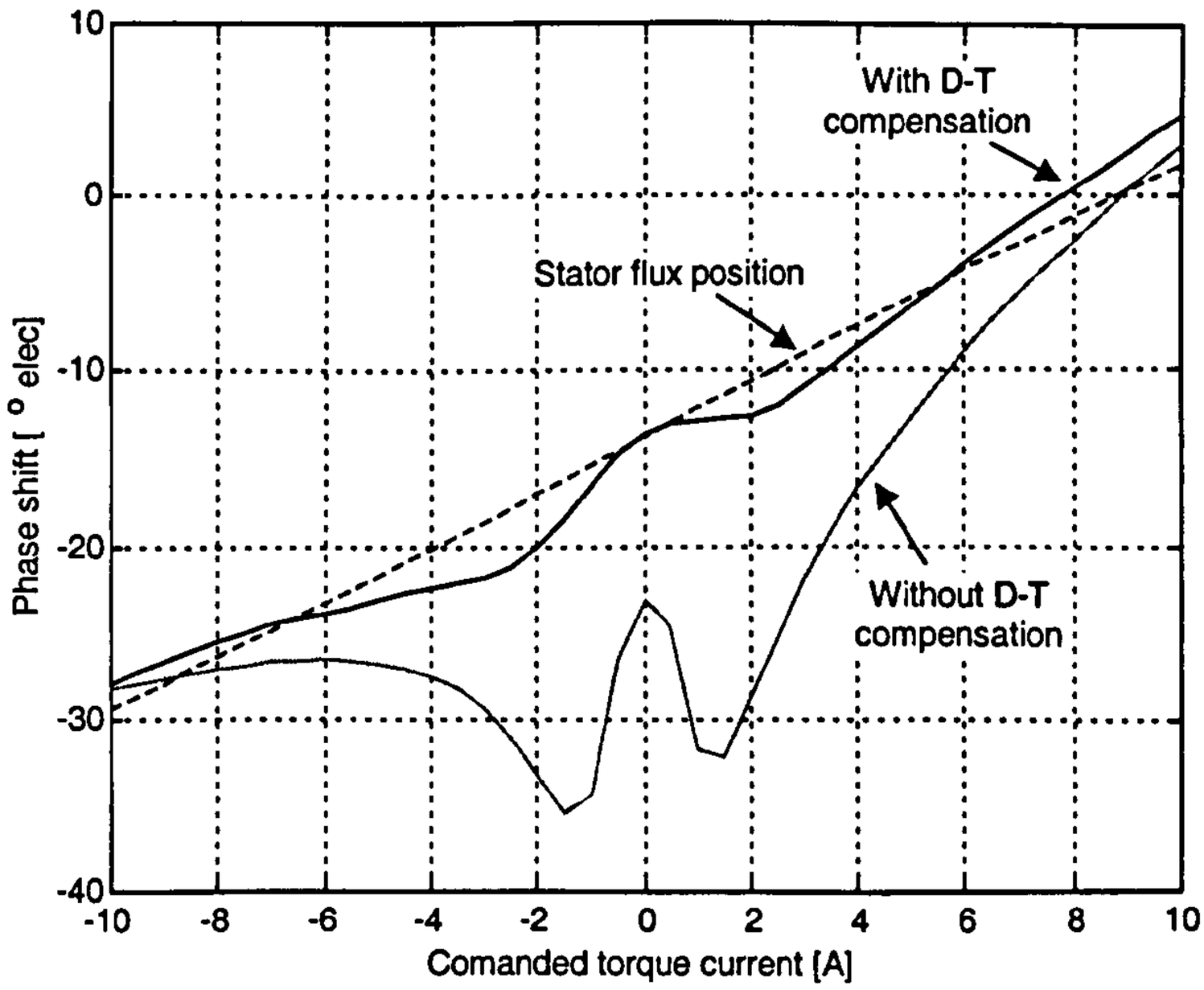

Figure 5.23: Phase shift $\Delta\theta$ between rotor and estimated saliency position as function of torque current.

The compensation depicted in of Fig. 5.23 is obtained for stationary conditions. Nevertheless, because the saliency is influenced by the stator flux, the dynamic of the phase shift can be approximated by the dynamic of the stator current [84]. Therefore the phase compensation can be performed using the measured value of i_q or, if the commanded value is used instead a filter is applied to emulate the dynamics of the *q-axis* current loop. This second alternative is preferred because it results in a smoother signal free from the components at injection frequency; the same torque current estimation is used to address the SMP tables. The rotor position estimator with the phase correction is shown in Fig. 5.24

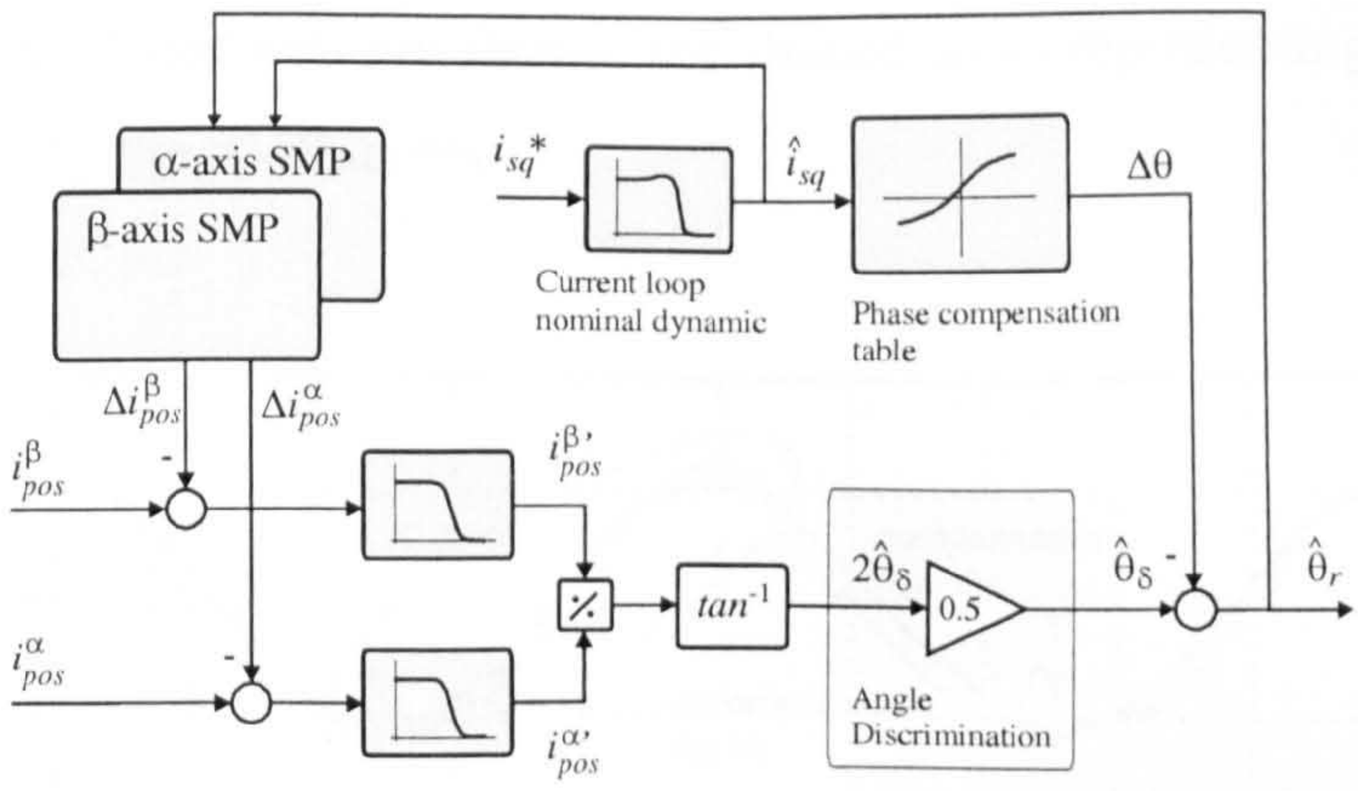

Figure 5.24: Rotor position estimation including phase correction.

The use of phase compensation tables is generally seen as a disadvantage of the method because the correct orientation depends on the open loop correction of the position of the rotor flux. This is particularly critical in induction machines where different machine designs or even different operation conditions such as flux level [57] and torque current [85] of the machine produce dramatic changes in saliency position. These changes are associated to saturation of different elements of the machine that dominates the saliency at different operational conditions. Although the difficulty of compensation for the phase shift also exist in PM motors they are not as severe. The absence of a rotor circuit simplifies the flux path and the saliency on the magnetising inductance produced by saturation of the stator main flux path is dominant through out the operating range, as shown by Fig. 5.23. The flux level in this type of machine is fixed by the magnets and the machine is operated normally with zero flux current. Furthermore in machines with high-energy magnets the magnitude of the flux imposed by the magnets is considerably larger than that produced by the stator inductances so limiting the phase change between the saliency and rotor positions.

5.4.4 Enhancement in Position Estimates Using SMP Technique

The combined use of harmonic compensation by SMP tables and the correction of the load phase shift yields enhanced position detection. The operation of the compensation is illustrated in Fig. 5.25. In this figure results of position tracking at a speed of 40 rpm and constant i_q current are shown. The two position signals with

their characteristic distortions are shown, the shaded areas representing the magnitude of the correction by the SMP tables.

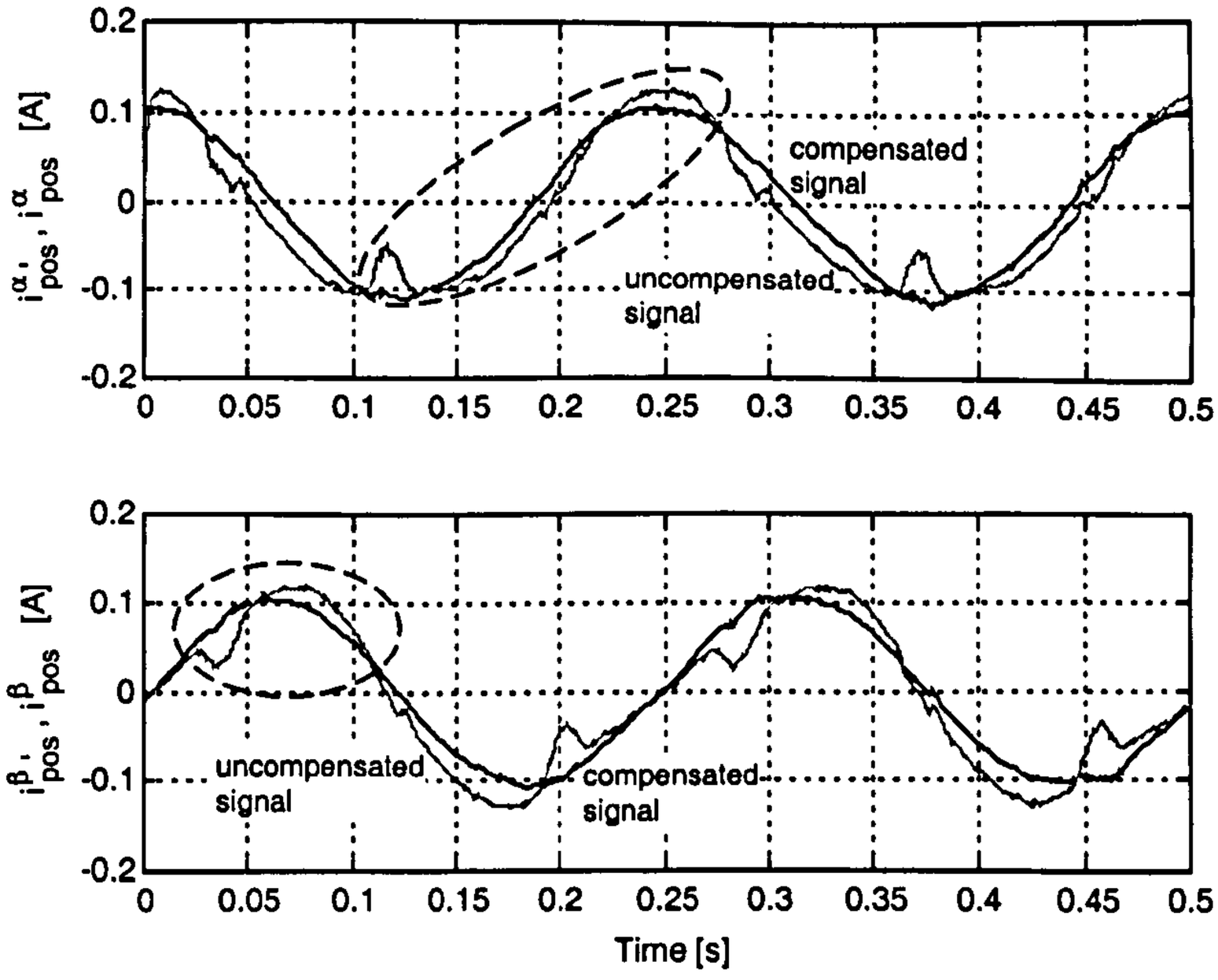

Figure 5.25: Compensation of the position signals.

The improvement on the position signals is better appreciated in the saliency loci plots of Fig. 5.26. The traces produced by these signals are very close to the ideal sinusoidal position signals depicted in Fig. 5.16. The phase shift between the saliency and the rotor position can be appreciated by the misalignment of the maximum of i^{α}_{pos} and the zero rotor position.

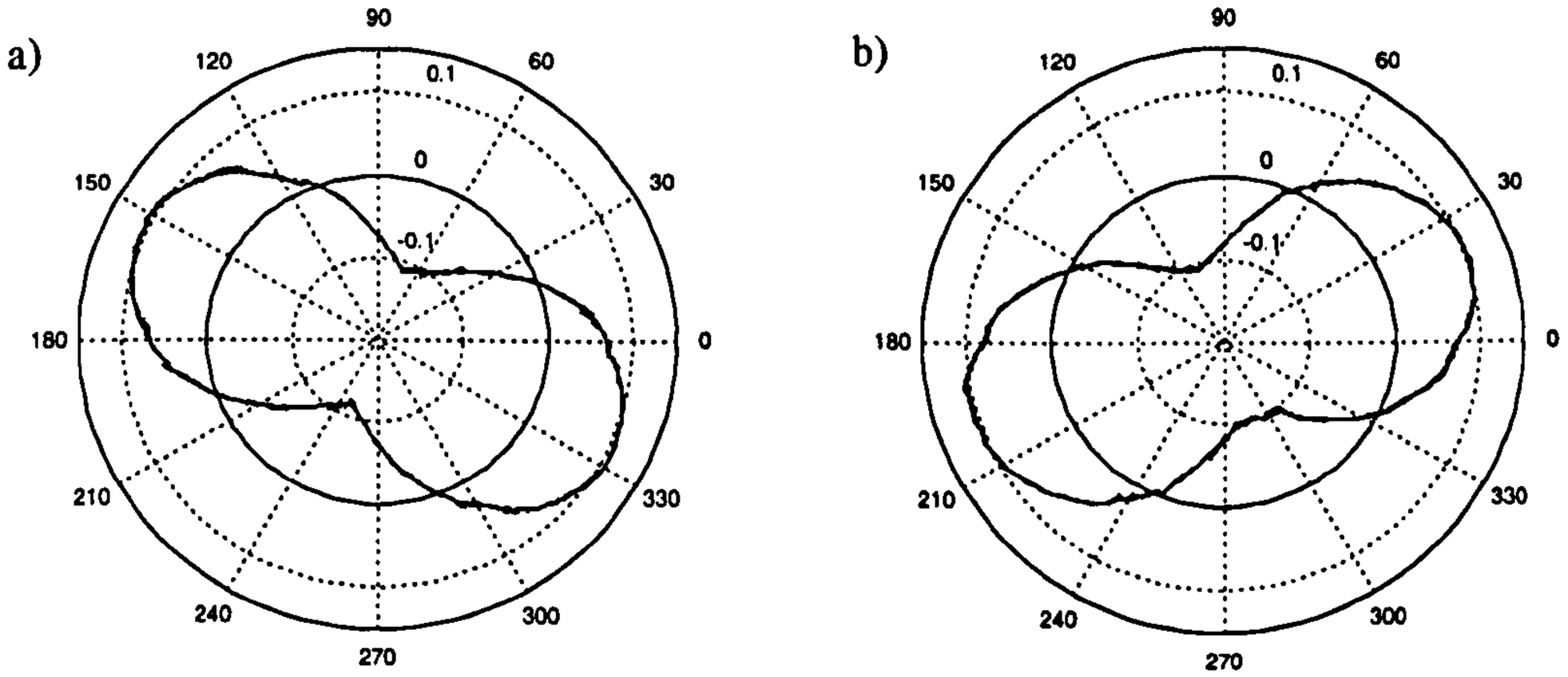

Figure 5.26: Compensated saliency loci plots. a) i^{α}_{pos}, b) i^{β}_{pos}.

Finally the compensated saliency signals and the phase shift compensation result in the rotor position estimation of Fig. 5.27. The error between the measured and the estimated rotor position is limited to approximately 2° electrical (0.67° mech.).

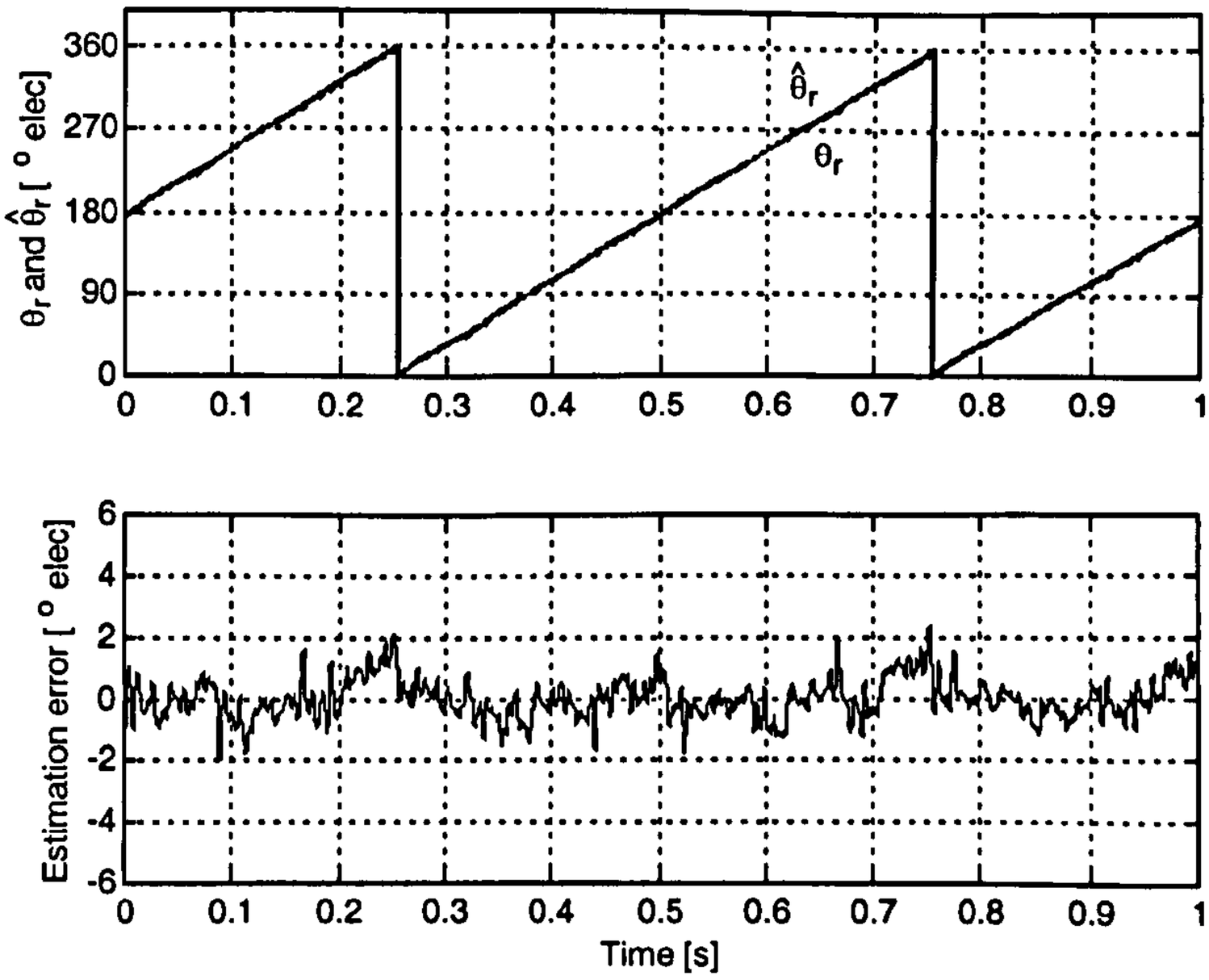

Figure 5.27: Rotor position estimation using SMP compensation.

5.4.5 Discussion of SMP Technique

The presented SMP technique has been shown to improve the quality of the rotor position estimation. Nevertheless this technique uses, in this work, a sensored commissioning process. In general this is difficult to achieve in practice because sensorless techniques are applied in drives where position feedback devices are not fitted. Furthermore in industrial applications the loads are not able to control torque to create the different operation points required for sensored commissioning. The underlying assumption in the SMP technique is that the same compensation tables are suitable for all drives of similar characteristics. This means motors of the same design and same power converters. Therefore tables could be adjusted for different inverter-motor combinations and provided by the manufacturer. The validity of this assumption has not been tested in this work but the nature of the sources of distortion

in the position signals, such as harmonics in the saturation saliency and inverter non-linearities, support it.

An alternative approach to the SMP has been reported in [30] for elimination of saturation harmonics when tracking rotor slot position signals in induction machines. This method relies on the position signals being asynchronous and using a *spatial filter* to extract the synchronous saturation saliency. This technique cannot be applied to decouple saliencies that are synchronous to each other (such the fundamental of the saturation saliency and it's harmonic components) and therefore is not a viable alternative when tracking saturation harmonics as proposed in the present work. As presented in [30], the method appeared to establish the compensation values in a sensorless manner. However, closer inspection reveals that the method still requires the torque current i_q to vary during 'commissioning' and still requires a load drive to perform the quantifiable load variations.

A more viable approach to sensorless commissioning is to take advantage of the fact that the SMP and phase angle compensation values are theoretically independent of rotor speed. Hence the 'real' rotor position can be provided by a mechanical model and the commissioning process carried out at a frequency where the model is valid e.g. above 20 Hz for the machine used in this work.

A further alternative would be online tuning of the compensation SMP tables. The sensorless drive initially relying on either on uncompensated saliency tracking or that provided by a model-based commissioning scheme as described above. The compensation could be gradually adjusted with a training algorithm to improve quality of the estimation. In this case, the absence of position transducer impedes the empirical adjustment of the phase compensation table and therefore an analytical approximation has to be used and might limit the final accuracy of the method. The auto-calibration of a fuzzy angle-error estimation have being proposed in [80] for use in a salient machine, The application of similar technique to the position signals i^{α}_{pos}, i^{β}_{pos} of this work may be worth investigating.

It worth noticing that, as shown in this chapter, the inverter non-linearities such as dead-time have a large impact on the harmonic content of the position signals and therefore they affect the SMP tables. Dead-time compensation has been investigated and shown to yield improved saliency estimations. However remnants of the inverter's non-linearity distortions are still observable. From this it follows that more linear converters or further improved compensation methods, necessarily hardware based, would yield better position signals. This in turn may be sufficient for low accuracy applications. However compensation of other effects such as the motor saliency spatial harmonics are still required for further accuracy improvements.

Chapter 6

6 Closed Loop Sensorless Position and Speed Control

6.1 Introduction

Experimental results of close-loop sensorless control using the two different injection methods presented, namely α-β *hf* rotating voltage and *d-axis hf* pulsating voltage injection are presented and compared in this chapter. To obtain a fair comparison, the same control design, previously introduced in Section 4.3, is used for both implementations. In this way the differences in performance are therefore dependent on the different noise levels in, and dynamics of, the sensorless position estimation scheme.

The implementation of the α-β injection includes dead-time compensation and SMP (as discussed in sections 5.3 and 5.4) for improved performance. On the other hand the tracking nature of the *d-axis* injection does not allow for compensation with an SMP technique. However the *d-axis* injection detects the orientation error by measuring *q-axis* current which is largely unaffected by dead time (the largest source of distortion) and so its performance may be adequate for some applications even without compensation against signal distortion. The impossibility of applying compensation to the *d-axis* technique, either by harmonic cancellation or SMP, becomes a disadvantage only when the quality of its estimation is insufficient for the desired application. Finally it noted that as in any saliency tracking technique, the *d-axis* pulsation injection does not detect directly the rotor position and therefore the

relation between the saturation saliency and actual rotor position must be determined and taken into account in the same way as it is in the α-β injection. Section 6.2 presents the tuning of the saliency-tracking loop and the implementation of the phase compensation for the *d-axis* injection. The experimental results for sensorless position and speed control for both techniques are presented in section 6.3.

Finally in section 6.4 the limitations of the *hf* injection approach for operation at higher speeds is discussed and a hybrid structure combining one of the injection methods with a model-based flux observer is proposed for position estimation valid over the whole speed range. This hybrid structure is applicable to any injection method that yields rotor position estimation at low speed. The α-β rotating injection, including compensation, is used in the present work to illustrate its operation. Experimental results are presented to show the smooth transition between the model-base operation and the low-speed injection operation.

6.2 Design of the d-axis Injection Tracking-Loop

The implemented saliency-taking algorithm for the *d-axis* injection has been developed in subsection 3.3.2.2 and is described by the tracking-loop of Fig. 3.8. The dynamic of this loop is critical for the performance of the *d-axis* injection method and is discussed below. This loop yields saliency position estimation; this is not sufficient to obtain correct orientation due to the shift in the saturation saliency position with load. The commissioning of a phase-shift table for this method is also described in this section. It is worth noticing that the table is used to correct the rotor position estimation for position feedback and orientation of the vector control, but not to correct the angle used to orientate the pulsating injection. This method works by orienting the voltage injection along the saliency *δ-axis* rather than actual rotor position.

6.2.1 Dynamic of the Saliency Tracking Loop

Controllers with too high a tracking loop gain will amplify measurement noise and disturbances such as inverter effects in the *hf* current $\tilde{i}_\gamma^e$ currents, yielding noisy or perturbed saliency position estimates. On the other hand limiting the bandwidth of this loop to filter such noise or perturbations will limit the dynamics of the position and speed feedback path under sensorless control. In Chapter 4, the controllers for the sensorless case where designed with a nominal bandwidth of 2.2 Hz (assuming no dynamic in the position feedback and a first order filter with cut-off frequency of 60 Hz in the speed feedback). The saliency-tracking loop should therefore be designed with a bandwidth much higher than this in order to keep the 2.2 Hz position bandwidth as a target figure.

There are two filters in the tracking loop of Fig. 3.8. The software band pass filter for i_γ^e is set as a second order Butterworth band-pass filter with cut-off frequencies of 800 and 1250 Hz. The low-pass filter used in the output stage of the heterodyne demodulation of the injection current $\tilde{i}_\gamma^e$ is set as a first order filter with cut-off frequency of 500 Hz.

The saliency tracking loop is a non-linear structure, but by linearizing about the operation point $\hat{\theta}_\delta\big|_{o.p.} = \theta_r$, its dynamic can be approximated by the linear loop of Fig. 6.1 which is use for control design. With this approximation the parameters of the controller are functions of the actual saliency angle error $\Delta\theta_\delta$, not current signal amplitude ζ. Therefore in the final implementation, the scaling factor derived from (3.25) must be considered:

$$\zeta \approx \frac{\hat{V} \cdot \Delta L_s}{L_\delta L_\gamma \cdot \omega_i} \Delta\theta_\delta \approx 0.1442 \cdot \Delta\theta_\delta \tag{6.1}$$

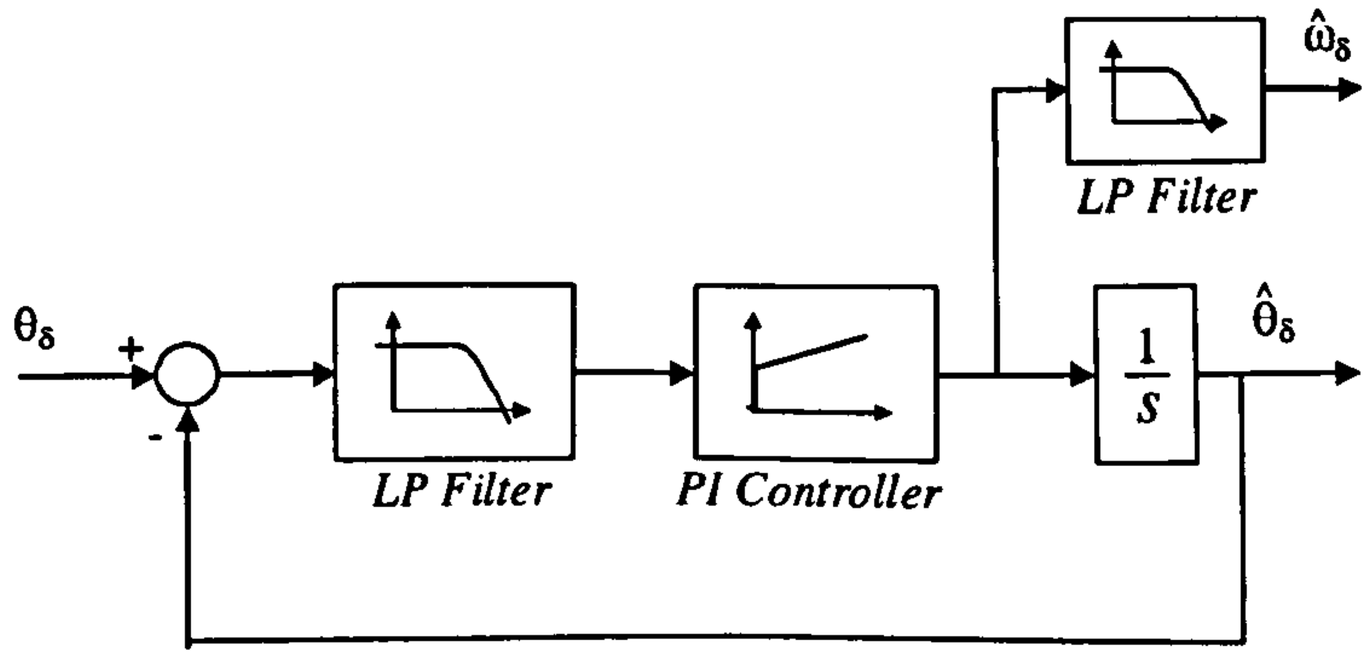

Figure 6.1: Linear approximation of the saliency tracking-loop.

Using this linear model the PI controller has been set to $G_c(s) = \frac{300 \cdot (s+150)}{s}$, achieving a nominal bandwidth of approximately 75 Hz, which is sufficiently high for the design bandwidth of the position loop. The speed feedback signal is obtained from the same observer by filtering the output of the PI controller. This signal is inherently noisy and therefore the cut-off frequency of the low pass filter in the speed signal path has to be set to a relatively low value. The filter pole is chosen such that it cancels the PI zero, i.e. $H_{LP}(s) = \frac{150}{s+150}$ obtaining a nominal bandwidth of 34 Hz. This acts as a delay in the speed feedback path.

The estimation bandwidth obtained in the angle and speed estimation are lower than those obtained for the α-β compensated injection method which are 200 Hz and 60 Hz respectively. Hence when the same position and speed loop controllers are used, the *d-axis* injection method is expected to yield poorer dynamics for the close loop sensorless operation. It will be shown that this is certainly true for the disturbance rejection.

6.2.2 Phase Correction

The *d-axis* injection method determines saliency position rather than actual rotor position. In this section a commissioning procedure is use to determine the phase relation as previously done for the α-β injection method. Ideally a similar curve to that of Fig. 5.19 should be obtained, i.e. the *hf* saliency should show an orientation with the stator flux position. It is noted that the for the α-β method the constant offset due to the shift in the *hf* currents produced by the current controllers, and theoretically

estimated to be –13.8° elec., is not expected in the resulting phase shift for the *d-axis* injection method. This is because the different signal processing in the *d-axis* injection strategy is such that the shift in the currents affects only the amplitude of the error signal driving the tracking algorithm, not the phase of the position estimation.

The commissioning process consists in the sensored operation of the drive in steady state at a speed of 60 rpm and at different load levels corresponding to i_q from –10 A to 10 A. The saliency is measured, each test consisting of 6 seconds of steady state operation. The average phase difference between the estimated saliency position and the measured rotor position is obtained for each operation point. The process is repeated for positive and negatives speeds and the average result is shown in Fig. 6.2 together with the theoretical stator flux position as calculated form:

$$\theta_s = \arctan\left(\frac{i_q \hat{L}_q}{\hat{\psi}_m}\right) \tag{6.2}$$

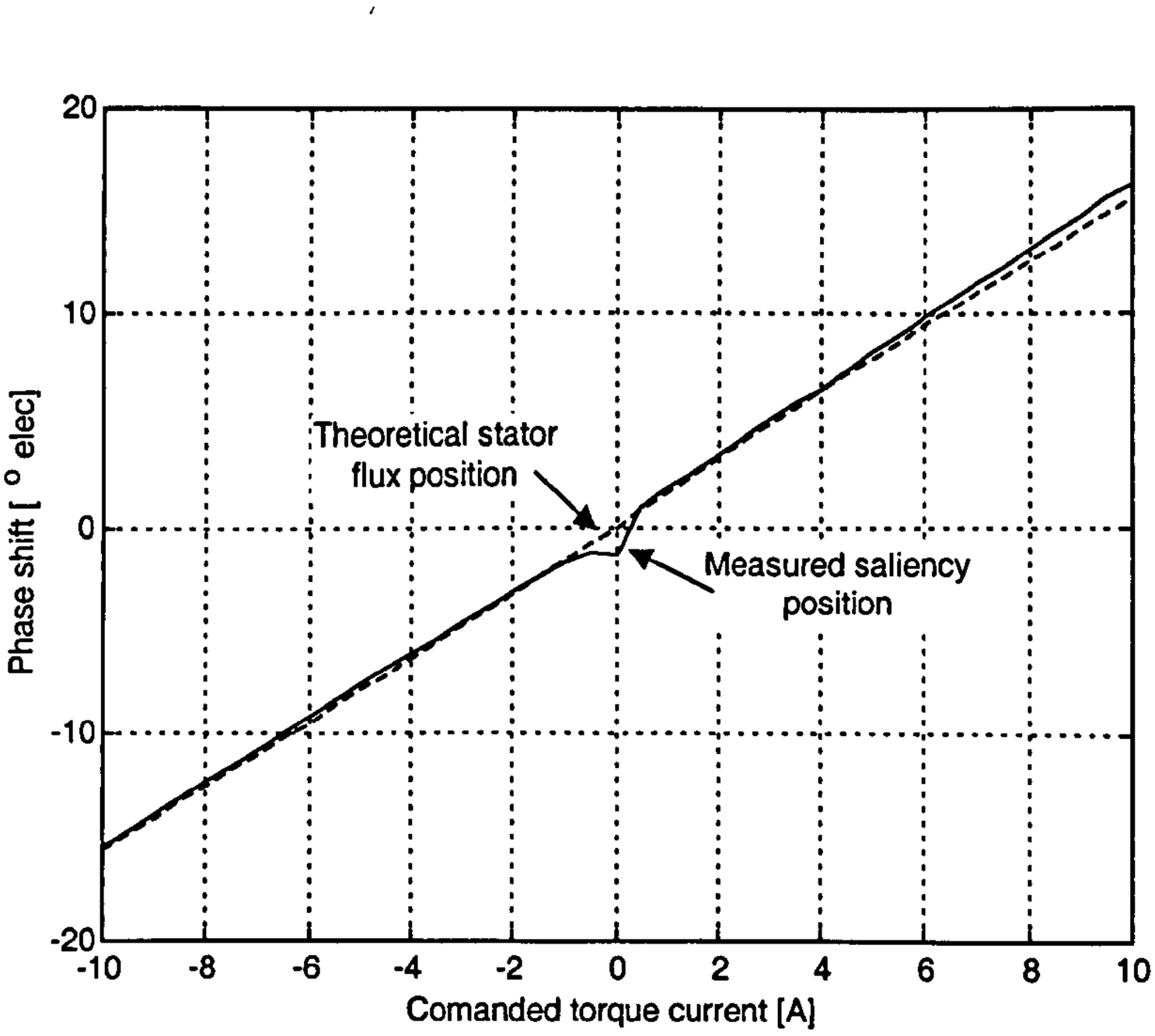

Figure 6.2: Phase shift between rotor and estimated saliency position for *d-axis* injection method.

In Fig. 6.2 it can be noticed that except at low loads the saliency position matches the calculated position of the stator flux. Because the band-pass filtering for separation of

the fundamental and *hf* currents is performed synchronously in the *d-q* frame, this curve is not influence by speed. At very low loads the estimated saliency position departs form the theoretical flux position; furthermore at low loads the estimation was found to be inconsistent, yielding different values each time the commissioning process was performed. This behaviour of consistency at higher loads and larger random errors at very low loads can be explained from the tracking nature of the method and the use of *q-axis hf* current for the saliency detection. Under sufficient load the *hf* current is always superimposed onto a constant value of i_q current and therefore no zero crossings of the resultant current occur in the measuring γ^e-axis. This gives the method an inherent immunity to the effects to the inverter non-linearities and allows for successful tracking of the maximum saliency which is dominated by stator saturation. Under very low loads the *hf* current constantly crosses zero and therefore the saliency information is affected by distortion produced by the inverter non-linearities, yielding noisier estimation. If the low load portion of the curve in is omitted, Fig. 6.2 provides strong evidence that the saliency orientation of the motor used in this work is dominated by stator flux.

In order to perform the phase compensation, the values obtained for low load levels are discarded and the table is completed by interpolating from the sections of the curve obtained for larger load levels. With the commissioning of this phase shift table the *d*-axis injection method is complete and can be used for sensorless vector control of the PM synchronous motor. Equally, as Fig.6.2 shows, the compensation could have been implemented using (6.2). This is advantageous for an industrial implementation, because it does not require the commissioning process, and only estimations of the magnitude of the magnets flux $\hat{\psi}_m$ and machine inductance $\hat{L}_q$ are necessary.

6.3 Comparative Experimental Results

In this section, experimental results for both techniques, the α-β frame rotating injection including compensation, and the *d-axis* pulsating injection are presented. With the exception of the hardware band-pass filters, which are not used in the *d-axis* injection method, the hardware and software used for the implementation of both techniques, including the speed and position controller, are the same and are described in detail in Section 4.3.3. It is worth mentioning that in the α-β injection the speed estimate $\hat{\omega}_r$ is obtained by derivation of the position estimate $\hat{\theta}_r$ and a first order filter with cut-off frequency of 60 Hz is applied to suppress noise. In the *d-axis* injection method on the other hand, the $\hat{\omega}_r$ is obtained directly from the tracking loop and, as discussed in section 6.2.1, this estimate has a bandwidth of 34 Hz. The control structure, for both sensorless methods, is depicted in Fig. 6.3.

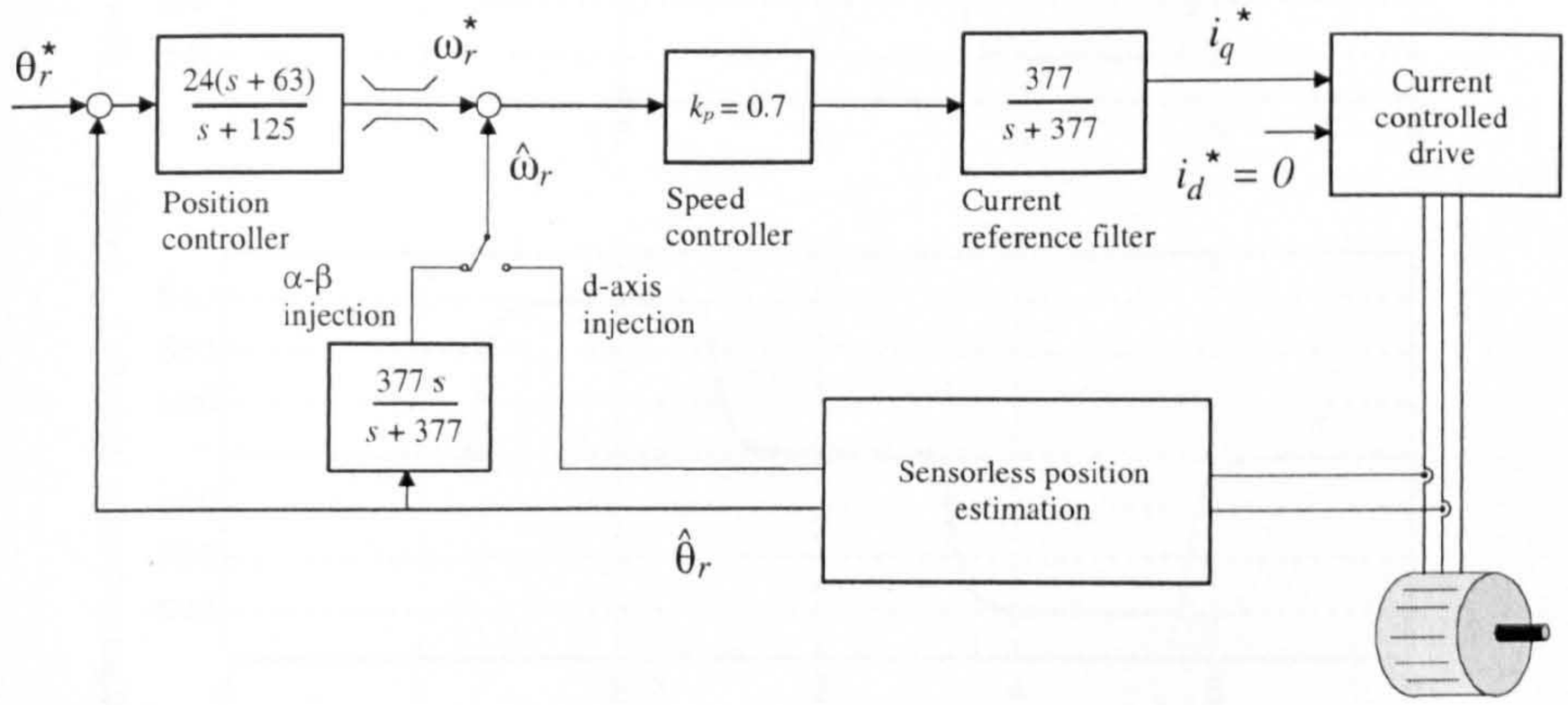

Figure 6.3: Control structure for sensorless operation.

6.3.1 Step Changes in Position Demand

A series of positive and negative steps in position demand corresponding to half a mechanical turn, i.e. 540° electrical, are applied to test the dynamic performance of the control loops including the position estimation algorithm. The test is repeated under load values of 0, 50 and 100% to show the viability of sensorless position control at any load and to assess the effect of load in the quality of the estimation.

i. Zero load

The result for sensorless position with α-β rotating voltage injection under zero load is shown in Fig. 6.4. The actual rotor position response correspond to a dominant real pole (as designed) and the estimated rotor position shows a good correspondence with the measured value. The estimation error, calculated as the difference between the measured rotor angle θ_r and the estimated value $\hat{\theta}_r$ is shown in Fig. 6.5. Under steady state this error presents no significant offset and a ripples that is bounded to ±5° electrical (or ±1.7° mech.). However, during transients the error increases exceeding 14° electrical. The reasons for this increase of the error during transient is discussed later in this section.

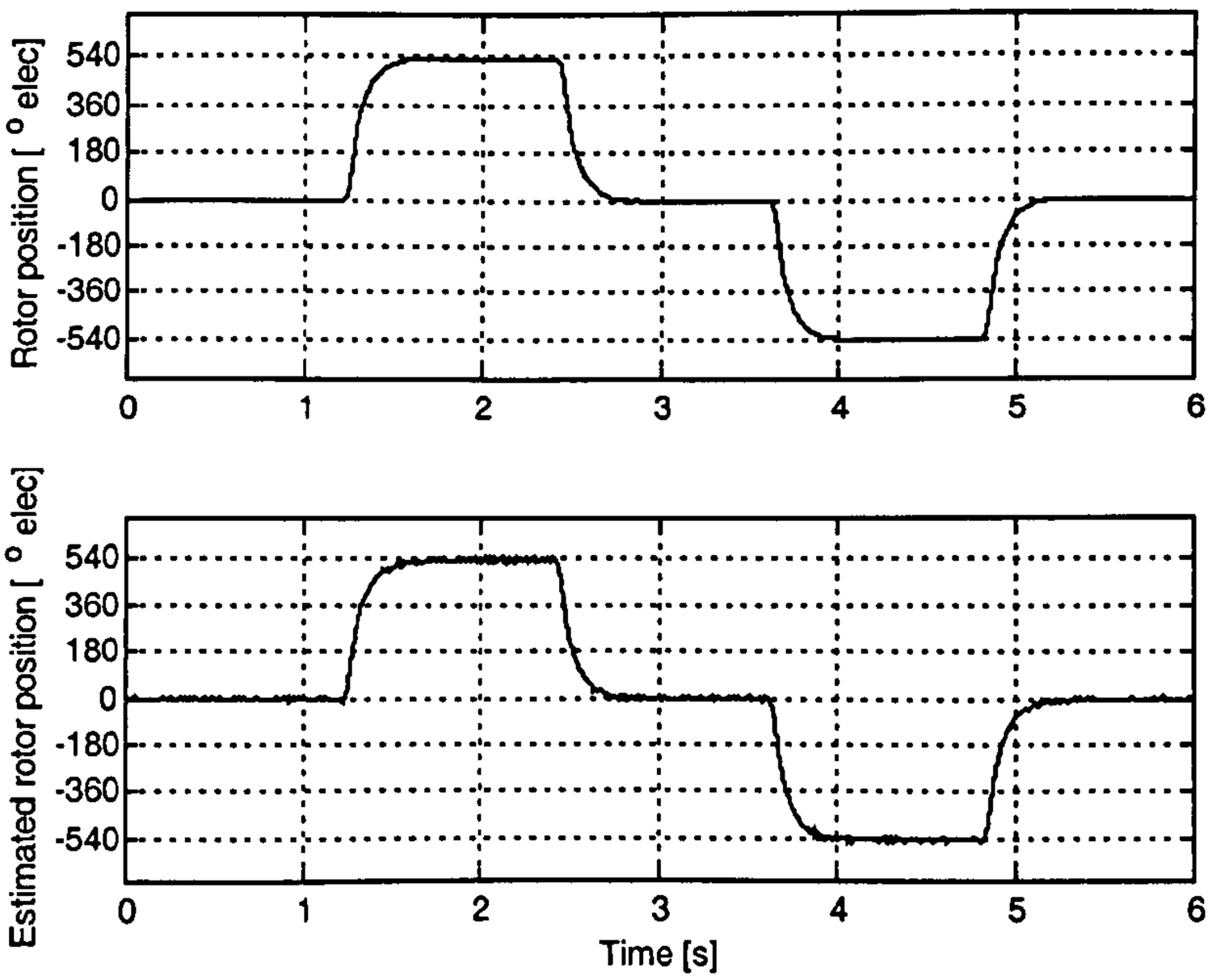

Figure 6.4: α-β rotating injection sensorless position control at no load; *top*: measured rotor position, *bottom*: estimated rotor position.

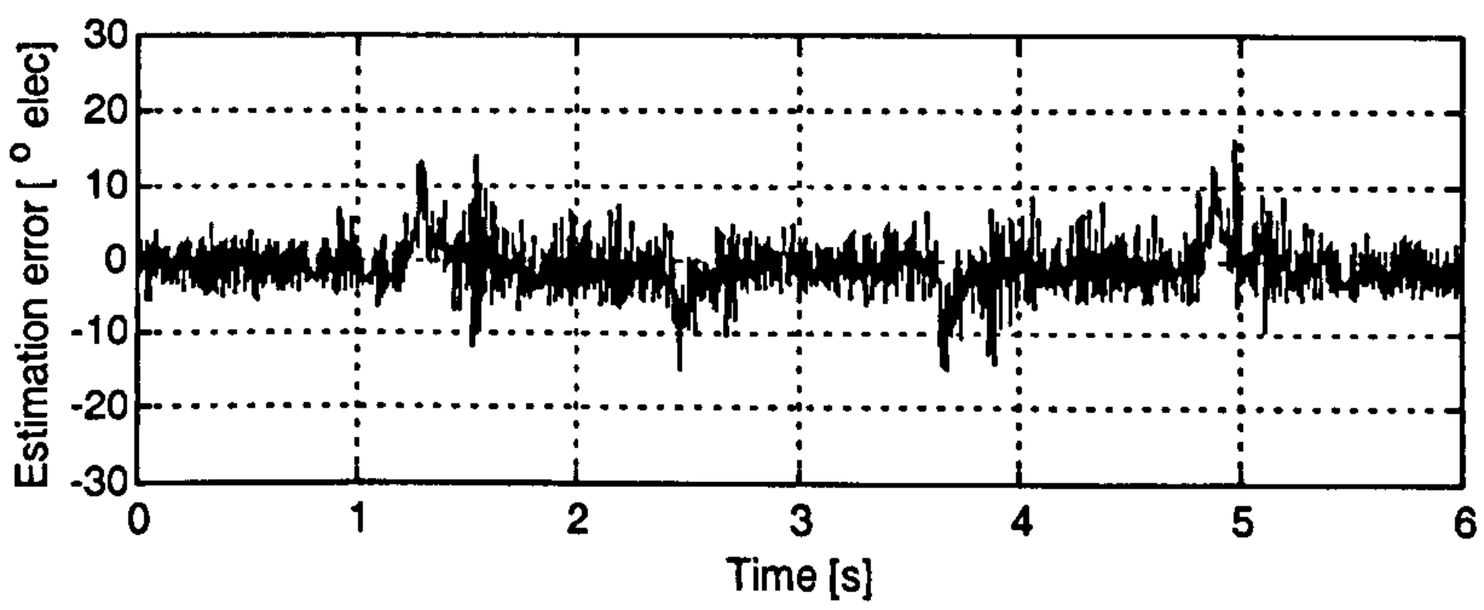

Figure 6.5: α-β rotating injection rotor angle estimation error at no load.

The results for the *d-axis* injection are shown in Fig. 6.6 and Fig. 6.7. The position response shows similar dynamics although some disturbance is observable during position settling. This disturbance may be produced by the cogging of the machine in which rotor the rotor magnets try to align with the rotor teeth in the position of minimum reluctance. This cogging is a machine characteristic and is present regardless of the sensorless technique applied for the rotor position detection. However, due to the lower bandwidth of the *d-axis* injection method it would have a more significant impact on the position response waveforms for this method.

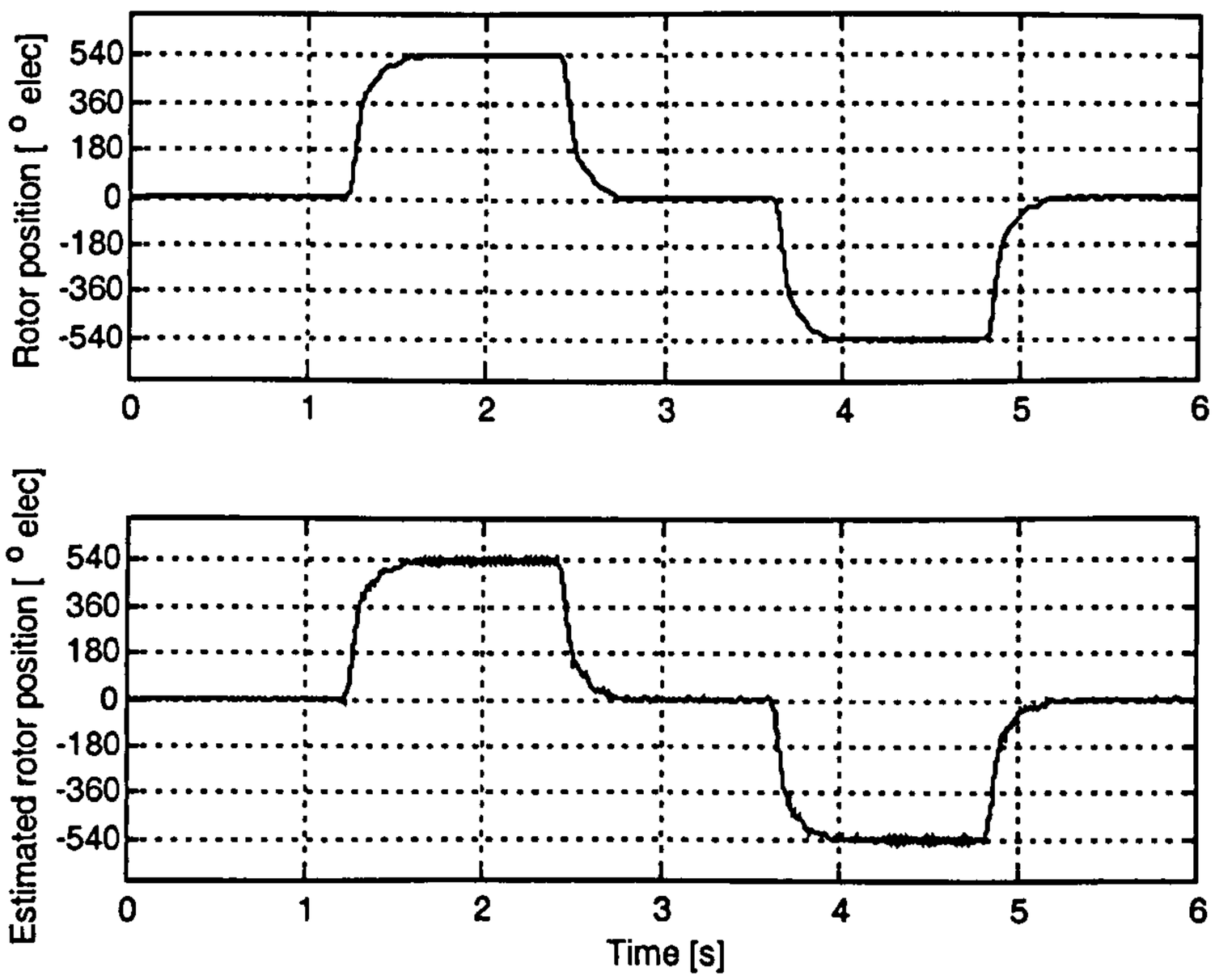

Figure 6.6: *d-axis* pulsating injection sensorless position control at no load; *top*: measured rotor position, *bottom*: estimated rotor position.

The amplitude of the ripples on the estimation error, shown in Fig. 6.7, presents a dependency on the settled position (probably due to the cogging), but in general is limited to $\pm 13^{\circ}$ electrical. During the transient a narrow increase in error is observable, reaching to 19° electrical on amplitude.

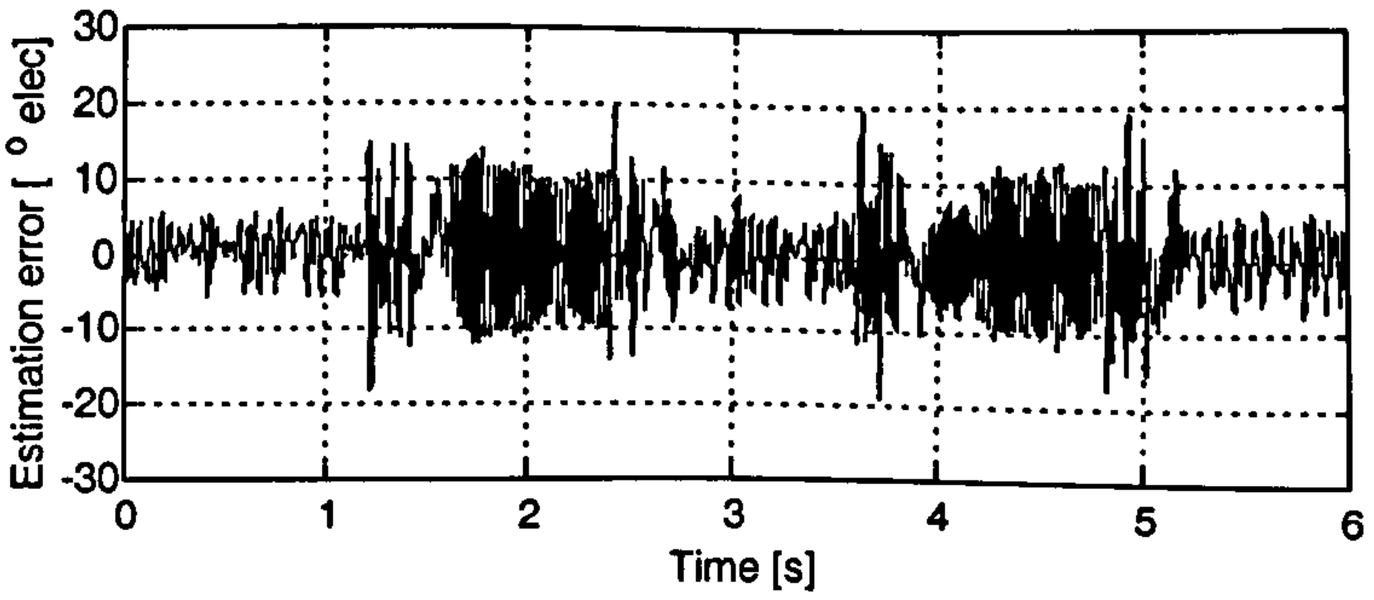

Figure 6.7: *d-axis* pulsating injection rotor angle estimation error at no load.

ii. 50 % load

The application of the load is by means of a constant torque reference to the loading induction machine drive. The position results for the α-β injection method are presented in Fig. 6.8. There is a large error between the reference, that starts at 0 and steps to 540° and –540° electrical, and both the measured and estimated rotor position. This error is expected and is produced by the use of only a proportional controller in the speed loop; this results in the need for steady state position error to compensate for the load torque. The selected controller design arose from the need for a low cut-off frequency low-pass filter in the torque demand which increases the order of the system and makes the design of a PI controller for this loop difficult. See sections 4.3.2 and 4.3.3 for a more detailed discussion. Nevertheless the drive is able to hold the load and perform the position steps relative to the original steady state position.

The estimation error in Fig. 6.9, shows very good performance, with small ripples around zero of less than 2° electrical of amplitude (0.67° mech.) in steady state operation. During transients the average value of the estimation error deviates form zero, to values of approximately 5° for the positive position steps and –8° for the negative ones. The ripples around this average value also increase during the transient. During the position settling the ripples on the error shows a characteristic increase in the amplitude (labelled *a b c* and *d*) sometimes reaching up 7° electrical approximately.

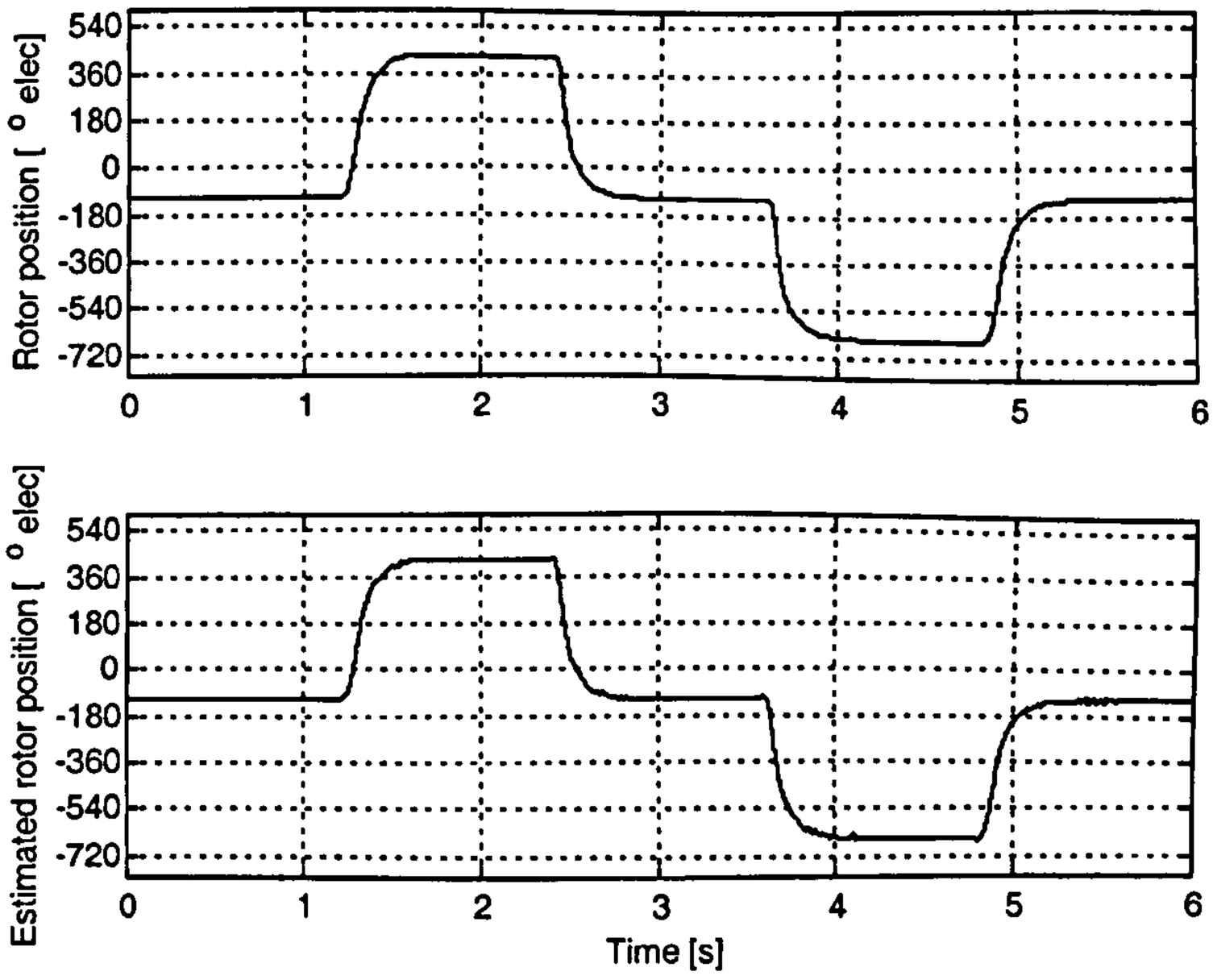

Figure 6.8: α-β rotating injection sensorless position control at 50% load; *top*: measured rotor position, *bottom*: estimated rotor position.

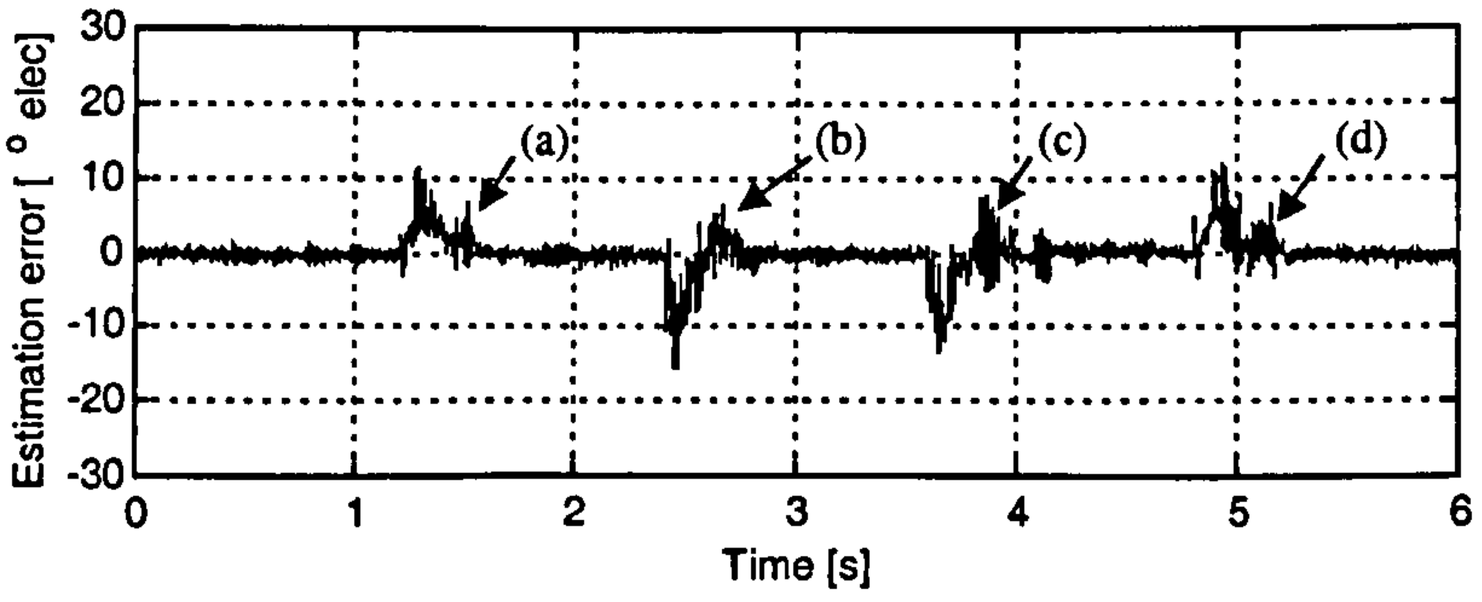

Figure 6.9: α-β rotating injection rotor angle estimation error at 50% load.

The position response for the *d-axis* injection under 50% load is shown in Fig. 6.10, it present a poorer position holding than that of α-β injection, the disturbance having a greater effect on the position response.

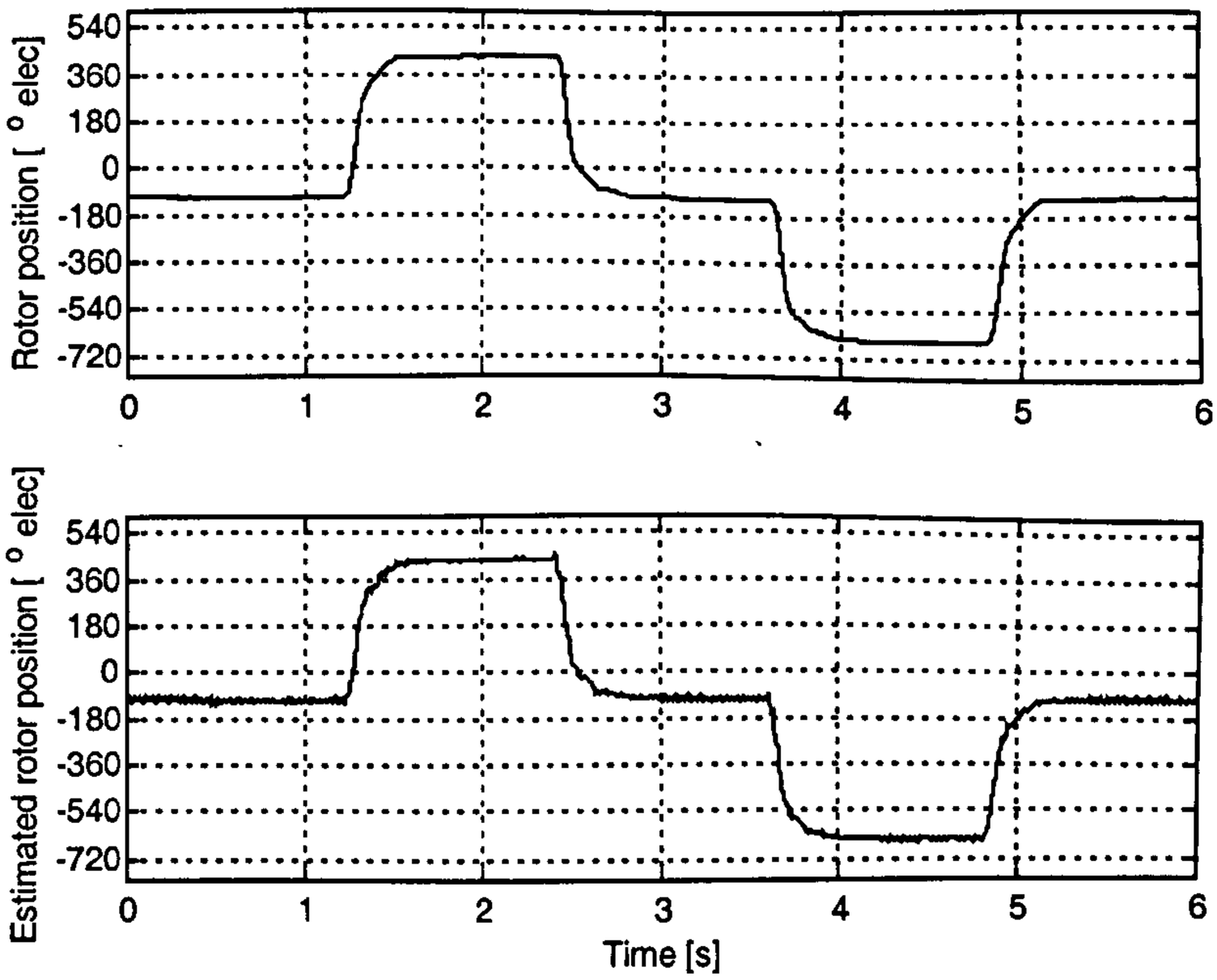

Figure 6.10: *d-axis* pulsating injection sensorless position control at 50% load; *top*: measured rotor position, *bottom*: estimated rotor position.

The estimation error shown in Fig. 6.11, again shows a dependency on the position at which the rotor is settled, however it is generally bounded by ±14° electrical. It is also noted that the error shows some constant offset whose magnitude also depends on the settling position, with a maximum measured value of 4° electrical. During the fast acceleration of the negative transients the error increases significantly to values above 20° elec.

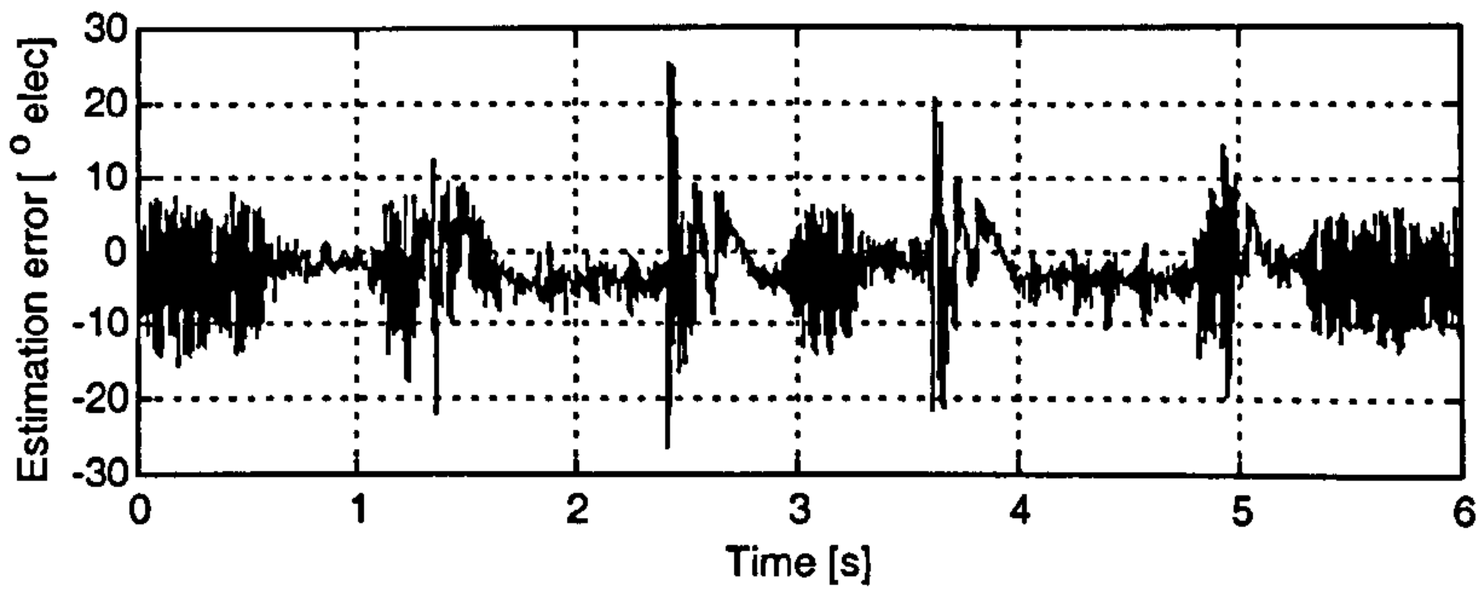

Figure 6.11: *d-axis* pulsating injection rotor angle estimation error at 50% load.

iii. 100% load

Operation under full load is possible under both sensorless schemes. As expected, the steady state position error relative to the reference demand is increased. The rotor position step response using α-β rotating injection is shown in Fig. 6.12, the result

exhibiting good position holding. The maximum amplitude of the estimation error in Fig. 6.13 is limited to within 2^{o} electrical under steady state. The offset produced in the estimation error due to the increase in speed during transients is clearly noticeable.

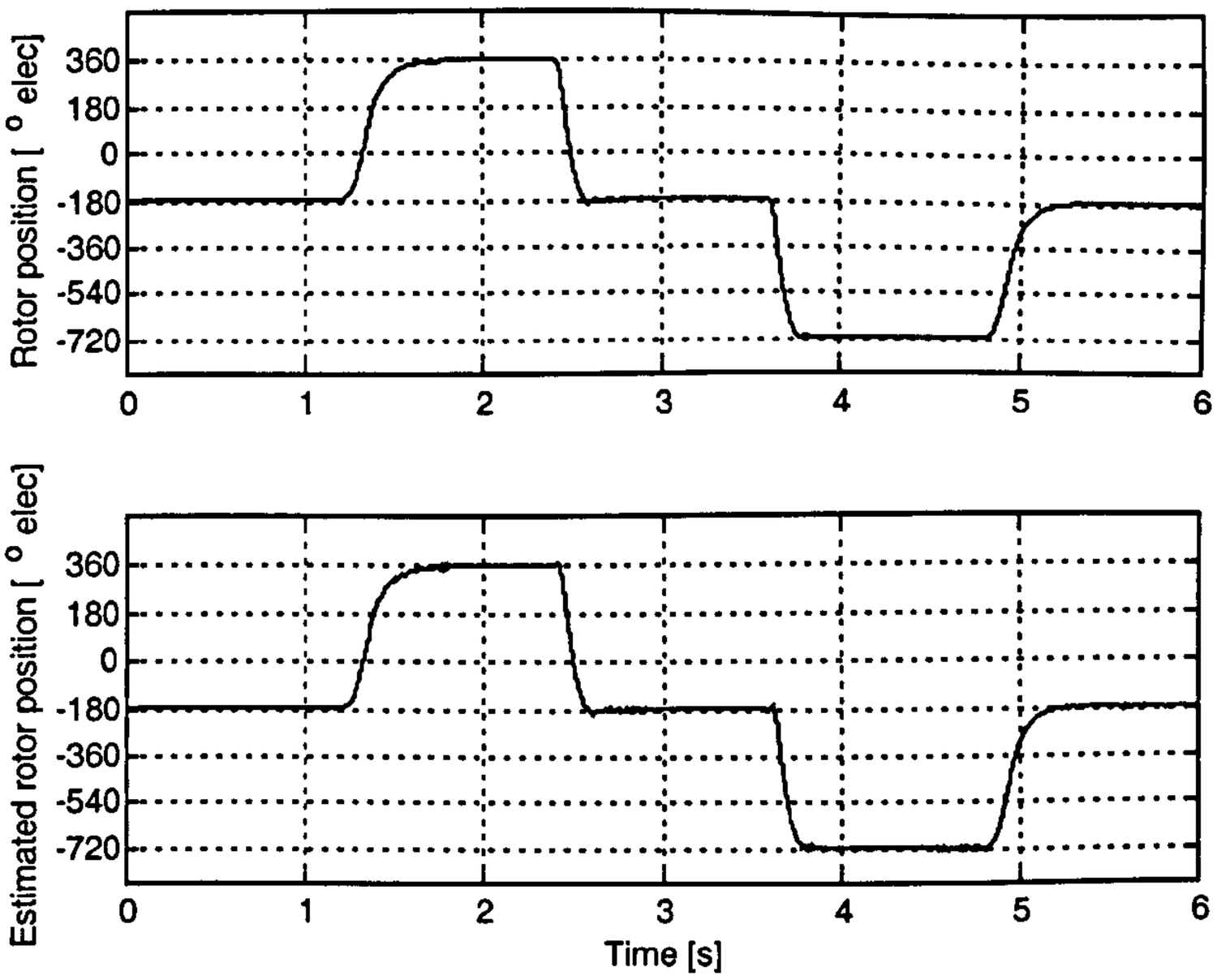

Figure 6.12: α-β rotating injection sensorless position control at 100% load; *top*: measured rotor position, *bottom*: estimated rotor position.

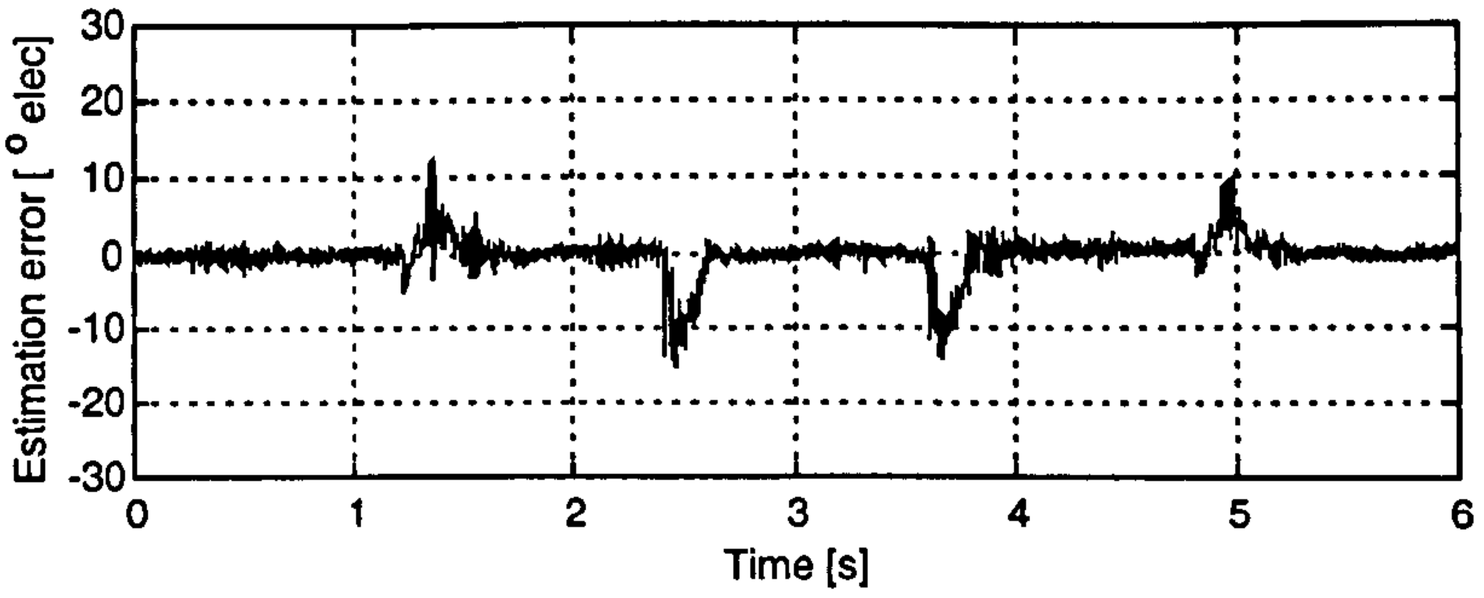

Figure 6.13: α-β rotating injection rotor angle estimation error at 100% load.

The position control results using *d-axis* injection are shown in Fig. 6.14. This figure shows a significant deterioration in position holding with respect to the α-β injection method, with oscillations around the steady state position.

The estimation error is shown in Fig. 6.15 and again shows large errors under steady state position holding with amplitudes generally bounded by ±10° electrical but with peaks reaching up to 16° electrical. There is also present the characteristic larger error during fast accelerations.

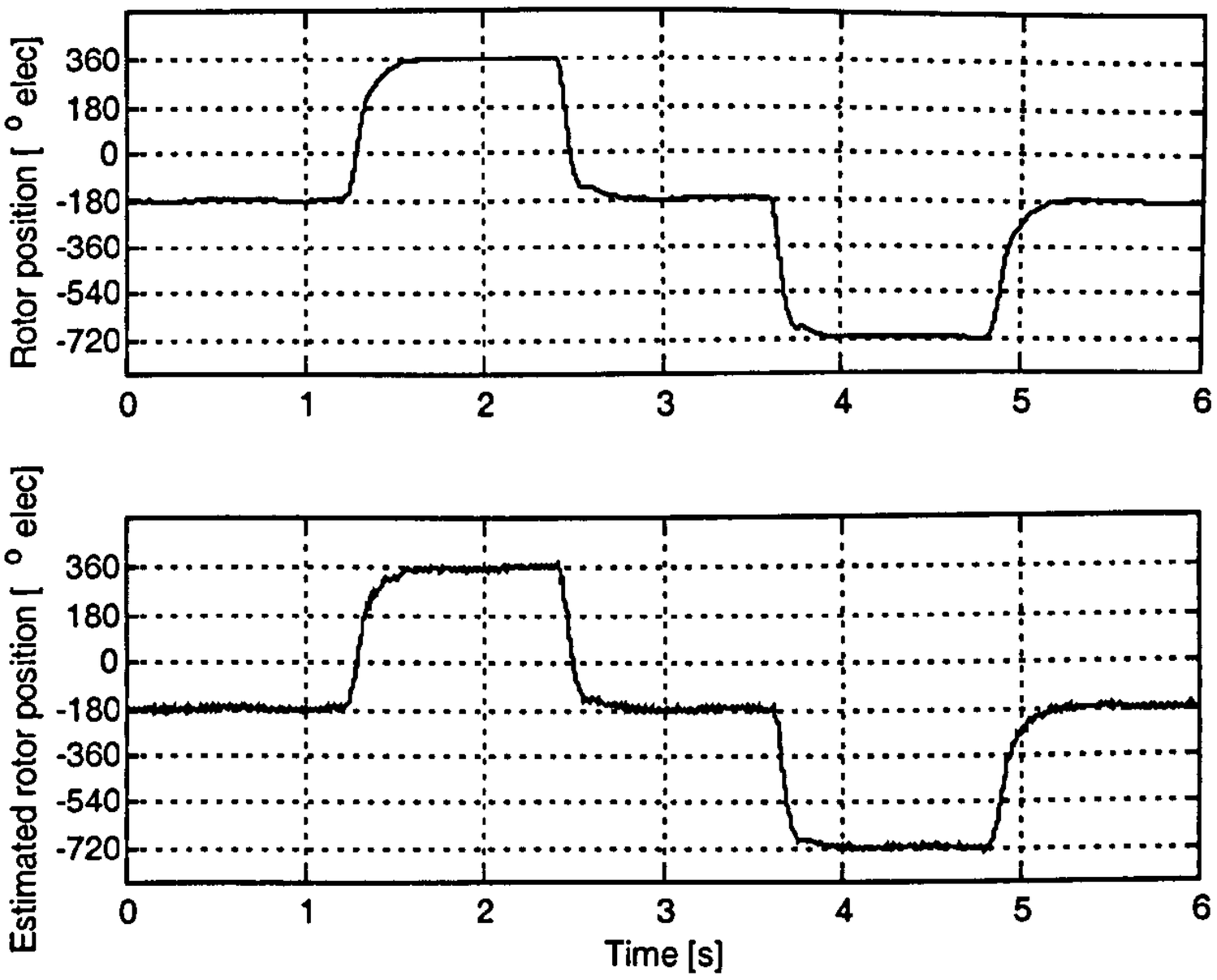

Figure 6.14: *d-axis* pulsating injection sensorless position control at 100% load; *top*: measured rotor position, *bottom*: estimated rotor position.

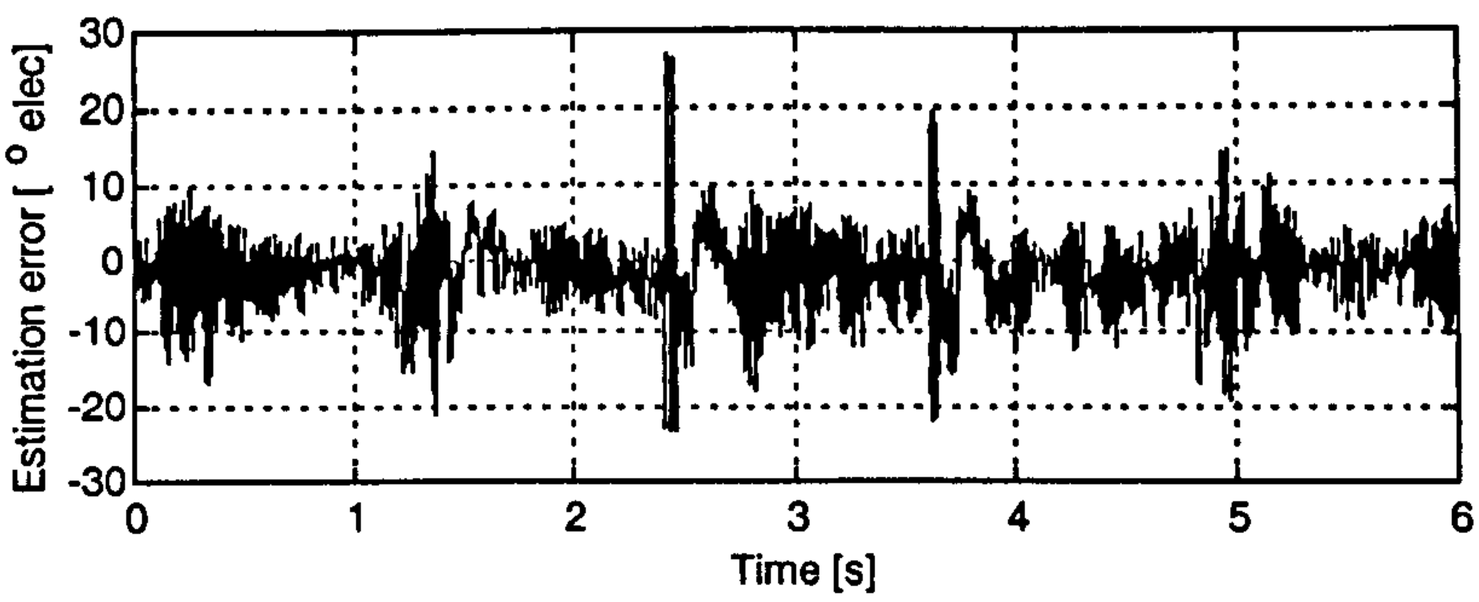

Figure 6.15: *d-axis* pulsating injection rotor angle estimation error at 100% load.

The presented results show that sensorless position control using saturation induced saliency tracking in a surface mounted PM machine is achievable even under loaded conditions, and has been demonstrated up to 100% nominal load. Therefore, the viability of the two voltage injection methods for this purpose has been proven.

From the comparison of the results for both methods several conclusions can be reached. Firstly it can be seen that, in general terms, the α-β injection method (including SMP compensation) yields smaller steady state estimation errors than that of the *d-axis* injection techniques. The performance of the α-β injection position estimation under significant load is very good with steady state error within 2° electrical (0.67° mechanical). Nevertheless, the remains of dead-time distortion due to incomplete compensation, means that at very low loads the accuracy of the estimation degrades to about 5° electrical. Even so, this still significantly better than the errors for the *d-axis* injection method, which were measured to be higher than 10° electrical for all loading conditions. The *d-axis* injection method present a lower bandwidth in the estimation of position and specially speed (75Hz and 34Hz respectively, see section 6.2.1) than that of the α-β injection. This lower bandwidth results in worse dynamic performance that is noticeable in the larger effect of disturbances like cogging and load toque variations, in the position regulation.

A general deterioration of the accuracy of the angle estimation during transients was seen to occur. In the case of the α-β rotating injection this error is most evident in Fig. 6.9 and Fig 6.13. The main contributor to this is the phase shift produced by the hardware band-pass filters on the currents due to the shift in the frequency of the position harmonics with rotor speed, see Appendix B. The offset in estimated rotor position angle also produces an offset in the addressing of the SMP table, which deteriorates the compensation leading to increased noise in the angle estimation. Although compensation of this band-pass filter phase shift is theoretically possible (because the phase shift characteristic of the filter is known from its Bode plots), the estimated speed signal is too noisy for this purpose. The phase shifts introduced by the band-pass filters establish a limit on the speed at which this injection technique is applicable. In the *d-axis* injection on the other hand, the filtering is performed synchronously with the rotor speed and therefore the speed does not have such a negative impact in the angle estimation. The structure of the tracking loop has a double integration in its open loop transfer function, and this allows the tracking of a constant speed without stationary error. Nevertheless this structure is not able to track position or speed accurately under acceleration. This explains the sharp increase of estimation error during the transients, especially when the load assists the accelerating

torque (causing faster accelerations as in Fig. 6.11 and Fig. 6.15). Increasing the bandwidth of the tracking loop could ease this phenomenon, but this would results in noisier steady state estimates.

6.3.2 Position Holding Under Load

In previous results, the error was shown as $\theta_r - \hat{\theta}_r$. One can also look at the motor position θ_r itself. When this is done it is apparent that there is an external load torque variation due to the control of the load induction machine, producing low frequency oscillation in the rotor position. High bandwidth controllers would reject the disturbances thus minimising the amplitude of this oscillations. Nevertheless, the controller bandwidth has been limited by the inclusion of a filter in the i_q demand. Therefore, if the same control design and i_q filter is used, oscillations are expected even under sensored operation. This is indeed the case, as shown in Fig. 6.16. Also, the use of a proportional speed controller results in a steady-state rotor position offset. This is also evident under sensorless conditions as seen in Fig. 6.17. The steady state error, given by $\overline{\theta}_r$ (reference is set to zero), is -177.6° elec. at full load.

The bandwidth restrictions on the rotor position estimation has a detrimental effect on the disturbance rejection capability of the loop. To compare the impact of the load disturbances on each strategy, measurement of the rotor position for sensorless operation, under full load for both techniques have being carried out. The results are shown in Fig. 6.17, the offset error of –177.6° having been removed. The oscillations produced by the load torque disturbance in sensorless mode when using the α-β injection method have an amplitude of 2° electrical. The use of *d-axis* injection method on the other hand yields oscillations of 5° electrical. The comparison of the relative amplitudes of this oscillations (0.7 °, 2° and 5° electrical for sensored and sensorless with α-β injection and *d-axis* injection respectively), gives a good indication of the bandwidth of the disturbance response of the three systems.

Finally, it is noted that the oscillation in Fig. 6.16 and Fig. 6.17 are at approximately 1.3 Hz. This the excitation frequency of the 2-pole load induction machine. The phenomenon of excitation frequency oscillation in vector controlled drives is well known and arises from offset and scaling errors in the current measurement signals at the A/D converter (the DC errors translating into excitation frequency by the coordinate transformations).

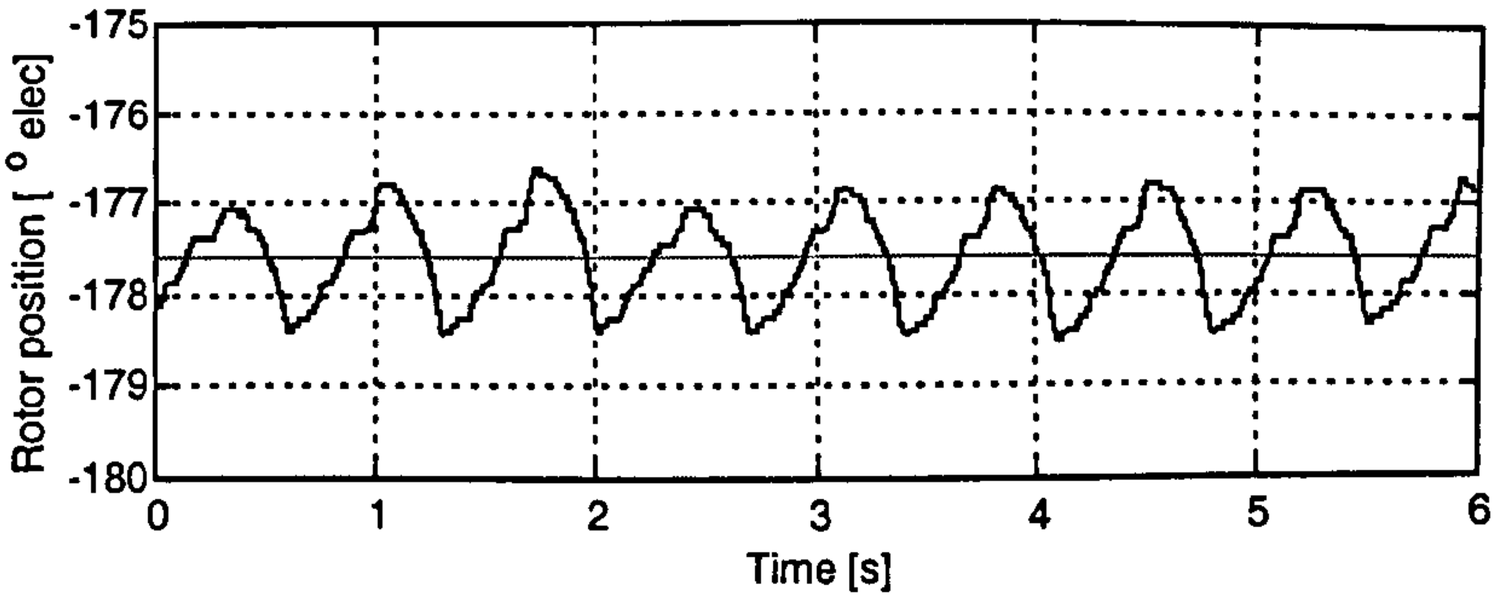

Figure 6.16: Sensored rotor position holding ($\theta_r^* = 0$) at 100% load.
Position θ_r and $\overline{\theta}_r = 177.6$.

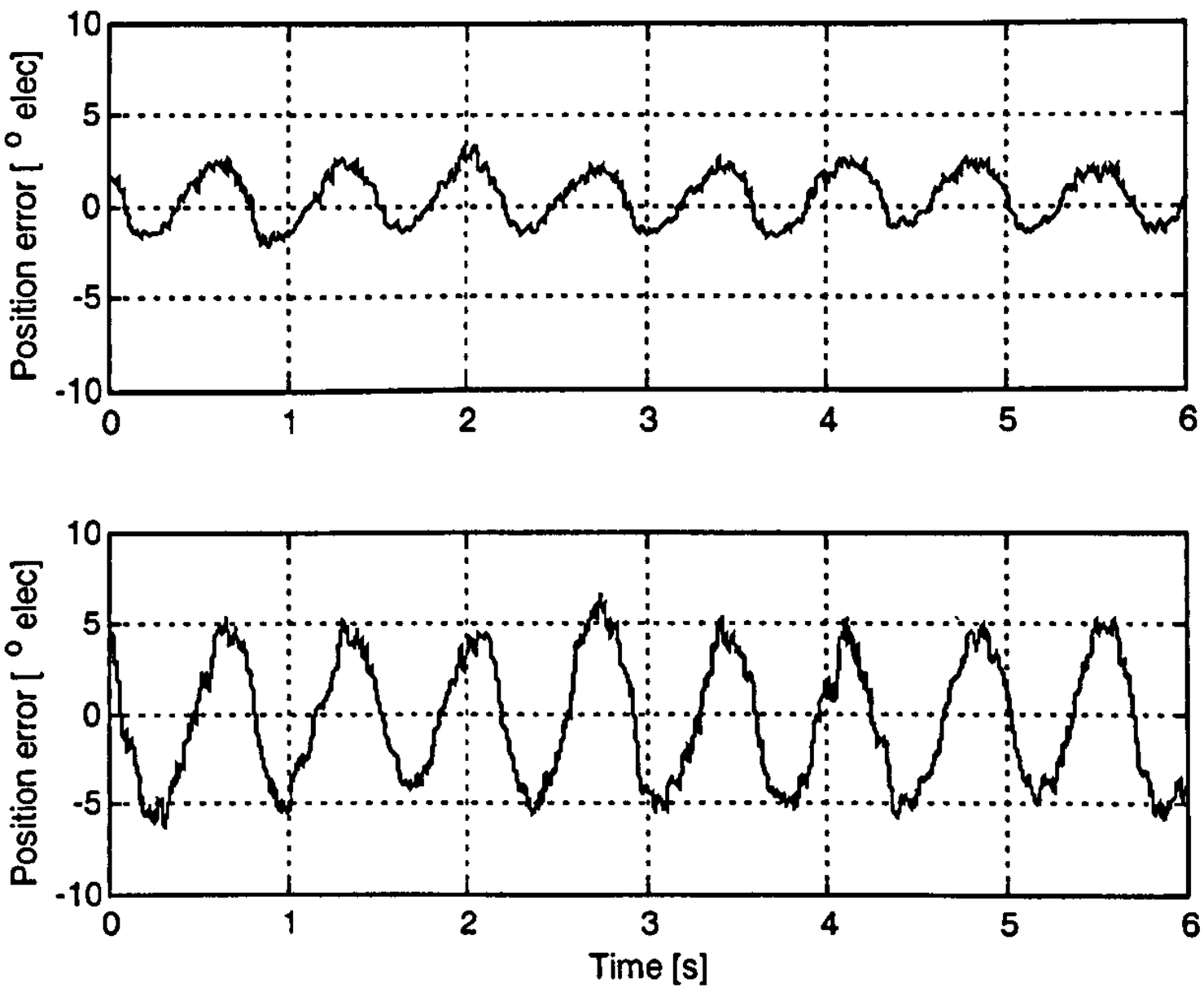

Figure 6.17: Sensorless rotor position error ($\theta_r - \overline{\theta}_r$) at 100% load.
a) α-β injection. b) *d-axis* injection.

6.3.3 Load Impact at Zero Speed

The response of the sensorless position control loop to step changes in load have been tested. The load step is achieved by a change in the torque reference of the load induction machine from 0 to 60% nominal torque. The position and speed response of the loop using the α-β rotating injection and *d-axis* pulsating injection are shown in Fig. 6.18 and 6.19 respectively. Both systems respond to this transient disturbance with a maximum transient speed of –55 rpm approximately. It is difficult to evaluate the speed of the response of both systems due to the influence of disturbances, especially in the *d-axis* injection method.

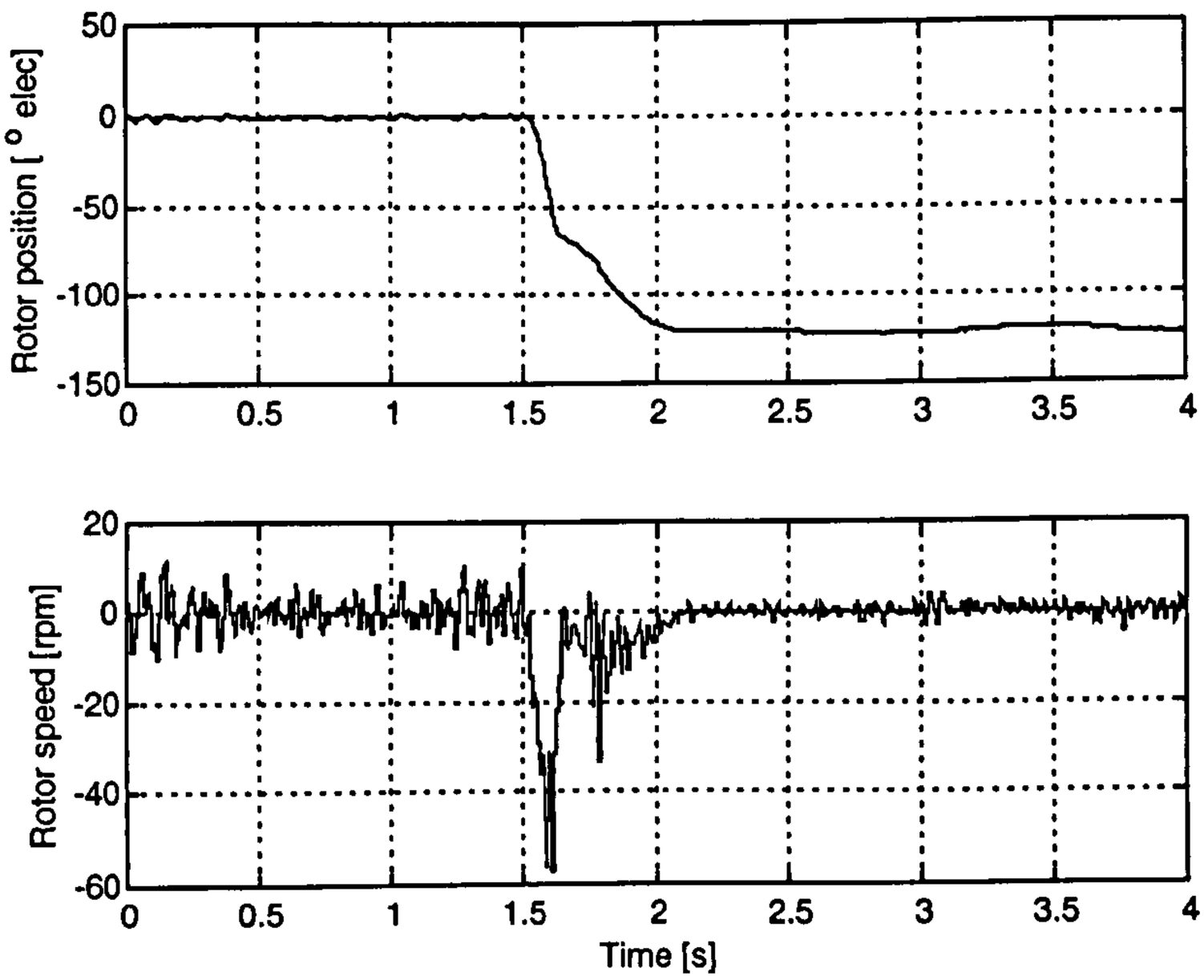

Figure 6.18: 60% load impact under α-β injection sensorless operation; *top*: position response, *bottom*: speed response.

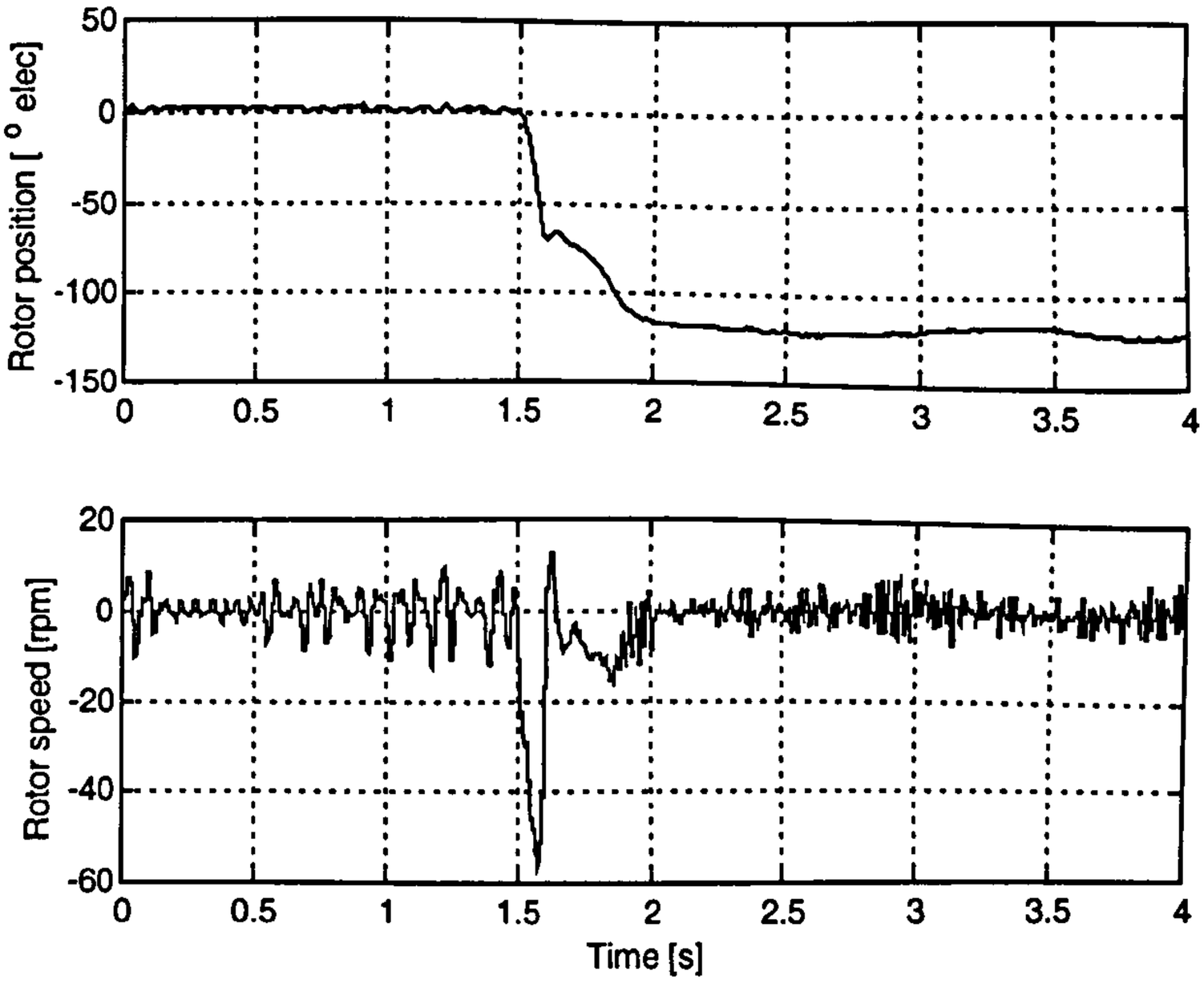

Figure 6.19: 60% load impact under *d-axis* injection sensorless operation; *top*: position response, *bottom*: speed response.

6.3.4 Low Speed Reversal

The ability of sensorless control at low speeds is assessed by speed reversals from 30 to –30 rpm, i.e. 1.5 Hz of fundamental excitation. To avoid the steady state speed error due to the use of a speed proportional controller, a position ramp reference is given rather than a constant speed reference. This test is repeated for zero and full load.

i. Zero load

The speed and position response when no external load is applied are shown in Fig. 6.20 and 6.21 for the sensorless operation using the α-β injection and the *d-axis* injection respectively. The speed response of the α-β injection shows better speed holding, i.e. disturbance rejection than that of the *d-axis* injection where the ripple in the speed and position is evident, as seen in Fig. 6.21. The $6f_e$ periodicity of this disturbance suggest that it may be produced by the cogging of the machine or to the non-linearities of the inverter manifested during the zero crossing of the fundamental currents. The better performance of the α-β injection method may be explained by the higher bandwidth of its position estimation that would account for a better rejection of

the cogging effect and for the use of compensation of the inverter non-linearities by means of dead-time compensation and SMP tables.

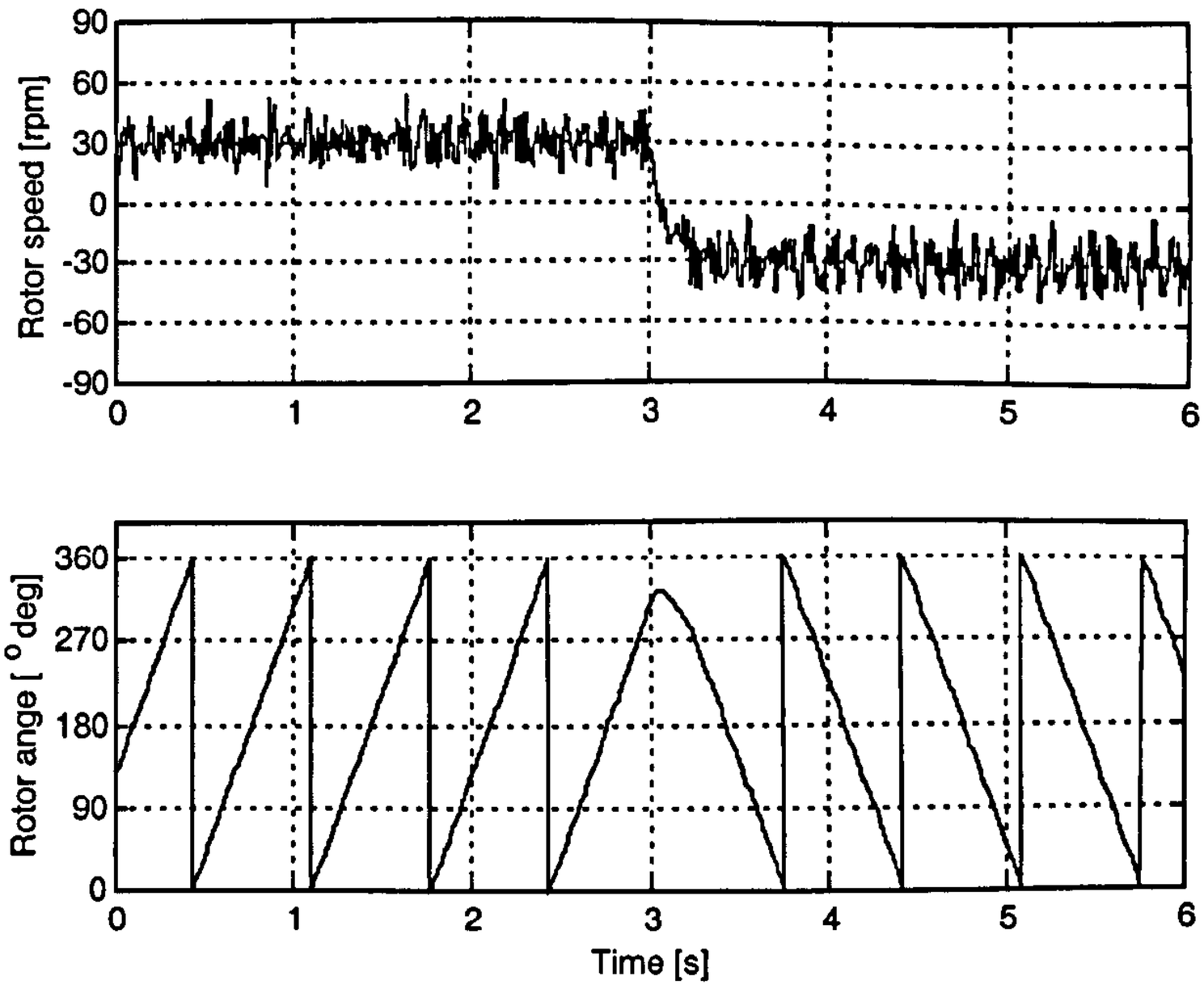

Figure 6.20: No load sensorless speed reversal at 30 rpm using α-β injection; *top*: rotor speed, *bottom*: rotor position.

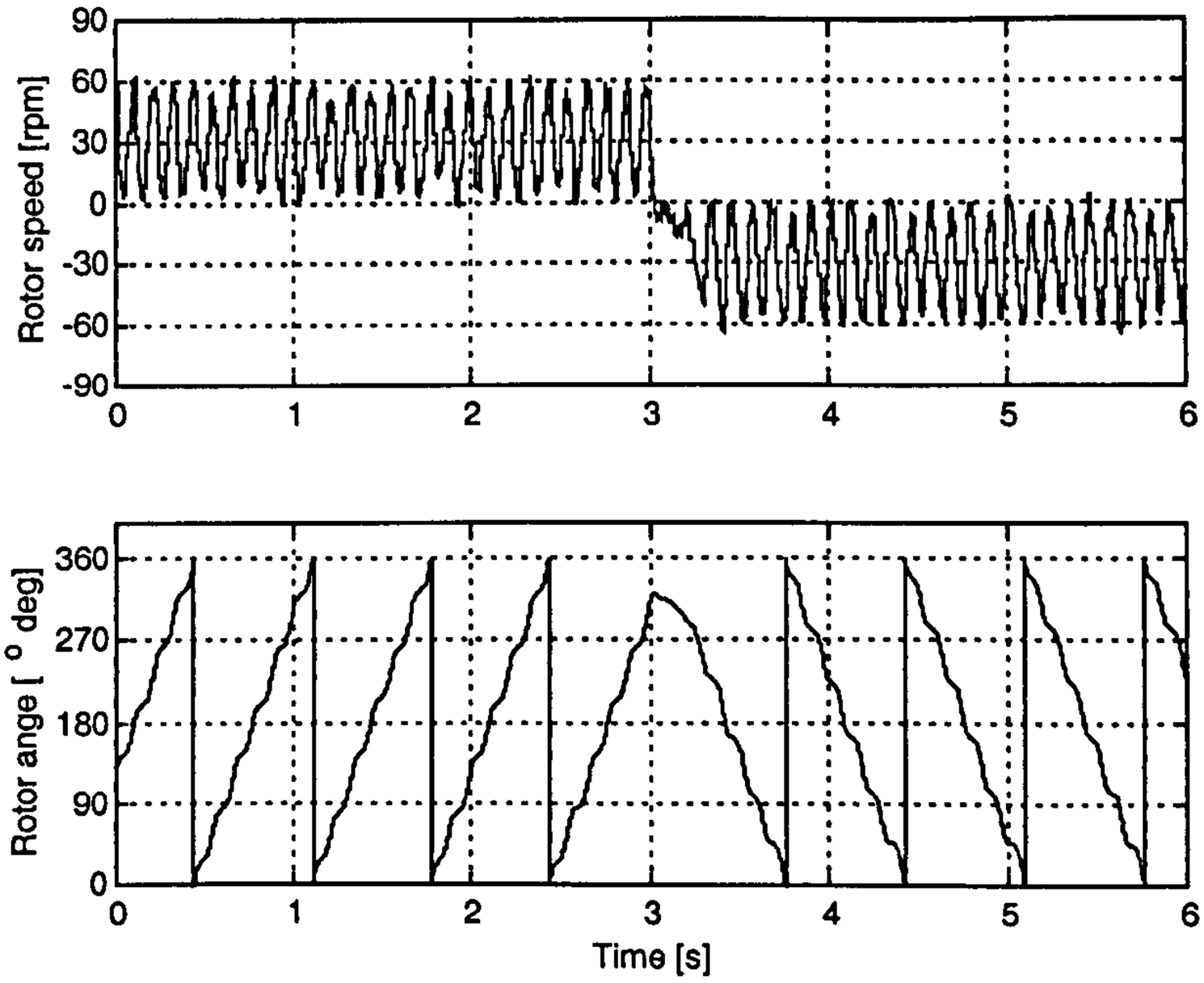

Figure 6.21: No load sensorless speed reversal at 30 rpm using *d-axis* injection; *top*: rotor speed, *bottom*: rotor position.

ii. 100% load

The results under full nominal load operation are shown in Fig. 6.22 and Fig. 6.23. Both sensorless implementations are able to control low speed under this loaded condition. The loaded operation in the α-β injection results in a reduction in the speed noise. The application of load does not change significantly the magnitude of the effect of the $6f_e$ disturbance in the *d*-axis injection sensorless system, remaining significantly larger than that in the α-β injection sensorless operation.

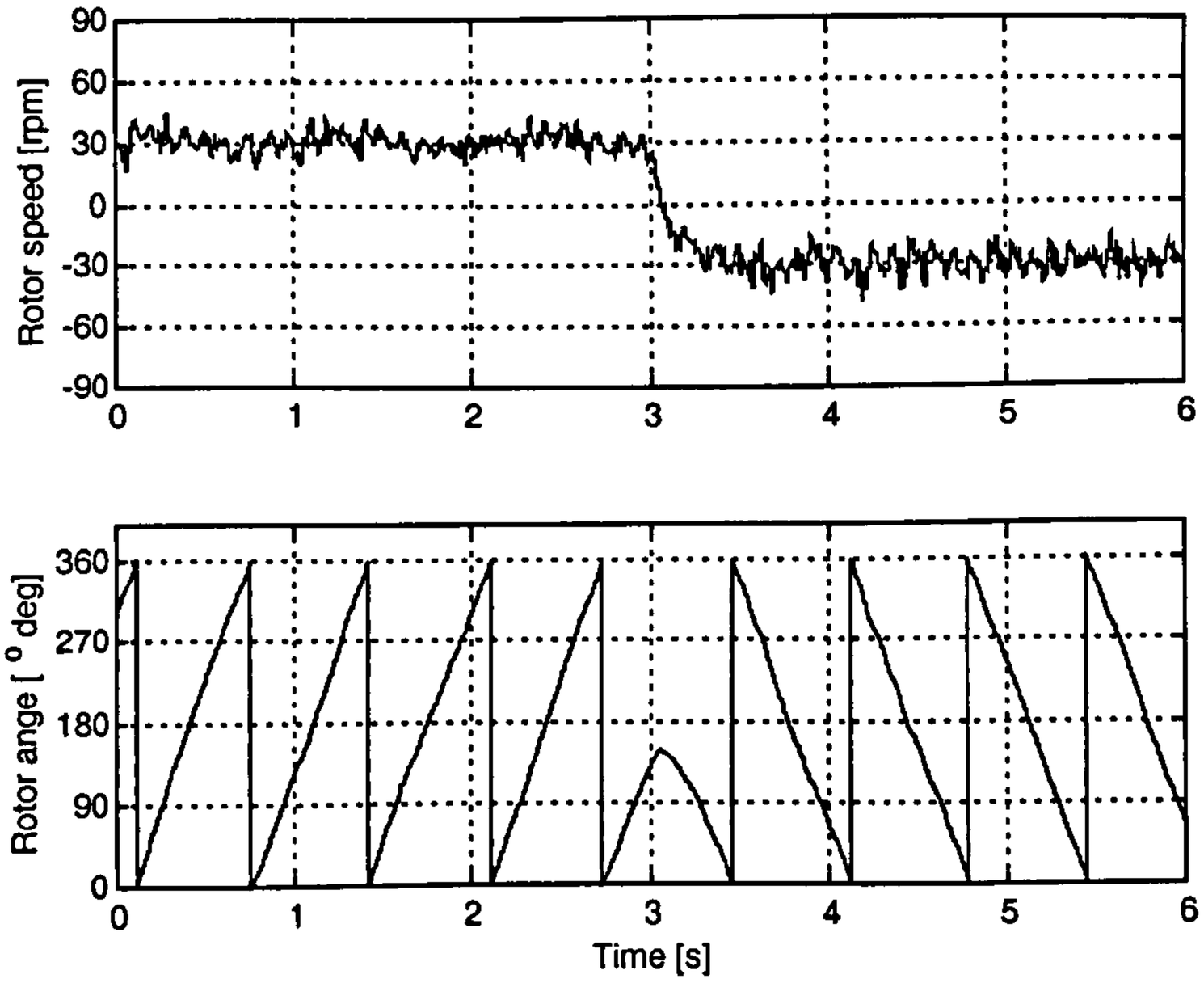

Figure 6.22: Full load sensorless speed reversal at 30 rpm using α-β injection; *top*: rotor speed, *bottom*: rotor position.

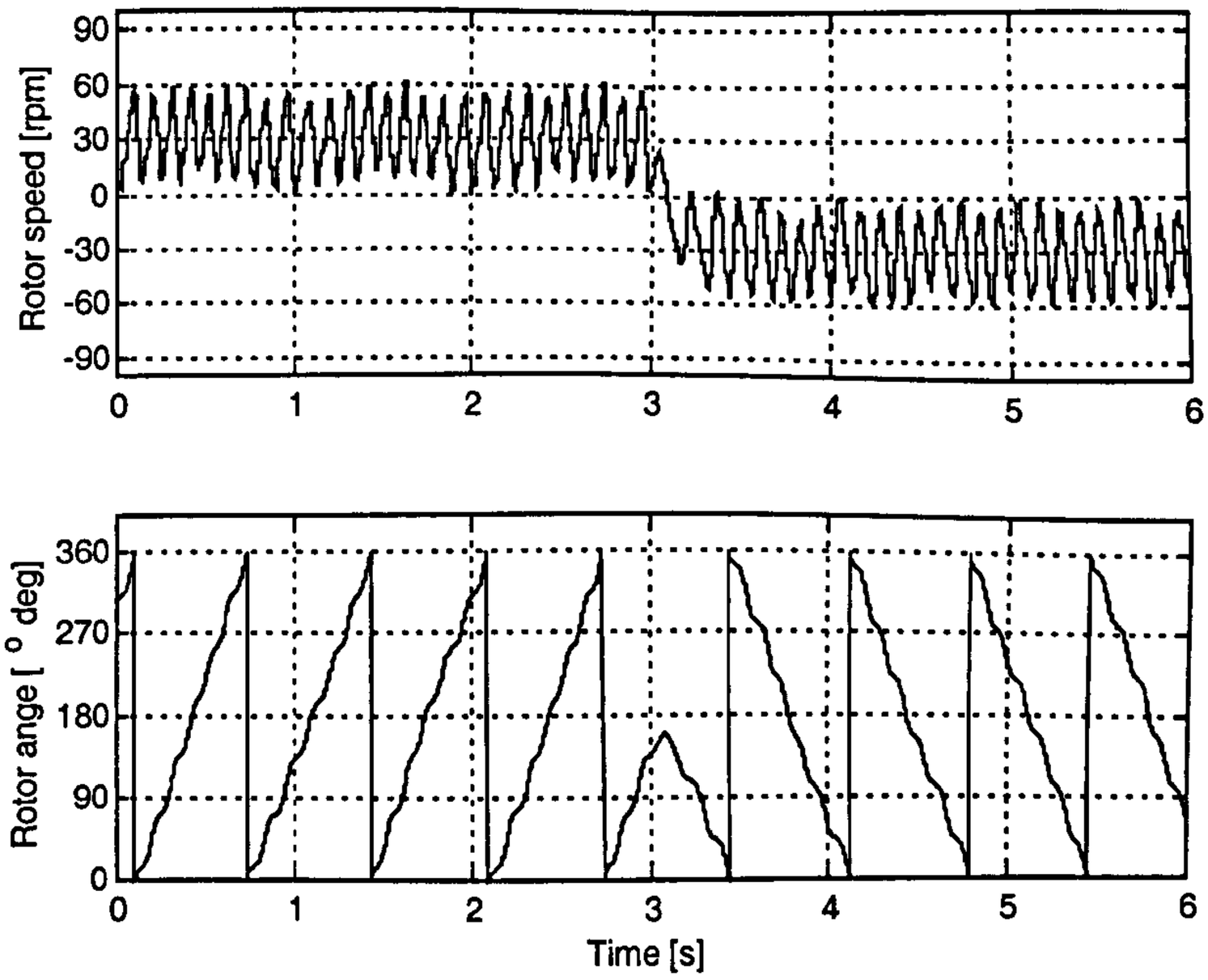

Figure 6.23: Full load sensorless speed reversal at 30 rpm using *d-axis* injection; *top*: rotor speed, *bottom*: rotor position.

6.4 Hybrid Structure for Wide-Speed Operation

6.4.1 Introduction

The main motivation for the use of *hf* injection techniques is the failure of the classical model-based techniques to operate at low/zero speed which impedes the use of model base techniques in applications such as position control. However, the use of injection techniques at higher speeds operation where the model-based methods provide a viable alternative is hard to justify because the *hf* injection current produce extra losses and acoustic noise. It is also difficult to implement at higher speeds due to practical implementation constraints such as the use of band-pass filters. For these reasons a combination of both methods is considered i.e.: *hf* injection estimation at low speed and model-based estimation for higher speeds. This approach presents the challenge of performing a smooth transition between the *hf* injection and model-based method and to avoid excessive perturbation in the speed estimate during the transition. This is particularly critical for sustained operation in or near the region of transition rather than fast transitions through it. In this work the smooth transition is

achieved by incorporating the injection estimate as part of a flux observer. This in addition also improves the feedback signal quality.

6.4.2 Proposed Hybrid Structure

A simple flux observer can be used to obtain rotor position by calculating the flux induced by the rotor magnets. The total stator flux can be computed as the integral of the stator voltage minus the stator resistive drop. In practice the commanded voltage is used instead of the measured value. The flux due to the rotor magnets $\underline{\psi}_r$ is obtained by compensating for the flux induced by the stator current. This is referred to as the "voltage model" and is given by:

$$\underline{\hat{\psi}}_r^v = \frac{1}{s}(\underline{v}_{\alpha\beta}^* - \hat{r}_s \underline{i}_{\alpha\beta}) - \hat{L}_s \underline{i}_{\alpha\beta} \tag{6.2}$$

where all flux quantities are in the stationary α-β frame. To avoid integration drift on the flux observer a negative feedback path with a small gain k_1 is provided. This results in a voltage model that is a high-pass filtered version of (6.2):

$$\underline{\hat{\psi}}_{r\,HP}^v = \frac{1}{s+k_1}(\underline{v}_{\alpha\beta}^* - \hat{r}_s \underline{i}_{\alpha\beta}) - \frac{s}{s+k_1}\hat{L}_s \underline{i}_{\alpha\beta} \approx \frac{s}{s+k_1}\underline{\hat{\psi}}_r^v \tag{6.3}$$

The use of the feedback gain k_1 in the integration limits the effectiveness of the voltage model to fundamental frequencies above the cut-off frequency of the filter. However, it is not the only factor that impedes the operation of the flux observer at low frequencies. As discussed in section 2.2, the decreasing magnitude of the induced back-EMF and the increasing influence of stator resistance estimation error both degrade the accuracy of the flux estimation and deteriorate the performance of the vector control. To overcome this problem, at low speed an injection method is used to generate an estimate of the magnet induced flux that serves as a reference for the voltage model at low speeds. The voltage model is forced to follow this reference by closing the loop with a high gain proportional controller. At higher speeds the injection flux estimate ceases to have a significant influence and is finally

disconnected. The proposed hybrid observer is shown in Fig. 6.24. This structure is independent of the injection method used to generate the injection position estimate $\hat{\theta}_r^{inj}$, and in the present work has been implemented with the α-β rotating injection.

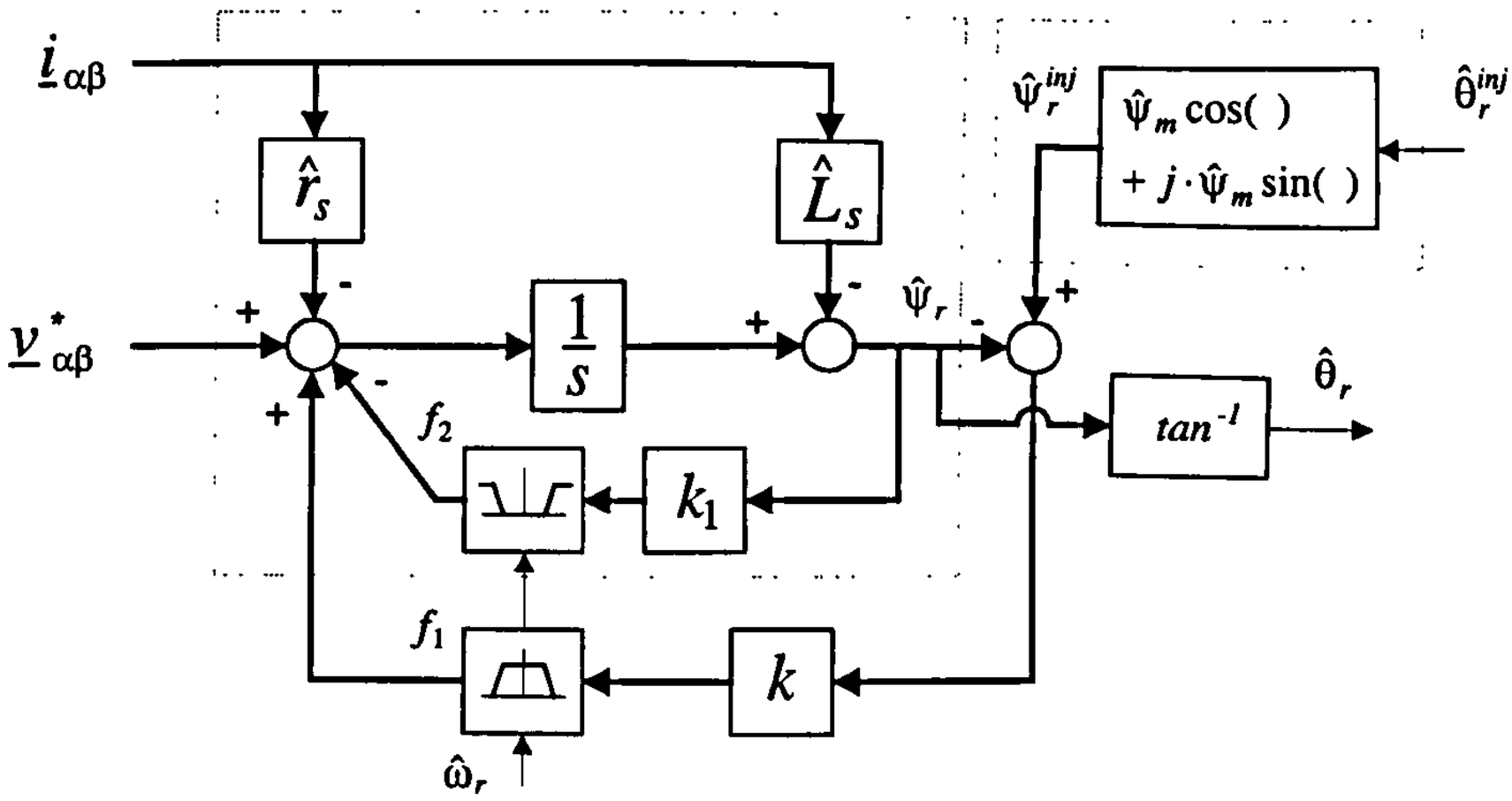

Figure 6.24: Hybrid flux observer structure for coupling of injection and voltage model estimates.

At low speed the function $f_1(\hat{\omega}_r)$ and $f_2(\hat{\omega}_r)$ have the values one and zero respectively, therefore the observer is described by:

$$\underline{\hat{\psi}}_r = \frac{1}{s}\left\{(\underline{v}^*_{\alpha\beta} - \hat{r}_s \underline{i}_{\alpha\beta}) + k(\underline{\hat{\psi}}_r^{inj} - \underline{\hat{\psi}}_r)\right\} - \hat{L}_s \underline{i}_{\alpha\beta} \tag{6.4}$$

yielding:

$$\underline{\hat{\psi}}_r = \frac{s}{s+k}\underline{\hat{\psi}}_r^{v} + \frac{k}{s+k}\underline{\hat{\psi}}_r^{inj} \tag{6.5}$$

In (6.5) the rotor flux estimation $\underline{\hat{\psi}}_r$ is a combination of the injection estimate $\underline{\hat{\psi}}_r^{inj}$, dominant at low frequencies, and the voltage model estimate $\underline{\hat{\psi}}_r^{v}$ dominant at higher frequencies. The injection flux estimate is filtered by the low pass characteristic of the closed loop reducing the noise of the rotor angle estimation. However this does not have a big detrimental effect on the dynamic of the estimation because, during transients, the voltage estimate provides a path for the estimation of the high frequency components of the flux.

At higher speeds the voltage model yields good estimations and does not need the injection estimate to be used as a reference. Furthermore at frequencies higher than the crossover $f_c = \frac{k}{2\pi}$, the relative influence of the injection estimate becomes less significant and it can be disconnected. The disconnection of the injection estimate is performed gradually by reducing the controller gain by means of multiplying function of the speed $f_1(\hat{\omega}_r)$. This function decreases linearly above the lower transition speed, reaching zero at the upper transition speed. At the same time the feedback gain k_1 is connected to avoid drifting of the flux estimator. The gain k_1 is multiplied by $f_2(\hat{\omega}_r)$ which is complementary to $f_1(\hat{\omega}_r)$. At speeds above the upper transition speed the functions f_1 and f_2 have values of zero and one respectively thus reducing the hybrid system to the simple voltage model of (6.3). The voltage injection itself is turned on and off using a hysteresis band at speeds slightly higher that the upper transition speed.

The value of k should be sufficiently high so the injection method dominates the hybrid estimation before the voltage model starts braking down at low speed due to the lack of back-EMF. On the other hand k must be limited so the voltage model dominates the estimation at the frequencies of transition to minimize the impact of the disconnection of the injection reference.

Finally the feedback gain k_1 is chosen to be sufficiently small so it produces negligible phase shift of the flux estimate at the upper transition frequency.

6.4.3 Results of Hybrid Position Estimator for Sensorless Operation

The proposed hybrid system has been implemented with the following parameters: the lower and higher threshold speeds have been set to 400 and 600 rpm, i.e. 13.3 and 20% of nominal speed. The controller gain is set to $k = 94.3$ giving a crossover frequency of 15 Hz and the voltage model feedback gain set to $k_1 = 12.6$.

Experimental results obtained for sensorless speed reversals and position step response are presented in this section.

A speed reversal from 1500 rpm to –1500 rpm under no load has been carried out. Note that both initial and final speeds are in the region where only the voltage model is operative. The speed response, in Fig. 6.25, shows a smooth transition in and out of the low speed region. In Fig. 6.26 the measured position and the estimated value are shown in the same plot to emphasise the good correspondence of both variables. In the same figure, the bottom plot show the injection estimated only at low speed during the period in which it is used for driving the hybrid estimation.

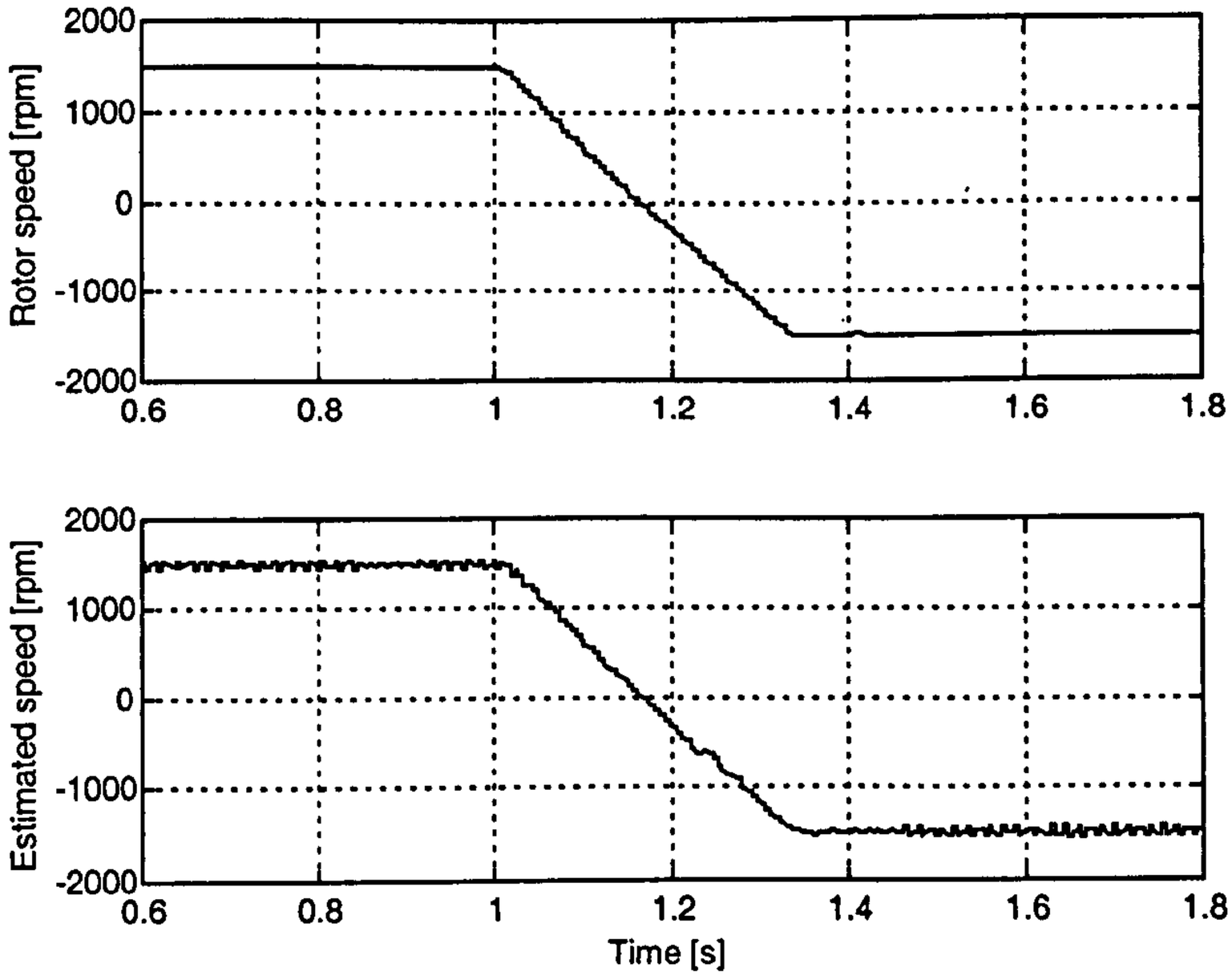

Figure 6.25: Speed response of sensorless speed reversal at no load; *top*: measured speed, *bottom*: estimated speed.

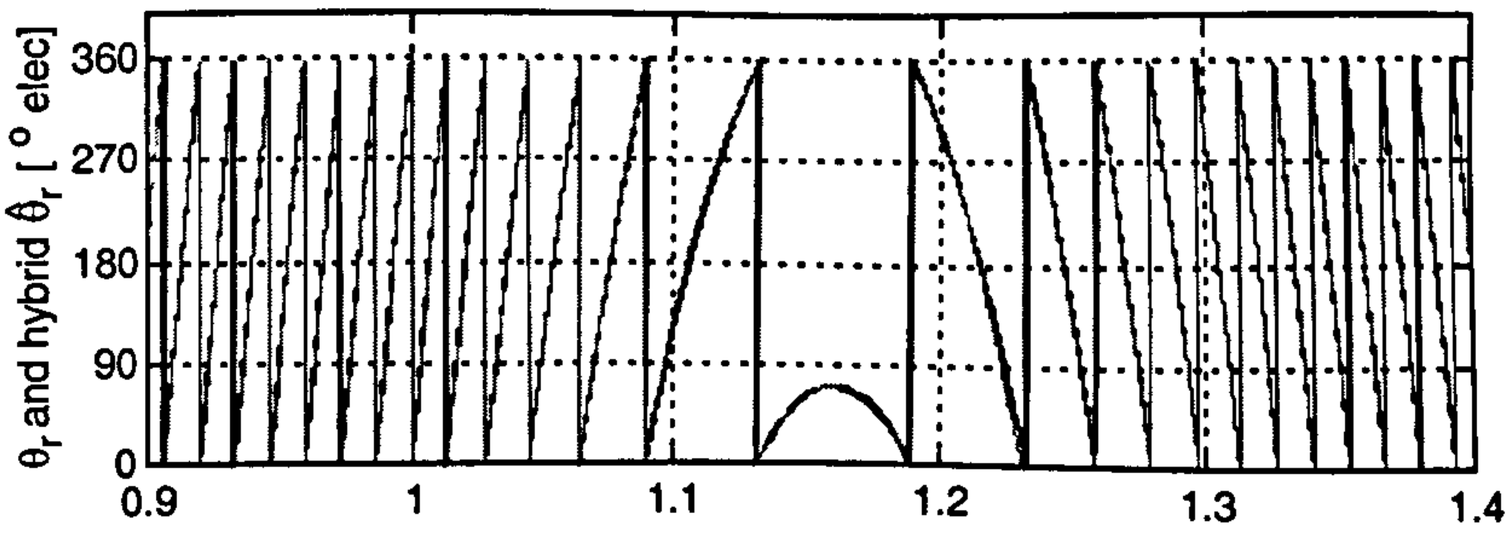

Figure 6.26: Position response of sensorless speed reversal at no load; *top*: measured and estimated rotor position, *bottom*: injection position estimation.

The good performance of the hybrid estimation is maintained for operation under load. Figures 6.27 and 6.28 show a similar speed reversal transient at 100% nominal load. In this case the acceleration is faster because the load torque assists the drive's electric torque. Very good speed estimation is seen in Fig. 6.27, especially during motoring operation, i.e. positive speed. A steady state error in the tracking of the speed reference (±1500 rpm) is seen. As already discussed, this is caused by the use of only a proportional controller in the speed loop. In the speed estimate, shown in the bottom plot of Fig. 6.27, an error is appreciable during the transition between the injection estimate region to the voltage model estimate region. This is due to the large acceleration of the rotor that produces a fast transition; small differences between the two rotor angle estimates will result in speed errors during the transition. Nevertheless, this condition of operation results in transition at maximum acceleration, i.e. worst case, and it can be seen that the speed estimate error is limited.

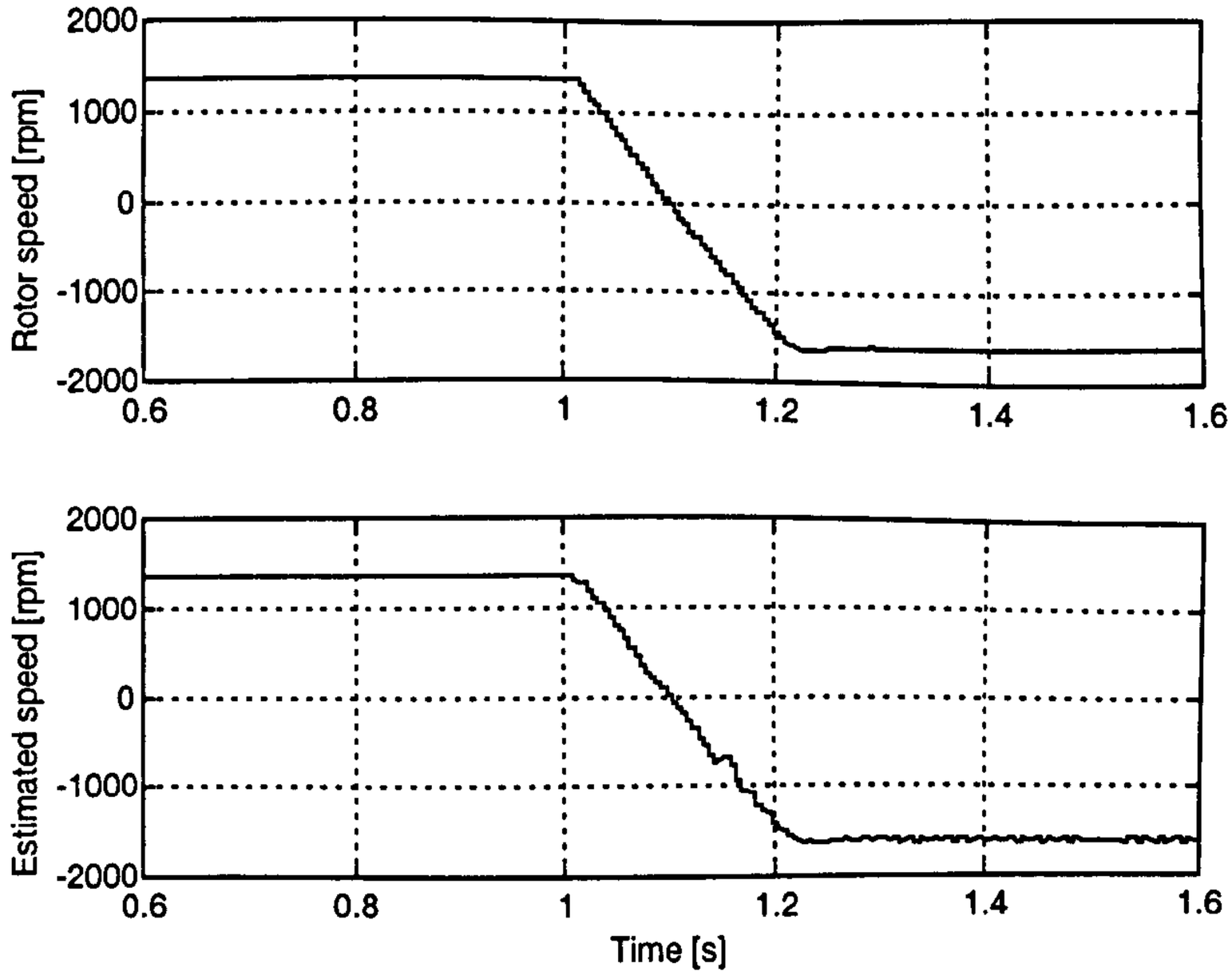

Figure 6.27: Speed response of sensorless speed reversal at 100% load; *top*: measured speed, *bottom*: estimated speed.

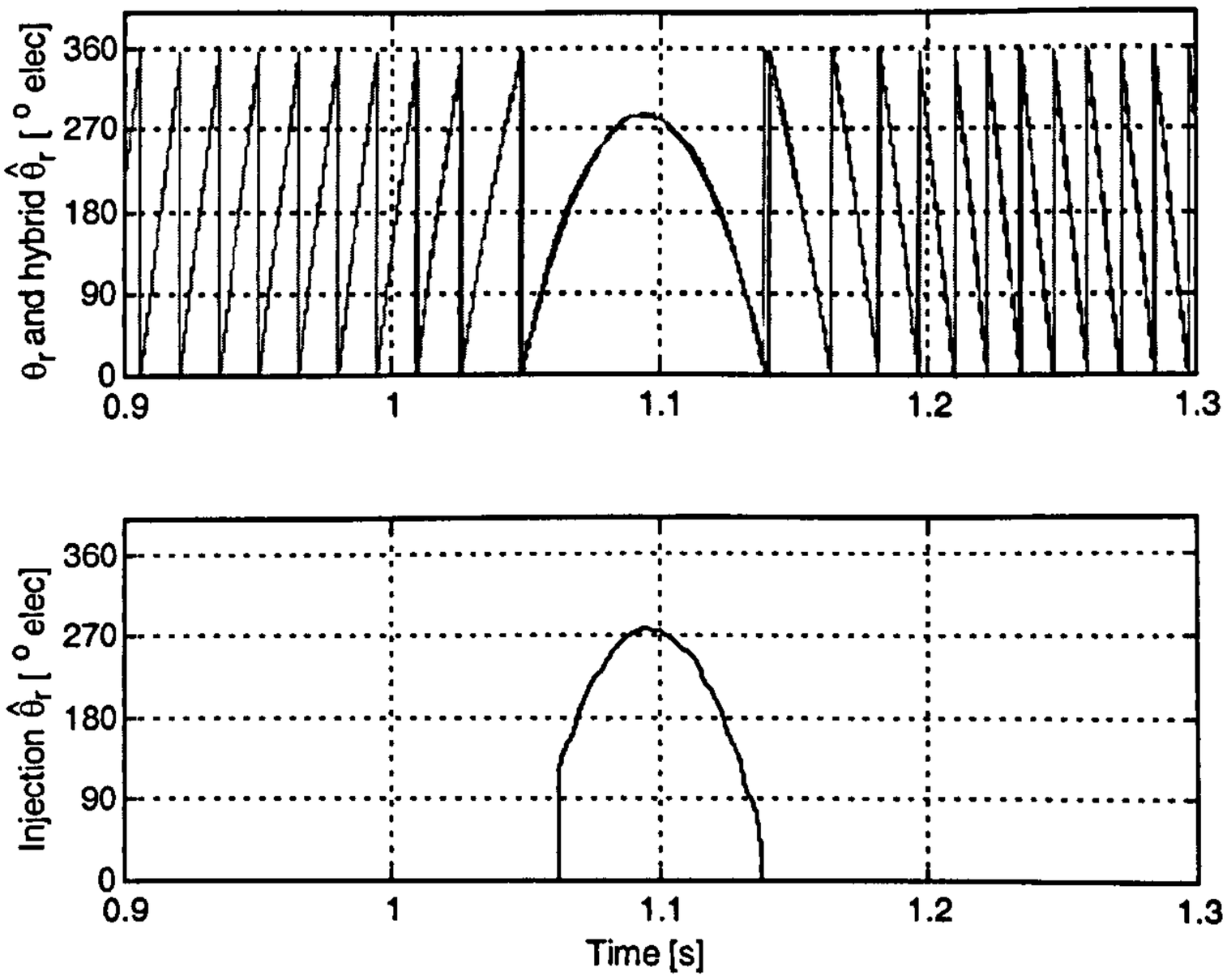

Figure 6.28: Position response of sensorless speed reversal at 100% load; *top*: measured and estimated rotor position, *bottom*: injection position estimation.

The presented speed reversals results show good transition through zero speed. However, more critical is sustained sensorless operation at low/zero speed. The operation in this condition has been tested by considering the step response of the sensorless position control. The results shown in Fig. 6.29 and 6.30 correspond to the

machine operating at no load. The magnitude of the position steps is chosen to be 100 electrical radians, slightly over 5 full mechanical turns, and is sufficiently high for the machine to accelerate to speeds outside the *hf* injection region and in to the voltage model sensorless region. Figure 6.29 shows the measured and estimated rotor position, demonstrating that the control is maintained at zero speed. In Fig. 6.30 the measured and estimated speed are shown. It can be seen that the speed increases at constant acceleration given by the maximum torque limit, going over the 600 rpm threshold where the injection estimate ceases to be used.

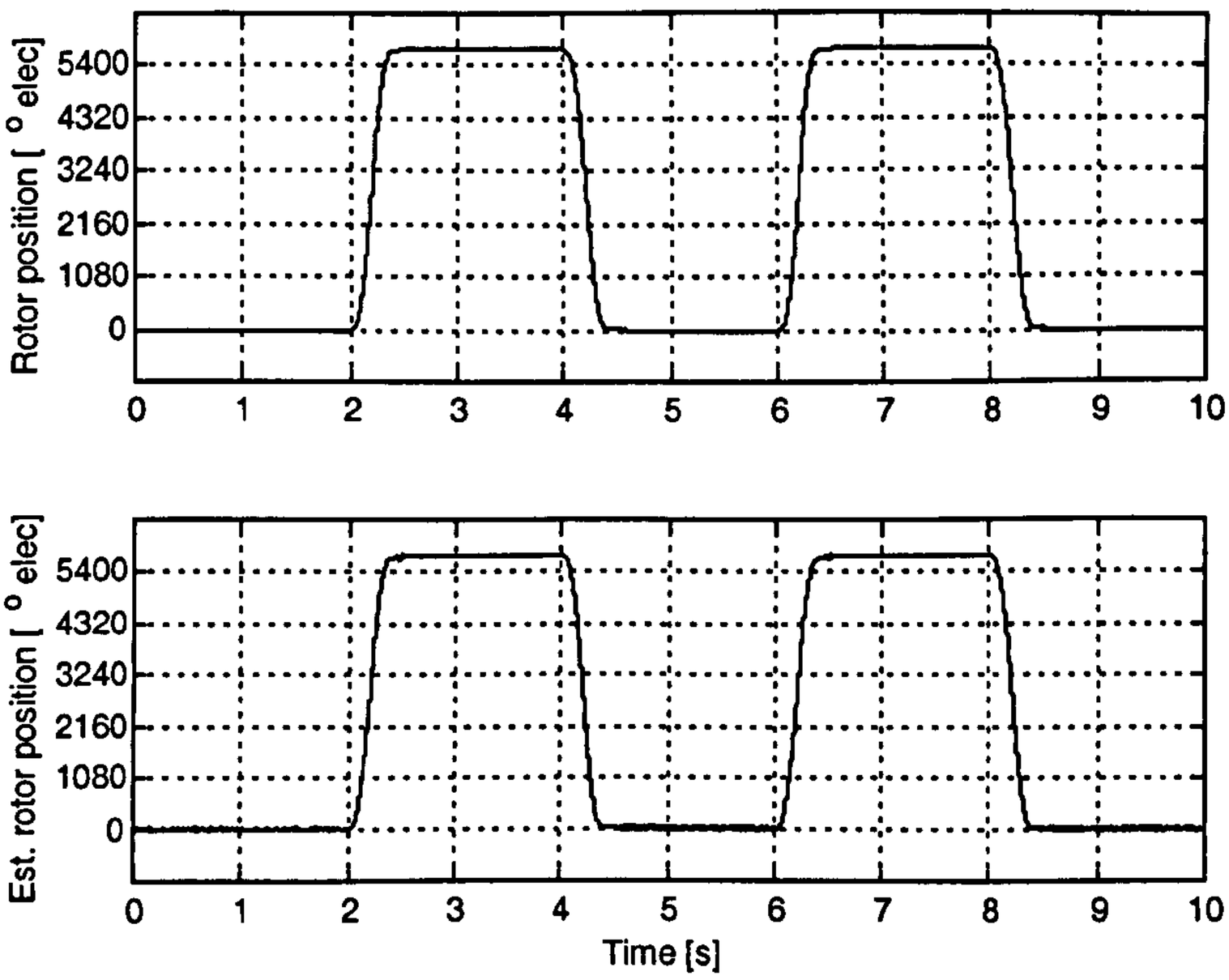

Figure 6.29: Sensorless response to position demand steps at no load; *top*: measured rotor position, *bottom*: estimated rotor position.

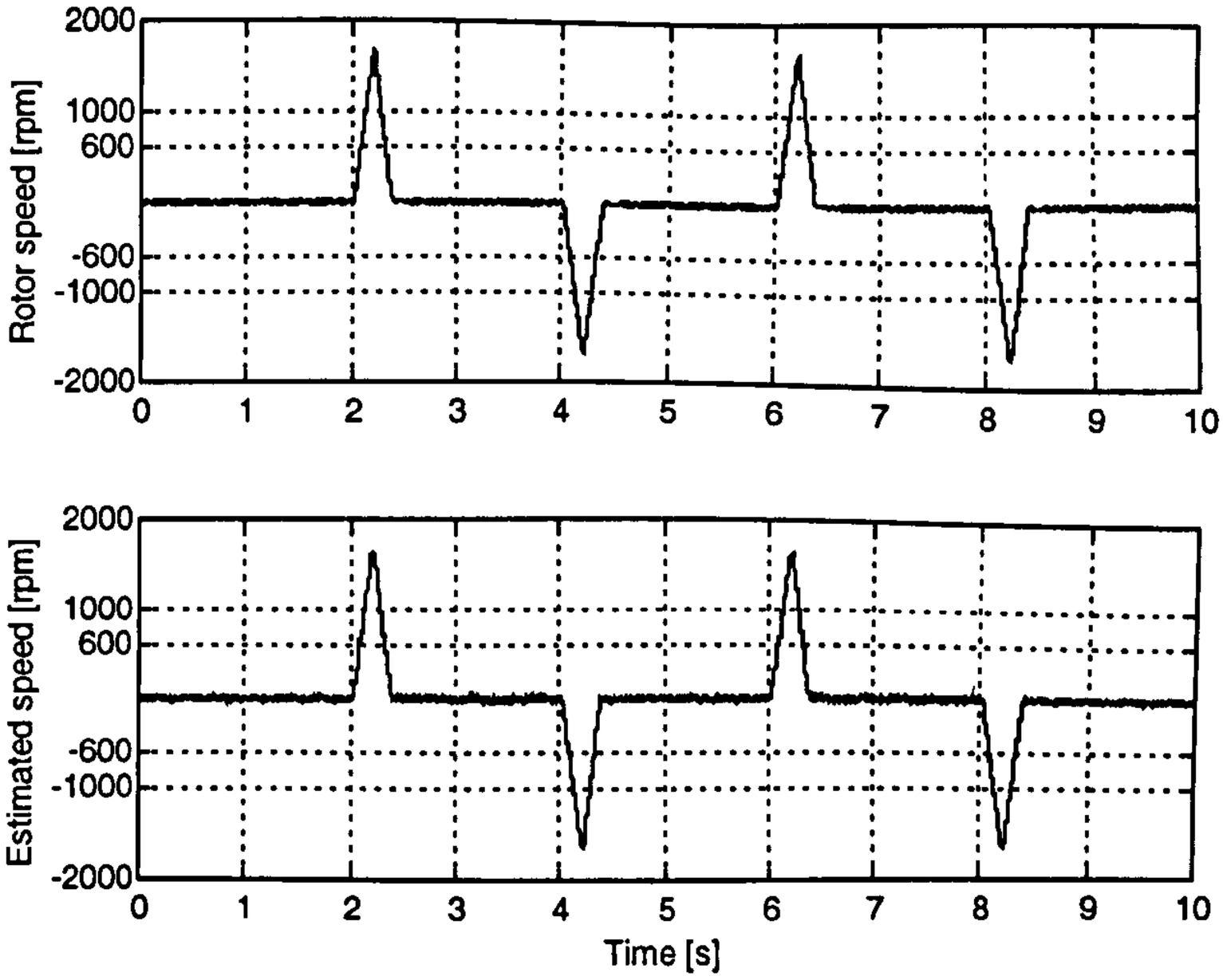

Figure 6.30: Speed response to sensorless position demand steps at no load; *top*: measured rotor speed, *bottom*: estimated rotor speed.

The result for a position step of the same magnitude under full load is shown in Fig. 6.31. The ability to hold position indefinitely under load is demonstrated. To show the correct sensorless orientation of the vector control during this transient, the measured and estimated rotor angle are shown in Fig. 6.32

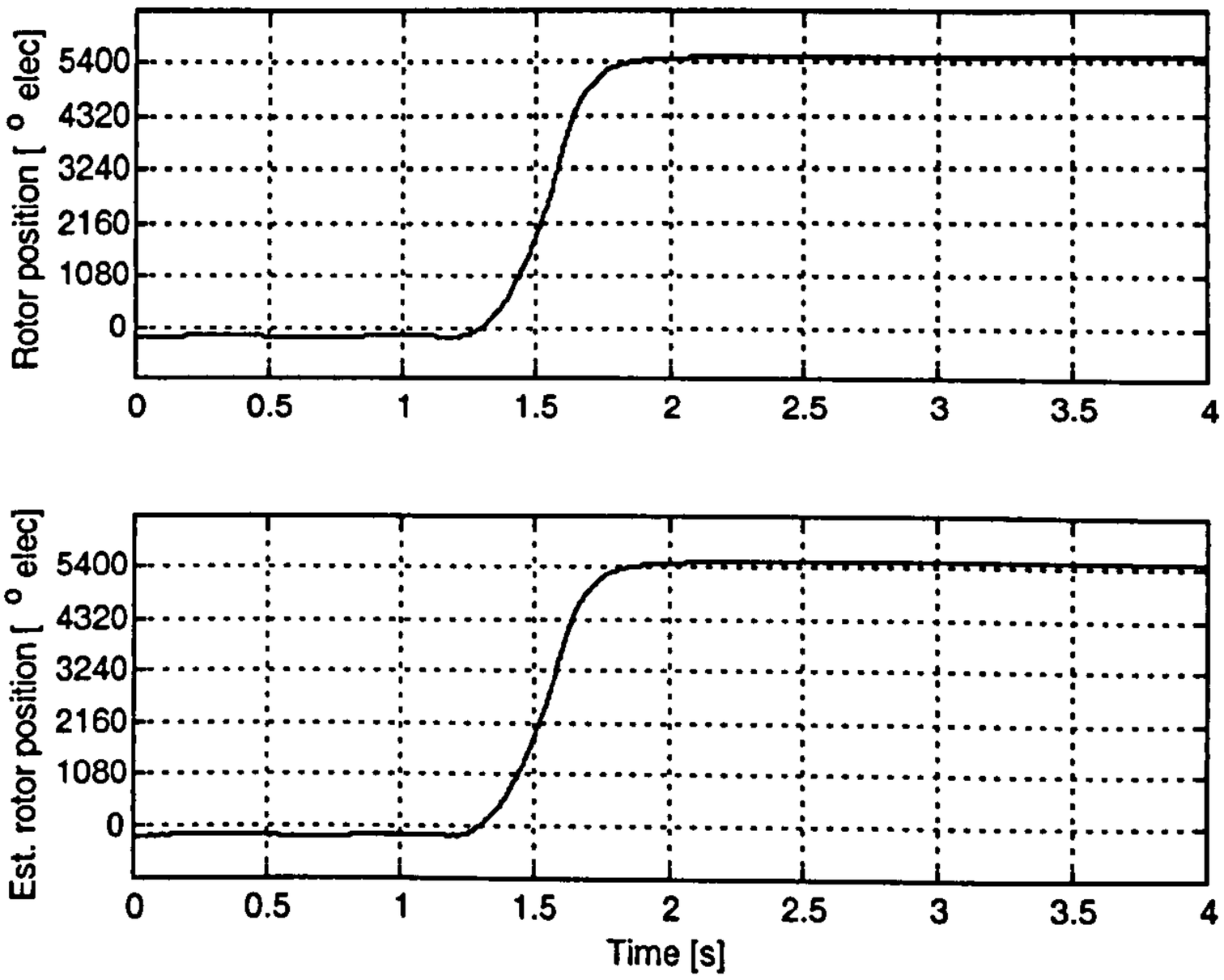

Figure 6.31: Sensorless response to position demand steps at full load; *top*: measured rotor position, *bottom*: estimated rotor position.

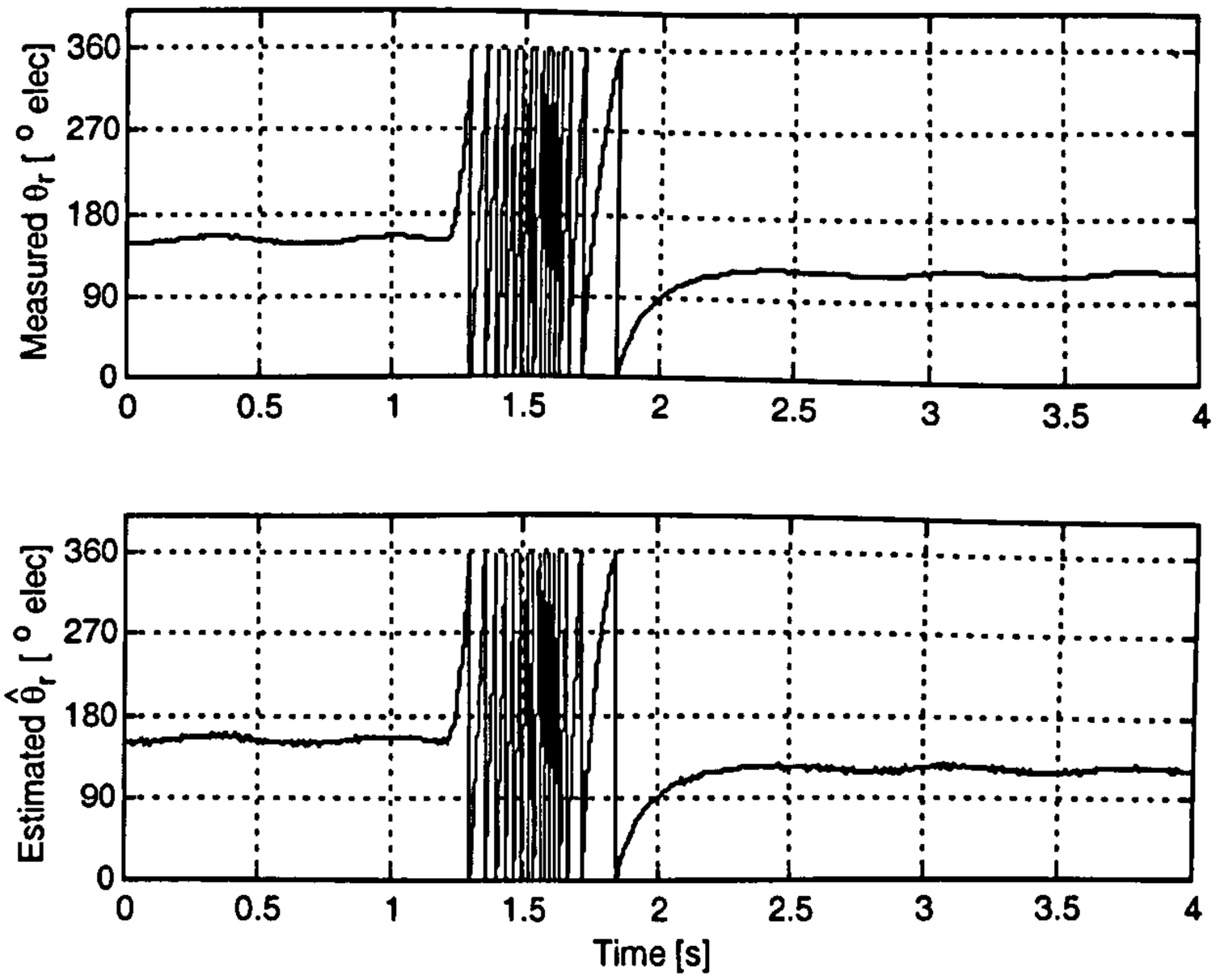

Figure 6.32: Rotor angle during sensorless position demand steps at full load;
top: measured rotor angle, *bottom*: estimated rotor angle.

The filtering action of the hybrid method at low speed is shown in Fig. 6.33 by closely comparing the pure injection angle estimate $\hat{\theta}_r^{inj}$ with the resulting hybrid estimation $\hat{\theta}_r$ for a portion of the time in which the sensorless drive is holding position under full load. In this figure the oscillation caused by the torque pulsations at 1.3 Hz of the induction machine is again appreciable. The amplitude of the position response to this disturbance is increased to about 3.5° electrical (from 2° electrical measured in Fig. 6.17 when only injection is used), this presents a deterioration of the bandwidth of the position estimation as a result of the low-pass filtering effect of the flux observer. Theoretically this filtering effect should be compensated by the voltage model estimation. Nevertheless, at very low frequency the voltage model yields poor flux estimations and is ineffective in correcting the lag introduced to the injection estimation. This result in some deterioration of the dynamic.

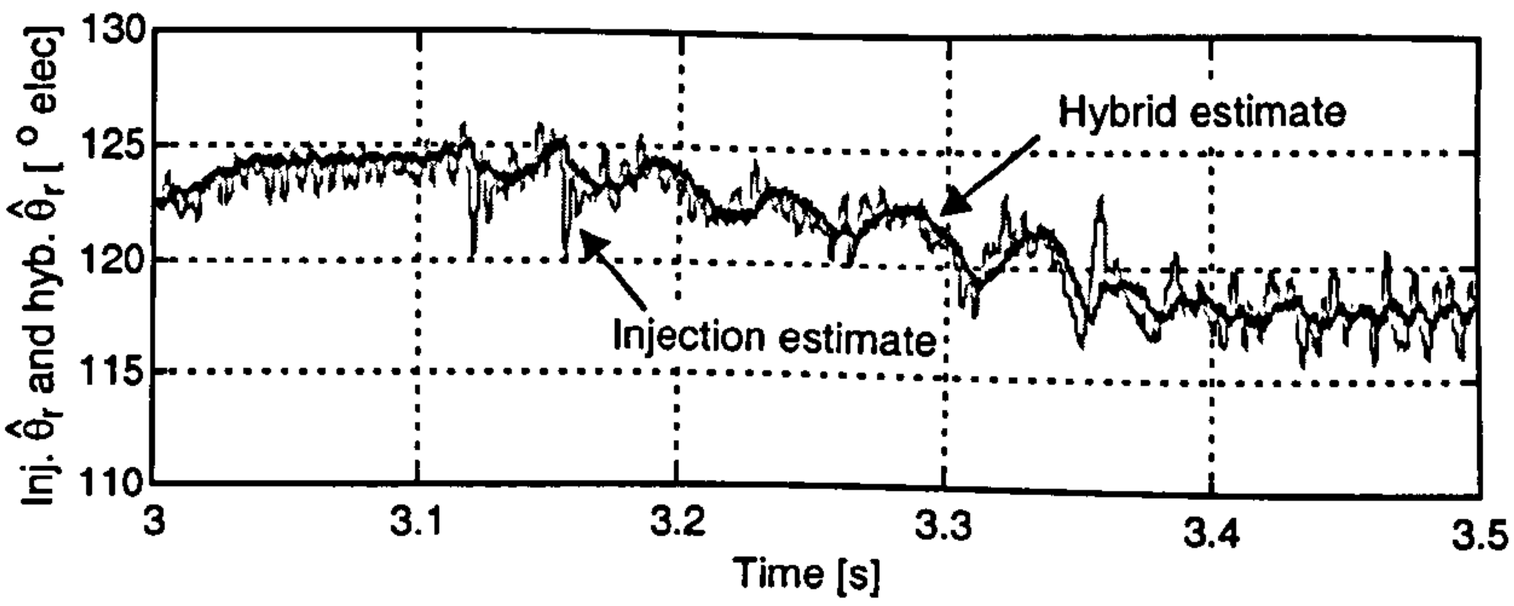

Figure 6.33: Improvement on the angle estimation.

Finally, to assess the smooth operation in the transition region a reference of 500 rpm has been given to the drive in sensorless speed control. The measured and estimated speeds and rotor angle are shown in Fig. 6.34. The estimated speed error is no larger than that of the voltage model alone when working at higher speeds, and therefore it can be concluded that continuous operation in the transition region between the two different sensorless techniques does not negatively affect the position and speed estimate.

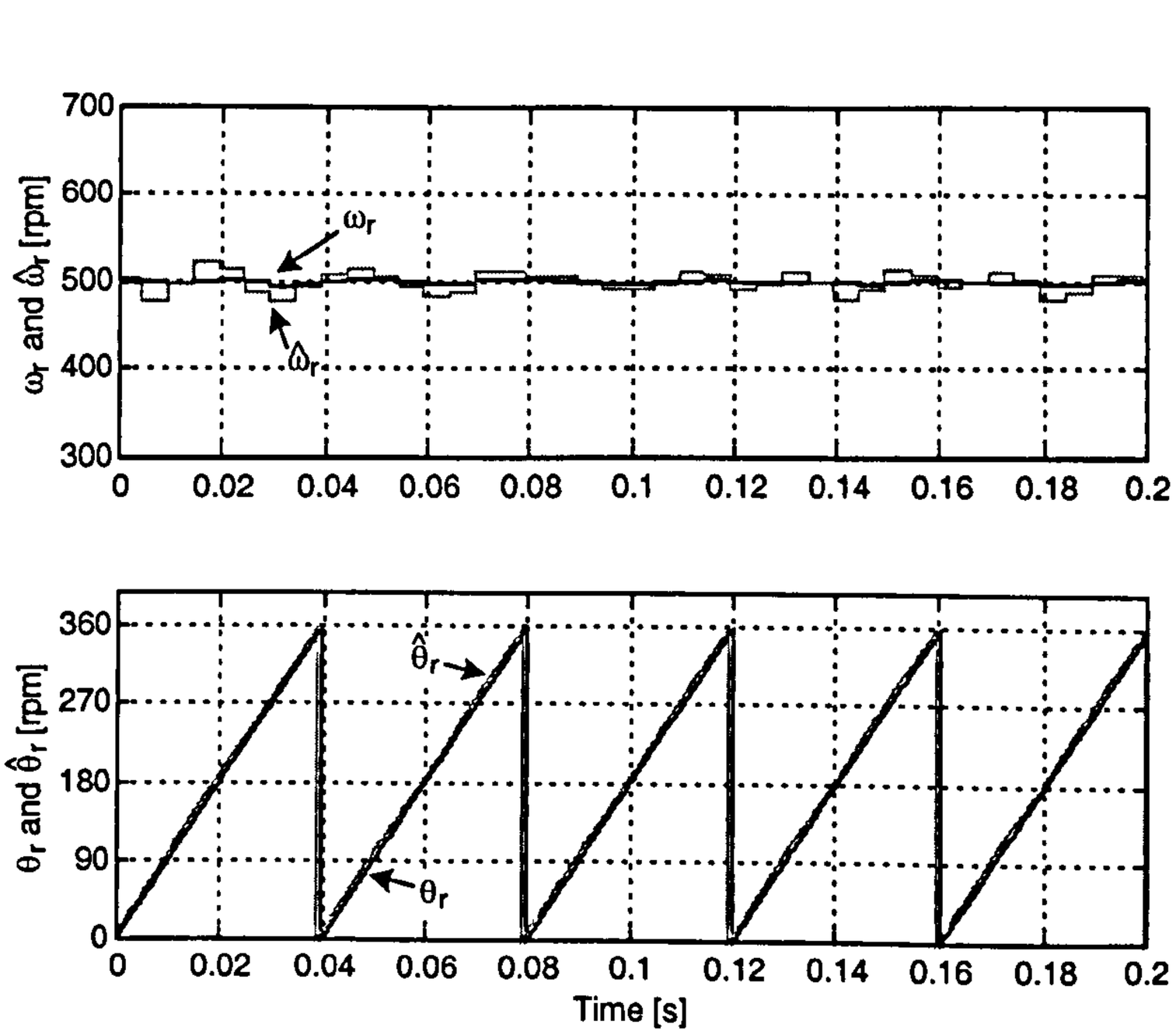

Figure 6.34: Sensorless operation in the transition band; *top*: measured and estimated speed, *bottom*: measured and estimated rotor position.

Chapter 7

7 Conclusions and Discussion

The aim of the work was to demonstrate experimentally the feasibility of sensorless vector control at low and zero speed, including position control, of a surface mounted PM machine by means of saturation saliency tracking. In order to do this a 4 kW experimental rig was constructed with an of-the-shelf SMPM, the details of the rig construction being the subject of Chapter 4.

In Chapter 3 a review of different injection methods for saliency tracking was presented. For this work, continuous *hf* voltage injection methods were selected due to their persistent excitation, their capability of providing position signal estimation at good bandwidth and their ease of implementation on existing PWM schemes. Detailed mathematical analysis of the rotating α-β and pulsating *d-axis hf* voltage injection methods were presented. Based on this analysis, demodulation strategies that maximise the rejection of the *hf* carrier component to improve the extraction of a small saliency position signal were derived for each of these methods and implemented experimentally.

7.1 Saturation Saliency in Surface Mounted PM Machines.

In Chapter 5 an experimental measurement of the saliency at different loads was carried out. This analysis lead to the conclusion that, although the saturation saliency changes in magnitude and phase due to the loading of the motor, a saliency value $\Delta L_s / L_s$ of approximately 10% is measurable at any loading condition. Also, the

phase of this saliency indicates that the saliency is dominated by the variation of the magnetizing inductance caused by stator flux, and not leakage inductance as suggested by some researchers. For both sensorless rotor position estimation strategies, this is confirmed when the phase shift is measured as a function of load. Although this can only be stated specifically for the machine used in this work, it is likely that other surface mounted PM machines of similar power level will show the same characteristics. The compensation of this phase shift allows for vector control at high loads. Lack of compensation leads to incorrect orientation of the vector control and loss of controllability altogether if the phase shift is considerable. This is believed to be the reason why in [33] only control at loads lower than 30% was achieved.

7.2 Sensorless Control of SMPM by Saturation Saliency Tracking

The experimental results shown in Chapter 6 demonstrate that saturation saliency can be exploited for sensorless position control of SMPM motors. Nevertheless, the small magnitude of this saliency leads to strong disturbances arising form three sources: (a) inverter non-linearity (mainly dead-time), which distorts the waveform of the *hf* currents; (b) spatial harmonics on the distribution of the saliency around the machine and (c) transient coupling of the torque current into the injection current frequency band. In this work the transient coupling phenomenon have been tackled by limiting the frequency content of the torque reference with a low pass filter. This was effective in reducing the noise, although it puts a constraint on the controller designs resulting in a reduced bandwidth of the speed and position loop.

For the α-β injection a dead-time compensation strategies were proposed. These strategies were effective in reducing, although not completely eliminating, the resulting modulation in the saliency position signals. The Space Modulation Profile (SMP) was introduced for compensating the machine spatial harmonics and the remaining dead-time effect. This technique was very effective under load, achieving position estimations within $\pm 2^{\circ}$ electrical (0.7° mech.) in sensorless operation. The higher content of dead-time distortion at no load meant that the improvement by the

combined technique was less dramatic and errors in the position estimation where within ±5° electrical (1.7° mech.).

The *d-axis* injection also was shown to provide means of sensorless vector control at zero speed. Nevertheless, this technique can not be compensated by the SMP technique and the results show significant estimation error of more than 10° electrical regardless the loading condition. Also, the dynamic of the tracking loop used for the *d-axis* injection method reduced the performance, especially its capability to reject load disturbances. In conclusion, the performance of the α-β compensated injection is superior in accuracy and dynamics to that obtained with the *d-axis* injection. Nevertheless, as shown in Section 6.2.2, the saliency phase shift correction used in the *d-axis* injection method can be implemented analytically, yielding simple implementation that does not require commissioning. This makes the *d-axis* injection method more attractive for less-demanding, lower bandwidth applications.

In this work the incorporation of the injection mechanism with a model-base strategy was presented and proven to provide sensorless operation over full speed range. The proposed structure shows a good transition between the low speed, injection-estimate region and the voltage-model region at higher speed. This type of hybrid structures is considered the best solution for full speed range sensorless operation.

7.3 Publications

The present work has resulted in three conference papers, which are included in Appendix D. An extended version of one of these papers has been submitted for journal publication.

7.4 Further Work

The improvement of the dynamic performance of the position and control loops requires the elimination of the torque current filter. To achieve this, the transients of torque current have to be decoupled from the injection currents by means of an

observer. The application of such a strategy to SMPM machines has yet to be researched.

Also, the main limiting factor in the accuracy yielded by the voltage injection method was found to be the non-linearity of the power converter. The largest of these effects is due to dead time. The use of converters with better switching characteristics such as zero dead-time matrix converters, or the implementation of hardware based (FPGA) dead-time compensation in inverters is worth researching as a way to improve signal quality and hence rotor position estimates.

Appendix A

A Schematics

In this Appendix the schematics circuit diagrams of the peripheral boards are presented. Details regarding the operation of the boards are also discussed. Although some boards are derived from designs used in previous works they have been included for completeness.

A.1 Back Plane

The back plane consists of a buffer board and a extension board with 64 ways C type erurocard connectors. The pin-out of these connectors is given in Table A.1.

	A	C
1	DGND	+5VDIG
2	DGND	+5VDIG
3	DGND	/RESET
4	NC	/IACK
5	NC	R/W
6	/WAIT	/IOE
7	A1	A0
8	A3	A2
9	A5	A4
10	A7	A6
11	A9	A8
12	A11	A10
13	NC	A12
14	NC	NC
15	DGND	NC
16	DGND	NC

	A	C
17	/INT1	/INT0
18	DGND	TCLK0
19	DGND	NC
20	D17	D16
21	D19	D18
22	D21	D20
23	D23	D22
24	D25	D24
25	D27	D26
26	D29	D28
27	D31	D30
28	AGND	+5VANA
29	AGND	-5VANA
30	+15V	AGND
31	-15V	+15V
32	AGND	-15V

Table A.1. Pin-out of the back-plane connectors.

The control signals of the bus are:

R/W: High for read and low for write from the C44 to the bus.

/IOE: Low when the C44 access the bus.

/RESET: Active low signal from C44 to reset all peripherals.

TCLK0: (unused) C44 CPU clock pulse.

/WAIT: (unused) Active low signal that allows the peripheral boards to extend the access to the bus.

/INT0 and /INT1: (unused) Interrupts request signals to the C44 module.

/IACK: (unused) Interrupt acknowledge signal. Active low output signal to indicate that interrupt has being received.

The buffer board is used to decouple the DSPLINK signals coming from the motherboard protecting it from possible faults on the peripheral board and reducing the effective length of the connector avoiding electromagnetic interference. The schematic circuit of the buffer board is shown in Fig. A.1. It uses bi-directional buffers 74F245 for the data lines and the direction of these buffers is control by the R\W signal. Unidirectional buffers 74F573 are used for the address and the control lines. Of these only the signals /INT0, /INT1 and /WAIT are read by the DSP from the peripheral boards, the remaining control lines are written by the DSP. So the buffers 74F573 are connected accordingly.

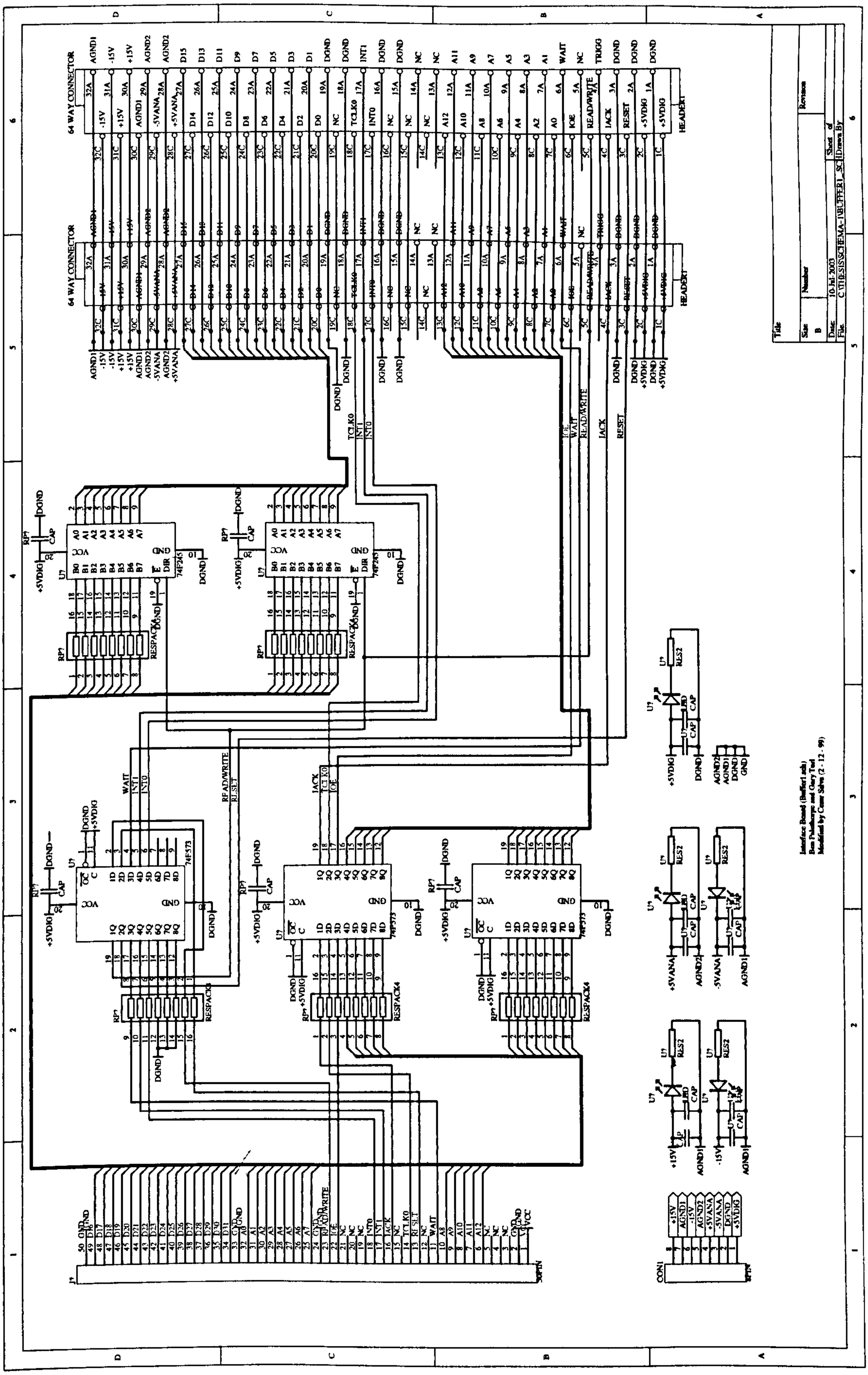

Figure A.1. Back-plane buffer board schematic.

A.2 Digital I/O Board

A simple digital I/O board has being built for general purpose. It consists of eight digital inputs and eight outputs. The outputs are displays on LEDs and are used for monitoring events. Three of the inputs are constructed with current detecting optocouplers HCPL2611 and are used to read the signals of the current direction detection circuit.

The decoding of the board address is executed by a 74F521 comparator. This IC is used to compare bits A3-A6 lines of the address bus with the board address which is set with a four bits wide DIP-switch. When a read or write is performed to this address the three less significant bits of the address bus A0-A2 are decoded by a 1 of 8 decoder 74LS138 addressing individual devices within the board. Similar address decoding scheme is used in all the logic boards achieving a maximum of 16 boards each with a maximum of 8 devices. The digital I/O board only has two devices, an 8 bit output latch 74F273 and an 8 bit input buffer 74F245.

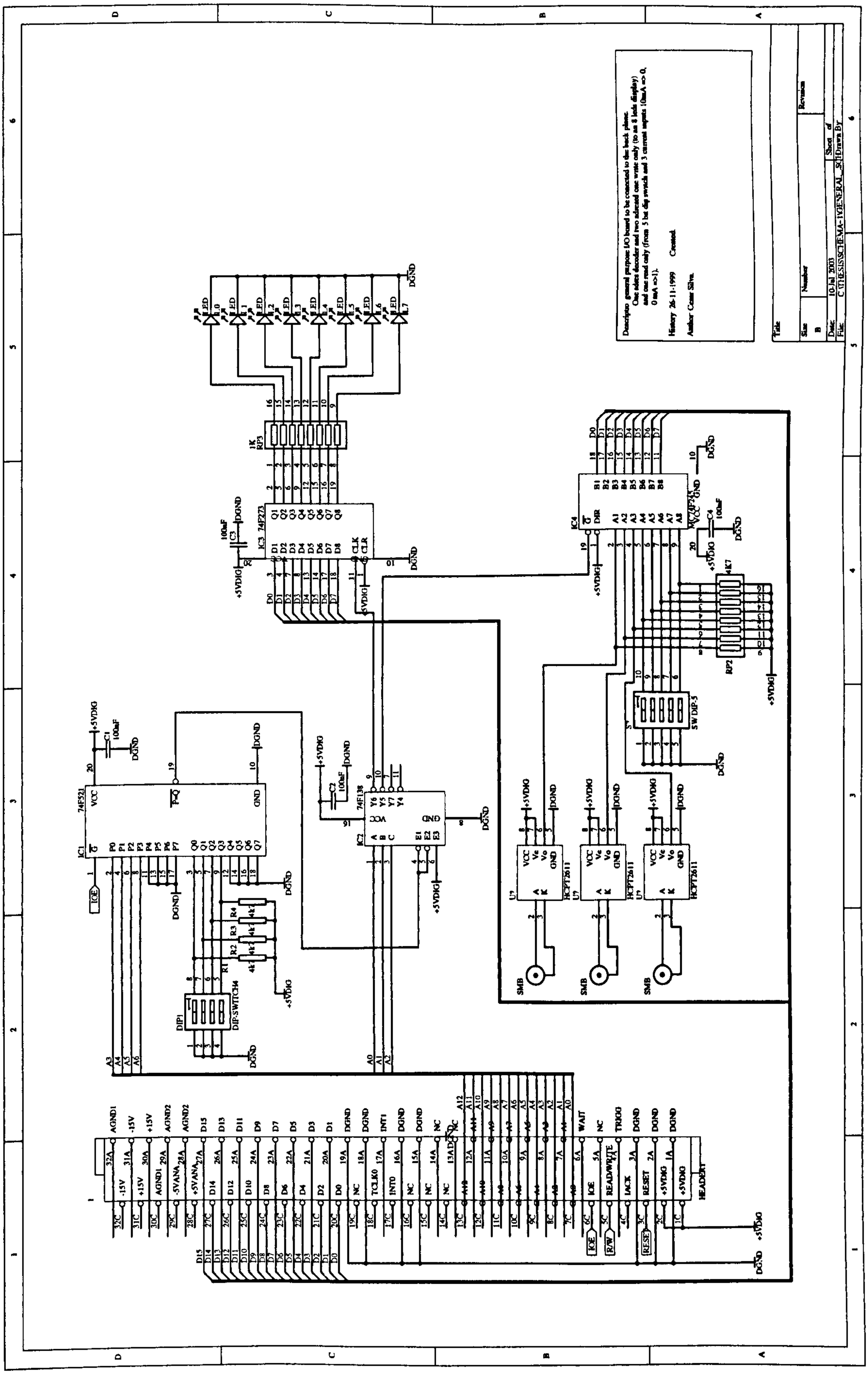

Figure A.2. Digital I/O board schematic.

A.3 Encoder Board

The encoder transmit six differential signals: the 1024 ppr quadrature pulses A and B, a zero marker pulse Z and the commutation signals U,V and W. The encoder board, shown in Fig. A.3 decodes the quadrature signals into a useful position count and provide an interface for the encoder into the DSPLINK.

The differential signals are received trough a 25 way D type connector. This connector also provides the 5V to power the encoder. Differential receivers SN75173 are used for TTL level conversion. To count the encoder pulses the quadrature decoder/counter HCTL2016 is used. This IC is specific for this application; it increments or decrements the count depending on the direction of rotation and it counts both edges of A and B signals, quadrupling the encoder resolution. The zero marker signal is used to reset the count obtaining absolute position (after a initial turn has been completed). This IC has a 16-bit internal counter but only 8-bit parallel output. Therefore two read operations must be carried out to obtain the complete position count. The three least significant bits of the address A2-A0 are used for this purpose: (000) addresses the most significant byte (MSB) of the count and (001) the least significant byte. Additionally in the same read operation the commutation signals U,V and W are read, the signals separated by software masking.

In order to use the same quadrature encoder signals A, B and Z for feedback in the IM load drive, a split board has been constructed. The schematic circuit of this board is shown in Fig. A.4. The encoder differential signals are converted to TTL levels by a SN75173 differential receiver in the input. A second electrically isolated path for these signals is created using logic-to-logic optocouplers 74OL6000. Differential line drivers are use to transmit each channels to the encoder board and to the *Control Technique* inverter driving the load machine. It is noted that the operation of this board is totally transparent for the encoder board.

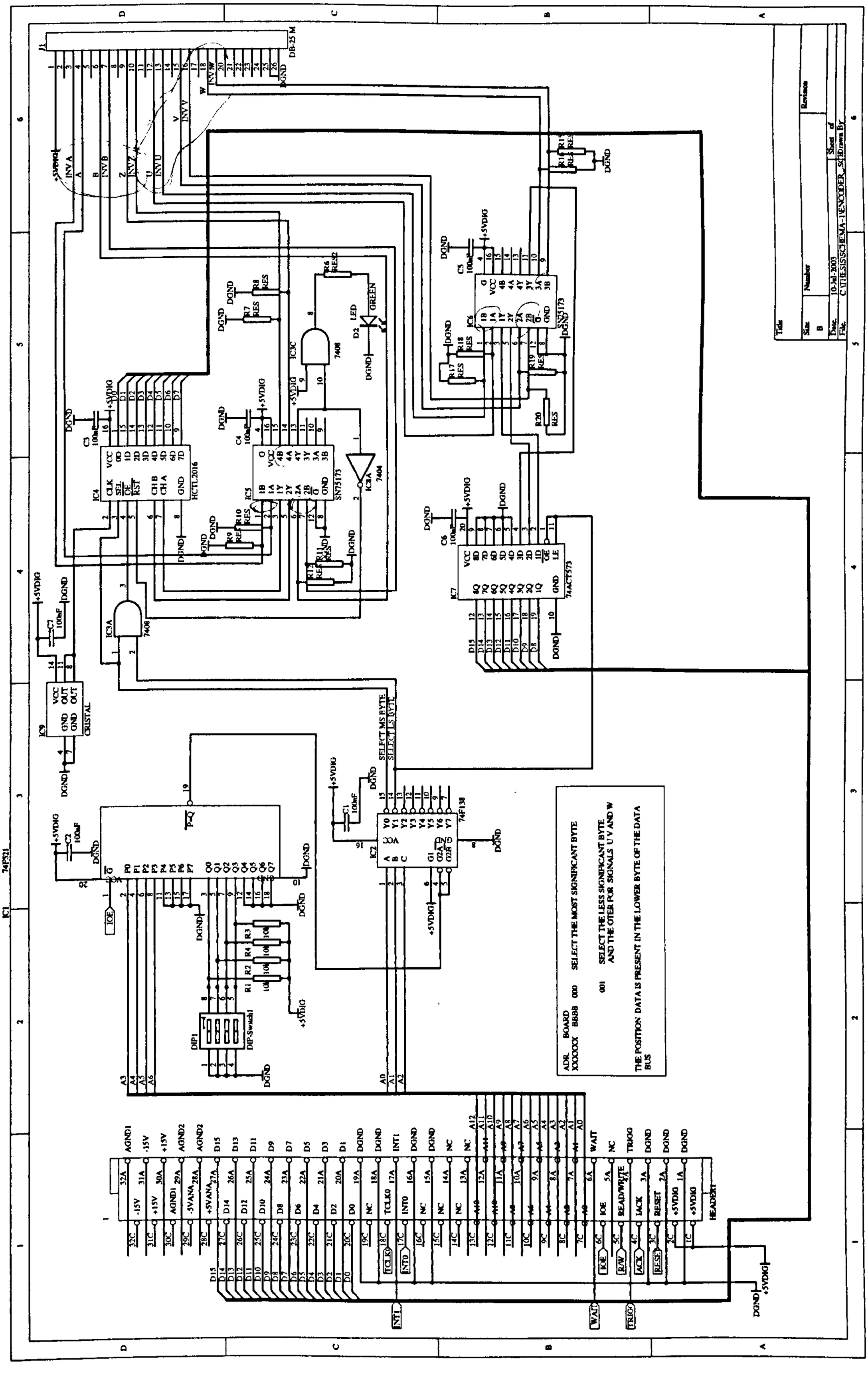

Figure A.3. Encoder board schematic.

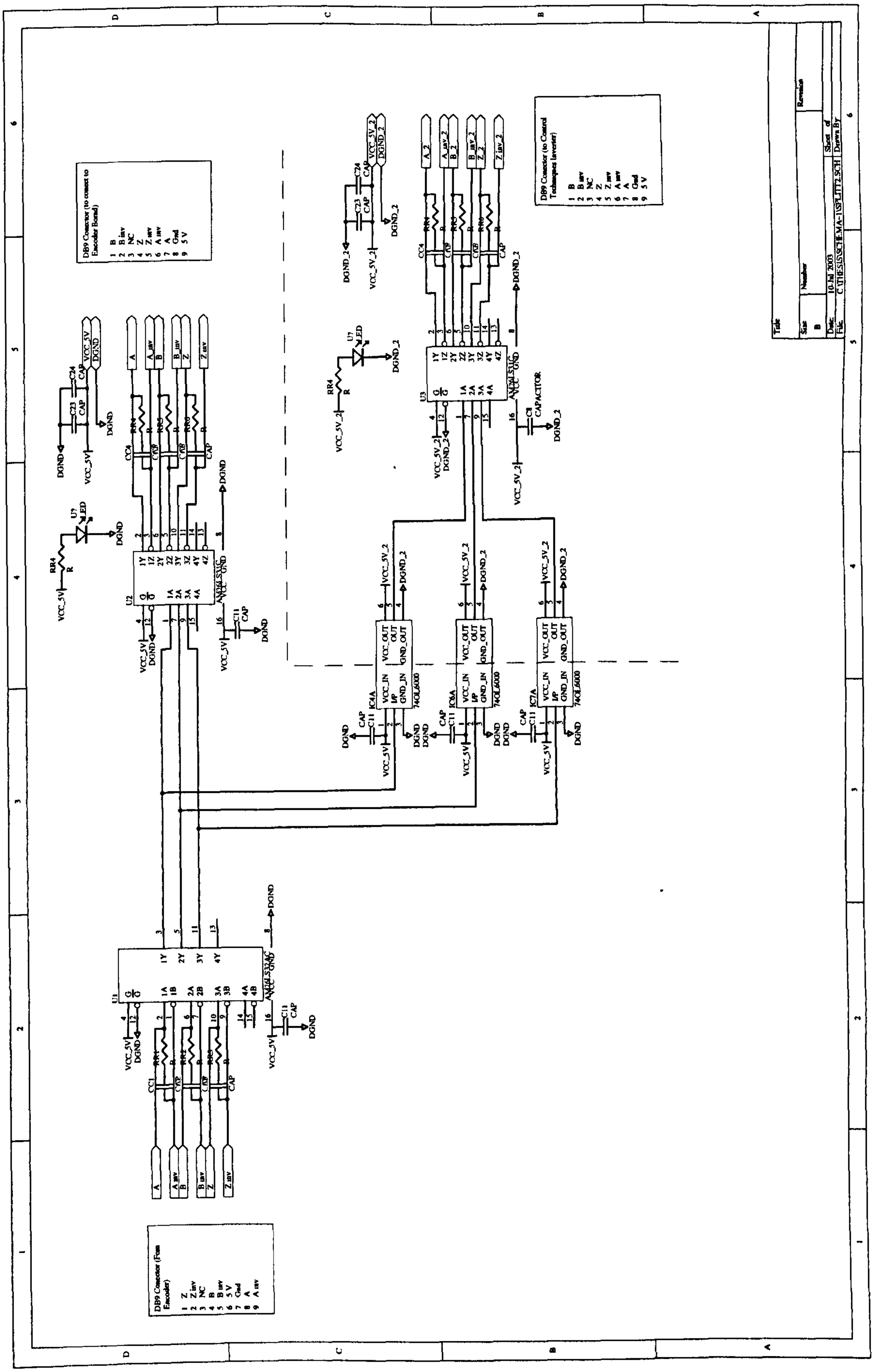

Figure A.4. Encoder signal split board schematic.

A.4 The PWM Board

The general layout of the board is shown in Fig. A.5. The 82C54 timer runs from a 10 MHz clock on the board achieving a resolution of 100 ns, the maximum pulse width being set to 100 μs so the values preloaded by the C44 in to the counter register (CR) of each timer is between 0 and 1000. This board contains only a single device and therefore only the address bits A6-A3 are used for address decoding. Four of the upper address lines A8-A12 are used as control lines for the 82C54 and the pulse inverting circuit:

A8: /WR, active low write pulse for the 82C52

A9-A10: ADDR0 and ADDR1 to select TIMER0, TIMER1 or TIMER2.

A11: /GATE, active low trigger pulse for the three timers.

A12: INVERT the PWM pulses.

The main timer circuit is shown in Fig. A.6. The use of address lines as strobe control signals /WR and /GATE of the 82C54 force the bus to be accessed twice for each write or timer triggering operation. In addition the CR is a 16-bit register and only an 8-bit data input is available. So two write operations are needed to load the CR: the first write operation automatically accesses the LSB and the second the MSB. The following example shows the code for the writing of the TIMER0 counter register.

```
#define _PWM0       0x0A0220118              /* A8=1 and addrs A9=0, A10=0 */

  t = (int)((ta * 10e6)+0.5);                /* t is time in sec. Clk is 10 MHz */
  *(_PWM0) = t << 16;                        /* Puts LSB in the bus */
  *(_PWM0 - 0x0100) = t << 16;               /* Change A8 to zero to /WR LSB */
  *(_PWM0) = t << 8;                         /* Puts MSB in the bus */
  *(_PWM0 - 0x0100) = t << 8;                /* Change A8 to zero to /WR MSB  */
```

The inversion is achieved by latching the INVERT signal synchronously with the PWM pulse using D-type latches 74F74 and passing this signal and the original pulse through XOR gates. The output stage is built as a current mirror to achieve immunity against the electromagnetic noise generated by the switching of the inverter. The

current mirrors produce digital current signals of amplitudes set to 0 and 10 mA, adequate to drive the receiving optocouplers.

Finally the board also contains a watchdog circuit, shown in Fig. A.7. This is a independent 12-bit counter built by the cascade of three 74LS163 and count the same onboard 10 MHz clock. These counters are reset with the trigger of the PWM pulses. A failure to trigger PWM pulses will allow the watchdog counter to reach the trip value set by the dipswitches (1152) and trigger a TIP signal.

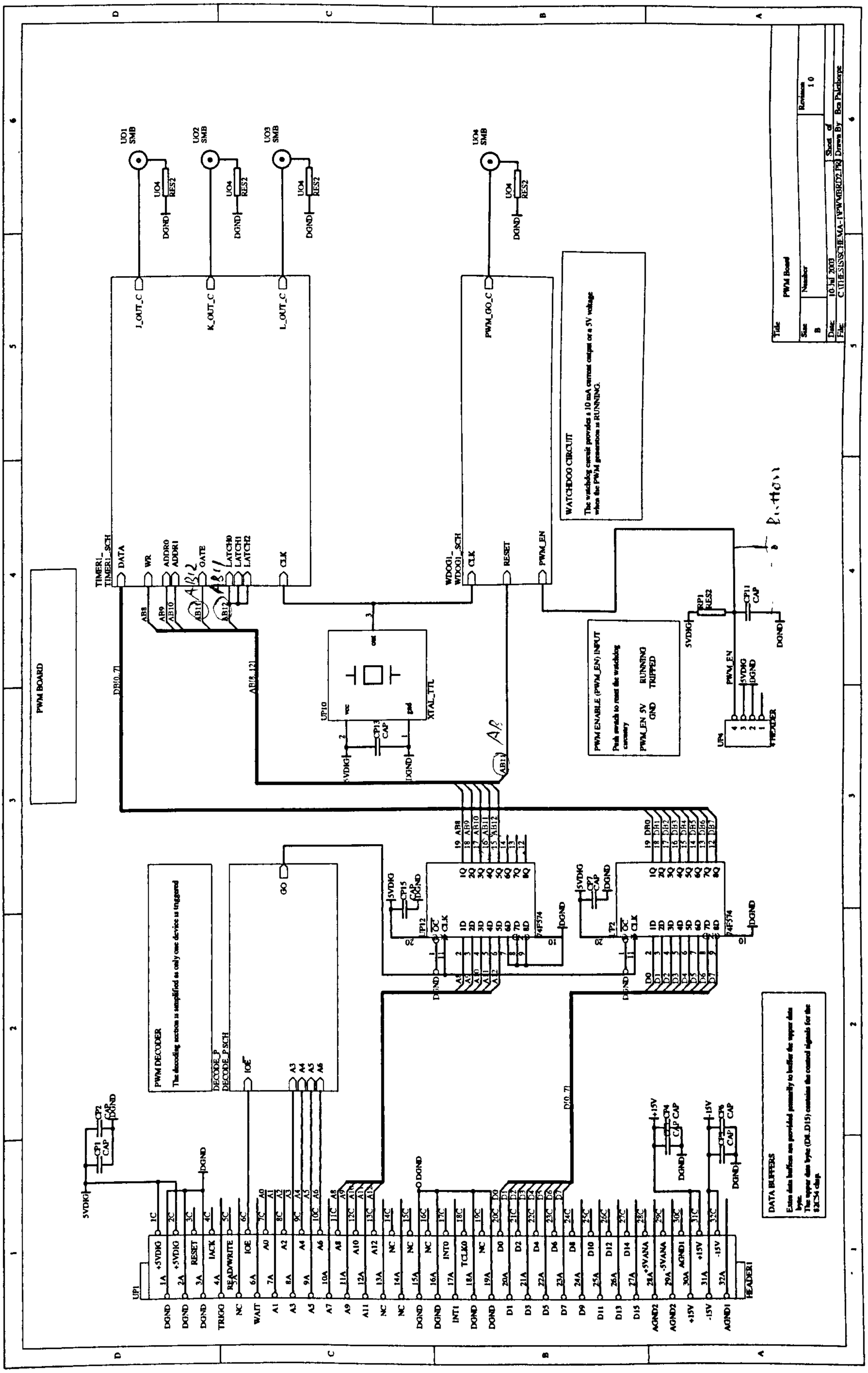

Figure A.5. PWM board schematic.

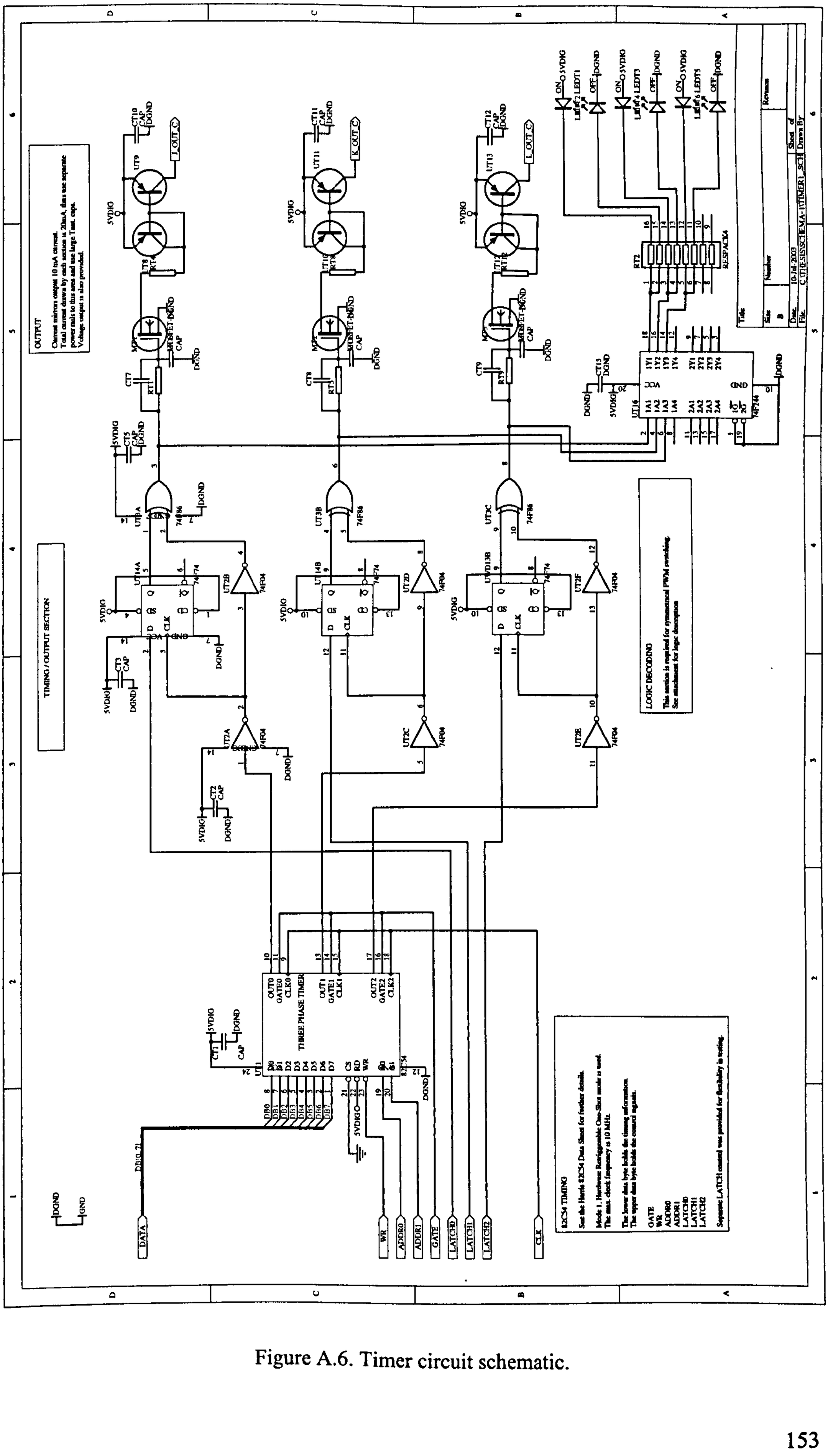

Figure A.6. Timer circuit schematic.

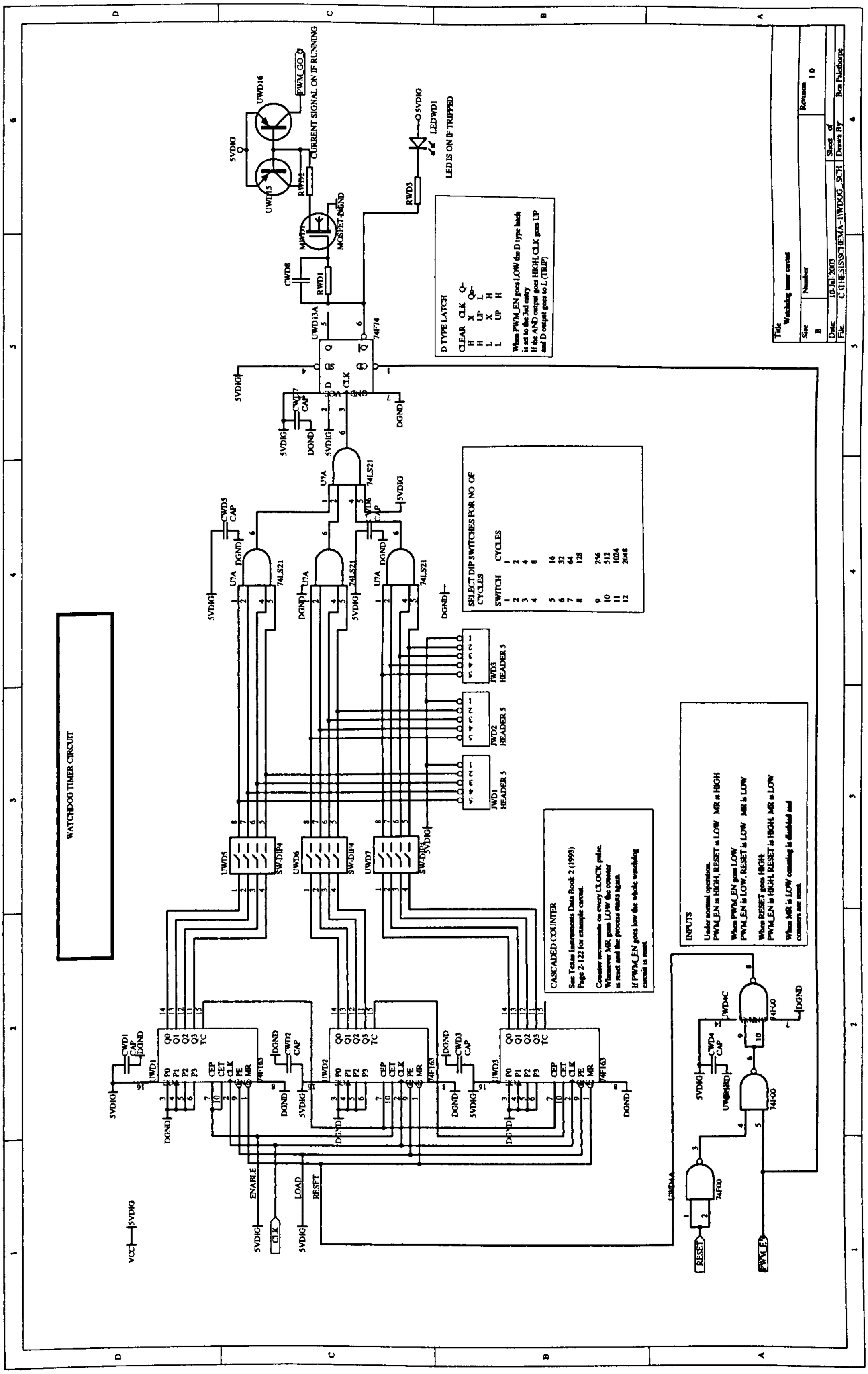

Figure A.7. Watchdog circuit schematic.

A.5 The Analogue to Digital Converter Board

The A/D board consists of four identical channels based on the 16-bit analogue to digital converter LTC1605. The general layout of the board is shown in Fig. A.8. The address decoding of this board is similar to that of the previous boards. Each channel is address individually for read operations by the four lower addresses of A2-A0. An access to the next address (100) is used to trigger the conversion of the four channels.

The schematic of the A/D channels is shown in Fig A.9. A differential receiver of unitary gain is used in the analogue input. The acquisition/conversion time of the LTC1605 is 10 μs. After the conversion, the /busy signal (pin 26 of the LTC1605) store the converted values in to the 74F574 buffers from where they can be read individually by the DSP.

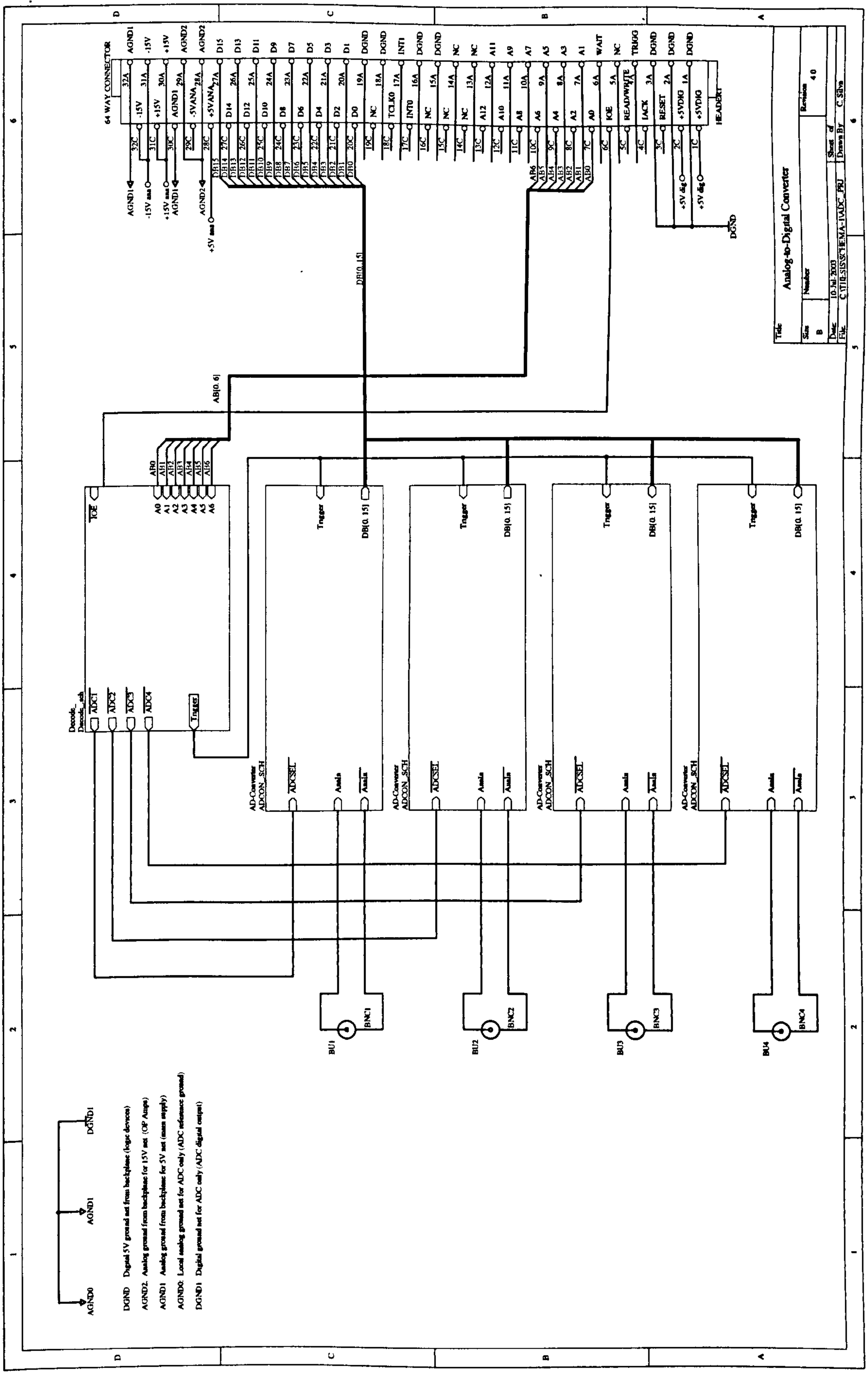

Figure A.8. A/D board connections.

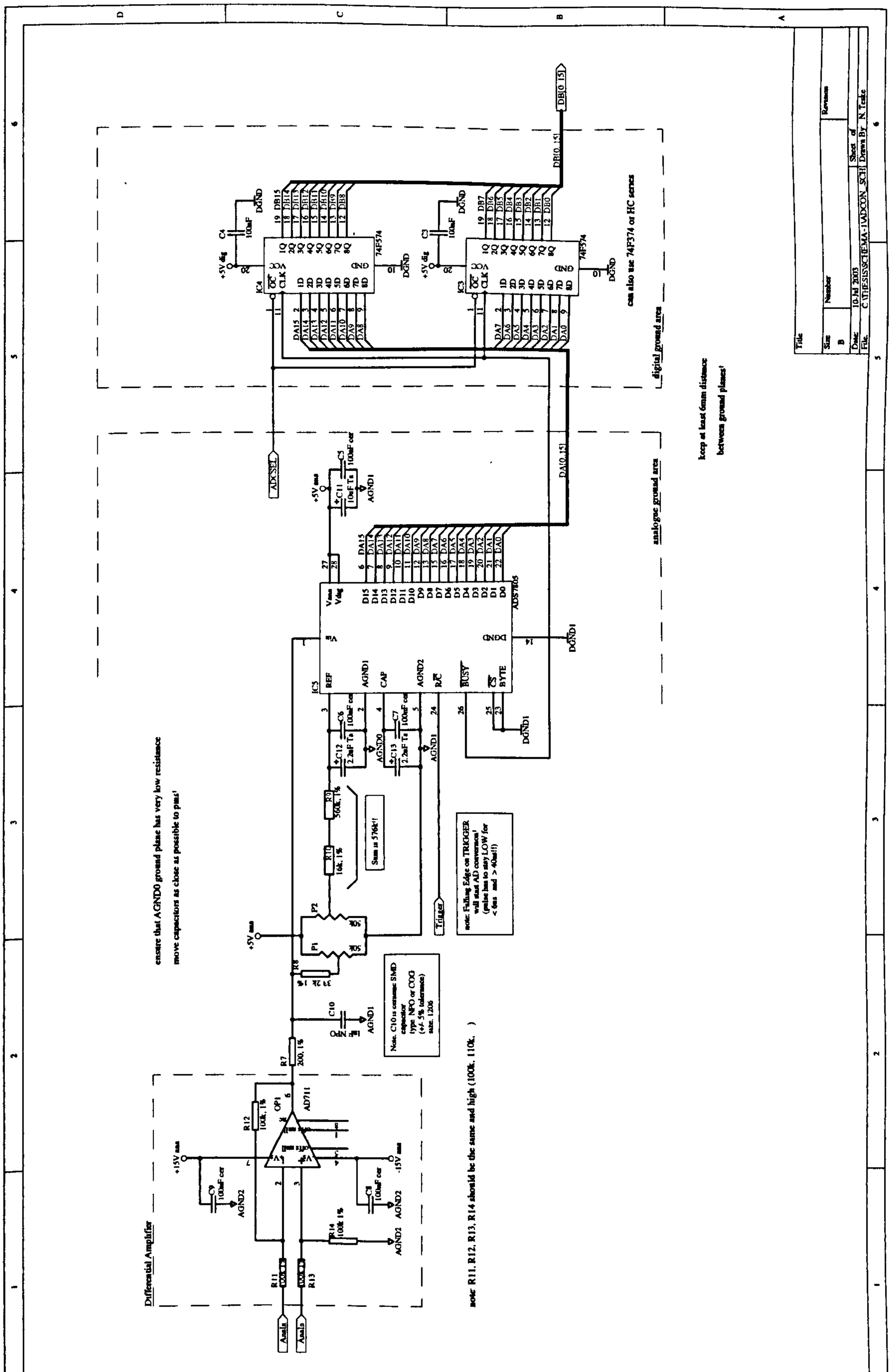

Figure A.9. Single A/D channel schematic.

A.6 The Inverter Interface

The *Eurotherm* inverter sends the gate pulses from a control board to the power circuit through a 26-way ribbon-cable. In order to interface the inverter with the DSP this cable is received on the interface board and the gates pulses replaced by those generated by the PWM board. The circuit diagram of the inverter interface board is shown in figure A.10. The PWM pulses and the watchdog signals are received by optocouplers to provide electrical isolation. The level of these signals is adequate to drive the internal LED of the optocouplers HCPT2611. The inverter side of the electric isolation provided by the optocouplers is powered from the inverters internal 5V power supplied that is available from the ribbon cable.

The gate pulses going into the inverter's power board need to include dead time. The delay in the turn-on edge of the gate pulse is achieved by a RC circuit cascaded by a Schmitt trigger inverter gate 74LS14. To avoid the delay in the turn-off edge a diode in parallel with the resistor is used. It is important to note that the gate drive pulses in the power circuit are active low so that the dead-time is introduced as an overlap of the gate drive signal.

The schematic in Fig. A.11 shows the trip logic. The objective of this circuit is to disable the gate pulses in the event of a watchdog trip coming from the PWM board, a trip coming form the inverter or from the STOP switch. After any trip the disable signal is latched by the 74LS74. The latch can only be cleared manually by the RESET push button and only if the all trip signals have been cleared.

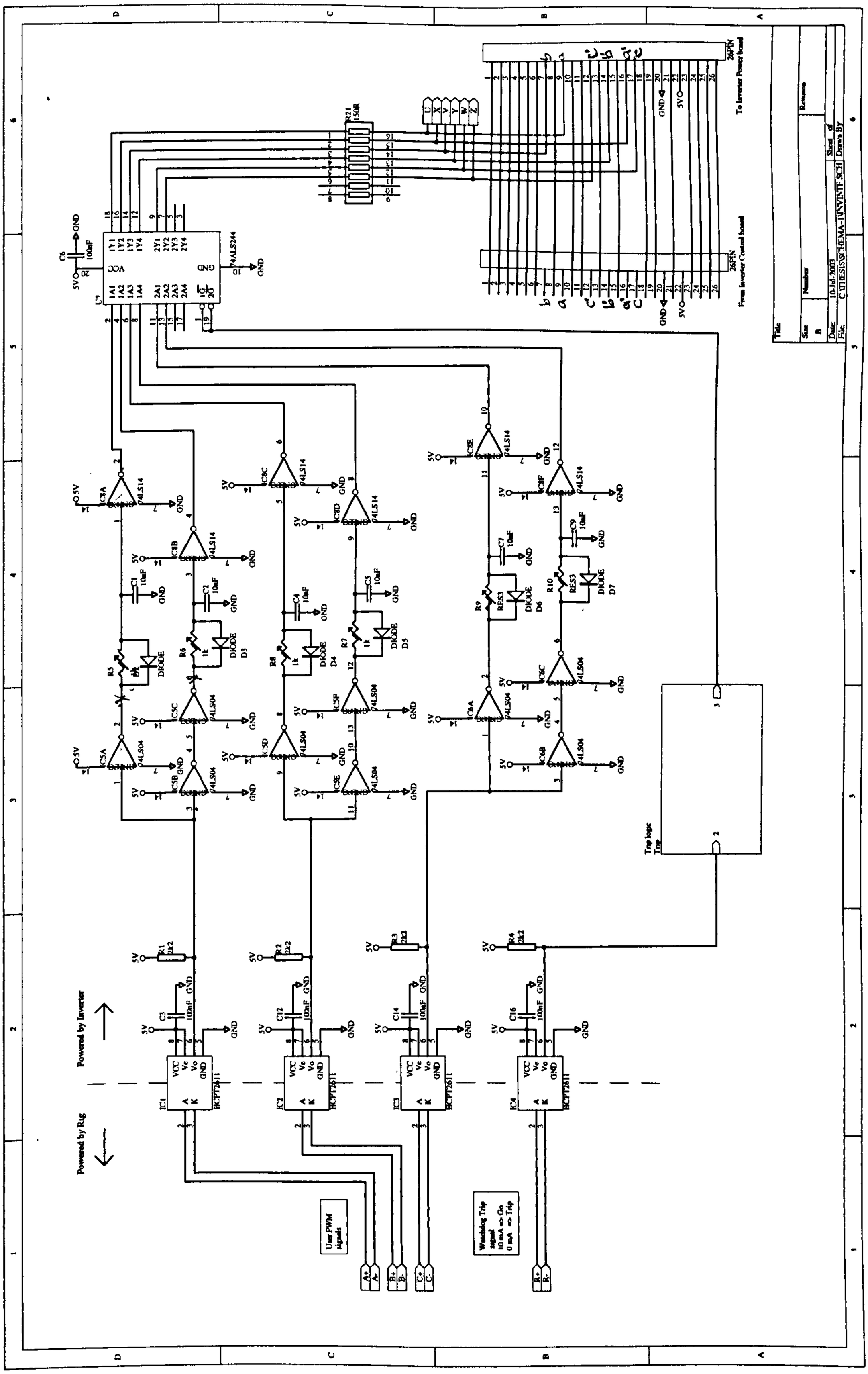

Figure A.10. Interface board schematic.

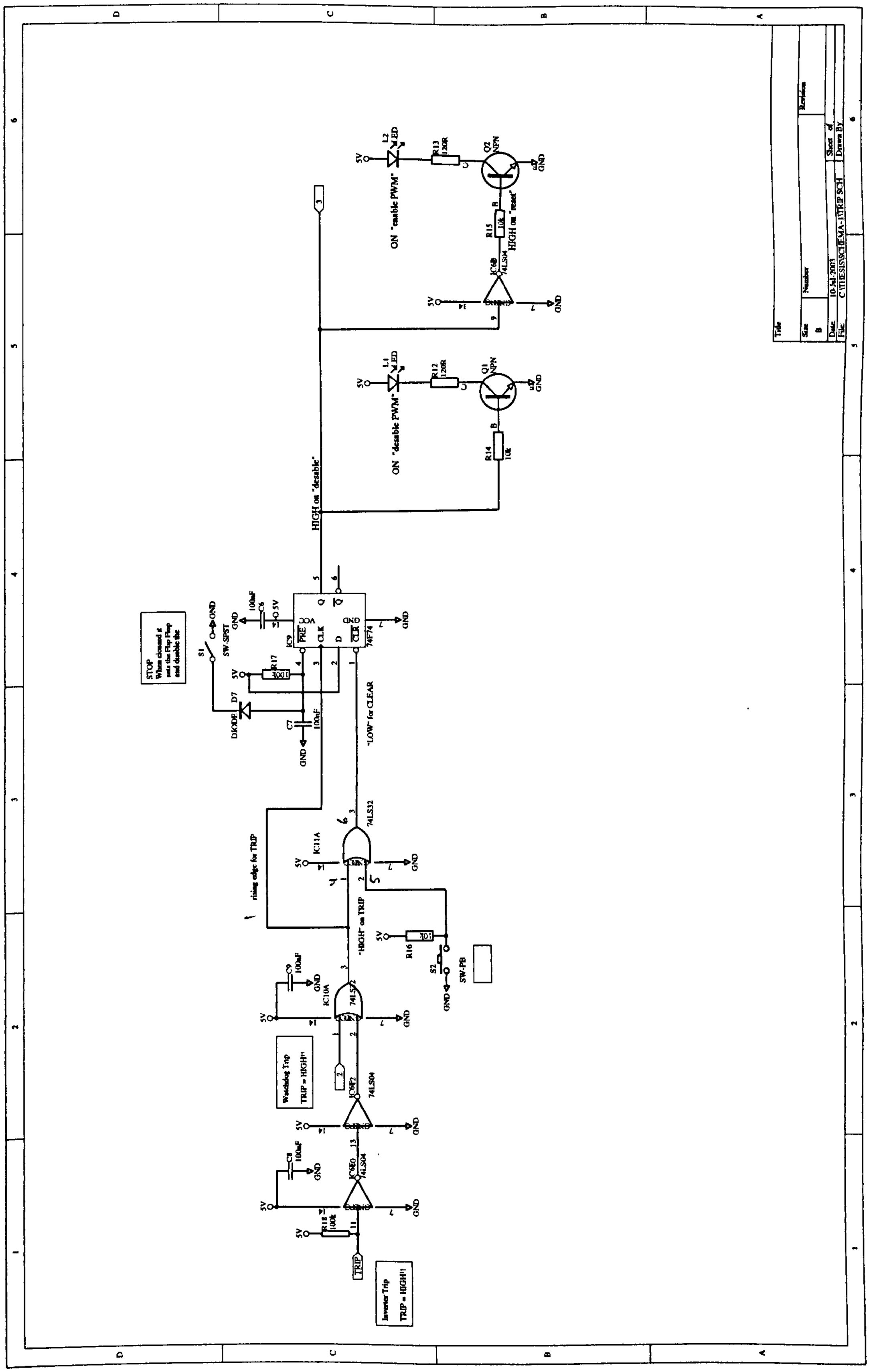

Figure A.11. Interface board trip logic schematic.

A.7 Current Detection Circuit

To detect current direction in the inverter phases two back-to-back power diodes are connected in series with the converter as explained in subsection 5.3.2.2. The voltage drop in the diodes is measured with comparators to detect the current direction, as shown in the circuit of Fig. A.12. Identical channels are used in each phase, these channels being isolated form the others because their potential varies from the positive to the negative DC-link potential depending on the switching state of the phase. The circuits are isolated using DC to DC isolated power supplies NMA0515S and opto-couplers (HCPT2611) for the output current direction signal. The signals are then transmitted to the digital I/O board as current logic signals of 0-10 mA using current mirrors to improve noise immunity. The board is powered by an external 5 V regulated power supply.

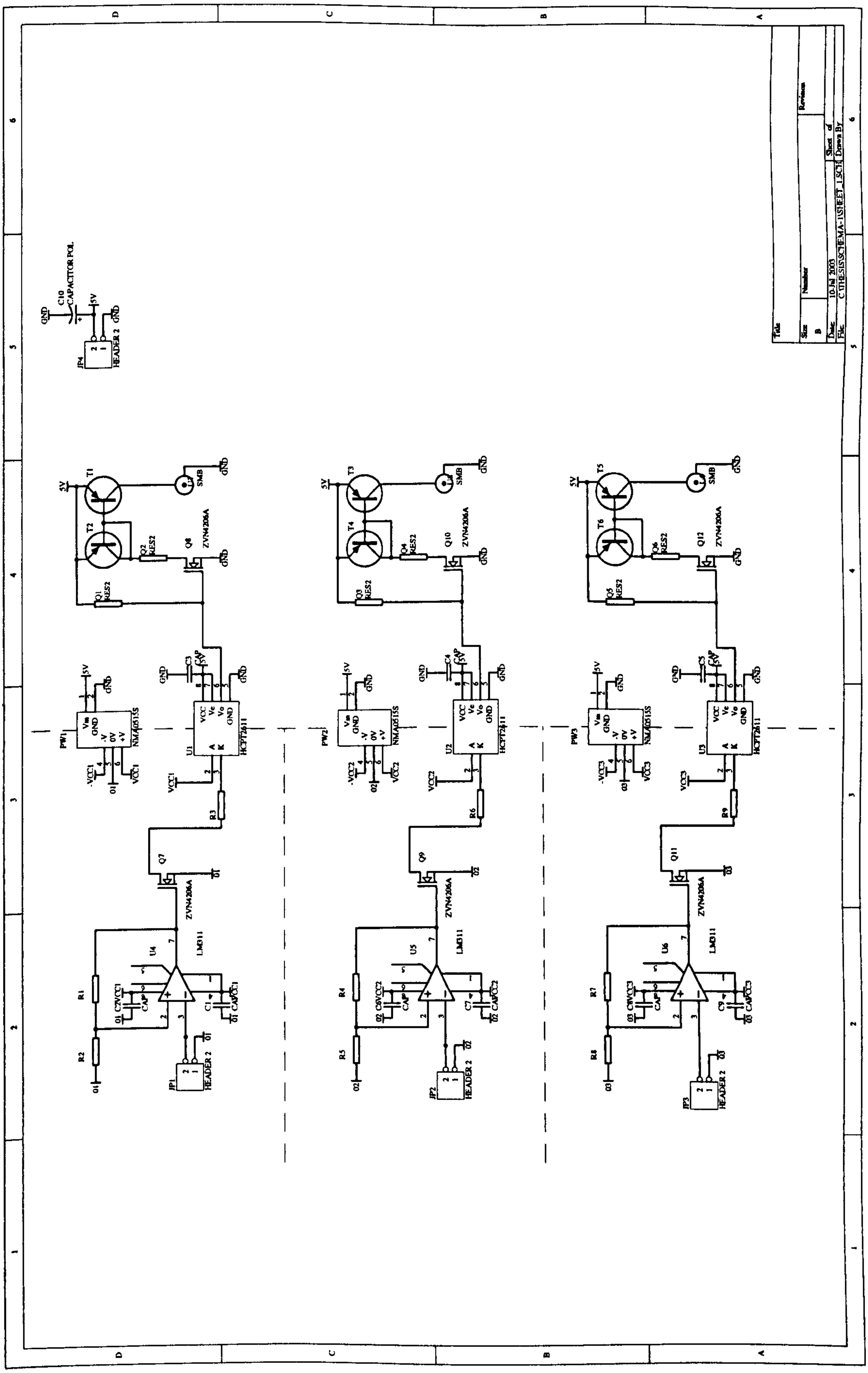

Figure A.12. Current detection circuit

Appendix B

B Phase-Shift Introduced by the Hardware Band-Pass Filters

In section 3.3.1 has been shown that in α-β rotating injection the negative sequence position harmonic frequency in the stationary α-β frame is $\omega_i - 2\omega_r$. The use of hardware band-pass filters, unavoidably in stator coordinates, for the separation of the *hf* injection component from the total phase current, introduces a speed dependent phase-shift in the position harmonic. Although the centre frequency of the filters has been chosen to match the injection frequency to assure zero phase shifts at zero rotor frequency, the change in frequency of the position harmonic when the machine is rotating results in a speed dependant phase-shift. The structure of the implemented filters is discussed and the phase shift introduced by them is analysed in this appendix.

The hardware band-pass filters are created by cascading a low-pass and high-pass Butterworth filters, both 4^{th} order, to obtain a centre frequency at 1 kHz which is the frequency of the injection voltage. The cut-off frequency of the filters have been chosen at values at the same logarithmic distance from this design centre frequency. The values of the cut-off frequency are chosen to be 1250 Hz and 800 Hz for the low-pass and the high-pass filters respectively. The nominal transfer functions for the 4^{th} order Butterworth filters are:

Low pass:

$$H_{lp} = \frac{\omega_{lp}^4}{\left(s^2 + 2\zeta_1\omega_{lp}s + \omega_{lp}^2\right)\left(s^2 + 2\zeta_2\omega_{lp}s + \omega_{lp}^2\right)} \tag{B.1}$$

and high pass:

$$H_{hp} = \frac{s^4}{\left(s^2 + 2\zeta_1\omega_{hp}s + \omega_{hp}^2\right)\left(s^2 + 2\zeta_2\omega_{hp}s + \omega_{hp}^2\right)} \tag{B.2}$$

Where the damping factors have the values $\zeta_1 = \cos(\frac{\pi}{8})$, $\zeta_2 = \cos(\frac{3\pi}{8})$ and the natural frequency values are determined by the designed cut-off frequencies $\omega_{lp} = 2\pi \cdot 1250$ and $\omega_{hp} = 2\pi \cdot 800$. The Bode plot for the resulting transfer function of the cascade of both filters is shown in Fig. B.1.

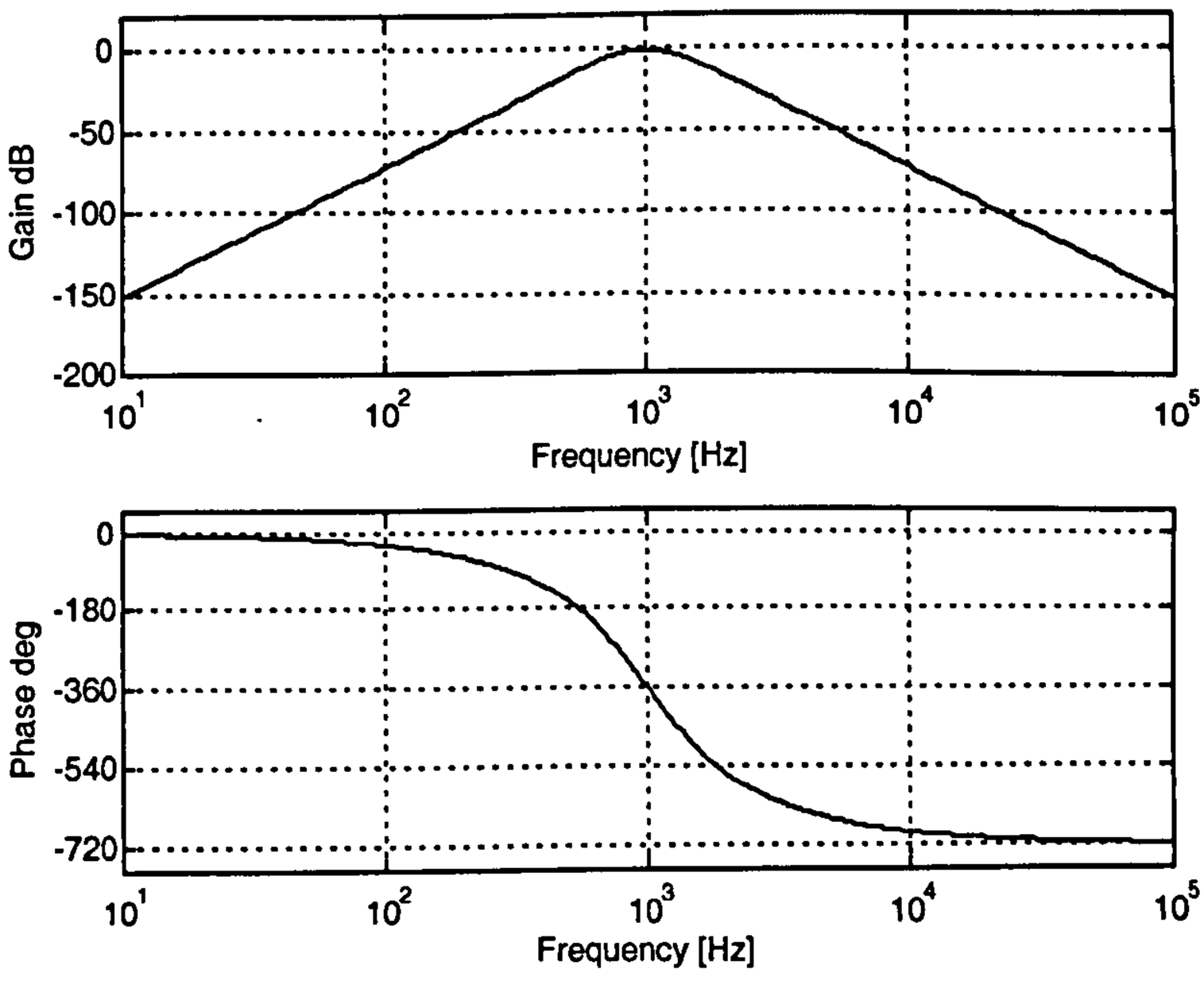

Figure B.1: Bode plot of the hardware band-pass filters.

Naturally the phase introduced by the filter is not a linear function of frequency. Nevertheless in the vicinity of the injection frequency, shown in Fig. B.2, the phase can be approximated by a linear equation. In this figure the 360° periodicity of the AC signals has been considered and therefore the phase curve crosses zero at the injection frequency. The approximate slope of this curve is given by:

$$\frac{\Delta\phi}{\Delta f} = \frac{3.50^\circ + 3.46^\circ}{20\,[\text{Hz}]} = 0.348\ [^\circ/\text{Hz}] \tag{B.3}$$

This number represent the rate of change of position harmonics phase shift per each Hz of deviation from the centre of the band-pass filter. The position harmonic is affected by double the excitation frequency. The demodulation of the saliency position harmonic also gives information on double the saliency position angle $2\theta_s$. Therefore the rate of change of ϕ given by (B.3) defines the shift in the saliency position estimation θ_s per Hz of excitation frequency f_e.

It is noted that this linear relationship is only valid at low excitation frequencies and it is only used for the commissioning of the SMP tables at the fixed excitation frequency of 3 Hz. No dynamic phase correction of saliency position estimation during operation is performed.

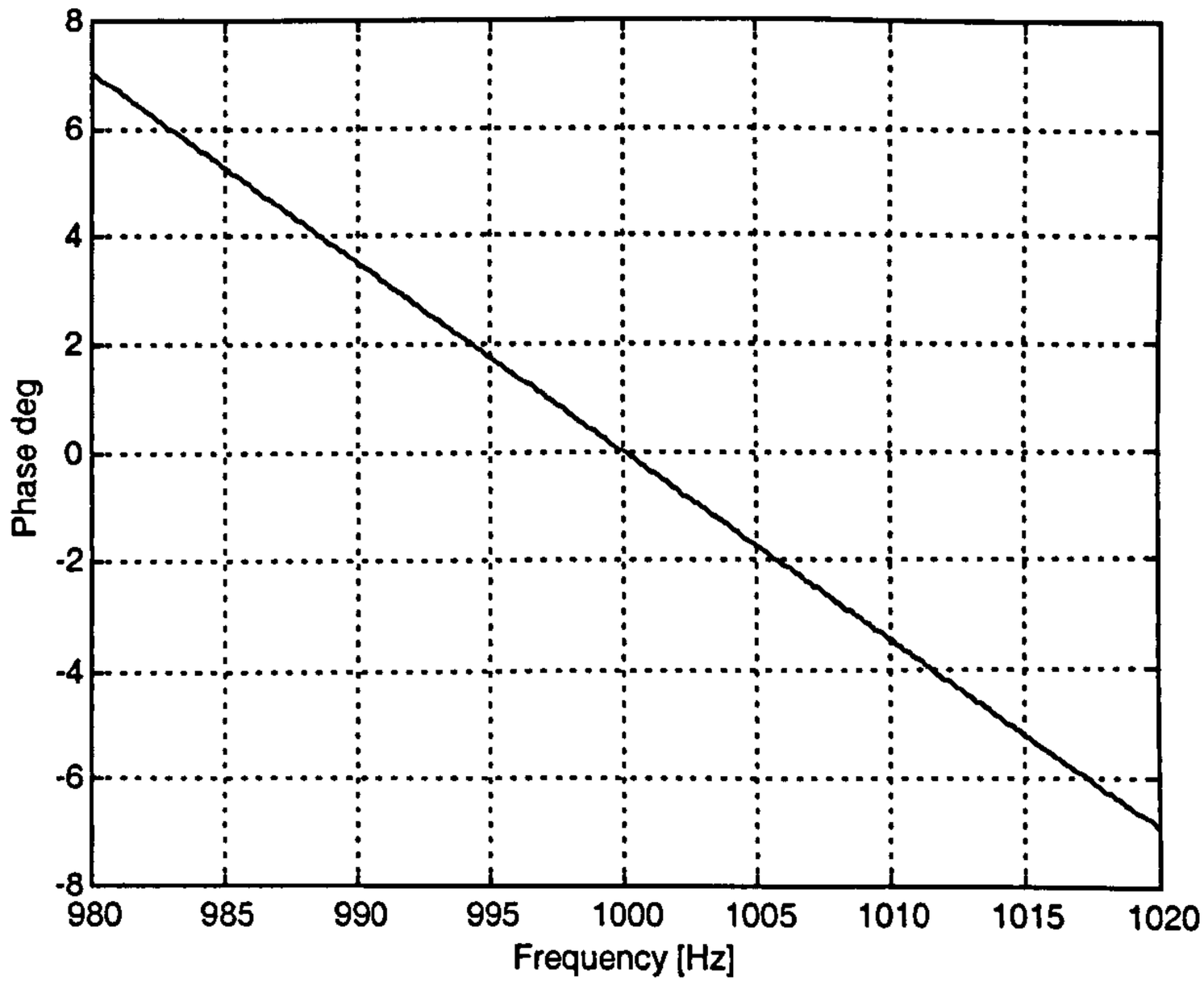

Figure B.2: Bode phase plot in the vicinity of the injection frequency.

Appendix C

C Effect of Hardware Band-Pass Filters in d-axis Pulsating Injection

In Section 3.2.2 it was mentioned that in all the implementations of synchronous frame pulsating injection presented in literature (normally *d-axis*, although *q-axis* also has been used), the band-pass filtering is performed in the rotating *d-q* frame and therefore is implemented in software. This is also the case for the *d-axis* injection method presented in this work. It as been stated in Chapter 3 that the phase introduced by the hardware band pass filters in the measured phase current signal path will result in loss of orientation at any speed significantly different than zero. In this Appendix an mathematical proof is presented to justify this. This proof consists of the reproduction of the signal processing equations of the *d-axis* injection presented in Chapter 3 and in assuming a phase shift introduced by the hardware band-pass filters as a result of non-zero speed. The propagation of this phase through the signal will result in an constant error signal which would cause the tracking algorithm to diverge.

Consider the pulsating voltage injection in the estimated saliency oriented δ^e-γ^e frame:

$$\begin{bmatrix} \tilde{v}_\delta^e \\ \tilde{v}_\gamma^e \end{bmatrix} = \hat{V}\begin{bmatrix} \sin(\omega_i t) \\ 0 \end{bmatrix} \tag{C.1}$$

The *hf* current response is

$$\begin{bmatrix} \tilde{i}_\delta^e \\ \tilde{i}_\gamma^e \end{bmatrix} = \frac{-\hat{V}\cos(\omega_i t)}{L_\delta L_\gamma \omega_i}\begin{bmatrix} L_s + \Delta L_s \cos(2\Delta\theta_\delta) \\ -\Delta L_s \sin(2\Delta\theta_\delta) \end{bmatrix} \tag{C.2}$$

The *hf* components of the currents in stationary frame can be found by the following transformation:

$$\begin{bmatrix} \tilde{i}_\alpha \\ \tilde{i}_\beta \end{bmatrix} = \begin{bmatrix} \cos(\hat{\theta}_\delta) & -\sin(\hat{\theta}_\delta) \\ \sin(\hat{\theta}_\delta) & \cos(\hat{\theta}_\delta) \end{bmatrix} \cdot \begin{bmatrix} \tilde{i}_\delta^{\,e} \\ \tilde{i}_\gamma^{\,e} \end{bmatrix} \tag{C.3}$$

At steady state the saliency frame rotates at synchronous speed and therefore, for the purpose of analysis, the position of the estimated saliency frame may be written as:

$$\hat{\theta}_\delta = \omega_e t + \Delta\theta_\delta \tag{C.4}$$

Substituting (C4) into (C.3), the transformation to the stationary frame is given by:

$$\begin{bmatrix} \tilde{i}_\alpha \\ \tilde{i}_\beta \end{bmatrix} = \begin{bmatrix} \cos(\omega_e t + \Delta\theta_\delta) & -\sin(\omega_e t + \Delta\theta_\delta) \\ \sin(\omega_e t + \Delta\theta_\delta) & \cos(\omega_e t + \Delta\theta_\delta) \end{bmatrix} \cdot \begin{bmatrix} \tilde{i}_\delta^{\,e} \\ \tilde{i}_\gamma^{\,e} \end{bmatrix} \tag{C.5}$$

Substituting (C.2) into (C.5), the *hf* currents in stationary frame are found to be:

$$\begin{aligned} \tilde{i}_\alpha = &-\frac{I_0}{2}[\cos(\omega_i t - \omega_e t - \Delta\theta_\delta) + \cos(\omega_i t + \omega_e t + \Delta\theta_\delta)] \\ &-\frac{I_1}{2}[\cos(\omega_i t - \omega_e t + \Delta\theta_\delta) + \cos(\omega_i t + \omega_e t - \Delta\theta_\delta)] \end{aligned} \tag{C.6}$$

$$\begin{aligned} \tilde{i}_\beta = &\frac{I_0}{2}[\sin(\omega_i t - \omega_e t - \Delta\theta_\delta) - \sin(\omega_i t + \omega_e t + \Delta\theta_\delta)] \\ &+\frac{I_1}{2}[\sin(\omega_i t - \omega_e t + \Delta\theta_\delta) - \sin(\omega_i t + \omega_e t - \Delta\theta_\delta)] \end{aligned} \tag{C.7}$$

Were the amplitude constants I_0 and I_1 are given by $I_0 = \dfrac{\hat{V} \cdot L_s}{L_\delta L_\gamma \omega_i}$ and $I_1 = \dfrac{\hat{V} \cdot \Delta L_s}{L_\delta L_\gamma \omega_i}$.

The currents given by (C.6) and (C.7) correspond exactly to that of (C.2), but expressed in the stationary frame.

The hardware band-pass filters are applied to the phase currents i_a, i_b and i_c. Nevertheless, for mathematical analysis they can be interpreted as directly applied to the stationary frame currents i_α and i_β because these are a linear combination of the phase currents. Therefore, the effect that the band-pass filters have on the *hf* components of the phase currents can be directly analysed in $\tilde{i}_\alpha$ and $\tilde{i}_\beta$.

The band-pass filters are design to give known phase shift at the central frequency ω_i. For the particular filter design used in this work this phase-shift is of 360° resulting in no effective phase shift (see bode plot shown in Fig. B.1). Nevertheless, a larger phase shift will be introduced when the *hf* component of the current is at a frequency higher than the central frequency resulting in an effective lag $-\phi_h$. Equally, *hf* current components at frequencies lower than the central frequency suffer a smaller phase-shift resulting in an effective positive phase shift ϕ_l or lead.

The *hf* currents at the stationary frame $\tilde{i}_\alpha$ and $\tilde{i}_\beta$ given by (C.6) and (C.7), are formed by two rotating components, at frequencies $\omega_i + \omega_e$ and $\omega_i - \omega_e$. When the machine rotates, i.e. $\omega_e \neq 0$, these two components move away from the centre frequency of the band-pass filter symmetrically and are affected by the filter phase shift $-\phi_h$ and ϕ_l respectively. Note that in reality the magnitude of the phase shift for the two components are different. Nevertheless, for small values of speed these magnitudes are approximately equal (as shown in Fig. B.2), i.e. $\phi_h \approx \phi_l$. In what follows both phase shifts will be considered to have the same magnitude ϕ for simplicity. Considering this phase shift in (C.6) and (C.7) the filtered *hf* current components, denoted by the super-index *f*, are given by:

$$\begin{aligned}\tilde{i}_\alpha^{\,f} = &-\frac{I_0}{2}[\cos(\omega_i t - \omega_e t - \Delta\theta_\delta + \phi) + \cos(\omega_i t + \omega_e t + \Delta\theta_\delta - \phi)] \\ &-\frac{I_1}{2}[\cos(\omega_i t - \omega_e t + \Delta\theta_\delta + \phi) + \cos(\omega_i t + \omega_e t - \Delta\theta_\delta - \phi)]\end{aligned} \tag{C.8}$$

$$\begin{aligned}\tilde{i}_\beta^{\,f} &= \frac{I_0}{2}[\sin(\omega_i t - \omega_e t - \Delta\theta_\delta + \phi) - \sin(\omega_i t + \omega_e t + \Delta\theta_\delta - \phi)] \\ &+ \frac{I_1}{2}[\sin(\omega_i t - \omega_e t + \Delta\theta_\delta + \phi) - \sin(\omega_i t + \omega_e t - \Delta\theta_\delta - \phi)]\end{aligned} \tag{C.9}$$

Rotating the currents of (C.8) and (C.9) back to the estimated saliency frame δ^e-γ^e by:

$$\begin{bmatrix}\tilde{i}_\delta^{\,ef} \\ \tilde{i}_\gamma^{\,ef}\end{bmatrix} = \begin{bmatrix}\cos(\omega_e t + \Delta\theta_\delta) & \sin(\omega_e t + \Delta\theta_\delta) \\ -\sin(\omega_e t + \Delta\theta_\delta) & \cos(\omega_e t + \Delta\theta_\delta)\end{bmatrix} \cdot \begin{bmatrix}\tilde{i}_\alpha^{\,f} \\ \tilde{i}_\beta^{\,f}\end{bmatrix} \tag{C.10}$$

yields:

$$\begin{bmatrix}\tilde{i}_\delta^{\,ef} \\ \tilde{i}_\gamma^{\,ef}\end{bmatrix} = \frac{-\hat{V}\cos(\omega_i t)}{L_\delta L_\gamma \omega_i} \begin{bmatrix}L_s\cos(\phi) + \Delta L_s\cos(2\Delta\theta_\delta + \phi) \\ -L_s\sin(\phi) - \Delta L_s\sin(2\Delta\theta_\delta + \phi)\end{bmatrix} \tag{C.11}$$

It must be noted that in the *d-axis* injection strategy, the quadrature component of the *hf* current vector $\tilde{i}_\gamma^{\,e}$ is used as a measure of the misalignment between the estimated and actual saliency frame $\Delta\theta_\delta$. A tracking loop is used to adjust the orientation of δ^e-γ^e in order to drive $\tilde{i}_\gamma^{\,e}$ to zero. If hardware band-pass filters are used, (C.11) shows that, the condition of $\tilde{i}_\gamma^{\,ef} = 0$ doesn't result in zero orientation error $\Delta\theta_\delta$ at synchronous speeds different than zero, i.e. the saliency position is tracked with error. Further more, if the speed is sufficiently large so that the phase shift ϕ introduced by the band pass filters results in:

$$L_s\sin(\phi) > \Delta L_s \tag{C.12}$$

Then the condition $\tilde{i}_\gamma^{\,ef} = 0$ can not be satisfied and the tracking is lost completely.

The critical value of phase shift that will cause the strategy to lose tracking can be calculated from (C.12) by considering the values for the inductance of the machine. For the purpose of estimating the critical phase shift, the inductances of the machine

used in this work can be approximated by $L_s = 5$ mH and $\Delta L_s = 0.5$ mH and the critical value of phase shift is given by:

$$\sin(\phi) = 0.1 \Rightarrow \phi \approx 5.7^\circ$$

If the band pass filters implemented for the α-β rotating injection were to be used for the *d-axis* injection, Fig. B.2 shows that the critical phase shift of $\phi \approx 5.7^\circ$ would be reached at a frequency of 16.3 Hz, i.e. at a rotor speed of 326 rpm. This shows that relatively low rotor speeds are sufficient to make the *d*-axis injection method fail to track saliency when hardware band pass filters are used. This phenomenon is illustrated in Fig. C.1, this figure corresponds to a large position step under sensored conditions and the *d-axis* injection applied only for tracking. The band-pass filters described in Appendix B are used for separation of the injection current. During the position transients the rotor reaches speeds above 40 rad/sec (approximately 380 rpm) and the angle estimation looses track momentarily, when the rotor slow down the PLL locks again but the rotor position has an accumulated error of 180° electrical.

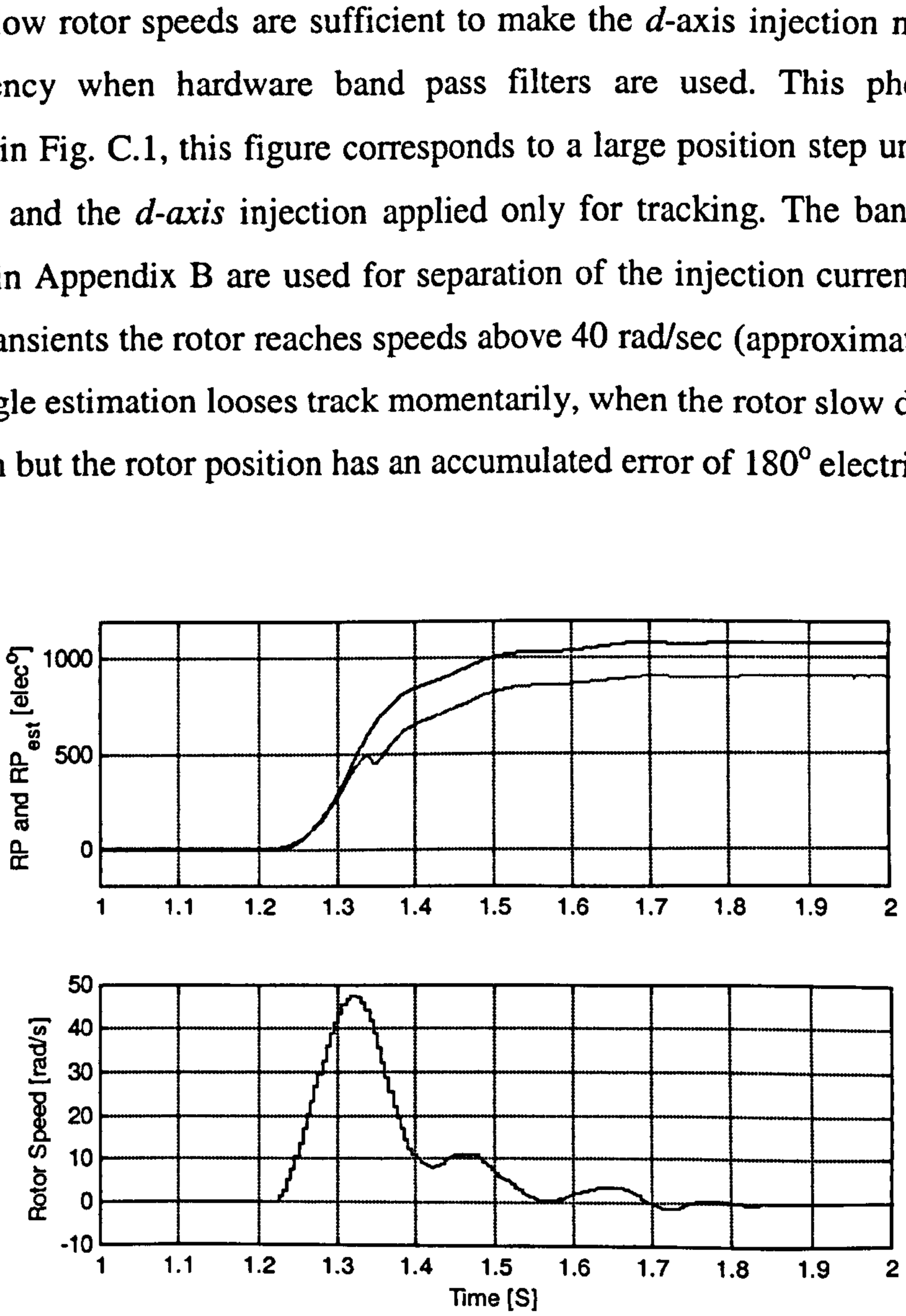

Figure C.1: Position tracking using *d-axis* injection and hardware band-pas filters.

Appendix D

D Published Papers

The work has resulted in the following papers having been published:

- Cesar Silva, Greg M. Asher and Mark Sumner, "Influence of Dead-Time Compensation on Rotor Position Estimation in Surface Mounted PM Machines using HF Voltage Injection," *in Proc. PCC Conf. Osaka, Japan,* on CD-ROM, April 2002.
- C. Silva, G.M. Asher, M. Sumner and K.J. Bradley, "Sensorless Rotor Position Control in a Surface Mounted PM Machine Using HF Voltage Injection," *in Proc. PEMC Conf. Cavtat & Dubrovnik, Croatia*, on CD-ROM, Sept. 2002.
- C. Silva, G. M. Asher, M. Sumner, "An hf Signal-Injection Based Observer for Wide Speed Range Sensorless PM Motor Drives Including Zero Speed," *accepted for publication in EPE Conf, Toulouse, France*, Sept. 2003.

Influence of Dead-Time Compensation on Rotor Position Estimation in Surface Mounted PM Machines using HF Voltage Injection

Cesar Silva, Greg M. Asher and Mark Sumner
School of Electrical and Electronic Engineering
University of Nottingham, Nottingham NG7 2RD, UK
E-Mail: csj@eee.nottingham.ac.uk

Abstract

This paper addresses the problem of rotor position estimation in a surface mounted permanent magnet (SMPM) machine using HF rotating voltage vector injection. The low saliency of these machines causes a relatively low magnitude of the modulated signals carrying the position information and engineering factors affect the resulting accuracy of the position angle estimate. The paper shows that the dominant effect is that of the inverter's dead time. The paper reviews and implements state-of the-art dead time compensations methods to enhance the accuracy of the position estimate. Experimental results show the numerical improvement in positional accuracy and prove the necessity of using good compensation methods for position estimation in low saliency machines.

Keywords: Permanent Magnet Synchronous Machine, Sensorless Position Estimation, Dead Time Compensation.

1 Introduction

Permanent magnet synchronous motors have numerous advantages over induction machines: higher efficiency, higher power density and better dynamic performance. To control a PM machine accurate knowledge of the rotor position is needed and PM machines drives use optical encoders for position measurement. This reduces the overall reliability and increases cost. For this reason, intensive research has been carried out in recent years to achieve sensorless vector control of PM machines. The sensorless position detection techniques can be divided into two main categories. The first is that of model based techniques which integrate the machine back EMF to obtain the flux; however these strategies fail at low speed when insufficient back EMF is induced. The second utilises an injected signal to track magnetic silences of the machine [1],[2].

High Frequency carrier injection has been used for rotor position detection on synchronous reluctance machines [3] and on buried magnet PM machines [4]-[6]. The technique relies on differences in the magnetic paths of the machine, or saliency, and is characterised by the variation in the direct and quadrature stator inductance L_d and L_q. In buried magnet machines ratios of L_q / L_d are in the region of 3 or greater [7] and application of HF injection is relatively straightforward.

The application of HF injection to SMPM machines is more problematic. The amount of saliency in this type of machines is small, with reported ratios L_q/L_d smaller than 1.5 [8]. Whilst these ratios are quite adequate in principle, the small saliencies make the position estimation strategy more prone to perturbance and noise. In this paper the voltage distortion due to the inverter's dead time is identified as the most important source of perturbance for the HF injected voltage method. It is also noted that because the intrinsic saliency of SMPM machines is lower, the influence of the magnetic saturation in the stator teeth, which causes a load dependent phase shift between the *d* axis of the machine and the derived saliency position, also becomes more significant. This "saturation saliency" is a separate effect and is not addressed in the paper.

It is well known that commutation due to the finite turn off time of the semiconductor devises, dead time is needed to prevent shoot-through during the commutation. The dead time voltage distortion, although small, is significant when compared with the magnitude of the injected HF carrier voltage which has to be kept as small as possible to reduce the additional losses, the HF pulsating torque and acoustic noise. The dead-time compensation strategies investigated in this paper are those recently reported in [9][10][11]. It is noted these works addressed the improvement in the fundamental current waveform at low speed motor operation. In this paper, the dead time compensation techniques are exploited to improve the sensorless rotor position detection by reducing the perturbances in the HF voltage carrier.

The paper briefly reviews the use of HF voltage injection method for estimating the rotor position angle in a SMPM machine. The dead time phenomenon is briefly reviewed and it's effect on the HF voltage

injection method is presented. The compensation strategy based on [9][10] is discussed and experimental results are shown to illustrate the improvement in the position estimates of the HF voltage injection method by means of dead time compensation.

2 Position estimation of SMPM machine through HF Rotating Voltage Vector Injection

To detect rotor position by high frequency injection a magnetic saliency is needed in the machine. This means that the inductance measured in the stator terminals of the machine must be a function of the rotor position. Asymmetric rotor construction and magnetic saturation produce this saliency. The first type of saliency is fixed to the rotor and therefore gives absolute rotor position information. SMPM machines are generally considered to have symmetrical rotors, but a small amount of geometrical asymmetry is normally present due to the semi-insertion of the magnets into the rotor iron, as shown in Fig. 1. This saliency, although small, is shown here to be quite sufficient for rotor position estimation. Saturation-induced saliency on the other hand is not fixed to the rotor and will be affected by the stator currents. This will produce a load dependent shift of the saturation position which has to be taken in to account in the final design of the estimator.

In a SMPM machine with semi-inserted magnets, as shown in Fig. 1, the extra iron in the quadrature magnetic path q and the stator's teeth saturation in the flux direction d result in small saliency in the effective air gap length. As a result, the inductance in the flux axis L_d is smaller than the inductance in the quadrature axis L_q producing the stator inductance to be a function of the rotor position as shown in Fig. 2.

The stator frame (α-β) model of a salient PM machine [5] is given by (1).

$$\begin{bmatrix} v_\alpha \\ v_\beta \end{bmatrix} = \begin{bmatrix} r_s & 0 \\ 0 & r_s \end{bmatrix} \cdot \begin{bmatrix} i_\alpha \\ i_b \end{bmatrix} + \begin{bmatrix} s & 0 \\ 0 & s \end{bmatrix} \cdot \begin{bmatrix} \lambda_\alpha \\ \lambda_\beta \end{bmatrix}$$
$$\begin{bmatrix} \lambda_\alpha \\ \lambda_\beta \end{bmatrix} = \begin{bmatrix} L_s - \Delta L_s \cos(2\theta_r) & -\Delta L_s \sin(2\theta_r) \\ -\Delta L_s \sin(2\theta_r) & L_s + \Delta L_s \cos(2\theta_r) \end{bmatrix} \cdot \begin{bmatrix} i_\alpha \\ i_\beta \end{bmatrix} + \lambda_m \begin{bmatrix} \cos(\theta_r) \\ \sin(\theta_r) \end{bmatrix} \quad (1)$$

A high frequency rotating voltage vector v_i and frequency ω_i, (2), is superimposed on to the fundamental actuation voltages, and provided that ω_i is outside the bandwidth of the current loops the resulting high frequency currents i_i is determined by the high frequency impedance of the machine. Further more, if $\omega_i L >> r_s$ the impedance is dominated by the inductance matrix and (1) can be approximated by (3).

$$v_i = \begin{bmatrix} v_{\alpha i} \\ v_{\beta i} \end{bmatrix} = \begin{bmatrix} -v_i \sin(\omega_i \cdot t) \\ v_i \cos(\omega_i \cdot t) \end{bmatrix} = v_i e^{j\omega_i t + \frac{\pi}{2}}, \quad (2)$$

$$\begin{bmatrix} v_{\alpha i} \\ v_{\beta i} \end{bmatrix} \approx s \cdot \begin{bmatrix} L_s - \Delta L_s \cos(2\theta_r) & -\Delta L_s \sin(2\theta_r) \\ -\Delta L_s \sin(2\theta_r) & L_s + \Delta L_s \cos(2\theta_r) \end{bmatrix} \cdot \begin{bmatrix} i_{\alpha i} \\ i_{b i} \end{bmatrix} \quad (3)$$

Substituting (2) in to (3) and solving for i_i gives:

$$i_i = \frac{L}{L^2 - \Delta L^2} \frac{v_i}{\omega_i} \cdot e^{j\omega_i t} + \frac{\Delta L}{L^2 - \Delta L^2} \frac{v_i}{\omega_i} \cdot e^{j(2\theta_r - \omega_i t)} \quad (4)$$

In (4) the position information θ_r is contained only in the negative sequence of i_i and therefore this sequence has to be extracted. An efficient way of doing this is using the synchronous filter shown in Fig. 3. The first rotation of co-ordinates converts the positive sequence in DC current, which can be totally eliminated by a high pass filter. The second rotation brings the negative sequence to the base-band where the angle information can then be extracted by mean of a tan^{-1} function, a *PLL* or a tracking observer [1].

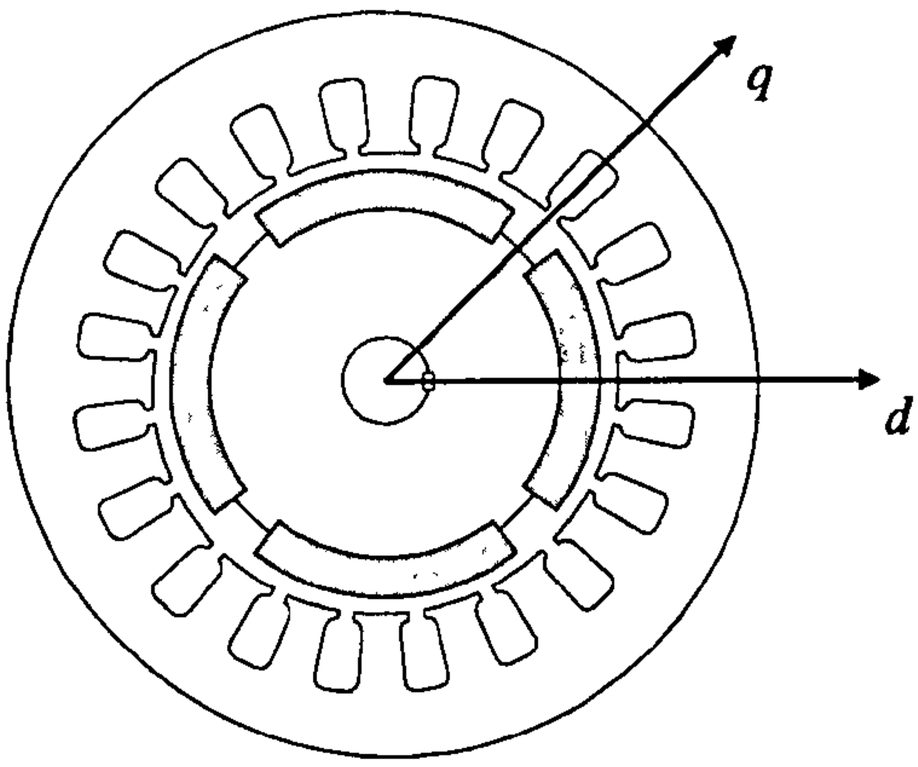

Fig. 1. Surface mounted PM machine with semi-inserted magnets

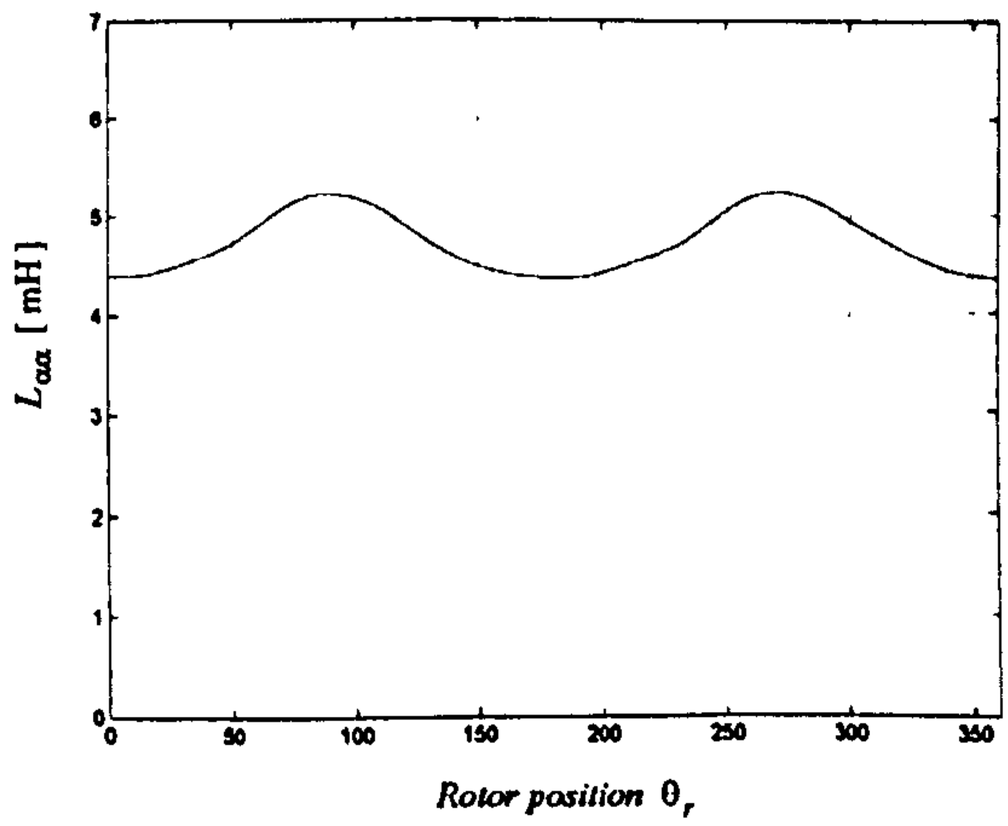

.Fig. 2. Machine stator inductance L_{hf}, measured at 1kHz, no-load

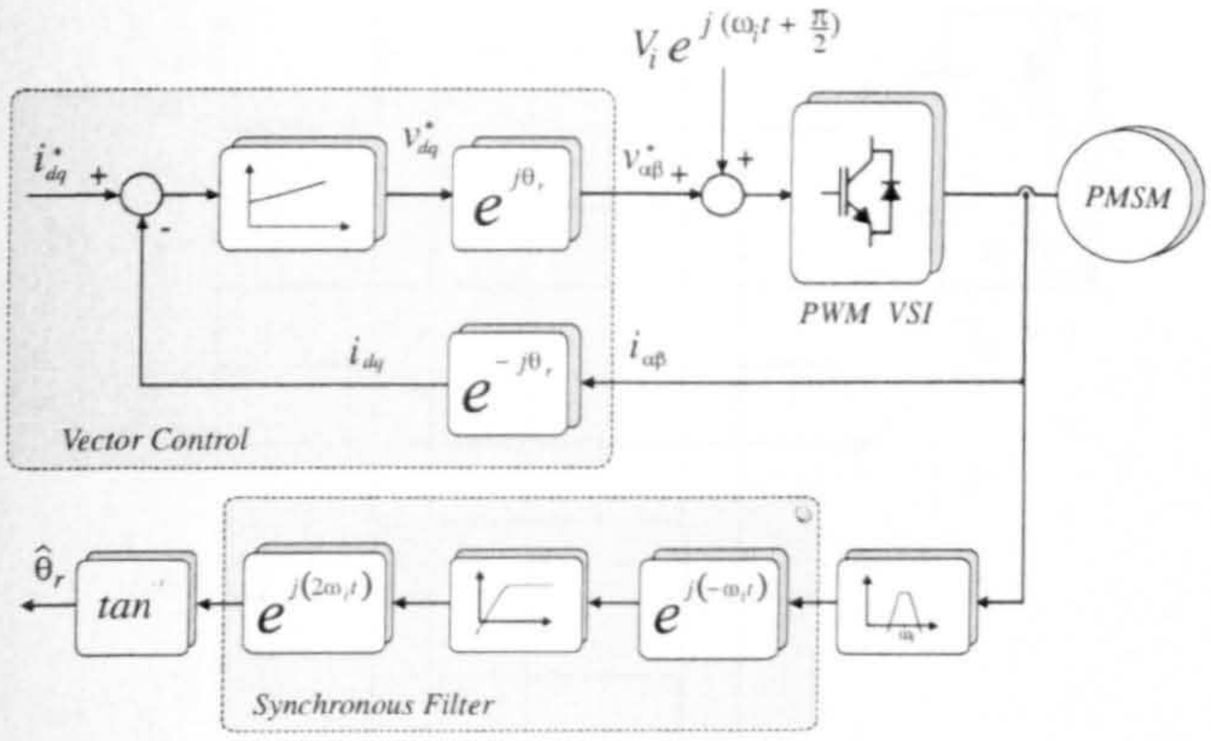

Fig. 3. Synchronous filter to eliminate the positive sequence.

3 Influence of the inverter's dead time in the HF voltage injection

It is well known that the inverter's dead time generates a distortion on the output voltages of a PWM voltage source inverter. This perturbance can be modelled as a voltage of constant magnitude, which is added or subtracted to the inverter's phase voltage when the phase current is negative or positive respectively [8]. Fig. 4 shows the block diagram used to simulate a single-phase inductive load being exited by a fundamental voltage and HF injection voltage where the dead time perturbance voltage v_d has being included using the model described above [8].

The simulation results of this model are presented in Fig. 5. When the load current i_L is sufficiently small in magnitude its high frequency component will produce multiple zero crossings, this generates the dead time voltage distortion v_d shown in (b). This voltage has a strong component at the injection frequency during the current zero crossing and results in a reduction in the amplitude of the HF current at these instants; this effect is called *dead time modulation* and can be seen in the HF current component i_i shown in (c).

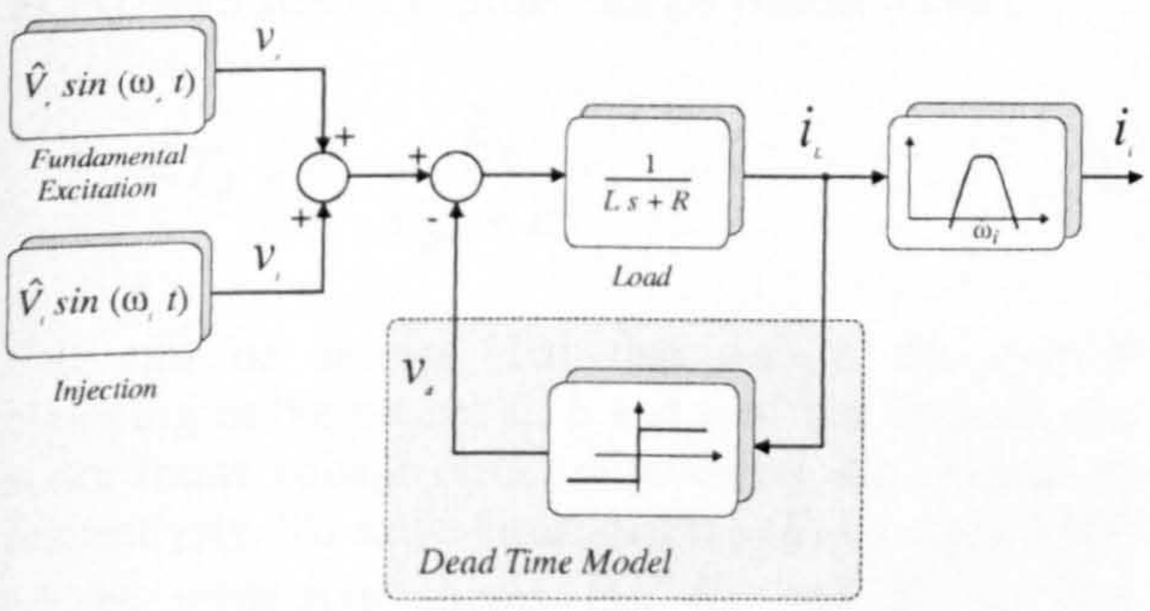

Fig. 4. Basic dead time model.

4 Dead-time compensating methods

The dead time modulation will produce considerable errors in the rotor position estimation if its magnitude is comparable with the modulation produced by the rotor saliency. This is the case for an SMPM machine and a dead time compensation strategy is required. In this paper the dead time distortion is compensated by two complementary techniques: First a *standard dead time compensation* is implemented by advancing or delaying the inverter's gate pulses depending on the phase current direction [9]. This technique tends to be less accurate when the phase current is near zero due to current clamping. Therefore a *current clamping feed forward compensation* is also implemented by estimating the voltage distortion due to this effect and adding it to the PWM voltage reference [10].

4.1 Standard Dead Time Compensation

Fig. 6 illustrates the principle of the *standard dead time compensation*. Fig 6(a) shows the reference voltage pulse calculated by the PWM algorithm. Fig. 6(b) and (c) correspond to the gate signals including the dead time or turn on delay. The direction of the current, positive in this case, will produce the output voltage V_{a0} of Fig 6(d); the error between V_{a0} and $V_{a0}{}^*$ is evident. To overcame this problem the first edge of the reference voltage can be advance in T_{comp} generating the new gate signals g_1' and g_2' of Figs 6(e) and (f) respectively. This results in the output voltage V_{a0}'shown in Fig 6(g). In the same way if the phase current i_a is negative, the second edge of the reference voltage is advanced by T_{comp}.

The value of T_{comp} is approximately equal to the dead time T_d but it can be further adjusted to take in to account the difference between the turn on and turn off times of the device.

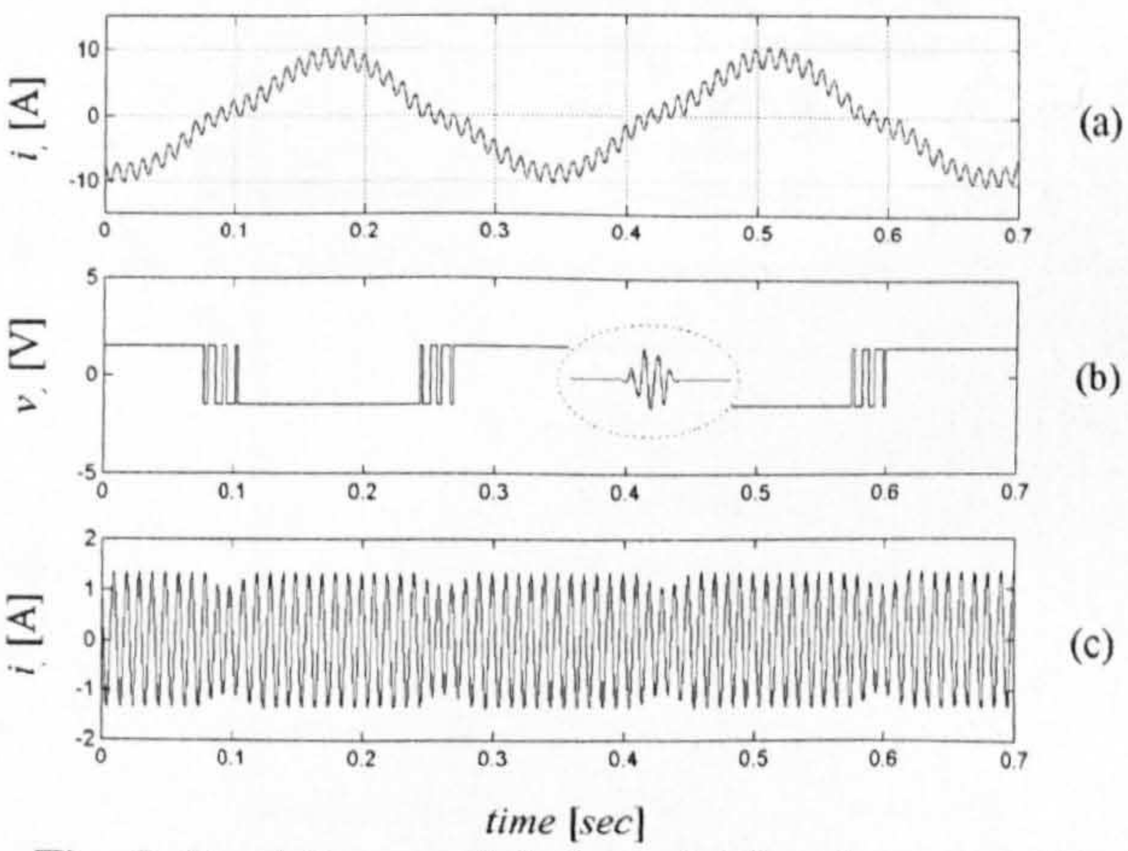

Fig. 5. Dead time modulation: (a) Load current, (b) Dead time perturbance voltage, (c) HF frequency current component.

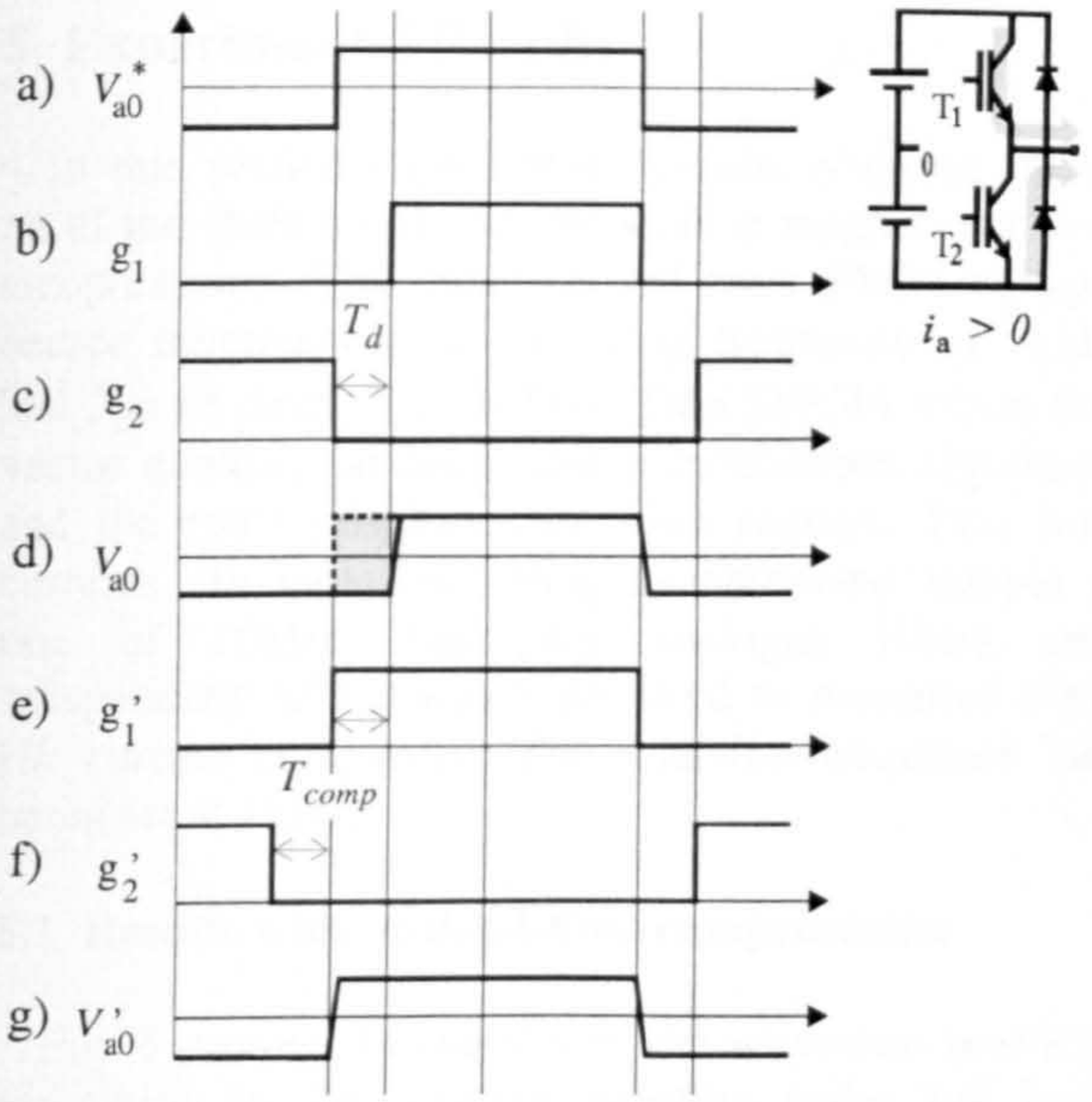

Fig. 6. Standard dead time compensation by edge shift.

4.2 Current Clamping Feed Forward Compensation

The effectiveness of the strategy described above can be improved further if the current clamping is accounted for [10]. Current clamping occurs if the magnitude of the phase current is sufficiently small at the beginning of the dead time period T_d. During T_d the phase current is being conducted by one of the freewheeling diodes and it is decreasing in magnitude: if the phase current reaches zero during the dead time period the diode will become reversed bias and the inverter output will be floating during the remaining of T_d. As a consequence the load phase to neutral voltage will not have the commanded value but will be determine by the load's back EMF. This phenomenon is illustrated in Fig. 7. T_z is the zero current clamping time and is derived using a first-order approximation for the i_{abc} trajectories during T_d. From Fig 7 it is seen that, for phase *a*, the clamping time may be estimated as (5), with similar expressions for phases *b* and *c*.

$$T_z = T_d + i_a' \cdot \frac{L_s}{V_{an}^* - E_a}, \tag{5}$$

It can be shown [10] that during the current clamping in the phases *a*, *b* and *c* of the inverter, the stator frame voltage error are given by (6), (7) and (8) respectively. To solve equations (6)-(8) the back EMF of the respective phases E_a, E_b and E_c, is first estimated using a simplified model of the PM machine.

$$\begin{aligned} v_{\alpha\_err} &= v_{an}^* - E_a \\ v_{\beta\_err} &= 0 \end{aligned} \tag{6}$$

$$\begin{aligned} v_{\alpha\_err} &= -\frac{1}{2}\left(v_{bn}^* - E_b\right) \\ v_{\beta\_err} &= \frac{\sqrt{3}}{2}(v_{bn}^* - E_b) \end{aligned} \tag{7}$$

$$\begin{aligned} v_{\alpha\_err} &= -\frac{1}{2}\left(v_{cn}^* - E_c\right) \\ v_{\beta\_err} &= -\frac{\sqrt{3}}{2}(v_{cn}^* - E_c) \end{aligned} \tag{8}$$

The voltages $v_{\alpha\beta\_err}$, (6) to (8), represent the load voltages error during current clamping. Compensation may be effected by increasing the PWM voltage demand by the mean voltage error during the sample period T_s (10). If T_z, estimated with (5), is smaller than zero or greater than T_d , it means that no current clamping will occur and no compensation to the PWM reference voltage is performed. If T_z is greater than zero and smaller than T_d then clamping will occur during the next switching and the estimated error (9) is added to the PWM reference.

$$\overline{v}_{\alpha\beta\_err} = v_{\alpha\beta\_err} \frac{T_z}{T_s} \tag{9}$$

It is noted that the current direction in the *standard dead time compensation* and the current value for the *current clamping feed forward compensation* at the time at which the commutation takes place should be known. This presents a difficulty because in most drives the current is sampled at the beginning of the previous modulation period. A software solution is implemented in this work using a step by step linear current predictor [11].

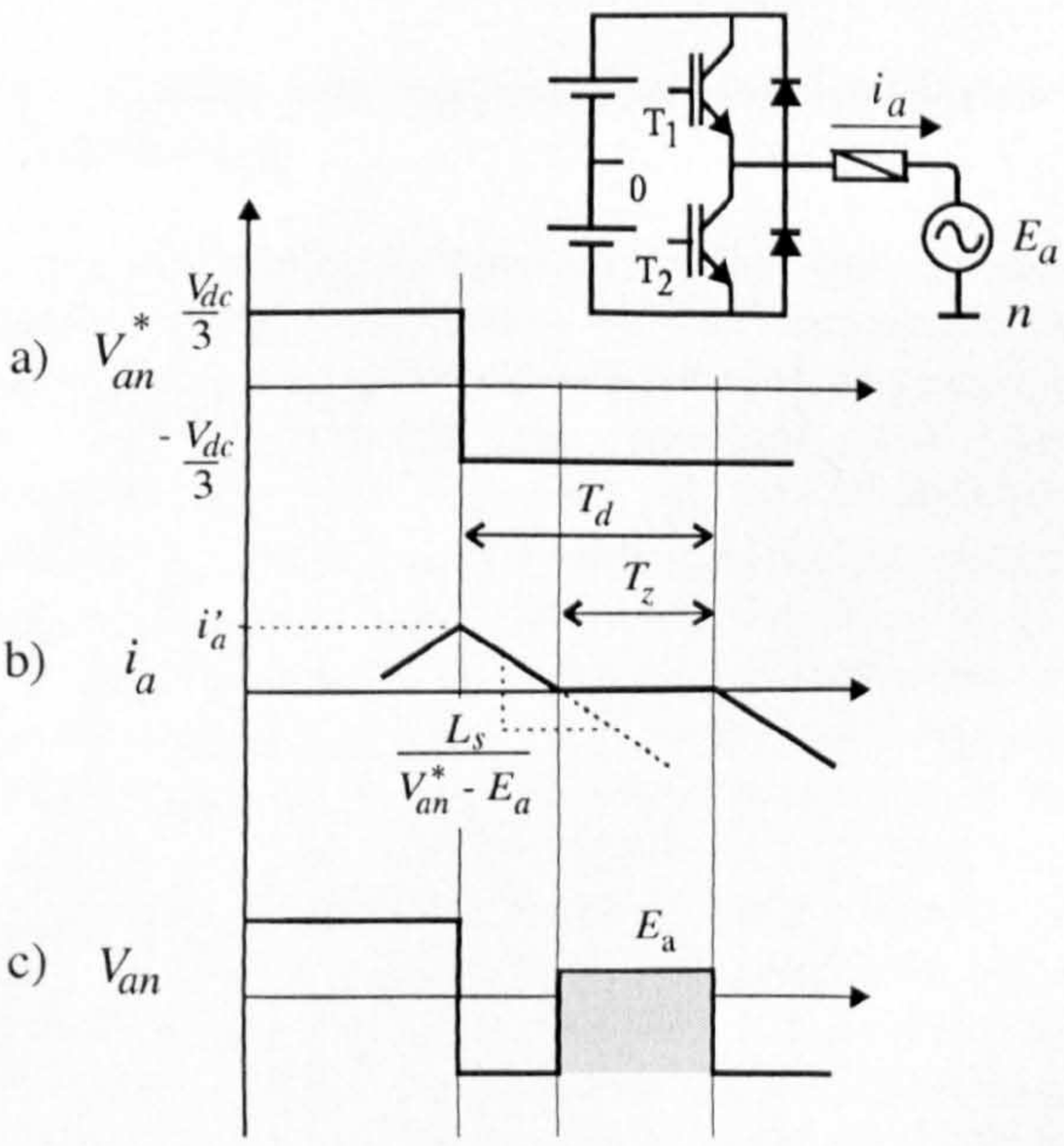

Fig. 7. Zero current clamping during a commutation on phase a.

5 Experimental Results

In this section experimental results obtained using an of the shelf 6-pole 3.8kW surface magnet machine are presented. This motor is fed by a PWM voltage source inverter with a switching frequency of 5kHz and 2μs of dead time. A DSP TMS320C44 solves the vector control, the dead time compensation algorithm and the rotor position estimation routine. Two line currents are measured using synchronised sample a rate of 10kHz, band-pass analogue filters and independent A/D channels are used to measured their HF current component. The injection frequency has being set at 1kHz.

5.1 Results with no dead-time compensation

Fig. 8 presents the results of the sensorless position estimation by HF voltage injection under full load operation when no dead time compensation is applied. Fig. 8(a) shows the phase current i_a, while Fig. 8(b) shows the output of the demodulated HF currents ($i_{\alpha de}$ and $i_{\beta de}$) which are the outputs of the synchronous filter. It can be seen that when the phase current i_a crosses zero a strong distortion occurs in the demodulated currents. Similar distortions are observed when i_b or i_c crosses zero. Fig. 8(c) shows the estimation of $2\theta_r$ by means of the tracking observer with a band with of 100Hz. The magnitude of the position error is shown in Fig. 9, where the difference between the measured rotor angle and the estimated rotor angle is plotted. This error reaches a maximum value of 24 electrical degrees.

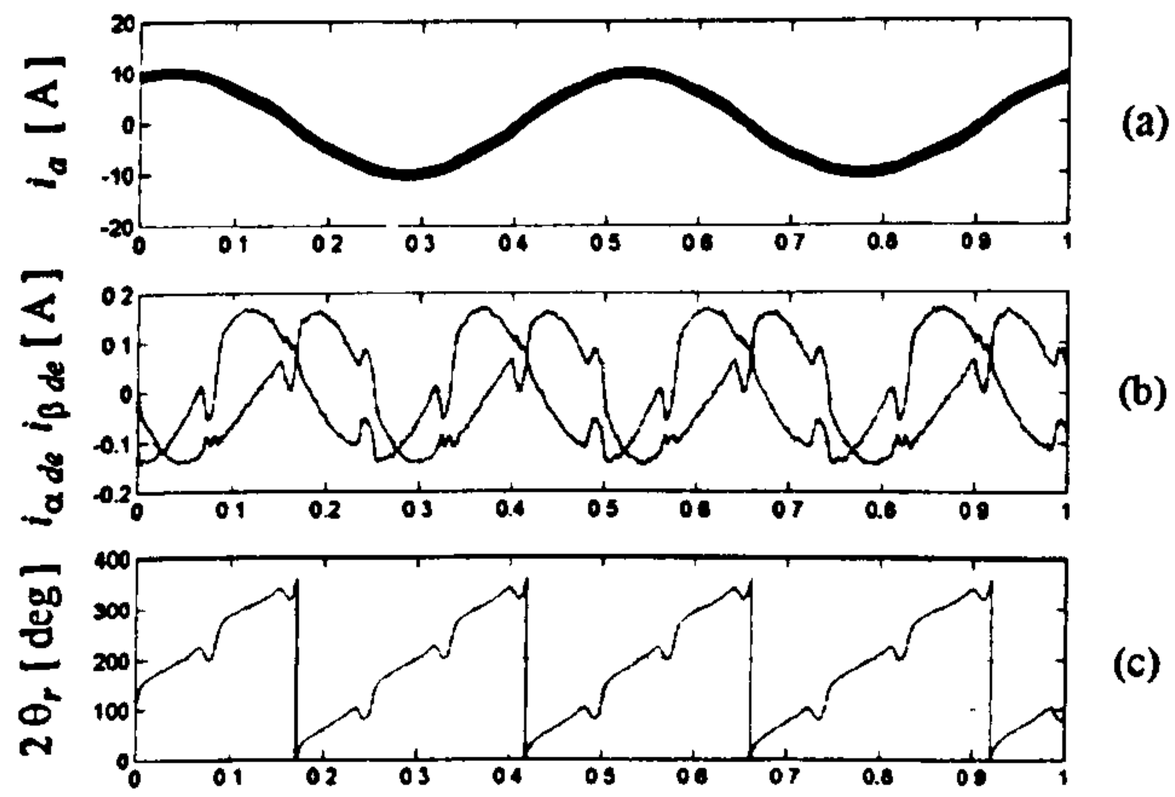

Fig. 8. Rotor angle estimation without any dead time compensation.

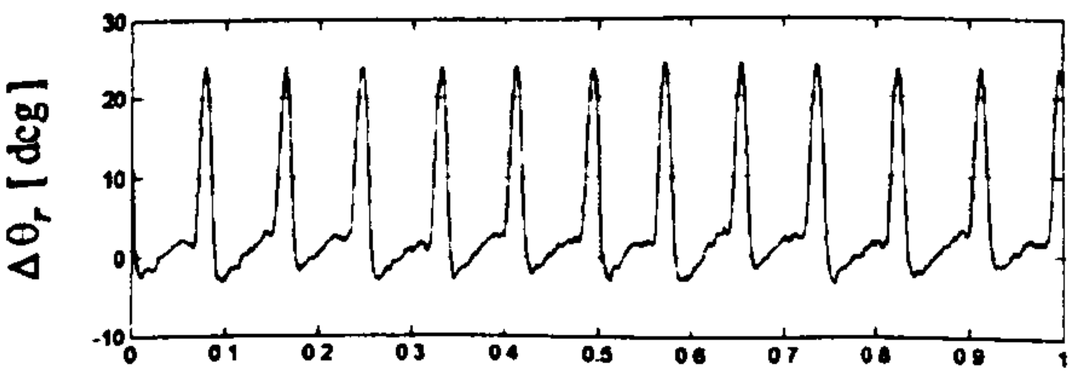

Fig. 9. Error in the rotor angle estimation without any dead time compensation.

5.2 Results with standard dead-time compensation

A similar test is as been run with the *standard dead time compensation* introduced in section IV*a*. These are shown in Fig. 10 and it is seen that the waveforms significantly improve. Nevertheless errors in the estimation angle due to the zero current clamping can still be noticed in Fig. 11. Therefore the complementary *current clamping feed forward compensation* is used to further improve the angle estimation.

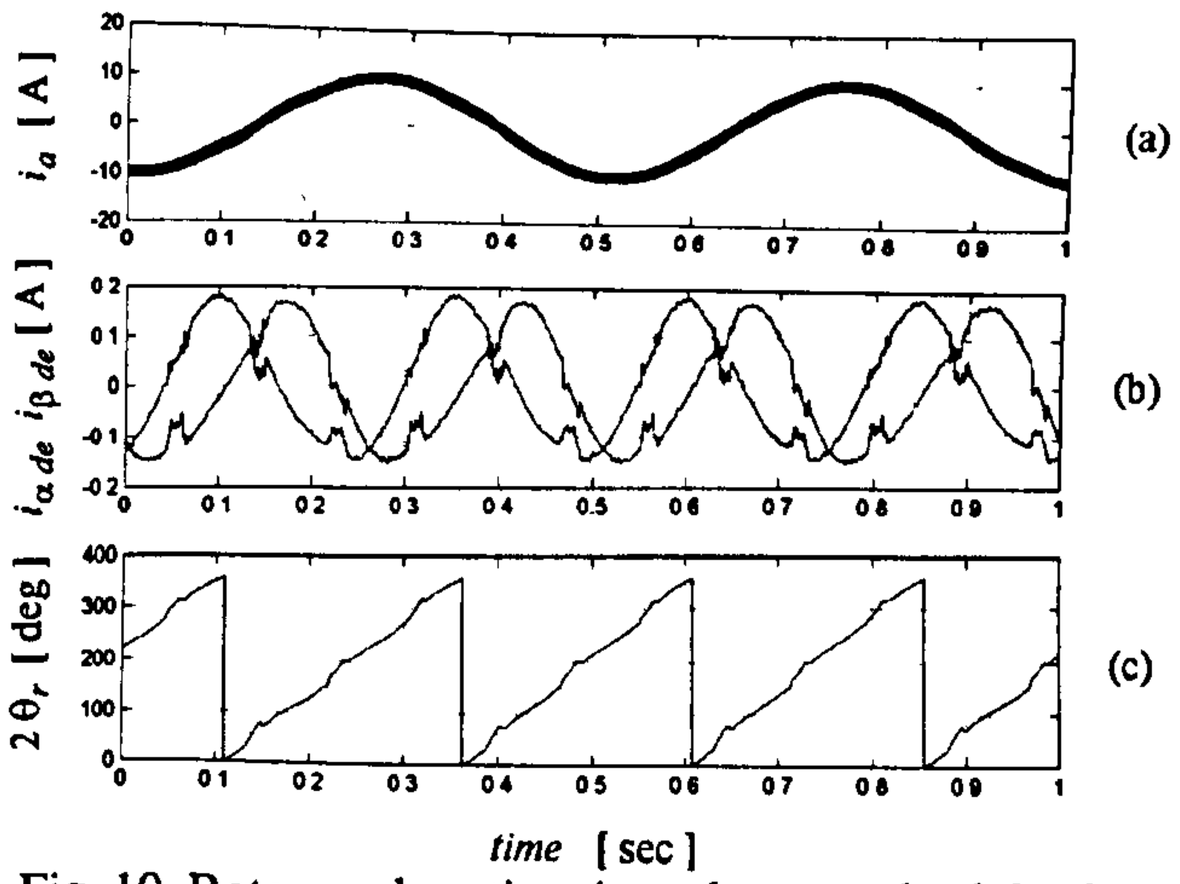

Fig. 10. Rotor angle estimation when *standard dead time compensation* is used.

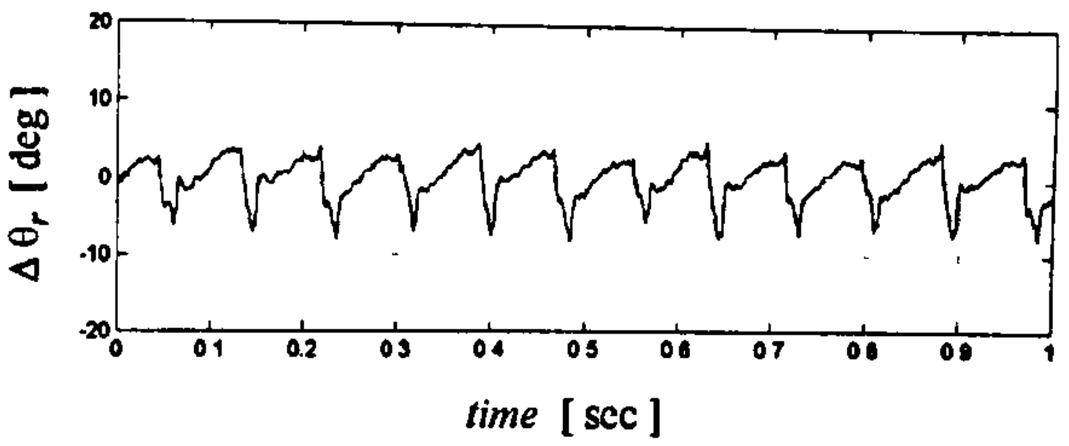

Fig. 11. Error in the rotor angle estimation when *standard dead time compensation* is used.

5.3 Results with current clamping feed-forward compensation

Fig. 12 presents the results obtained when the dead time is being compensated by both techniques, i.e. when the *current clamping feed-forward compensation* is used to enhance the *standard dead time compensation*. The distortion in the demodulated currents $i_{a\,de}$ and $i_{b\,de}$ has been significantly reduced producing a better angle estimation, shown in Fig.13 . The error has been reduced from 24 degrees electrical to ±4 electrical degrees (±1.3 mechanical degrees), which is mostly due to the space harmonics of the impedance of the machine rather than to dead time modulation. The higher frequency spikes seen in the error of Fig.13 is still due to the dead-time effect caused by the approximations made in the calculation of the zero-current clamping time. To overcome these, it is felt that current measurement would be necessary in order to accurately determine the instants at which the currents reach zero.

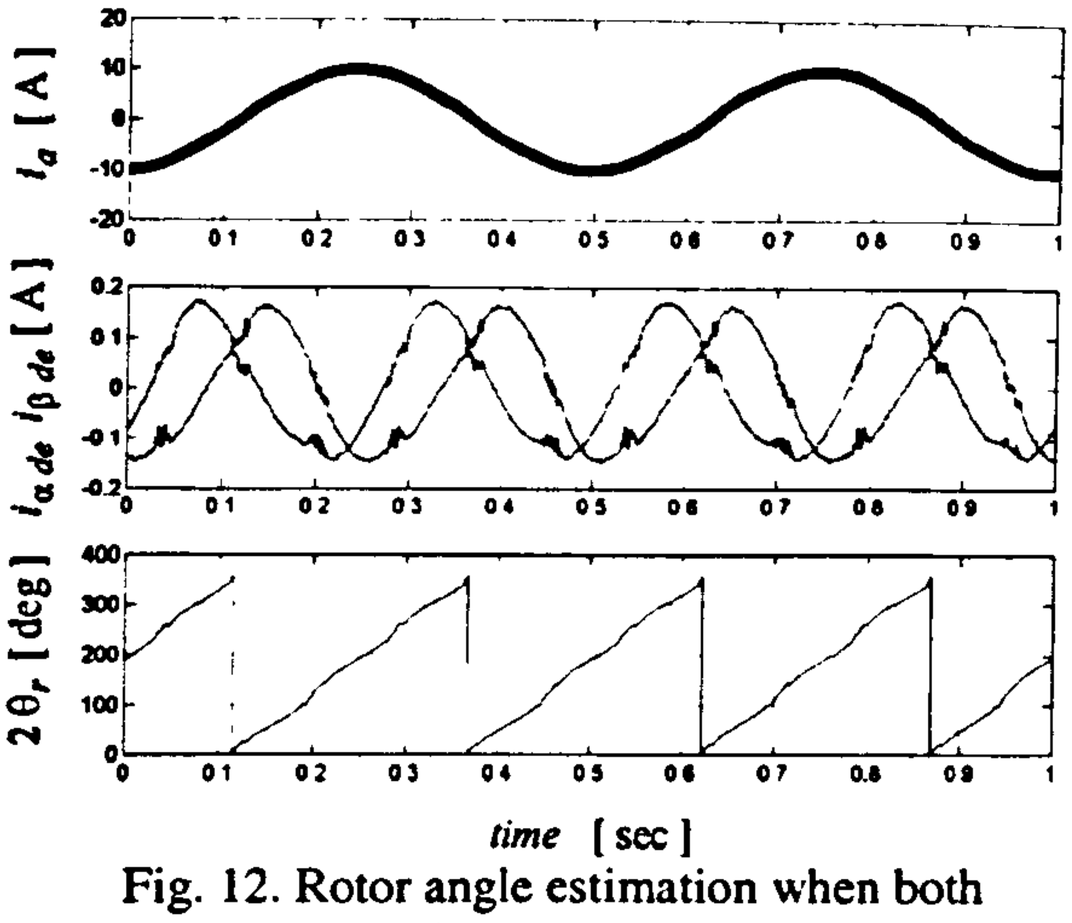

(a)
(b)
(c)

Fig. 12. Rotor angle estimation when both compensation strategies are used.

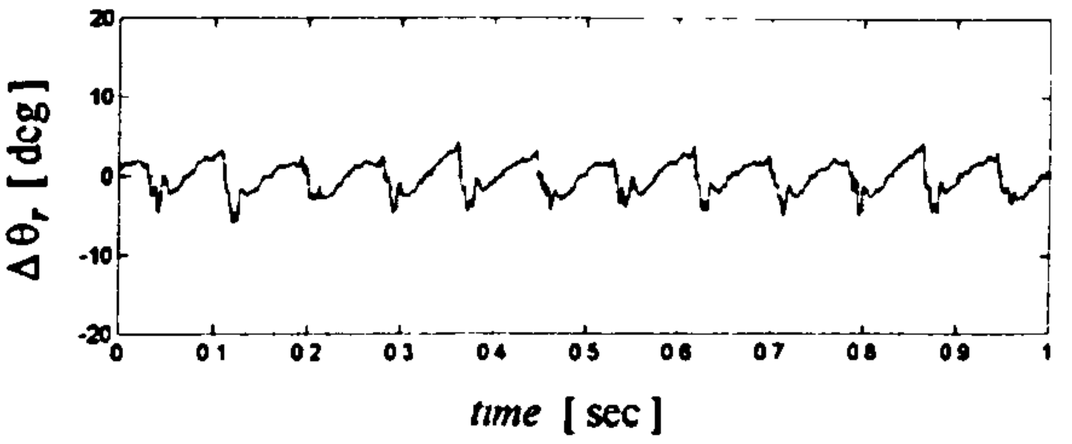

Fig. 13. Error in the rotor angle estimation when both compensation strategies are used.

6 Conclusions

The influence of inverter dead time upon sensorless position estimation in SMPM machines using HF voltage injection has been presented. It is shown that the small saliency of the SMPM machine makes the estimation prone to perturbances dominated by the influence of inverter dead time. A *standard dead time compensation* has been shown to significantly reduce the errors in the angle estimation but not to completely eliminate them. Further improvements are obtained using *current clamping feed forward compensation* at the expense of some increased computation in predicting the zero-current clamping times.

The results of this combined method almost eliminates the dead time modulation making possible the use of sensorless position detection by HF voltage injection in low saliency machines such as the SMPM machine. Experimental results using a 6-pole 3.8 kW surface mounted permanent magnet machine shows angle estimation with in an accuracy of 4 electrical degrees up to full load operation.

References

[1] P.L. Jansen and R. D. Lorenz, "Transducerless position and velocity estimation in induction and salient AC Machines," *IEEE Trans. on Industry Applications*, Mar/Apr, 1995, pp. 240-247.

[2] M. Schrödl, "Sensorless control of AC machines at low speed and standstill based on the 'INFORM' method," in *Conf. Rec. IEEE-IAS Annual Meeting*, October 1996, pp. 270 - 277.

[3] S.-J. Kang, J.-I. Ha and S.-K. Sul, "Position controlled synchronous reluctance with out rotational transducer", *IEEE Trans. on Industry Applications*, vol. 35, no. 6, pp. 1393 - 1398, Nov./Dec. 1999.

[4] M. J. Corley and R. D. Lorenz, "Rotor position and velocity estimation for a salient-pole permanent magnet synchronous machine at standstill and high speeds," *IEEE Trans. on Industry Applications*, vol. 34, no. 4, pp. 784 - 789, July/Aug. 1998.

[5] L. Wang and R. D. Lorenz "Rotor position estimation for permanent magnet synchronous motor using saliency-tracking self-sensing method," in *Conf. Rec. IEEE-IAS Annual Meeting*, October 2000, vol. 1, pp. 445 - 450.

[6] A. Consoli, G. Scarcella and A. Testa, "Industry application of zero-speed sensorless control techniques for PM synchronous motors," *IEEE Trans. on Industry Applications*, vol. 37, no.2, March/April 2001.

[7] Bimal K. Bose, *Power Electronics and Variable Frequency Drives, Technology and Applications*, IEEE Press.

[8] J.-H. Jang, J.-I. Ha, and S.-K. Sul, "Vector control of surface mounted permanent magnet motor without any rotational transducer," in *Conf. Rec. IEEE-APEC Annual Meeting*, March 2001, vol. 2, pp. 845 - 849.

[9] J.-W. Choi and S.-K. Sul, "Inverter output voltage synthesis using novel dead time compensation," *IEEE Trans. on Power Electronics*, vol. 11, no. 2, pp. 221 - 227, March 1996.

[10] J.-W. Choi and S.-K. Sul, "A new compensation strategy reducing voltage/current distortion in PWM VSI systems operating with low output voltages," *IEEE Trans. on Industrial Electronics*, vol. 31, no. 5, pp. 1001 - 1008, Sept./Oct. 1995.

[11] C. Attaianese and G. Tomasso, "Predictive compensation of dead-time effects in VSI feeding induction motors", *IEEE Trans. on Industry Applications*, vol. 37, no. 3, pp. 856 – 863, May/Jun 2001.

[12] N. Mohan, T. M. Underland and W. P. Robbins, *Power Electronics: Converters, Applications and Design*, 2nd Edition, John Wiley & Sons.

Sensorless Rotor Position Control in a Surface Mounted PM Machine Using HF Voltage Injection

C. Silva, G. M. Asher, M. Sumner and K.J. Bradley
School of Electrical and Electronic Engineering, University of Nottingham
Nottingham, NG7 2RD, England.
Phone: +44 115 95 15545 / Fax: +44 115 95 15616
Email: csj@eee.nottingham.ac.uk
URL: http://www.eee.nott.ac.uk/pemc

Keywords

Sensorless drives, permanent magnet motors.

Abstract

This paper presents the use of HF voltage signal injection for tracking position in an off-the-shelf surface mounted permanent magnet machine. The inherent low saliency of this type of machines presents difficulties and makes the signal conditioning highly critical. In this paper the method of space-modulation profiling (SMP) is used to obtain a magnetic signature of the machine in order to correct for periodic errors in the position signals. Experimental results illustrate the effectiveness of this technique in providing position signals of high quality. These are then exploited to provide closed loop sensorless position control of good bandwidth.

I. Introduction

The control of synchronous AC machines requires the knowledge of the rotor position and speed for field orientation and closed loop speed and position control. Rotor shaft sensors are usually fitted adding to the total cost of the drive and reducing its reliability. For this reason extensive research has being carried out to develop sensorless strategies. Methods based on the model of the machine in which the back EMF is integrated to determine the linkage flux have being successfully implemented [1]-[3]. However, all these techniques fail at low speed due to lack of a reliable back-EMF estimate deriving from integrator drift and increasing sensitivity to errors in the parameter estimation. A second type of sensorless strategies suitable for zero and low speed operation are the so called "injection methods"[4]-[7]. In this methods HF voltages (or currents) signals are injected to the machine terminals, the position dependent inductance causing modulation in the resulting HF currents (voltages) that give the position information. This technique has been reported for high saliency machines such SR motors and buried magnets PM machines [8]-[10]. In surface mounted PM machines, characterised by small saliency, the technique has been tried [11] using the saliency created by main flux saturation, but operation was only possible at low loads.

In this paper techniques are presented to improve signal processing associated with the voltage injection technique and make its application in surface mounted PM more reliable. The injection technique used is the injection of HF voltages on the stationary α-β axis [4]. It was shown in [12],[13] that the inverter's dead time distorts the injected HF voltage and results in distortion in the HF current. The paper reviews the interfering effect of dead-time compensation failure at the zero-current crossovers and illustrates the effect of different compensation schemes on the estimated position accuracy. As a particular illustration, a hardware current direction detection is implemented and consequent dead time compensation [14] is used to obtain a more accurate position signal whilst minimising software computation. However, due to the higher harmonics of the machine saliency, good dead-time compensation alone is not sufficient to achieve good accuracy and some further compensation has to be included to correct for this type of error. In [10] a direct correction of the angle is used for a buried magnet machine, but this approach does not include the load dependency of the estimation error. In the present work the space-modulation profiling (SMP) technique [12], previously

applied to induction machines in which the saliencies are of low magnitude, is presented and shown to provide a significant enhancement of the quality of estimated position signal. The SMP consists of tables of the errors in the position signals as functions of the rotor position and load and requires a pre-commissioning phase. This pre-commissioning is discussed. The paper finally shows excellent sensorless closed loop performance made possible by the low distortion of the position estimate.

II. Position Estimation Using HF Voltage Injection

An AC synchronous machine is said to be salient if the stator inductance measure in the direction of the flux L_d is different than the inductance measure in the direction of the torque producing axis L_q. This difference is caused by asymmetry in the rotor design, as in the case of synchronous reluctance and interior magnets PM machines and/or by main flux saturation, as in surface mounted PM machines. The α-β model of a synchronous PM machine in the stator reference frame including the saliency is given by (1). It can be seen that due to the saliency the relation between the stator voltage and currents, or inductance matrix, is a function of the rotor position.

$$\begin{bmatrix} v_\alpha \\ v_\beta \end{bmatrix} = \begin{bmatrix} r_s & 0 \\ 0 & r_s \end{bmatrix} \cdot \begin{bmatrix} i_\alpha \\ i_b \end{bmatrix} + \begin{bmatrix} s & 0 \\ 0 & s \end{bmatrix} \cdot \begin{bmatrix} \lambda_\alpha \\ \lambda_\beta \end{bmatrix}$$
$$\begin{bmatrix} \lambda_\alpha \\ \lambda_\beta \end{bmatrix} = \begin{bmatrix} \overline{L}_s - \Delta L_s \cos(2\theta_r) & -\Delta L_s \sin(2\theta_r) \\ -\Delta L_s \sin(2\theta_r) & \overline{L}_s + \Delta L_s \cos(2\theta_r) \end{bmatrix} \cdot \begin{bmatrix} i_\alpha \\ i_\beta \end{bmatrix} + \lambda_m \begin{bmatrix} \cos(\theta_r) \\ \sin(\theta_r) \end{bmatrix} \quad (1)$$

where :

$$\overline{L}_s = \frac{L_q + L_d}{2} \text{ and } \Delta L_s = \frac{L_q - L_d}{2}$$

To extract the position information contained in the inductance matrix of (1) the HF rotating voltage vector given by (2) is added to the stator voltages.

$$v_i = \begin{bmatrix} v_{\alpha i} \\ v_{\beta i} \end{bmatrix} = \hat{V}_i \begin{bmatrix} -\sin(\omega_i t) \\ \cos(\omega_i t) \end{bmatrix} \quad (2)$$

If the injection frequency $\omega_i >> \omega_e$; where ω_e is the synchronous excitation frequency, the induced HF currents in the stator windings are given by:

$$i_i = \begin{bmatrix} i_{\alpha i} \\ i_{\beta i} \end{bmatrix} \approx \begin{bmatrix} I_0 \cos(\omega_i t) + I_1 \cos(2\theta_r - \omega_i t) \\ I_0 \sin(\omega_i t) + I_1 \sin(2\theta_r - \omega_i t) \end{bmatrix} \quad (3)$$

Where

$$I_0 = \frac{\hat{V}_i \overline{L}}{L_d L_q \omega_i} \text{ and } I_1 = \frac{\hat{V}_i \Delta L}{L_d L_q \omega_i}$$

$$\begin{bmatrix} i_{\alpha\_pos} \\ i_{\beta\_pos} \end{bmatrix} \approx \begin{bmatrix} I_1 \cos(2\theta_r) \\ I_1 \sin(2\theta_r) \end{bmatrix} \quad (4)$$

In (3) can be noticed that only the negative sequence component, proportional to the saliency value, contains rotor position information. To extract this useful signal form the total high frequency current the synchronous filter of Fig.1 is implemented. The first rotation of coordinates transforms the HF currents to a rotating frame synchronous with the voltage injection, this converts the positive sequence current in to DC and is completely removed using a high pass filter. Finally, a rotation back to a frame synchronous with the negative sequence produces the position signals at base band, as in (4). The angle $2\theta_r$ can be then extracted directly by a tan^{-1} calculation or by a PLL structure.

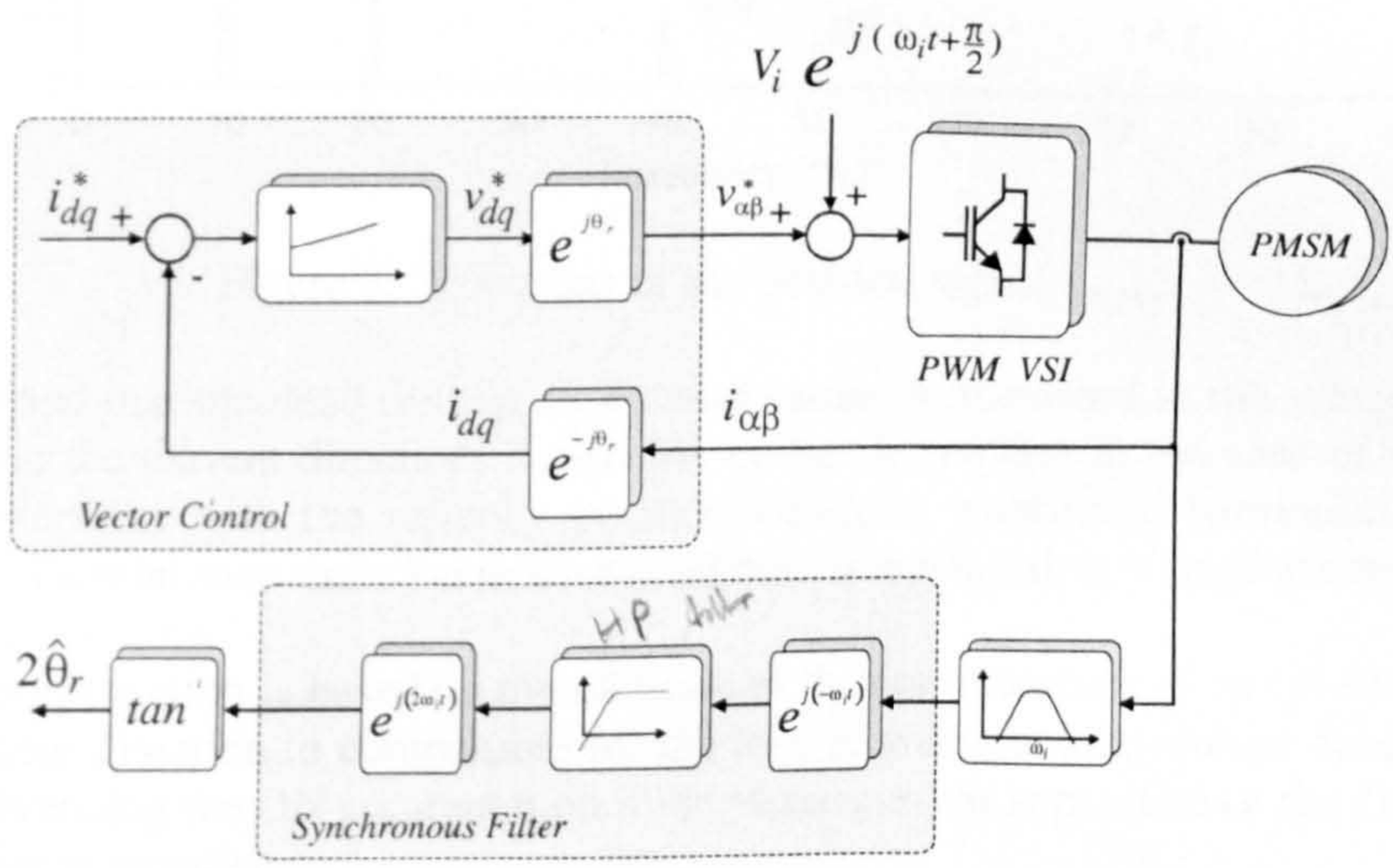

Fig. 1. Rotating HF injection and synchronous filter.

In a surface mounted PM machine, such that in Fig.2, the saliency is small and not perfectly sinusoidal, in Fig.2b the value of stator inductance is plotted as function of rotor position for no load condition. This has two major effects for the application of the voltage injection strategy. First the level of useful position signal is small and the distortion in the HF currents due to the inverter's no-linearity i.e. dead time becomes significant. Second, the saliency is not sinusoidal distributed and furthermore it's shape and phase shift respect to the rotor position will be load dependent [11]; this will produce harmonics in the position signals in (4) and in turn will produce angle estimation errors. Figure. 3 shows the spectrum analysis of the position signal i_{α_pos} obtained by the direct application of the method. In this figure can be easily identified the fundamental at $2f_e$ containing the position information and the spurious harmonics at $4\,f_e$, $8\,f_e$, $10\,f_e$ and $14\,f_e$, these will produce distortions in the angle estimation. This harmonics are caused by the combined effect of the machine saliency harmonics and the inverters dead time.

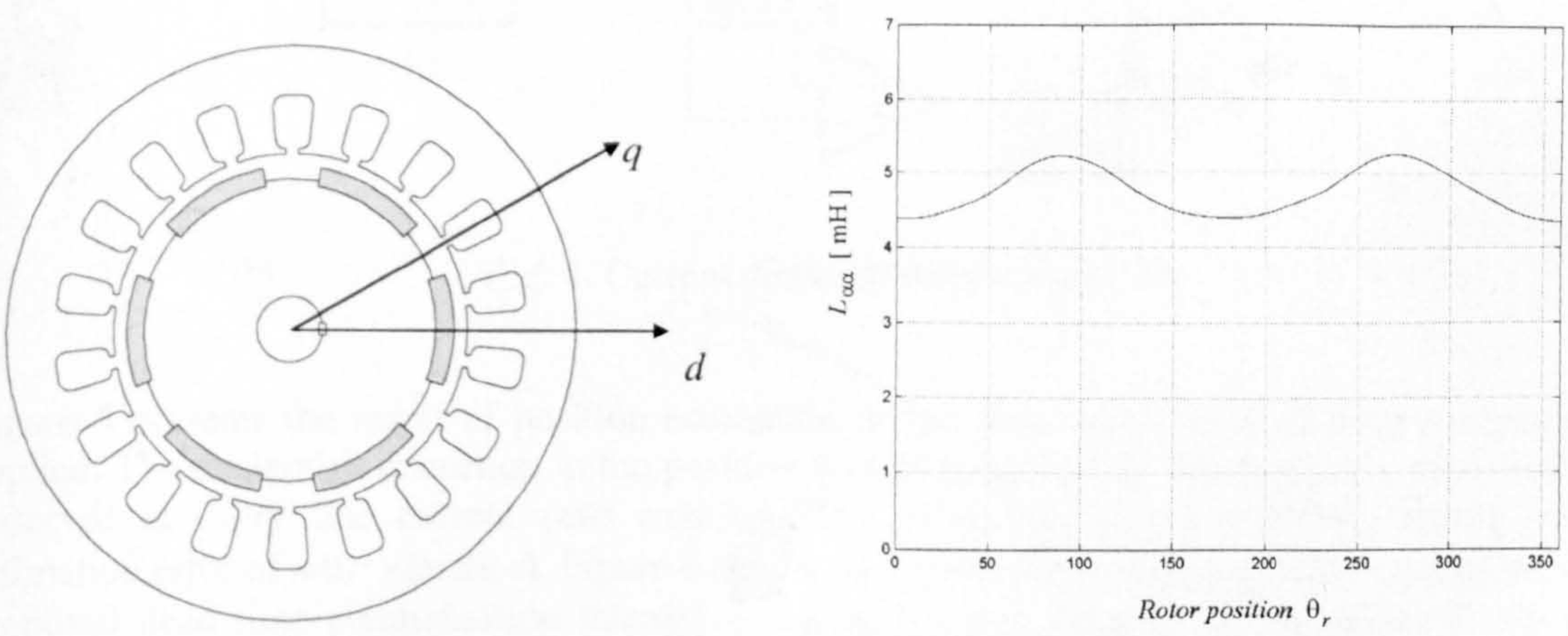

Figure 2. Surface mounted PM machine and HF inductance v/s rotor position.

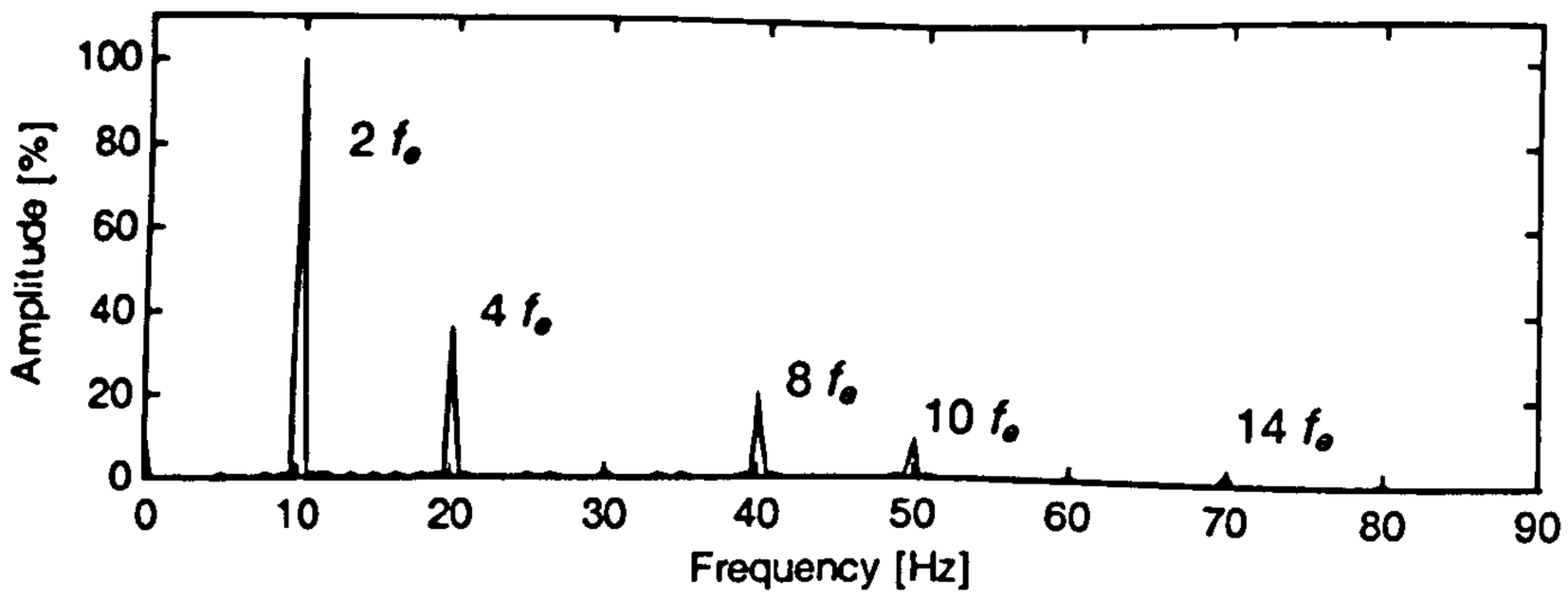

Figure 3. Spectrums of the position signal i_{α_pos}.

It is well understood that the dead time in an inverter causes a distortion in the voltage applied to the load depending on the current direction. It also has being shown that in the case of voltage injection this distortion interferes with the saliency position detection producing harmonics in the position signals [12] [13]. To minimize these harmonics dead time compensation is implemented in this work.

The dead time compensation is based on the advance of the commutation of an inverter leg depending on the phase current direction to compensate for the loss of volts-seconds due to dead time [14]. This is achieved by advancing the ON commutation if the phase current is positive or the OFF commutation if the phase current is negative.

For the purpose of the dead time compensation, the current direction can be determined by the current measurement at no extra cost, but the delay associated with the conversion and current measurements offsets will deteriorate the performance of the compensation. In this work a separate current direction-detection circuit, shown in fig. 4 have been used. This circuit has the disadvantage of adding semiconductors to the power circuitry, increasing the part count, the conduction losses and requiring extra isolated power supplies making it undesirable in an industrial application. Nevertheless for research purposes the circuit is easily implemented, gives accurate and almost instantaneous current direction reading.

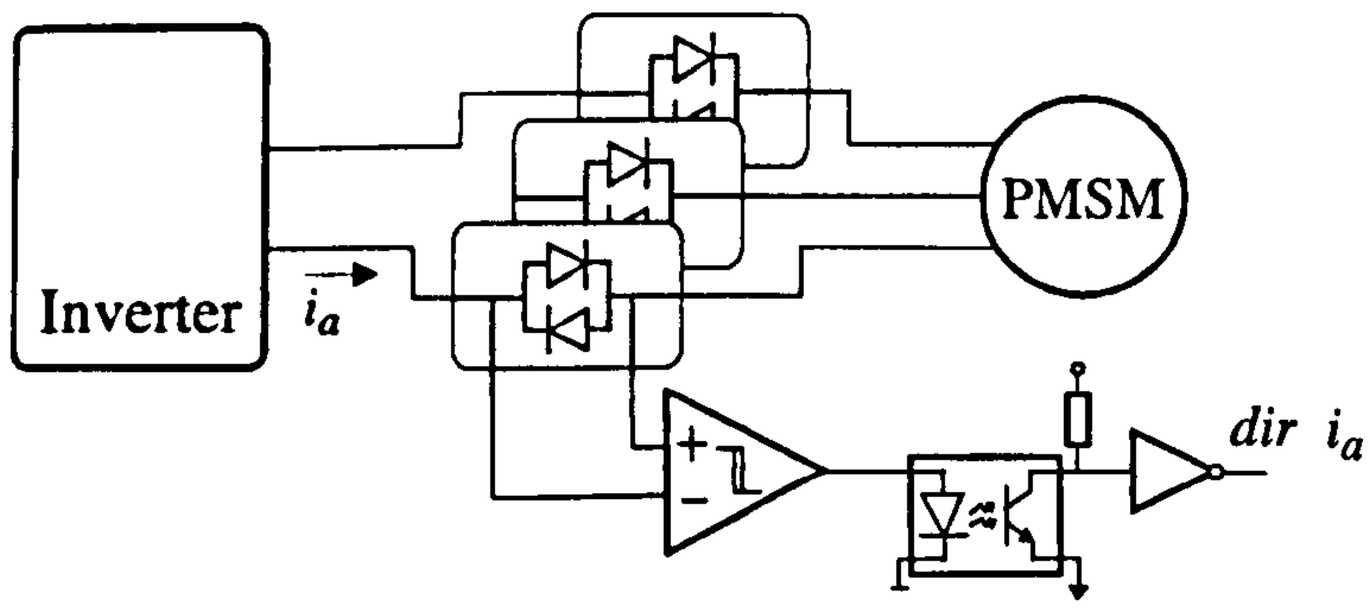

Fig. 4. Current direction detection circuit.

Figure 5 presents the result of position estimation at full load when no dead time compensation is applied. The distinctive distortion in the position signals produced by the inverter's dead time can be observed at every line current zero crossing. This distortion in the position signals causes an estimation error of ≈40° electrical. Figure 6 shows the results for similar operation conditions with the proposed dead time compensation strategy in operation, this reduces the distortion in the position signal producing an angle estimation with a error no bigger than 8° electrical.

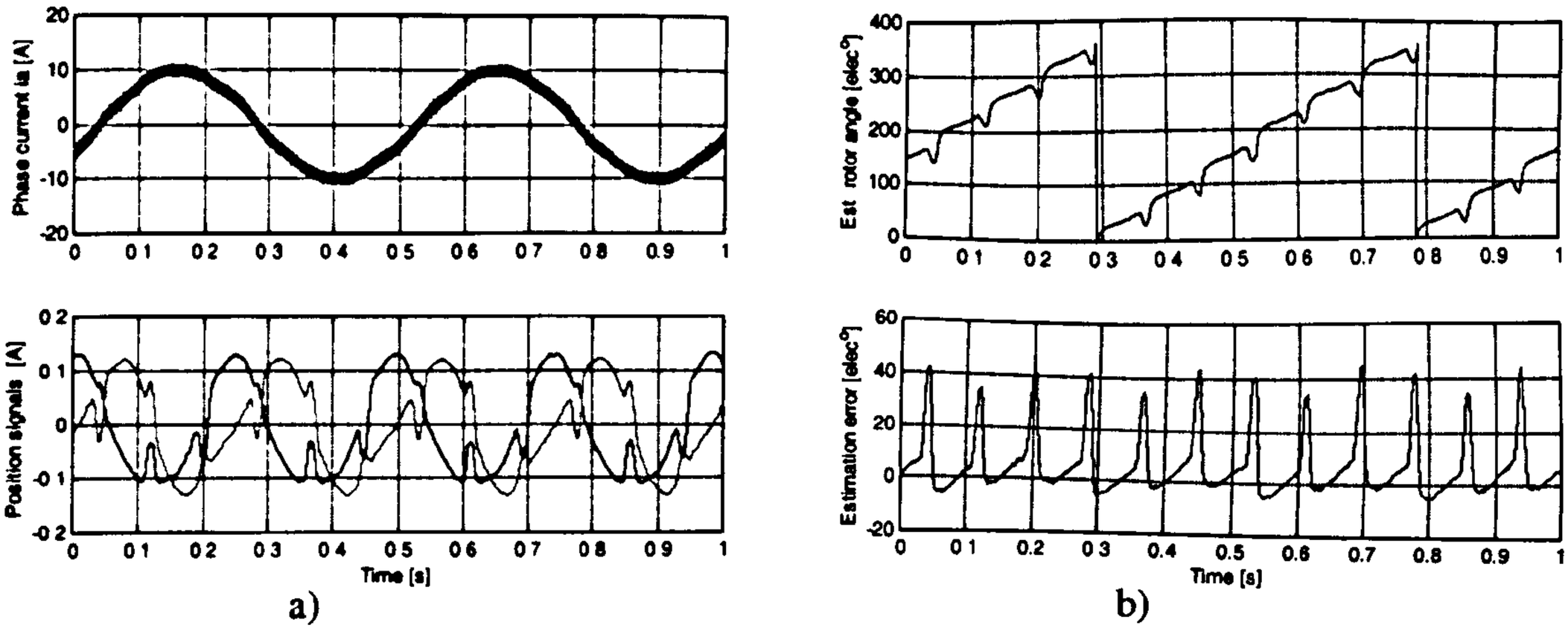

a) b)

Fig 5. Angle estimation with no dead time compensation

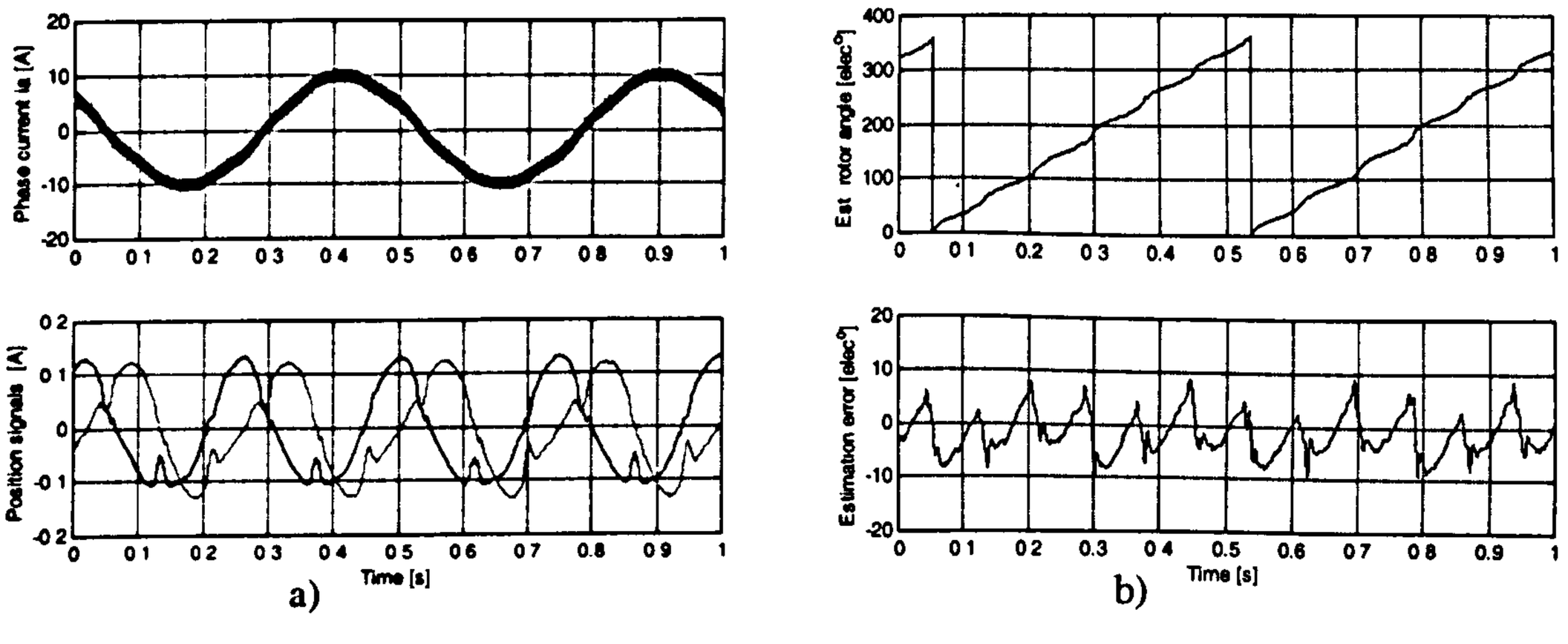

a) b)

Fig. 6. Angle estimation with dead time compensation.

III. Space modulation profile

The intrinsic harmonics of the machine saliency means that the position signals will contain harmonics even under perfect voltage excitation. This, added to some remaining inverter dead time modulation due to miss match in the compensation strategy explains the error in the angle estimation shown in Fig.6b. To achieve good sensorless rotor position control the accuracy of the rotor position estimation needs to be improved further. In this work this is done by means of spatial modulation profiling (SMP) [12].

The SMP technique consists of the use of tables to record the harmonics of the position signals as a function of rotor position angle. During operation the pre-commissioned tables are used to compensate for the distortions in the position signals in the time domain.

A. Commissioning of the SMP

Figure 7 shows the saliency position signals i_{α_pos} and i_{β_pos} as a function of the rotor position angle at 70% of load current for a number of electric cycles. In the same plots are shown the ideal traces of the fundamental of these currents. In this plot the periodicity of the position signal error Δi_{α_pos} and Δi_{β_pos} can be seen, this enables the characterization of this error as position dependent.

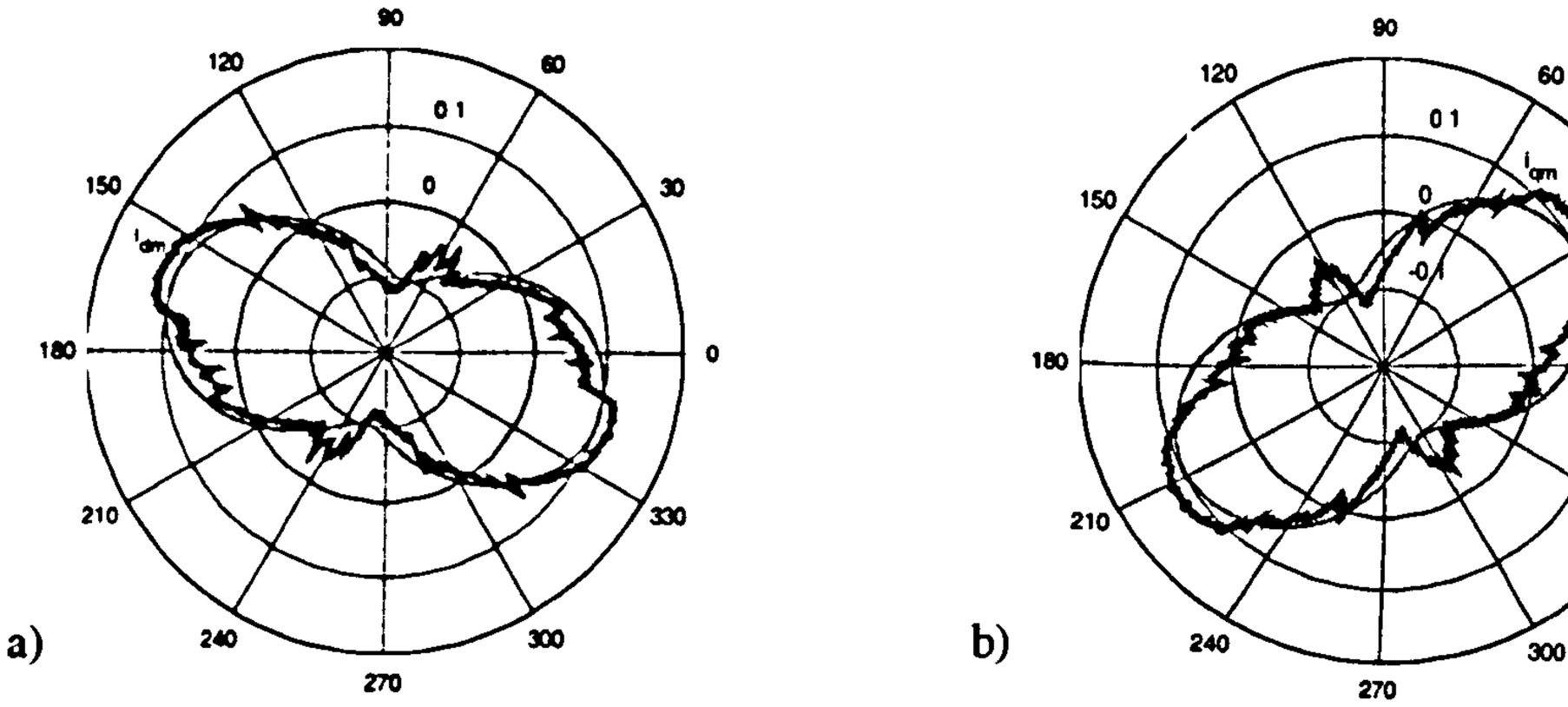

Figure 7. . Saliency position signals at 70% load: a) i_{α_pos}, b) i_{β_pos}.

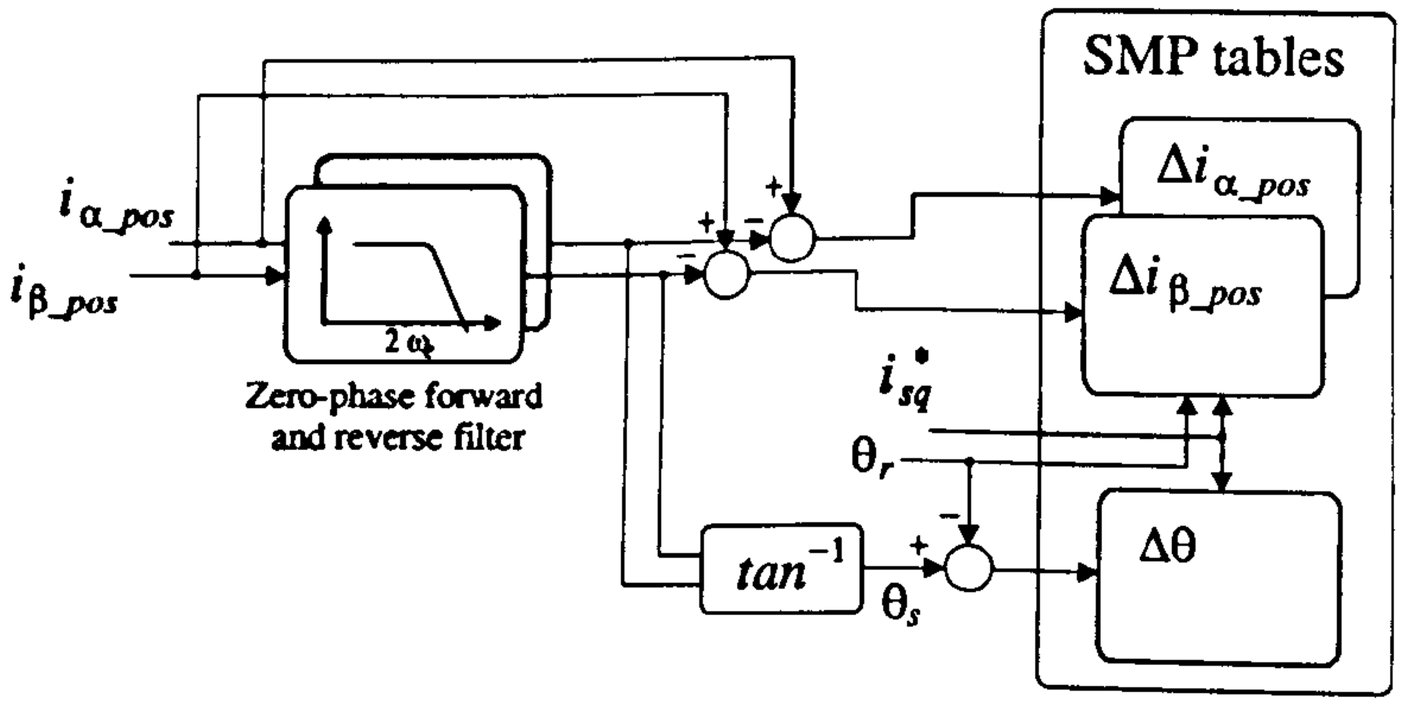

Fig. 8. Batch signal processing for SMP tables generation.

The commissioning of the SMP tables is done off-line with data captured during low speed sensored operation of the machine at a constant load. During this test the variables position signals i_{α_pos} and i_{β_pos}, rotor position θ_r and torque demand i_{sq}^{*} are captured. All the signal processing, shown in Fig.8, is then performed in batch form to allow high order non-causal filtering achieving high rejection of the harmonics and avoiding any phase shift of the fundamental. The position signals and their fundamentals are subtracted to obtain the error signals Δi_{α_pos} and Δi_{β_pos}. These are then stored in the SMP table as function of the rotor position angle. To avoid random measurement errors the result is averaged over a large number of periods. In order to account for variations in the saliency shape due to the load the extraction of this profile has to be repeated for a set of different loads values obtaining finally the bi-dimensional SMP-tables shown in Fig. 9.

B. Load dependent phase shift

The use of the SMP-tables allows the extraction of the fundamental component of the position signal, enabling the estimation of the saliency position θ_s. Under no load this position coincides with the rotor flux direction, or *d* axis. Under load, the stator saturation is influenced by the stator currents and will produce a shift of the saliency relative to the rotor flux axis, producing an offset between the estimated angle and the actual rotor position. In machines with a saliency dominated by rotor geometry this shift is negligible. Nevertheless when saturation induced saliency is being tracked as in surface mounted PM machines, the shift of the saliency becomes significant and has to be taken into account to achieve good orientation and accuracy in the position control. This phase shift is also quantified during the commissioning process by averaging the phase difference between the saliency angle θ_s and the measured rotor position θ_r for each load value as Fig.8 indicates. Figure 10 shows the saturation phase shift table obtained from the commissioning of a surface mounted PM machine; it can be seen that for the motoring condition the shift produced by stator teeth saturation reaches 23° electrical at maximum current.

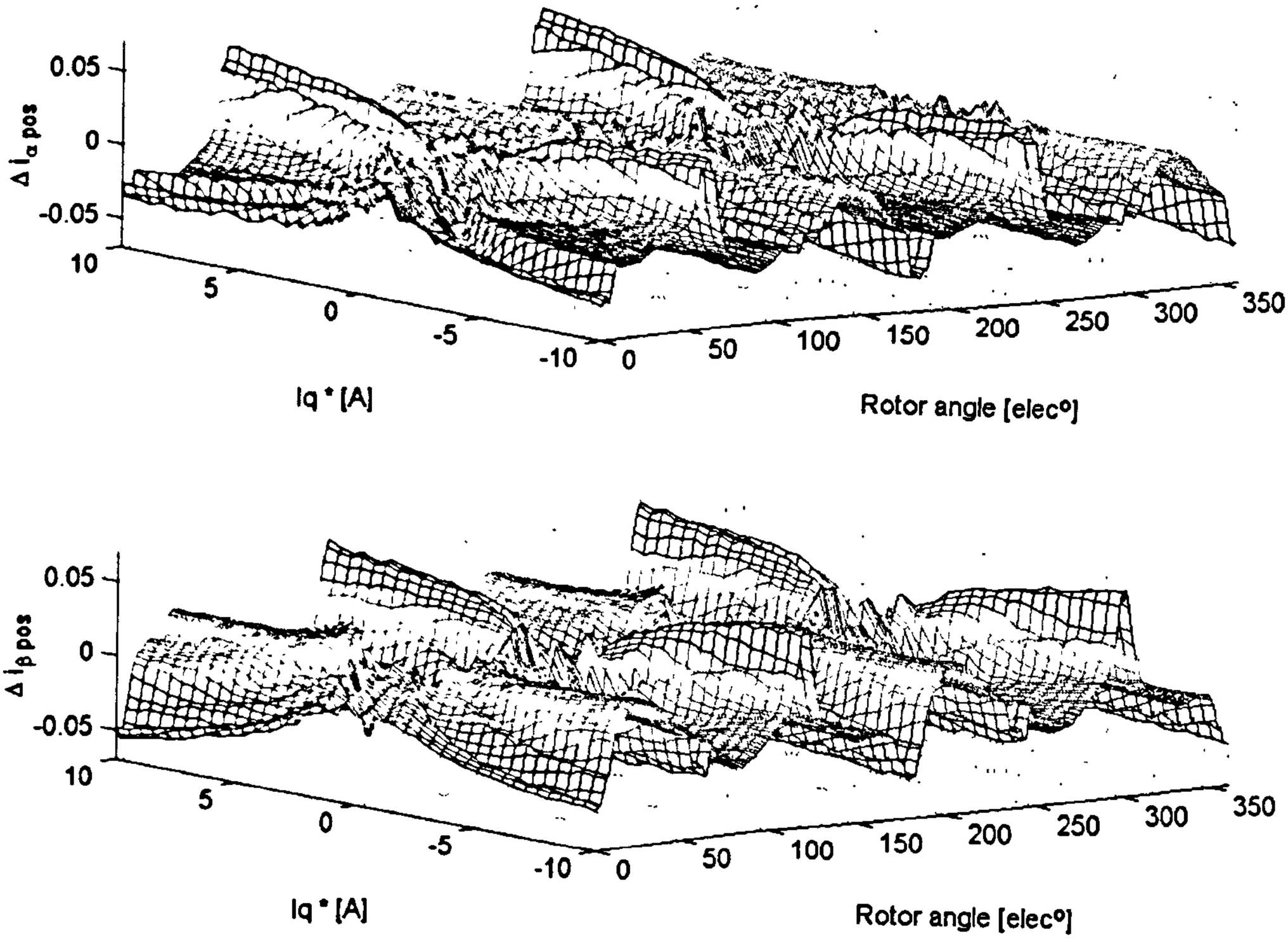

Fig. 9. Space Modulation Profile (SMP) for a 3.82 kW surface mounted PM machine.

Finally the complete rotor position estimation including the SMP and the saturation shift table is shown in Fig.11. Here the demanded torque current i_{sq}* and the estimated rotor position angle $\hat{\theta}_r$ are used to address the SMP tables to obtained the correcting quantities Δi_{α_pos} and Δi_{β_pos}. These are subtracted from the demodulated raw position signals i_{α_pos} and i_{β_pos} and the result filtered to obtain the corrected saliency position signals i_{α_pos}' and i_{β_pos}'. The saliency angle $2\theta_s$ is obtained by direct tan^{-1} extraction from quotient of this signals. Finally as indicated in this figure, the saliency angle θ_s is corrected for the saturation shift depending on the reference torque current i_{sq}* to obtain the rotor position estimation $\hat{\theta}_r$.

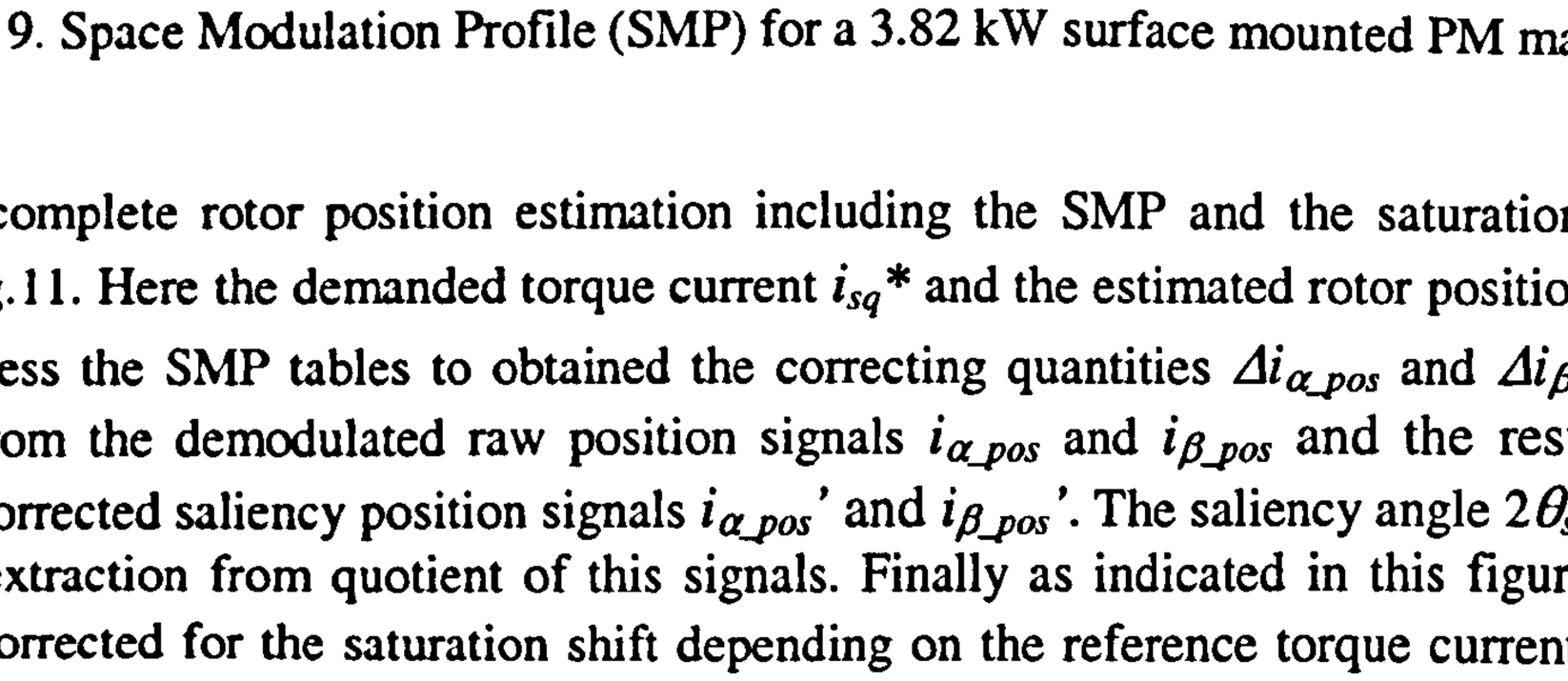

Fig 10. Saliency position shift respect to rotor angle.

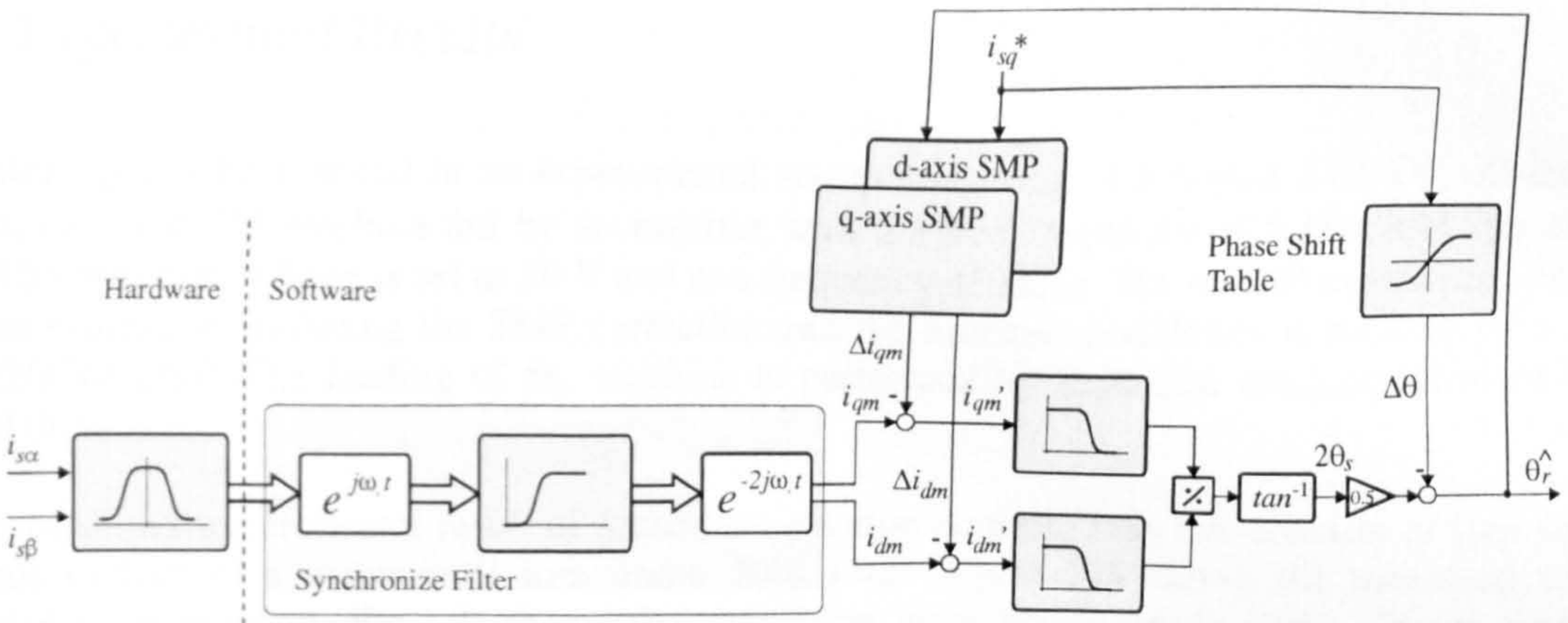

Fig. 12. Rotor position estimation strategie including profiling and phase shift correction.

A typical result of the rotor position estimation presented above is shown in Fig.12. The PM machine operates under speed control at 60 rpm and 100% load. Fig.12b shows an angle error within 2° electrical.

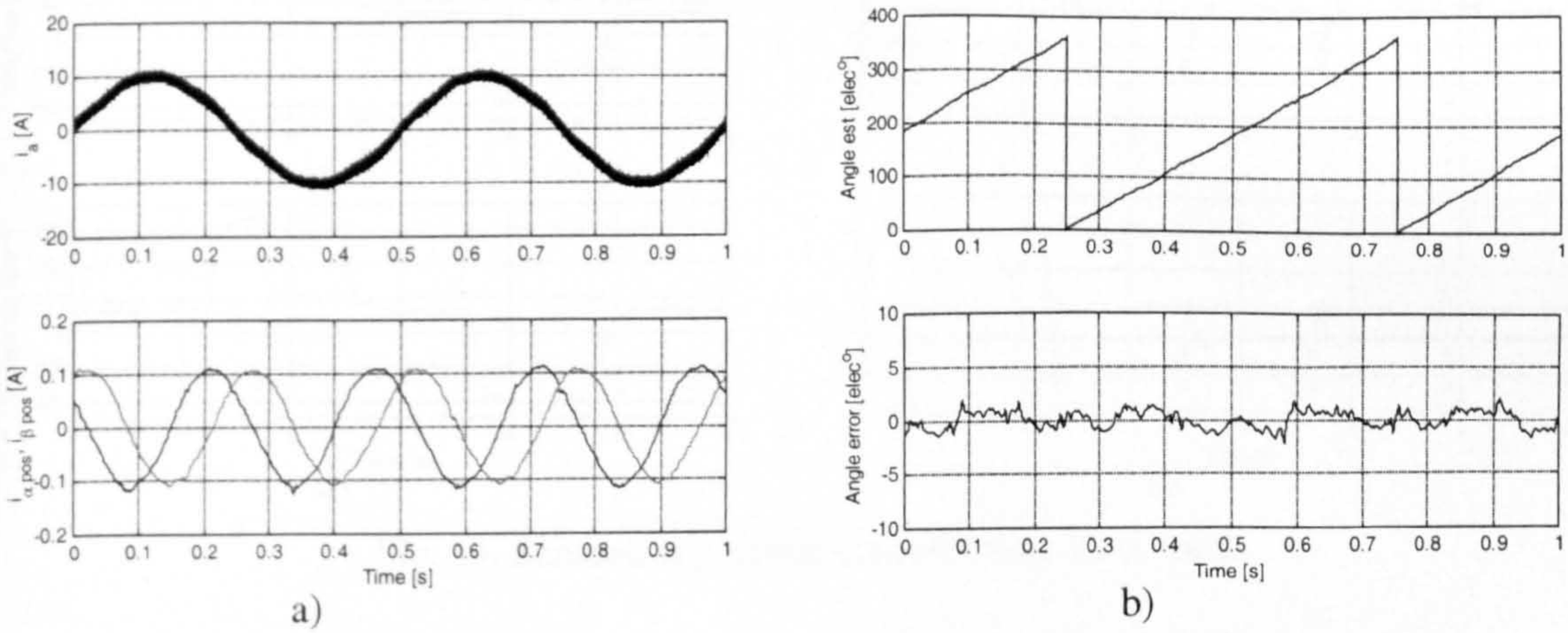

a) b)

Fig.12 Steady state angle estimation, using SMP-tables.

Finally, using the presented rotor position estimation, sensorless position control can be implemented as shown in Fig.13. The controller structure consists of position and speed cascaded loops and the position estimated is differentiated and filtered for speed feedback. The spectral contents of the torque demand i_{sq}* is band limited with the first order low pas filter shown in Fig.13 to prevent fast transients in the current reference and measurement noise feeding through from exciting the HF filters, and hence perturbing the position estimation.

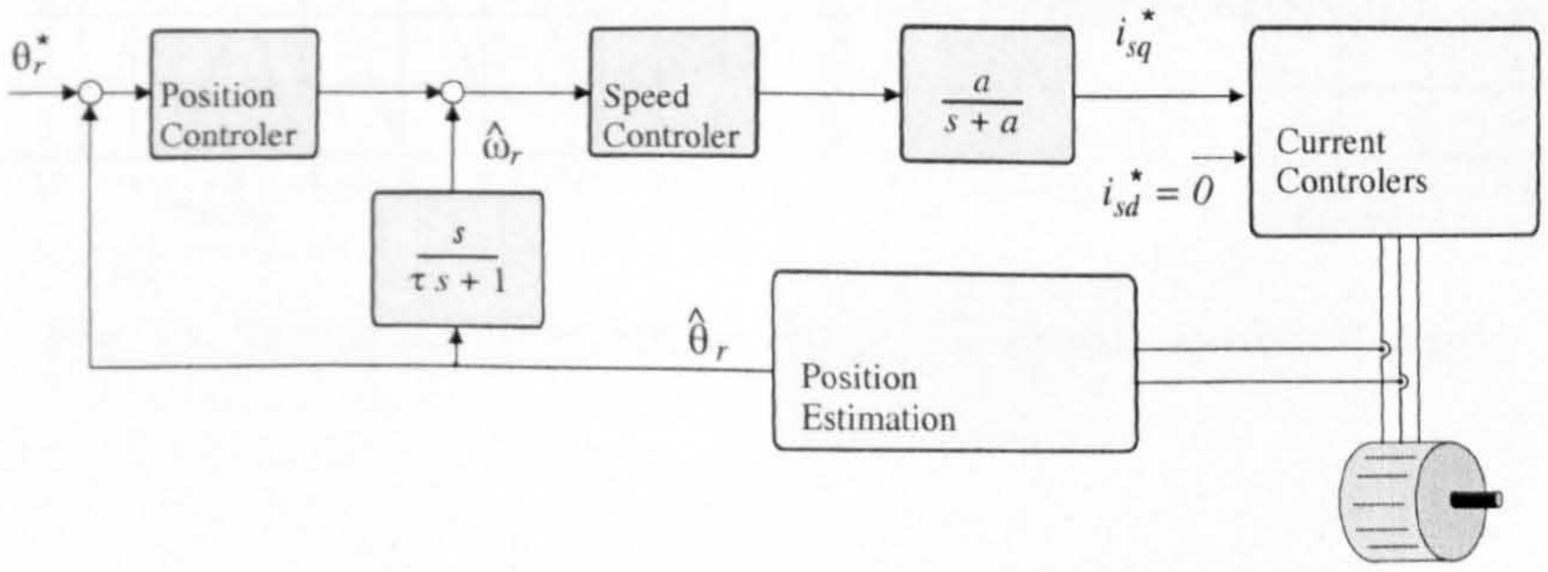

Fig 13. Sensorless postion control structure.

IV. Experimental Results

This strategy has been tested in an experimental set-up consisting of a 6 pole 3.82 kW off-the-shelf surface mounted PM machine fed by an inverter with a PWM frequency of 5 kHz and 2μs of dead time. The injection voltage is set to 20 V and at a frequency of 1kHz. The control algorithms, the rotor position estimation including the SMP correction and the inverter modulation is perform by a single TMS320C44 DSP. The loading of the machine is performed by induction machine sensored vector control drive.

Figure 14 shows experimental result of sensorless position control. This test consists of step position demands of half of a mechanical turn under 50% load. Figure 14a shows the measured and the estimated rotor position. Fig.14b shows the estimation error under steady state. This is within 2° electrical, although under dynamic conditions this error increases considerably. In Fig.15 the drive operates under speed control and a constant load of 50%. Fig.15a shows the response to a speed reversal command from 35 to –35 RPM, the measure and estimated rotor position are plotted. Fig.15b shows the position signals and the rotor position estimation error.

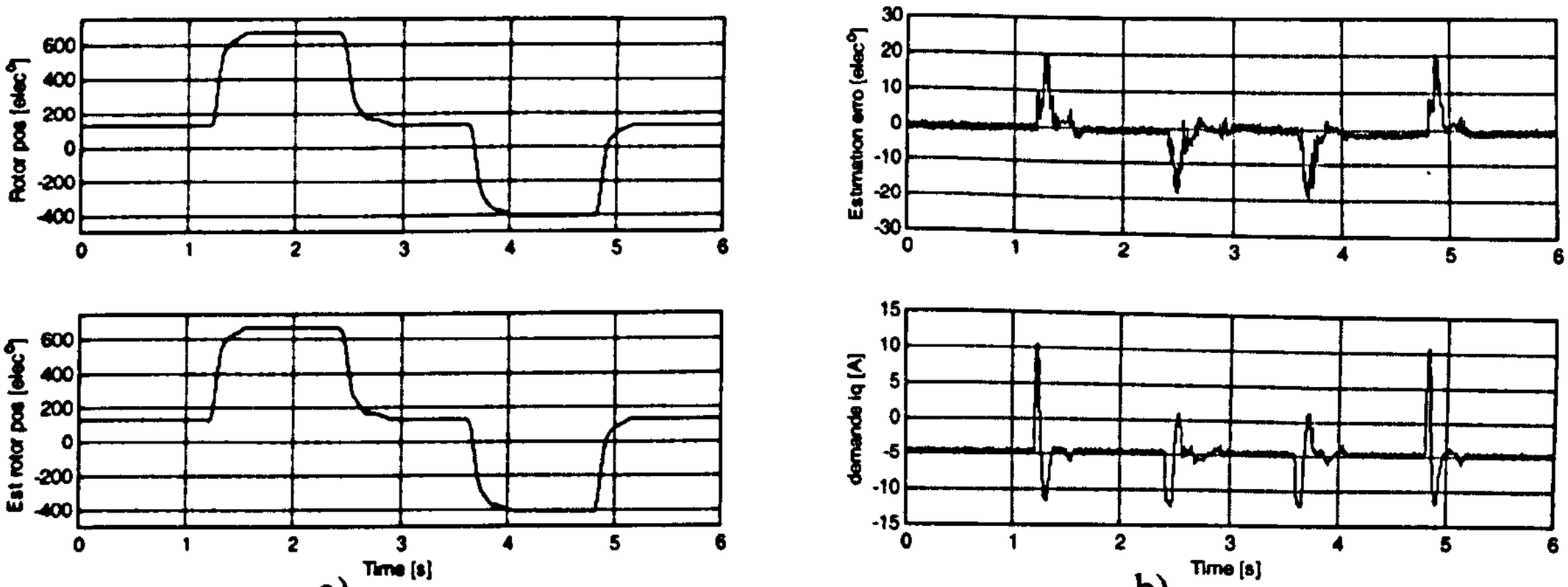

Fig. 14. Sensorless position control under 50 % load.

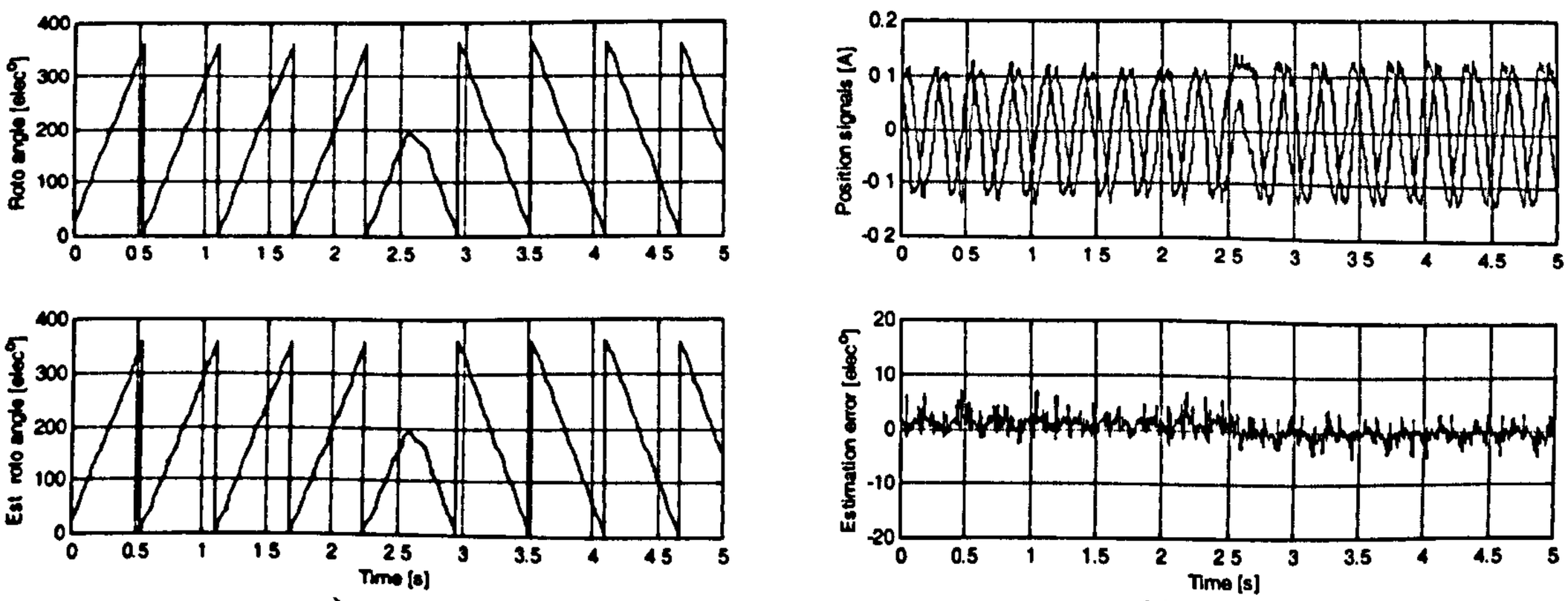

Fig. 15. Sensorless speed reversal from 35 RPM under 50 % load.

Conclusion

This paper has introduced the use of space modulation profiling to obtain low-distortion position estimates for an off-the-shelf surface mounted PM machine operating at low/zero speed and employing HF voltage injection on the stationary α-β axis. This technique has been used in conjunction with dead time compensation to minimise errors in the estimation. The use of the profiling method has resulted in position estimation with an accuracy of 2° electrical (0.6° mechanical) at zero speed under high loaded conditions. Experimental data has being given that shows the effectiveness of the proposed method. The angle estimation used for field orientation and is of sufficient accuracy and quality for sensorless position control with closed loop bandwidths approaching 10Hz.

References

[1] R. Wu and G. Slemon, "A permanent magnet motor drive without a shaft sensor", *IEEE Trans. Ind. Applicat.*, vol. 27, no. 5, pp. 1005-1011, Sept./Oct. 1991.

[2] G. D. Andreescu, "Position and speed sensorless control of PMSM drives based on adaptive observer," in *Proc. EPE'99*, 1999.

[3] R. Dhaouadi, N. Mohan, and L. Norum, "Design and implementation of an extended Kalman filter for the state estimation of a permanent magnet synchronous motor," *IEEE Trans. Power Electron.*, vol. 6, pp. 491-497, Sept./Oxt. 1994.

[4] P. L. Jansen, R. D. Lorenz, "Transducerless position and velocity estimation in induction and salient AC machines," *IEEE Trans. Ind. Applicat.*, vol. 31, no. 2, pp. 240-247, March/April 1995.

[5] F. Blaschke, J. van der Burgt, A. Vandenput, "Sensorless direct field orientation at zero flux frequency," in Proc. IEEE Ind. Applicat. Soc. Annual Meeting, Oct. 1996, pp 189–196.

[6] M. Schroedl, "Sensorless control of AC machines at low speed and standstill based on the "INFORM " method," in Proc. IEEE Ind. Applicat. Soc. Annual Meeting, Oct. 1996, pp 270–277.

[7] J.-I. Ha and S.-K. Sul, "Sensorless filed orientation control of an induction machine by high frequency signal injection," in Proc. IEEE Ind. Applicat. Soc. Annual Meeting, Oct. 1997, pp 426–432.

[8] M. J. Corley and R. D. Lorenz, "Rotor position and velocity estimation for a salient-plot permanent magnet synchronous machine at standstill and high speeds", ", *IEEE Trans. Ind. Applicat.*, vol. 34, No. 4, pp. 784-789, Jul./Aug. 1998.

[9] S-J. Kang, J-I. Ha and S-K. Sul, "Position controlled synchronous reluctance motor without rotational transducer", *IEEE Trans. Ind. Applicat.*, vol 35, no 6, pp. 1393-1398, Nov./Dec. 1999.

[10] N. Kasa and H. Watanabe, "A mechanical sensorless control system for salient-pole brusheless dc motor with autocalibration of estimated position angles", *IEEE Trans. Ind.Electron.*, vol 47, no. 2, pp. 389-395, Apr. 2000.

[11] J-H Jang, J-I Ha and S-K Sul, "Vector control of surface mounted permanent magnet motor without any rotational transducer", *Proc.* IEEE Applied Power Electronics Conference and Exposition (APEC), pp.845-849, USA, March.4-8, 2001.

[12] N. Teske, G. M. Asher, Keith J. Bradley and M. Sumner, "Analysis and Suppression of Inverter Clamping Saliency in Sensorless Position Controlled Induction Machine Drives", *Proc.* IEEE-IAS *Annual Meeting*, Chicago, Sept./Oct. 2001.

[13] C. Silva, G. M. Asher and M. Sumner, "Influence of Dead-time Compensation on Rotor Position Estimation in Surface Mounted PM Machines using HF Voltage Injection", *Proc.* Power Conversion Conference (PCC) 2002, Osaka, April 2002.

[14] J-W Choi and S-K. Sul, "Inverter output voltage synthesis using novel dead time compensation", *IEEE Trans. Power Electonics*, vol. 11, no. 2, pp. 221-227, Mar.1996.

An hf Signal-Injection Based Observer for Wide Speed Range Sensorless PM Motor Drives Including Zero Speed

C. Silva, G. M. Asher, M. Sumner
School of Electrical and Electonic Engineering
University of Nottingham, Nottingham NG7 2RD, UK
Tel: +44 (0)115 9515549 / Fax: +44 (0) 115 9515616
Email: eexcas1@nottingham.ac.uk
URL: http://www.eee.nott.ac.uk/pemc/

Keywords

Sensorless drives, Permanent magnet motors, Flux model.

Abstract

This paper addresses the problem of wide speed range sensorless control of a surface mount permanent magnet (SMPM) machine including zero speed operation. A new hybrid structure integrating a flux observer and signal injection techniques is proposed which results in a rotor position signal independent of motor parameters at low and zero speed. Experimental results are presented showing excellent performance for both sensorless speed and position control.

Introduction

Observer based sensorless control of SMPM motors relies on integrating the back-emf and hence deriving stator flux position. This flux position can be used directly for vector control orientation [1] or it can be corrected to estimate the magnet flux and hence rotor position [2]. Alternatively, the back-emf can be used to feed an close-loop observer to derive rotor position [3, 4]. It is well known that such methods break down at low speeds due to the lack of back-emf induced in the stator windings effecting an increasing influence on parameter estimation error and measurement noise.

In salient machines, voltage test signals can be injected and the resulting currents processed to obtain a rotor position estimates base on the saliency independent of the back-emf and model parameters. The test signal can be a continuous high frequency voltage [5-10], discrete voltage pulses [11] or modified PWM pulses [12, 13]. These methods work by tracking the intrinsic saliency of the machine arising from the difference between the *d*- and *q*-axis inductances. Even for SMPM machines, normally considered non-salient, the difference arising from the saturation induced by the rotor magnets in the stator teeth iron is sufficient for yielding robust position estimates [14]. Injection methods have two disadvantages however:

(i) They introduce extra losses or transient disturbances and hence should only be used in the low speed region.
(ii) The position estimates may contain low ripples that arise from the non-sinusoidal distribution of the saliency, coupling effects of fundamental current transients and from inverter non-linear effects. These ripples can be compensated for [14-16] but always effect a reduction in the control bandwidth in comparison with sensored methods.

In the present work, point (i) above is addressed by changing from the *hf* signal injection based estimate to a conventional model observer at an appropriately low excitation frequency, the transition being achieved by incorporating the injection estimate as part of a flux observer. This does not only

provide a smooth transition but also improves the feedback signal quality alleviating the effects described in (ii) above.

Fundamentals of the *hf* voltage injection method

The surface mounted PM machine is normally considered non-salient. Nevertheless the iron saturation, mainly in the stator teeth, creates a modulation of the machines inductance. In contrast with inherently salient machines like interior PM machines, the saliency in SMPM machines doesn't correspond exactly with the rotor position. Although the saliency position θ_δ is dominated by the rotor position θ, (due to the high magnetic flux density imposed by the rotor magnets and the low stator inductances), a shift occurs in the saliency position under load due to the relative shifts in stator flux. The saliency is described by the minimum value of inductance $L_\delta = \overline{L} - \Delta L$, which defines the saliency orientation θ_δ, and the maximum value of inductance $L_\gamma = \overline{L} + \Delta L$ measured in the axis in quadrature to it.

In this paper, the saliency detection method used at low speed consists of the injection of a *hf* voltage vector of constant amplitude rotating in the stationary α-β frame superimposed to the reference voltage [7, 14]. The *hf* voltage injection is given by:

$$\boldsymbol{v}_i = \begin{bmatrix} v_{\alpha i} \\ v_{\beta i} \end{bmatrix} = \hat{V}_i \begin{bmatrix} -\sin(\omega_i t) \\ \cos(\omega_i t) \end{bmatrix} \tag{1}$$

The voltage injection results in a *hf* current superimposed onto the fundamental excitation current. This *hf* component can be extracted using band-pass filters centered at ω_i. If the injection frequency is significantly high, such that the machines impedance is dominated by it's inductance and the injection current is outside the bandwidth of the current controller, the resulting injection current can be approximated by:

$$\boldsymbol{i}_i = \begin{bmatrix} i_{\alpha i} \\ i_{\beta i} \end{bmatrix} \approx \begin{bmatrix} I_0 \cos(\omega_i t) + I_1 \cos(2\theta_\delta - \omega_i t) \\ I_0 \sin(\omega_i t) + I_1 \sin(2\theta_\delta - \omega_i t) \end{bmatrix} \tag{3}$$

This current can be separated into a positive and a negative sequence, which respective amplitudes I_0 and I_1 are:

$$I_0 = \frac{\hat{V}_i \overline{L}}{L_\delta L_\gamma \omega_i} \text{ and } I_1 = \frac{\hat{V}_i \Delta L}{L_\delta L_\gamma \omega_i} \tag{4}$$

The analysis of (3) and (4) shows that only the negative sequence current, proportional to the difference of inductance, gives information on the saliency angle. This component can be separated and demodulated taking advantage of its vectorial characteristic, by a low-pass filter in a reference frame synchronous with the negative sequence of the injection current [10]. In this work a variation of this method is used for improved rejection of the positive sequence injection current. This consists of two cascades filters: a high-pass filter synchronized with the positive sequence and a low-pass filter in the negative sequence frame [14]. The resulting demodulation yields the saliency position signals:

$$\begin{bmatrix} i_{\alpha\_pos} \\ i_{\beta\_pos} \end{bmatrix} \approx \begin{bmatrix} I_1 \cos(2\theta_\delta) \\ I_1 \sin(2\theta_\delta) \end{bmatrix} \tag{5}$$

The extraction of the angle $2\theta_\delta$ is done by direct tan^{-1} calculation, although the use of PLL-type structures for this purpose has also being reported on the literature [7]. The uncertainty caused by the 180° periodicity of the saturation saliency must be solved by an appropriate starting procedure [17].

Due to the non-sinusoidal distribution of the saturation saliency and to nonlinear effects of the inverter, such as dead-time and device voltage drop, the position signal contains spurious harmonics. In the present work these are tackled by using the compensation method presented in [14]. However, the principle operation of the hybrid observer which integrates both voltage injection for low speeds and model-based method for the higher speeds is independent of this compensation method. Therefore the compensation method is omitted in this paper.

For the correct vector control orientation of the synchronous PM machine an estimation of the rotor position is needed. However, in a surface mounted PM machine the signal injection method yields only the saliency position and a phase correction must be applied to account for the shift of the saturation saliency due to stator current. The phase correction curve of Fig. 1 has being determined empirically in a sensored commissioning process. This figure shows that, for the machine used in this work, the saliency approximately follows the stator flux rather than the rotor position. At low loads it is suspected that the deviations from the stator flux positions are due to the inverter non-linearities upon the injection signals rather than actual shifts in the machines saturation.

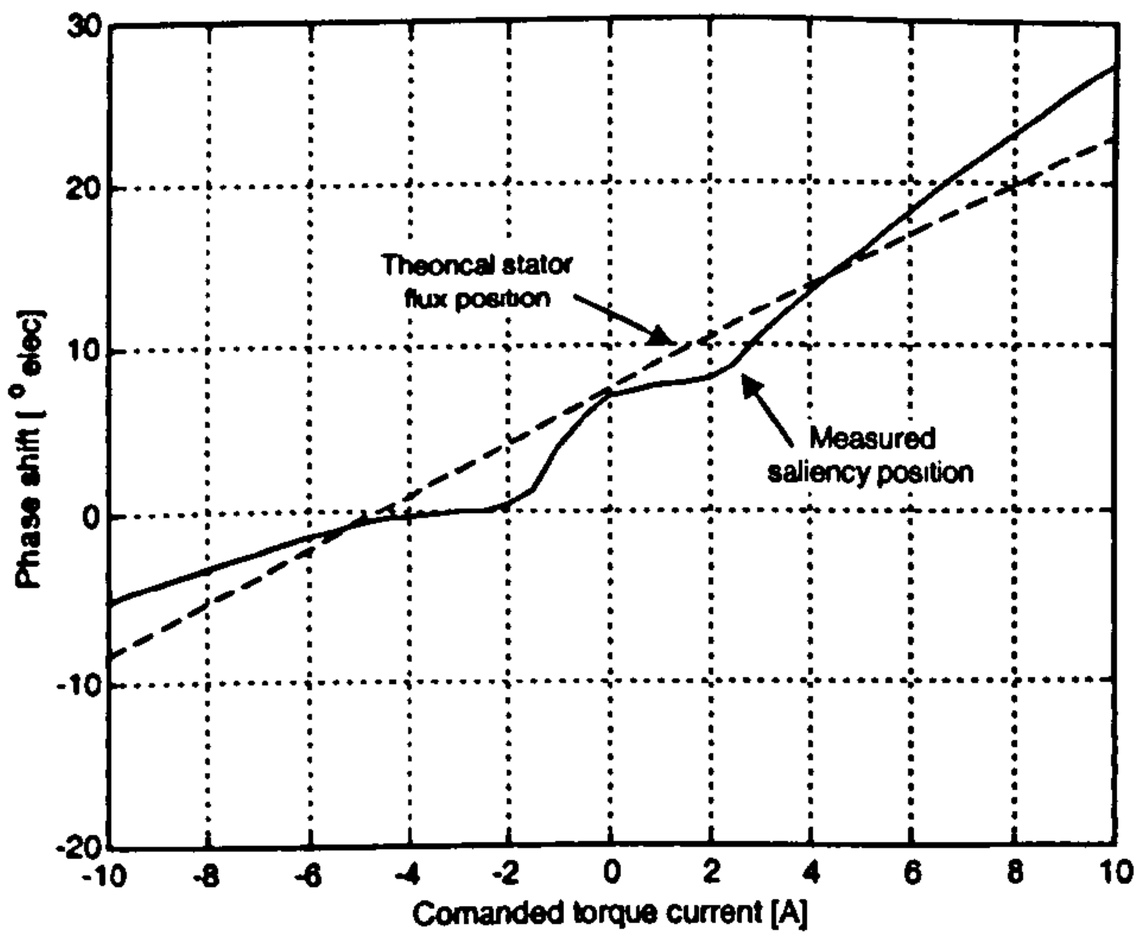

Figure 1: Phase shift between rotor and estimated saliency position as function of torque current.

The correction of the saturation phase shift completes the α-β voltage injection method yielding rotor position estimation $\hat{\theta}_r$. Figure 2 illustrates the signal processing applied to the measured currents to determine the saliency position, and through open loop compensation to estimate the rotor position.

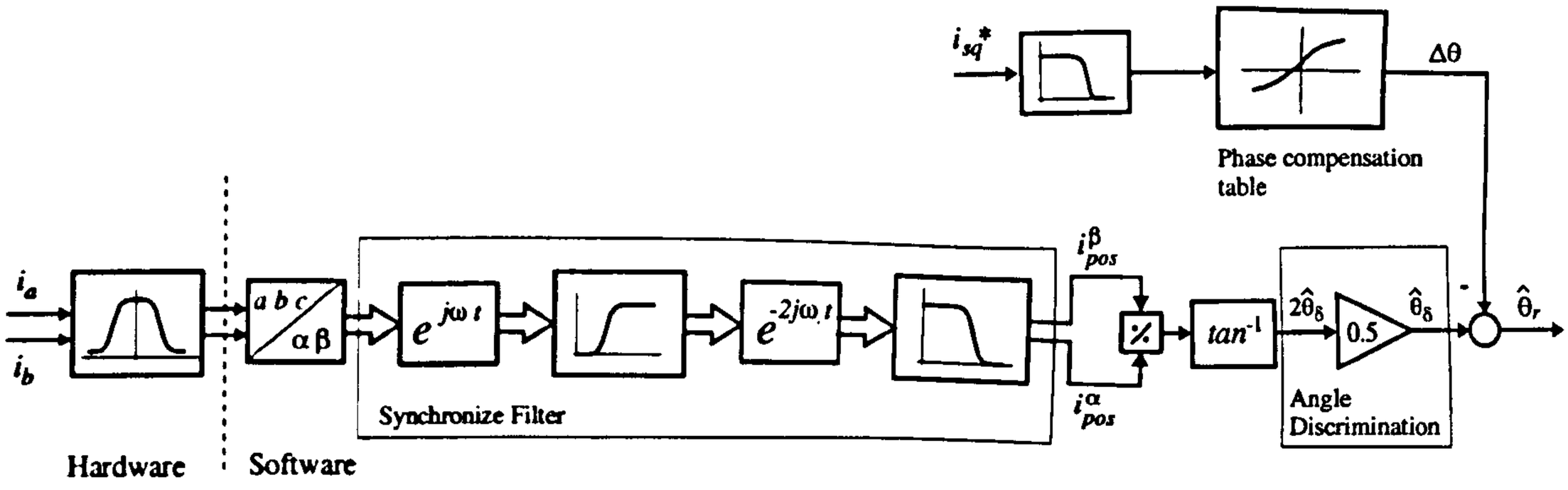

Figure 2: Signal processing of the measure currents in α-β voltage injection.

Model base estimation

A simple model can be used to obtain the same information, i.e. rotor position, by calculating the flux induced by the rotor magnets in the stator winding. The total stator flux can be computed as the integral of the back-emf of the machine, the flux due to the rotor magnets obtained by compensation of the flux generated by the stator currents. This is usually referred as the "voltage model" and it is given by:

$$\psi_r^v = \frac{1}{s}(v_s - i_s R_s) - i_s L_s \tag{6}$$

In the practical implementation of the flux observer, the commanded voltages are used instead of the actual measured values and a negative feedback path with low gain k_1 is provided to avoid integrator drift:

$$\hat{\psi}_r = \frac{1}{s+k_1}(v_s^* - i_s \hat{R}_s) - \frac{s}{s+k_1} i_s \hat{L}_s \approx \frac{s}{s+k_1}\psi_r^v \tag{7}$$

The use of a low pass filter as an approximation of the pure integrator limits the effectiveness of the voltage model to fundamental frequencies well above the cut-off frequency of the filter.

Hybrid system

The low pass characteristic of (7) is not the only factor that limits the use of voltage model flux estimate at low speed. The decreasing signal to noise ratio of the back-emf and the increasing effect of the parameter estimation errors and inverter non-linearities in the model with low speed also impede its use. Therefore at low speed the injection estimate introduced in section I is used. To perform a smooth transition between both strategies, a hybrid system where the influence of the injection estimate increase as speeds decreases is used. The hybrid system is described by Fig. 3. In this scheme the injection position estimated $\hat{\theta}_{inj}$ is used to construct an injection flux estimation $\hat{\psi}_{inj}$. This flux estimate serves as a reference for the model at low frequencies. At higher speeds the injection flux estimate ceases to have a significant influence and is finally disconnected by the speed dependent functions $f_1(\hat{\omega}_r)$ and $f_2(\hat{\omega}_r)$.

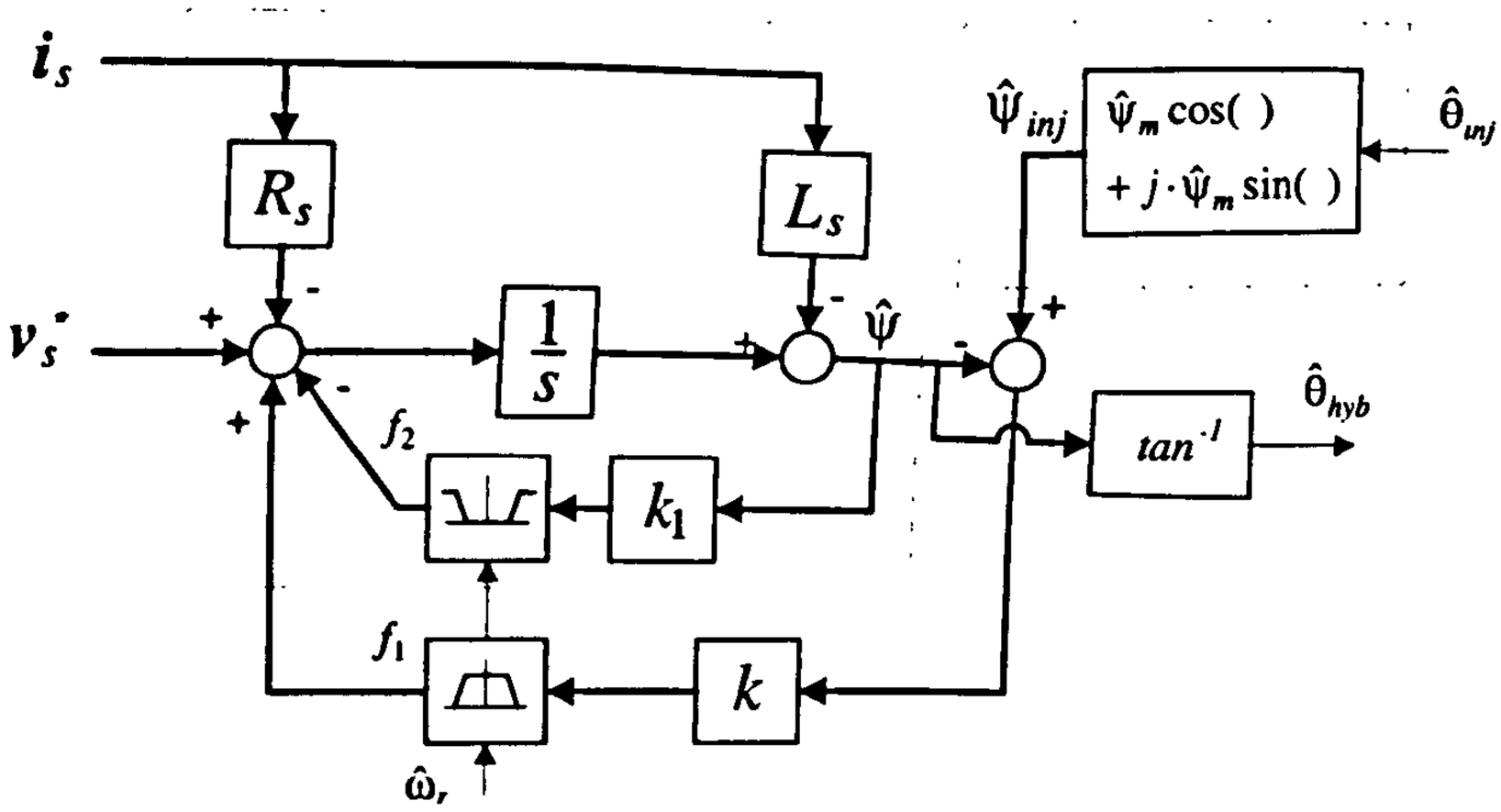

Figure 3: Hybrid structure for coupling of injection and voltage model estimates.

Low speed operation

At low speeds the functions f_1 and f_2 have the values one and zero respectively, therefore the following equation applies:

$$\hat{\psi}_r = \frac{1}{s}\left\{(v_s^* - i_s\hat{R}_s) + k(\hat{\psi}_r^{inj} - \hat{\psi}_r)\right\} - i_s\hat{L}_s \tag{8}$$

yielding:

$$\hat{\psi}_r = \frac{s}{s+k}\psi_r^v + \frac{k}{s+k}\hat{\psi}_r^{inj} \tag{9}$$

Therefore the rotor flux estimation $\hat{\psi}_r$ is a combination of the injection estimate $\hat{\psi}_r^{inj}$, dominant at low frequencies and the voltage model ψ_r^v dominant at higher frequencies. At steady state the flux is purely sinusoidal and therefore the flux estimate is a weighted average of both independent estimates. At very low speed the injection estimate is dominant and any noise on it is filtered by the low pass filter action of the close loop. Nevertheless this does not have a detrimental effect on the dynamic of the estimation because during transients the voltage estimate provides a path for the estimation of the high frequency components of the flux. This results in improved results from those obtained from the use of the injection method alone.

Transition to model base estimation

At higher speeds the voltage model yields good estimations and does not need the injection estimate to be used as a reference. Furthermore at frequencies higher than the crossover frequency $f_c = \frac{k}{2\pi}$, the relative influence of the injection estimate becomes less significant and it can be disconnected. The disconnection of the injection estimate is performed gradually by reducing the controller gain by means of a multiplying function of the speed $f_1(\hat{\omega}_r)$. This function decreases linearly above the lower transition speed, reaching zero at the upper transition speed. At the same time the feedback gain k_1 is connected to avoid drifting of the flux estimator, multiplying the feedback by $f_2(\hat{\omega}_r)$ which is complementary to $f_1(\hat{\omega}_r)$. At speeds above the upper transition speed the functions f_1 and f_2 have the values of zero and one respectively, reducing the hybrid system to the simple voltage model of (7).

The voltage injection itself is turned on and off using a hysteresis band at a speed slightly higher than the upper transition speed.

The main design criteria for the controller gain k are:

- A value sufficiently large so the injection estimate dominating the hybrid estimation $\hat{\psi}_r$ before the voltage model starts braking down at low speed because noise and error in the parameters.
- In the other hand it should be sufficiently small so that the voltage model dominates the hybrid estimation at the lower transition frequencies.

Finally the feedback gain k_1 is chosen to be sufficiently small so it produces a negligible phase shift of the flux estimate at the upper transition frequency.

Experimental results

The proposed method has been implemented in a 4 kW off-the-shelf surface-mounted PM motor. This is a 6 pole machine and with a base speed of 3000 rpm. The transition between each method is performed between the lower and upper threshold speeds of 400 and 600 rpm, i.e. 13.3 to 20 % of nominal speed. The controller gain is set to $k = 94.3$, giving a crossover frequency of 15 hertz and the negative feedback gain for convergence of the integrator is set to $k_1 = 12.6$.

The results of a sensorless speed reversal from 1500 rpm to –1500 rpm at no load are shown in Fig. 4. The measured and estimated speeds are plotted and both initial and final speeds are in the region where only the voltage model is operative. It can be appreciated that the transition to middle and low speed regions are smooth. In Fig. 5 the position estimated is plotted together with the measured value to show the good correspondence of both variables. In the bottom plot the injection estimate is shown only for the period in which it is used for driving the hybrid estimation.

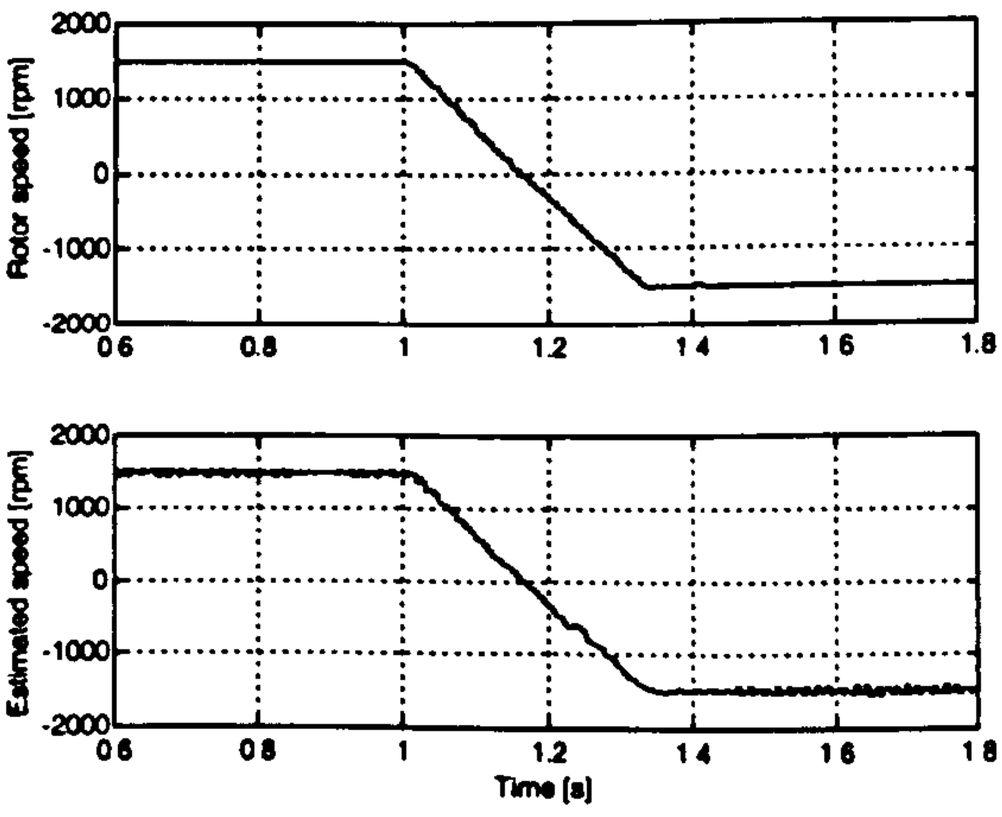

Figure 4: Sensorless speed reversal at no load;
top: measured speed, *bottom*: estimated speed.

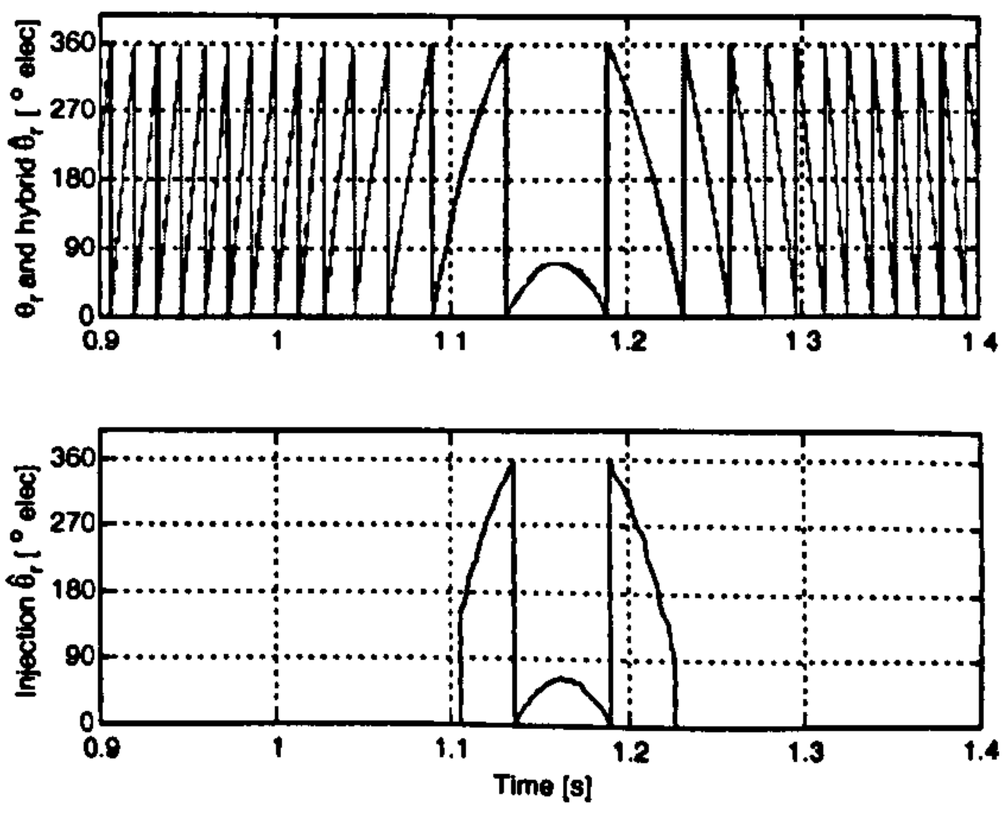

Figure 5: Sensorless speed reversal at no load;
top: measured and estimated rotor position,
bottom: Injection position estimation.

The good performance of the hybrid estimation is maintain for operation under load, Fig. 6 and Fig. 7 show a similar speed reversal transient under 100% nominal load. In this case the acceleration is faster because the load torque assists in the drives electric torque. In Fig. 6 very good speed estimation is observable, especially during motoring operation, i.e. positive speed. During the transition from injection to model-base estimation a small disturbance appears in the estimated speed but does not affect the control of the machine.

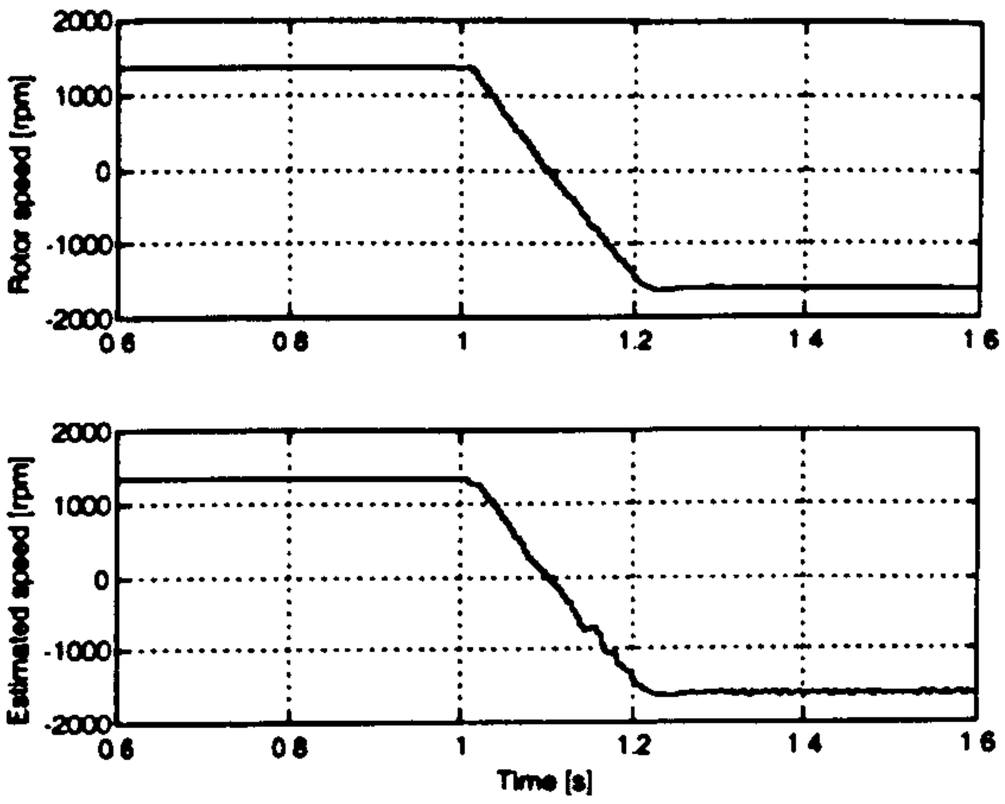

Figure 6: Sensorless speed reversal at full load;
top: measured speed, *bottom*: estimated speed.

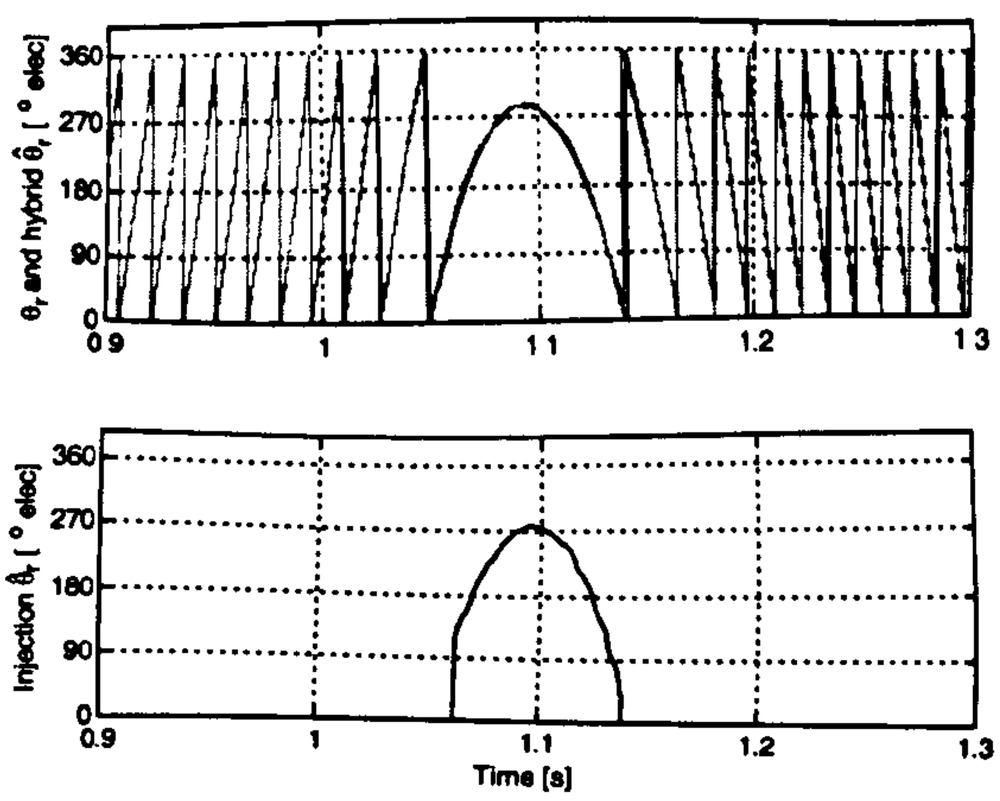

Figure 7: Sensorless speed reversal at full load;
top: measured and estimated rotor position,
bottom: Injection position estimation.

The presented speed reversal results show good transition through zero speed. However even more critical is sustained sensorless operation at low/zero speed. The good operation in this condition is demonstrated by sensorless position steps results. The results shown in Fig. 8 and Fig. 9 correspond to reference position steps applied with the machine at no load. The magnitude of the steps is chosen to be 100 elec. radians, slightly over 5 full mechanical turns, and is sufficiently high for the machine to accelerate to speeds outside the *hf* injection region and in to the voltage model sensorless region before. Figure 8 shows the measured and estimated rotor position, demonstrating that the control is maintained at zero speed. In Fig. 9 the measured and estimated speeds are shown. It can be seen that the speed does go over the 600 rpm threshold where the injection estimate cease to be used.

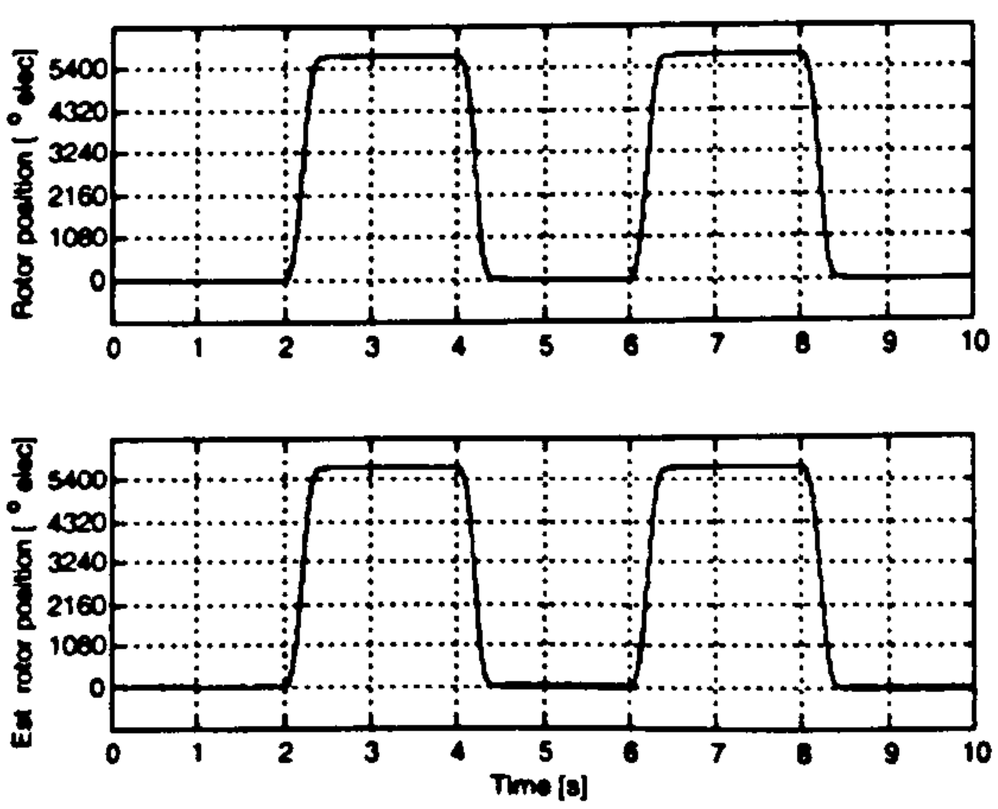

Figure 8: Sensorless position demand steps under no load; *top*: measured rotor position, *bottom*: estimated rotor position.

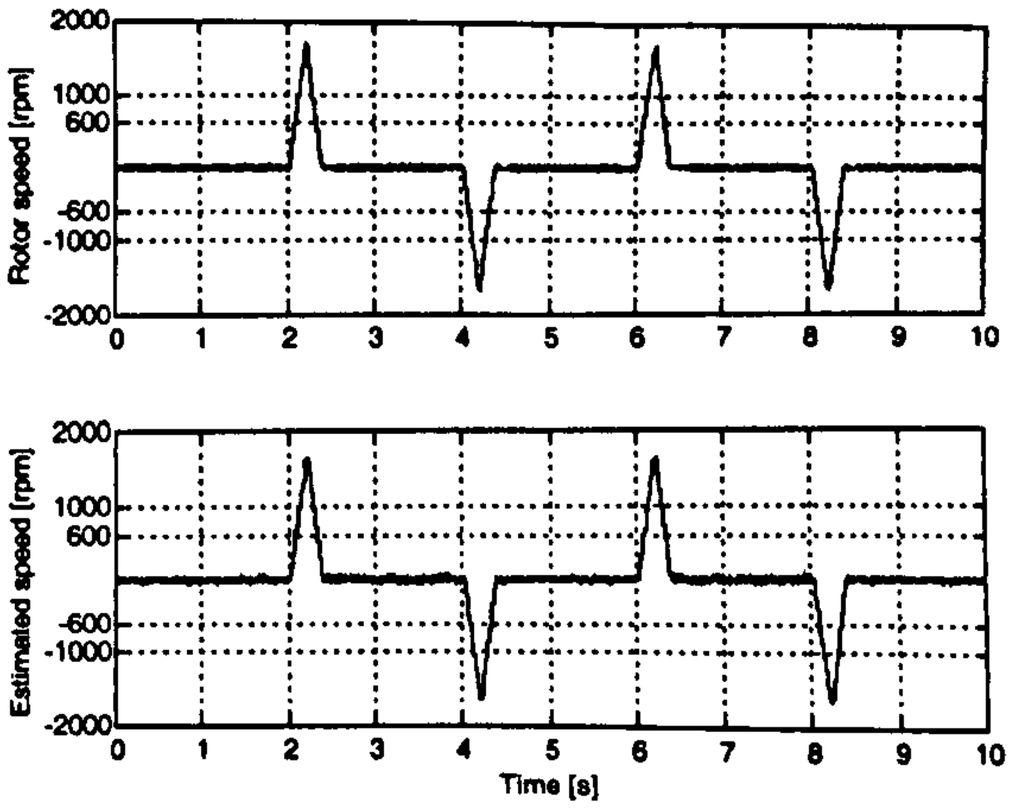

Figure 9: Sensorless position demand step under no load; *top*: measured rotor speed, *bottom*: estimated rotor speed.

Results for a position step of same magnitude, under full load is shown in Fig. 10 and the ability to hold position indefinitely under load is demonstrated. To show the correct orientation of the vector control during this transient, the measured and estimated angle are shown in Fig. 11. The filtering action of the hybrid method is shown in Fig. 12 by closely comparing the pure injection angle estimation $\hat{\theta}_{inj}$ and the resulting angle estimation $\hat{\theta}_{hyb}$ (see Fig. 3).

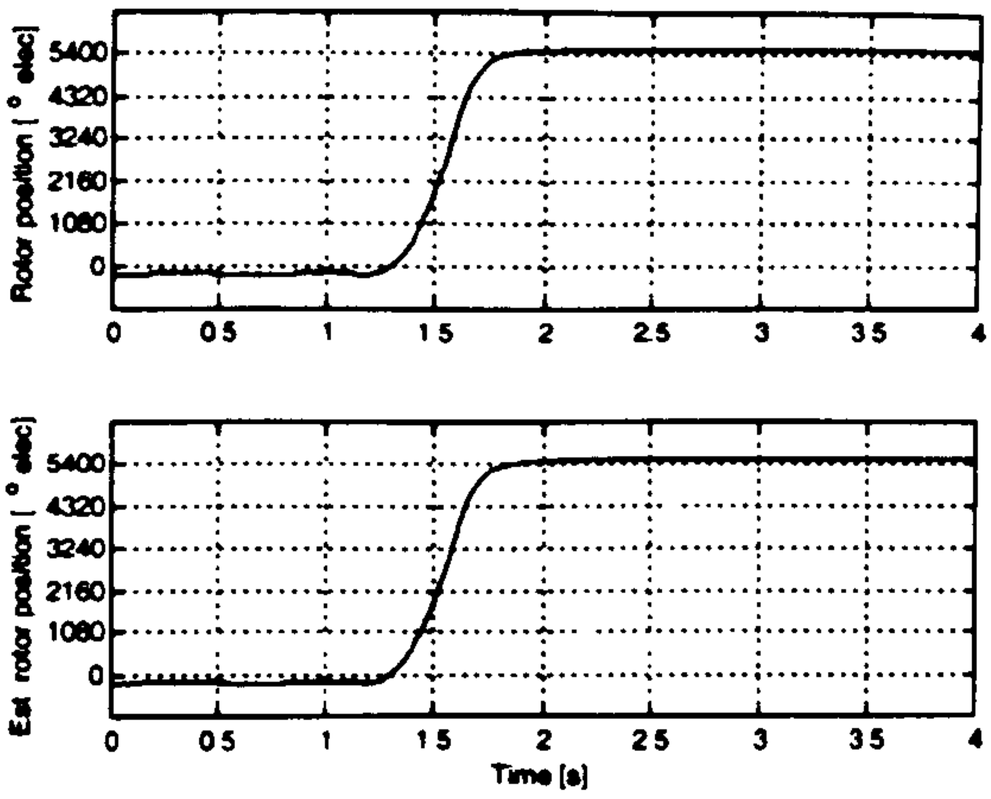

Figure 10: Sensorless position demand step under full load; *top*: measured rotor position, *bottom*: estimated rotor position.

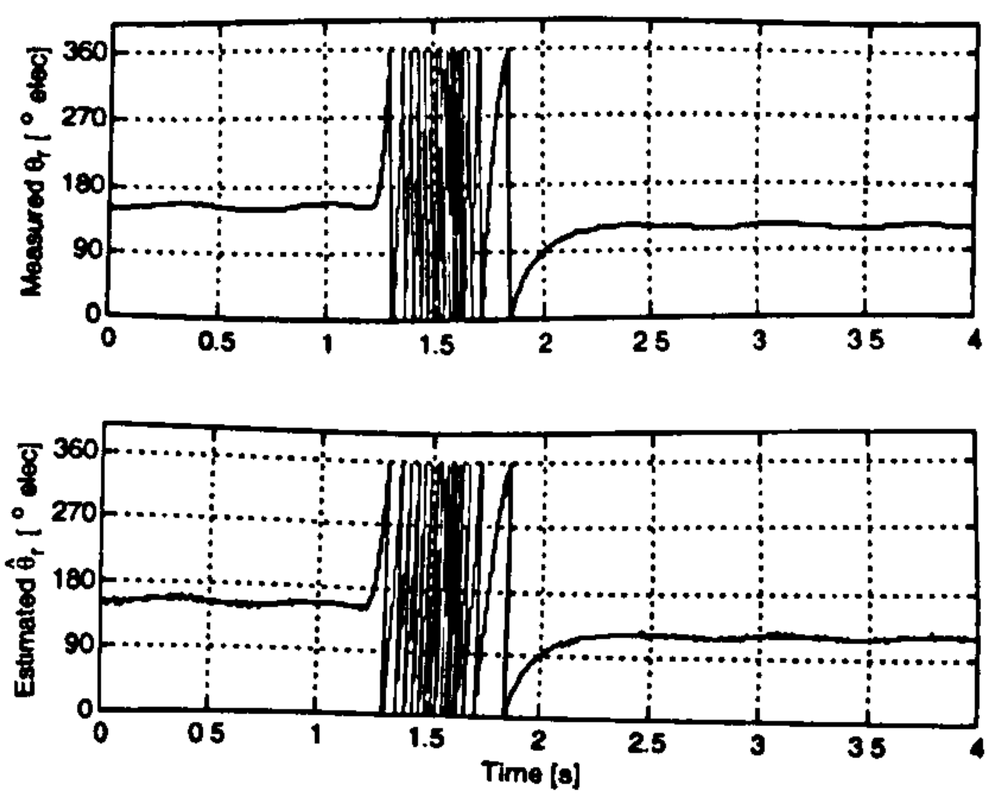

Figure 11: Sensorless position demand step under full load; *top*: measured rotor angle, *bottom*: estimated rotor angle.

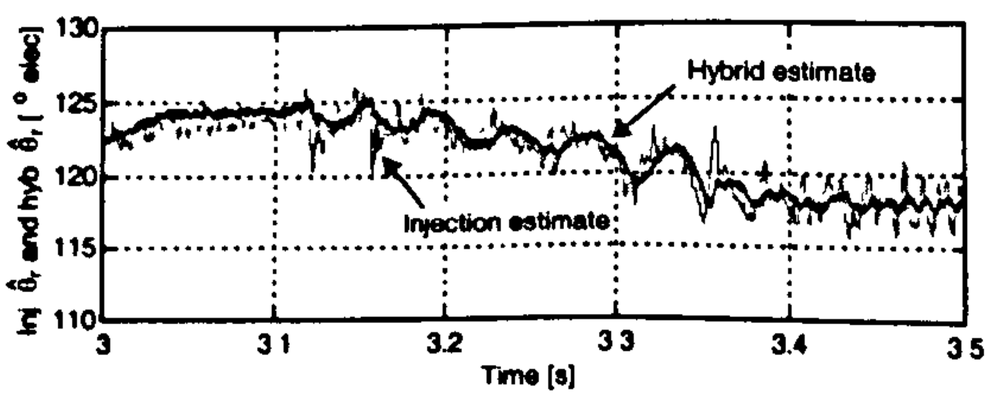

Figure 11: Improvement on the angel estimation.

Conclusions

A hybrid observer structure for deriving an estimated rotor angle at any speed has been proposed. The hybrid structure presents a smooth transition from a non-model based signal-injection method at low speed through to a model-based flux observer at higher speeds. Experimental results show good orientation in steady state and during transients under any load condition. The combination of the flux observer and the injection method right down to zero speed is shown and is seen to provide filtering action improving the injection angle estimate.

References

[1] R. Wu and G. R. Slemon, "A Permanent Magnet Motor Drive Without a Shaft Sensor," *IEEE Transactions on Industry Applications*, vol. 27, pp. 1005-1011, 1991.

[2] G. D. Andreescu, "Position and Speed Sensorless Control of PMSM Drives Based on Adaptive Observer," presented at 8th European Conference on Power Electronics and Applications, EPE, Lausanne, 1999.

[3] K. Urbanki and K. Zawirski, "Rotor Speed and Position Observer for PMSM Sensorless Control System," presented at 9th European Conference on Power Electronics and Applications, EPE, Graz, 2001.

[4] J.-S. Kim and S.-K. Sul, "High performance PMSM drives without rotational position sensors using reduced order observer," presented at IEEE-IAS Annual Meeting, 1995.

[5] P. L. Jansen and R. D. Lorenz, "Transducerless Position and Velocity Estimation in Induction and Salient AC Machines," *IEEE Transactions on Industry Applications*, vol. 31, pp. 240-247, 1995.

[6] J.-I. Ha and S.-K. Sul, "Sensorless Field Orientation Control of an Induction Machine by High Frequency Signal Injection," presented at IEEE-IAS Annual Meeting, Nwe Orleans, Lousiana, 1997.

[7] M. Corley and R. D. Lorenz, "Rotor Position and Velocity Estimation for a Salient-Pole Permanent Magnet Synchronous Machine at Standstill and High Speeds," *IEEE Transactions on Industry Applications*, vol. 34, pp. 784-789, 1998.

[8] A. Consoli, G. Scarcella, and A. Testa, "Insustry Application of Zero-Speed Sensorless Control Techniques for PM Synchronous Motors," *IEEE Transactions Industry Appplications*, vol. 37, pp. 513-521, 2001.

[9] M. Linke, R. Kennel, and J. Holtz, "Sensorless position control of Permanent Magnet Synchronous Machines without Limitation," presented at IECON 2002, Sevilla, Spain, 2002.

[10] N. Teske, G. M. Asher, K. J. Bradley, M. Sumner, and J. Cilia, "Sensorless Position Control of Induction Machines using Rotor Saliencies under Load Conditions," presented at 8th European Conference on Power Electronics and Applications, EPE, Lausanne, 1999.

[11] M. Schrodl, "Sensorless Control of AC Machines at Low Speed and Standstill Based on the 'INFORM' Method," presented at IEEE-IAS Annual Meeting, San Diego, USA, 1996.

[12] S. Ogasawara and H. Akagi, "Implementation and Position Control Performance of a Position-Sensorless IPM Motor Drive System Based on Magnetic Saliency," *IEEE Transactions on Industry Applications*, vol. 34, pp. 806-812, 1998.

[13] J. Holtz, "Sensorless Position Control of Induction Motors - An Emerging Technology," *IEEE Transactions Industrial Electronics*, vol. 45, pp. 840-852, 1998.

[14] C. Silva, G. M. Asher, M. Sumner, and K. J. Bradley, "Sensorless Rotor Position Control in a Surface Mounted PM Machine Using HF Voltage Injection," presented at 10th International Power Electronics and Motion Control Conference, EPE-PEMC, Dubrovnik, 2002.

[15] N. Teske, G. M. Asher, M. Sumner, and K. J. Bradley, "Suppression of Saturation Saliency Effects for the Sensorless Position Control of Induction Motor Drives Under Loaded Conditions," *IEEE Transactions Industrial Electronics*, vol. 47, pp. 1142-1150, 2000.

[16] F. Briz, A. Diez, and M. W. Dagner, "Dynamic Operation of Carrier-Signal-Injection-Based Sensorless Direct Field-Oreinted AC Drives," *IEEE Transactions on Industry Applications*, vol. 36, pp. 1360-1368, 2000.

[17] P. B. Schmidt, M. L. Gasperi, G. Ray, and A. H. Wijenayake, "Initial Rotor Angle Detection Of A Non-Salient Pole Permanent Magnet Synchronous Machine," presented at IEEE-IAS Annual Meeting, New Orleans, Lousiana, 1997.

Bibliography

[1] J. F. Gieras and M. Wing, *Permanent Magnet Motor Technology: Designe and Applications*, Second ed. New York - Basel: Marcel Dekker, Inc., 2002.

[2] R. Crowder and C. Maxwell, "Simulation of a prototype electrically powered integrated actuator for civil aircraft," *Proc. Instn Mech. Engrs*, vol. 211, part G, pp. 381-394, 1997.

[3] S. E. Lyshevski, V. A. Skormin, and R. D. Colgren, "High-Torque Density Integrated Electro-Mechanical Flight Actuators," *IEEE Transactions on Aerospace and Electronic Systems*, vol. 38, pp. 174-181, 2002.

[4] B. K. Bose, "Power Electronics and Variable Frequency Drives, Technology and Applications." Piscataway, NJ, USA: IEEE Press, 1997.

[5] G. R. Slemon, "Electrical Machines for Variable-Frequency Drives," *Proceedings of the IEEE*, vol. 82, pp. 1123-1139, 1994.

[6] J. F. Miller, *Brushlesss Permanent-Magnet and Reluctance Motor Drives*. Oxford: Clarendon Press, 1989.

[7] T. Jahns, G. Kliman, and T. Neumann, "Interior Permanent-Magnet Synchronous Motors for Adjustable-Speed Drives," *IEEE Transactions on Industry Applications*, vol. 22, pp. 738-747, 1986.

[8] T. Jahns, "Flux-Weakening Regime Operation of an Interior Permanent-Magnet Synchronous Motor Drive," *IEEE Transactions on Industry Applications*, vol. 23, pp. 681-689, 1987.

[9] B. K. Bose, "A High-Performance Inverter-Fed Drive System of an Interiror Permanent Magnet Synchronous Machine," *IEEE Transactions Industry Appplications*, vol. 24, pp. 987-997, 1988.

[10] W. Leonhard, *Control of Electrical Drives*. Berlin Heidelberg, Germany: Springer-Verlag, 1985.

[11] R. Wu and G. R. Slemon, "A Permanent Magnet Motor Drive Without a Shaft Sensor," *IEEE Transactions on Industry Applications*, vol. 27, pp. 1005-1011, 1991.

[12] G. D. Andreescu, "Position and Speed Sensorless Control of PMSM Drives Based on Adaptive Observer," presented at 8th European Conference on Power Electronics and Applications, EPE, Lausanne, 1999.

[13] L. Jones and J. Lang, "A State Observer for the Permanent-Magnet Synchronous Motor," *IEEE Transactions on Industrial Electronics*, vol. 36, pp. 374-382, 1989.

[14] J.-S. Kim and S.-K. Sul, "High performance PMSM drives without rotational position sensors using reduced order observer," presented at IEEE-IAS Annual Meeting, 1995.

[15] K. Urbanski and K. Zawirski, "Rotor Speed and Position Observer for PMSM Sensorless Control System," presented at 9th European Conference on Power Electronics and Applications, EPE, Graz, 2001.

[16] R. Dhaouadi, N. Mohan, and L. Norum, "Design and Implementation of an Extended Kalman Filter for the State Estimation of a Permanent Magnet Synchronous Motor," *IEEE Transactions on Power Electronics*, vol. 6, pp. 491-497, 1991.

[17] S. Bolognani, R. Oboe, and M. Zigliotto, "Sensorless Full-Digital PMSM Drive with EKF Estimation of Speed and Rotor Position," *IEEE Transactions on Industrial Electronics*, vol. 46, pp. 184-191, 1999.

[18] M. Corley and R. D. Lorenz, "Rotor Position and Velocity Estimation for a Salient-Pole Permanent Magnet Synchronous Machine at Standstill and High Speeds," *IEEE Transactions on Industry Applications*, vol. 34, pp. 784-789, 1998.

[19] A. B. Kulkni and M. Ehsani, "A Novel Position Sensor Elimination Technique for the Interior Permanent Magnet Synchronous Motro Drive," *IEEE Transactions on Industry Applications*, vol. 28, pp. 144-150, 1992.

[20] M. Schrodl, "An Improved position estimator for sensorless controlled permanent magnet synchronous motors," presented at 4th European Conference on Power Electronics and Applications EPE, Firenze (Italy), 1991.

[21] P. L. Jansen and R. D. Lorenz, "Transducerless Position and Velocity Estimation in Induction and Salient AC Machines," *IEEE Transactions on Industry Applications*, vol. 31, pp. 240-247, 1995.

[22] S. Ogasawara and H. Akagi, "Implementation and Position Control Performance of a Position-Sensorless IPM Motor Drive System Based on Magnetic Saliency," *IEEE Transactions on Industry Applications*, vol. 34, pp. 806-812, 1998.

[23] Y. Kazunori, S. Ogasawara, and H. Akagi, "Performance Evaluations of a Position-Sensorless IPM Motor Drive System Based on Detection of Current Switching Ripples," presented at Power Electronics Specialist Conference, 2000.

[24] J.-I. Ha, S.-J. Kang, and S.-K. Sul, "Position-Controlled Synchronous Reluctance Motor Without Rotational Transducer," *IEEE Transactions on Industry Applications*, vol. 35, pp. 1393-1398, 1999.

[25] J. Cilia, G. M. Asher, K. J. Bradley, and M. Sumner, "Sensorless Position Detection for Vector-Controlled Induction Motor Drives using an Asymmetric Outer-Section Cage," *IEEE Transactions on Industry Applications*, vol. 33, pp. 1162-1169, 1997.

[26] J. Holtz, "Sensorless Position Control of Induction Motors - An Emerging Technology," *IEEE Transactions on Industrial Electronics*, vol. 45, pp. 840-852, 1998.

[27] N. Teske, G. M. Asher, M. Sumner, and K. J. Bradley, "Encoderless Position Estimation for Symmetric Cage Induction Machines under Loaded Conditions," *IEEE Transactions on Industry Applications*, vol. 37, pp. 1793-1800, 2001.

[28] N. Teske, G. M. Asher, M. Sumner, and K. J. Bradley, "Encoderless Position Control of Induction Machines," presented at EPE Conference, Graz, Austria, 2001.

[29] N. Teske, G. M. Asher, K. J. Bradley, M. Sumner, and J. Cilia, "Sensorless Position Control of Induction Machines using Rotor Saliencies under Load

Conditions," presented at 8th European Conference on Power Electronics and Applications, EPE, Lausanne, 1999.

[30] J. Holtz and H. Pan, "Elimination of Saturation Effects in Sensorless Position Controlled Induction Motors," presented at IEEE-IAS Annual Meeting, 2002.

[31] M. Dagner and R. Lorenz, "Using Multiple Saliencies for the Estimation of Flux, Position, and Veloocity in AC Machines," *IEEE Transactions Industrial Electronics*, vol. 34, pp. 1097-1104, 1998.

[32] N. Teske, G. M. Asher, M. Sumner, and K. J. Bradley, "Suppression of Saturation Saliency Effects for the Sensorless Position Control of Induction Motor Drives Under Loaded Conditions," *IEEE Transactions Industrial Electronics*, vol. 47, pp. 1142-1150, 2000.

[33] J.-H. Jang, J.-I. Ha, and S.-K. Sul, "Vector Control of Surface Mounted Permanent Magnet Motor without any Rotational Transducer," presented at IEEE-APEC Annual Meeting, 2001.

[34] M. Linke, R. Kennel, and J. Holtz, "Sensorless position control of Permanent Magnet Synchronous Machines without Limitation," presented at IECON 2002, Sevilla, Spain, 2002.

[35] J.-I. Ha and S.-K. Sul, "Sensorless Field Orientation Control of an Induction Machine by High Frequency Signal Injection," presented at IEEE-IAS Annual Meeting, Nwe Orleans, Lousiana, 1997.

[36] L. Wang and R. D. Lorenz, "Rotor Position Estiamation for Permanent Magnet Synchronous Motor Using Saliency-Tracking Self-Sensing Method," presented at IEEE-IAS Annual Meeting, 2000.

[37] P. K. Kovács, *Transient Phenomena in Electric Machines*. Amsterdam, Netherlands: Elsevier Science Publishers B.V., 1984.

[38] D. W. Novotny and T. A. Lipo, *Vectror Control and Dynamics of AC Drives*. Oxford, UK: Clarendon Press, 1996.

[39] R. H. Park, "Two-reaction Theory o f Syncrhronous machines - Generalized method of analysis - Part 1," *AIEE Trans.*, vol. 48, pp. 716-727, 1929.

[40] G. F. Franklin, J. D. Powell, and A. Emami-Naeini, *Feedback Control of Dynamic Systems*, Third ed: Addison-Wesley Publishing Company, 1994.

[41] "Position Sensorless Control of Premanent Magnet AC Motors," in *Sensorless Control of AC Motor Drives: Speed and Position Sensorless Operation*, K. Rajashekara, A. Kawamura, and K. Matsuse, Eds. Piscataway, USA: IEEE Press, 1996, pp. 259-268.

[42] J. Hu and B. Wu, "New Integration Algorithm for Estimating Motor Flux over a Wide Speed Range," *IEEE Transactions on Power Electronics*, vol. 13, pp. 969-977, 1998.

[43] J. Holtz and J. Quan, "Drift and Parameter Compensated Flux Estimator for Persistent Zero Stator Frequency Operation of Sensorless Controlled Induction Motor," presented at IEEE-IAS Annual Meeting, 2002.

[44] A. Consoli, S. Musumeci, A. Raciti, and A. Testa, "Sensorless Vector and Speed Control of Brushless Motor Drives," *IEEE Transactions on Industrial Electronics*, vol. 41, pp. 91-94, 1994.

[45] N. Matsui and M. Shigyo, "Brushless dc Motor Control without Position and Speed Sensors," *IEEE Transactions on Industry Applications*, vol. 28, pp. 120-127, 1992.

[46] N. Ertugrul and P. Acarnley, "A New Algorithm for Sensorless Operation of Permanent Magnet Motor," *IEEE Transactions on Industry Applications*, vol. 30, pp. 126-133, 1994.

[47] C. French, P. Acarnley, and I. Al-Bahadly, "Sensorless Position Control of Permanent Magnet Drives," presented at IEEE-IAS Annual Meeting, 1995.

[48] P. L. Jansen and R. D. Lorenz, "Accuracy Limitations of Velocity and Flux Estimation in Direct Field Oriented Induction Machines," presented at EPE Conference, Brighton, UK, 1993.

[49] S. Kondo, A. Takahashi, and T. Nishida, "Armature Current Locus Based Estimation Method of Rotor Position of Permanent Magnet Synchronous Motor without Mechanical Sensor," presented at IEEE-IAS Annual Meeting, 1995.

[50] R. Mizutani, T. Takeshita, and N. Matsui, "Current Model-Based Sensorless Drives of Salinet-Pole PMSM at low Speed and Standstill," *IEEE Transactions on Industry Applications*, vol. 34, pp. 841-846, 1998.

[51] A. Consoli, F. Russo, G. Scarcella, and A. Testa, "Low- and Zero-Speed Sensorless Control of Synchronous Reluctance Motors," *IEEE Transactions on Industry Applications*, vol. 35, pp. 1050-1057, 1999.

[52] F. Blaschke, J. v. d. Burgt, and A. Vandenput, "Sensorless Direct Field Orientation at Zero Flux Frequency," presented at IEEE-IAS Annual Meeting, 1996.

[53] M. Schrodl, "Sensorless Control of AC Machines at Low Speed and Standstill Based on the 'INFORM' Method," presented at IEEE-IAS Annual Meeting, San Diego, USA, 1996.

[54] J.-I. Ha, S.-K. Sul, K. Ide, I. Murokita, and K. Sawamura, "Physical understanding of high frequency injection method to sensorless drives of an induction machine," presented at IEEE-IAS Annual Meeting, 2000.

[55] J.-I. Ha, M. Ohto, J.-H. Jang, and S.-K. Sul, "Design and Selection of AC Machines for Saliency-Based Sensorless Control," presented at IEEE-IAS Annual Meeting, 2002.

[56] K. Ide, I. Murokita, M. Sawamura, M. Ohto, Y. Nose, J.-I. Ha, and S.-K. Sul, "Finite Element Analysis of Sensorless Induction Machine by High Frequency Voltage Injection," presented at IPEC, Tokyo, 2000.

[57] T. M. Wolbank, R. Woehrnschimmel, and J. L. Machl, "Slot Geometry - an Important Design Parameter for Zero Speed Sensorless Control of Standard Induction Machines," presented at EPE-PEMC Conference, Dubrovnik & Cavtat, 2002.

[58] S.-J. Kang, J.-I. Ha, and S.-K. Sul, "Position Controlled Synchronous Reluctance Motor Without Rotational Transducer," presented at IEEE-IAS Annual Meeting, 1998.

[59] T. Aihara, A. Toba, T. Yanase, A. Mashimo, and K. Endo, "Sensorless Torque Control of Salient-Pole Synchronous Motor at Zaro-Speed Operation," *IEEE Transactions on Power Electronics*, vol. 14, pp. 202-208, 1999.

[60] J.-K. Ha and S.-K. Sul, "Sensorless Field-Orientation Control of an Induction Machine by High-Frequency Signal Injection," *IEEE Transactions Industry Appplications*, vol. 35, pp. 45-51, 1999.

[61] H.-M. Ryu, J.-I. Ha, and S.-K. Sul, "A New Sensorless Thrust Control of Linear Induction Motor," presented at IEEE-IAS Annual Meeting, 2000.

[62] C. Caruana, G. M. Asher, K. J. Bradley, and M. Woolfson, "Flux Position Estimation in Cage Induction Machines Using Synchronous HF Injection and Kalman Filtering," presented at IEEE-IAS Annual Meeting, 2002.

[63] M. Schrodl, "Detection of the Rotor Position of a Permanent Magnet Synchronous Machine at Standstill," presented at ICEM, Pisa, Italy, 1988.

[64] M. Schrodl, *Sensorless Control of A.C. Machines*. Dusseldorf: VDI-Verlag GmbH, 1992.

[65] S. Ogasawara and H. Akagi, "Rotor Position Estimation Based on Magnetic Saliency of an IPM Motor-Realization of a Wide-Speed Range from Zero to the Rated Speed," presented at IEEE-IAS Annual Meeting, 1998.

[66] "TMS320C4X Users guide," Texas Instrument 1996.

[67] "QPC/C40S User Documentation," Blue Wave Systems 1997.

[68] B. Palethorpe, "A Novel System Impedance Measurement for Power System Analysis and Improvement in Power Quality," in *School of Electrical and Electronic Engineering*: University of Nottingham, 2002.

[69] N. Teske, "Sensorless Position Control of Induction Machines Using High Frequency Signal Injection," in *School of Electrical and Electronic Engineering*. Nottingham: The University of Nottingham, 2001.

[70] H. W. V. d. Broek, H.-C. Skudelny, and G. V. Stanke, "Analysis and Realization of a Pulsewidth Modulator Based on Voltage Space Vectros," *IEEE Transactions Industry Appplications*, vol. 24, pp. 142-150, 1988.

[71] K. Zhou and D. Wang, "Relationship Between Space-Vectro Modulation and Three-Phase Carrier-Based PWM: A Comprehensive Analysis," *IEEE Transactions on Industrial Electronics*, vol. 49, pp. 186-195, 2002.

[72] J. Holtz, "Pulsewidth Modulation for Electronic Power Conversion," *Proceedings of the IEEE*, vol. 82, pp. 1194-1214, 1994.

[73] F. Briz, A. Diez, and M. W. Dagner, "Dynamic Operation of Carrier-Signal-Injection-Based Sensorless Direct Field-Oreinted AC Drives," *IEEE Transactions on Industry Applications*, vol. 36, pp. 1360-1368, 2000.

[74] N. Mohan, T. Underland, and W. Robbins, *Power Electronics: Converters, Applications and Design*. New York: John Wiley & Sons, Inc., 1995.

[75] A. Muñoz and T. A. Lipo, "On-Line Dead-Time Compensation Technique for Open-Loop PWM-VSI Drives," *IEEE Transactions on Power Electronics*, vol. 14, pp. 683-689, 1999.

[76] J.-W. Choi and S.-K. Sul, "Inverter Output Voltage Synthesis Using Novel Dead Time Compensation," *IEEE Transactions on Power Electronics*, vol. 11, pp. 221-227, 1996.

[77] Y. Mura, T. Watanabe, and H. Iwasaki, "Waveform Distortion and Correction Circuit for PWM Inverters with Switchig Lag-Times," *IEEE Transactions Industry Appplications*, vol. 23, pp. 881-886, 1987.

[78] J.-W. Choi and S.-K. Sul, "A new Compensation Stragegy Reducing Voltage/Current Distortion in PWM VSI Systems Operating with Low Output Voltages," *IEEE Transactions Industry Appplications*, vol. 31, pp. 1001-1008, 1995.

[79] J. Holtz and J. Quan, "Sensorless Vector Control of Induction Motors at Very Low Speed using a Nonlinear Inverter Model and parameter Identification," presented at IAS Annual Meeting, 2001.

[80] N. Kasa and H. Watanabe, "A Mechanical Sensorless Control System for Salient-Pole Brushless DC Motor With Autocalibration of Estimated Position Angles," *IEEE Transactions Industrial Electronics*, vol. 47, pp. 389-395, 2000.

[81] N. Teske, G. M. Asher, M. Sumner, and K. J. Bradley, "Suppression of Saturation Saliency Effects for the Sensorless Position control Induction Motor Drives under Loaded Conditions," *IEEE Transactions Industrial Electronics*, vol. 47, pp. 1142-1150, 2000.

[82] N. Teske, G. M. Asher, M. Sumner, and K. J. Bradley, "Analysis and suppression of high-frequency inverter modulation in sensorless position-controlled induction machine drives," *IEEE Transactions Industry Appplications*, vol. 39, pp. 10-18, 2003.

[83] P. B. Schmidt, M. L. Gasperi, G. Ray, and A. H. Wijenayake, "Initial Rotor Angle Detection Of A Non-Salient Pole Permanent Magnet Synchronous Machine," presented at IEEE-IAS Annual Meeting, New Orleans, Lousiana, 1997.

[84] F. Briz, M. W. Dagner, A. Diez, and R. D. Lorenz, "Static and Dynamic Behaviour of Saturation-Induced Saliencies and Their Effect on Carrier Signal Based Sensorless AC Drives," presented at IEEE-IAS Annual Meeting, 2001.

[85] C. Caruana, G. M. Asher, and K. J. Bradley, "Reduction of Secondary Saliencies for Improved sensorless Control of Induction Machines using HF Injection," presented at EPE-PEMC, Dubrovnik, Croatia, 2002.